Axial flux permanent magnet machines for direct drive applications

Martin, Richard

Axial Flux Permanent Magnet Machines for Direct Drive Applications

Richard Martin

School of Engineering
University of Durham

A thesis submitted in partial fulfilment of the requirements of the Council of the University of Durham for the Degree of Doctor of Philosophy (PhD)

2007

Axial Flux Permanent Magnet Machines for Direct Drive Applications

Richard Martin

2007

Abstract

This thesis explores aspects of the design, analysis, and experimental test of permanent magnet axial flux machines for use in diesel engine generator sets, vertical axis wind turbines, and wheel motors for solar cars.

The characteristic geometry of axial flux machines is naturally more suitable than that of conventional topologies in certain applications. However, convenient and accurate methods of electromagnetic design and analysis are less well established for such machines. The purpose of the research described herein is to benchmark a range of methods of analysis which can be extended to novel designs.

There is a particular focus on the use of Finite Element Analysis to facilitate greater understanding of these machines through the illustration and quantification of the electromagnetic aspects of their operation, and the verification of a selection of analytical approaches. Prototype TORUS machines are first considered; the various analyses are then extended to iron-cored axial flux machines having slotted conductors and finally to a selection of novel machines having concentrated coils and an ironless stator.

The analyses are successfully extended to a range of machines, and the particular suitability of axial flux permanent magnet machines in certain direct drive applications is demonstrated.

Declaration

I hereby declare that this thesis is a record of work undertaken by myself, that it has not been the subject of any previous application for a degree, and that all sources of information have been duly acknowledged.

This thesis is dedicated to the memory of Wally Jackson,

Electrical Engineer par excellence.

Acknowledgements

Firstly, I would particularly like to thank my supervisor, Dr Jim Bumby, for his unfailingly generous support and guidance throughout this work.

I would also like to thank Prof Ed Spooner and Prof Peter Tavner of the University of Durham for sharing their considerable experience with me; Dr Markus Mueller of the University of Edinburgh for his support in the early stages of this work; Roger Hill-Cottingham of the University of Bath for his assistance with the MEGA program; Dr Mariusz Jagiela of the Technical University of Opole, Poland, for sharing his Matlab expertise; Dr Neil Brown, Dr Nazar Al-Khayat, and Dr Salem Mebarki of Newage-AVK-SEG for their encouragement; the engineering technicians at the University of Durham for their assistance, and particularly David Jones for his profound knowledge of all things electrical; Dr Paul Gordon for his electromagnetic expertise; and my comrades in the New and Renewable Energy Group at the University of Durham for the grappa and the rest.

I would like to acknowledge the financial support of the Engineering and Physical Sciences Research Council and Newage-AVK-SEG.

Finally, special thanks go to my family and to Lucy Carey without whom I might never have finished.

Contents

List of Figures

List of Tables

Nomenclature

A, a	Area	m^2
A	Magnetic vector potential	Tm
$a_{conductor}$	Conductor cross sectional area	m^2
A_{RMS}	Electric loading at the mean diameter	A/m
a_{slot}	Slotted conductor cross sectional area	m^2
a_{wire}	Wire cross sectional area	m^2
A_{zn1}	Axial component of magnetic vector potential in region 1, *nth* harmonic	Tm
A_{zn2}	Axial component of magnetic vector potential in region 2, *nth* harmonic	Tm
B	Flux density	T
B_{core}	Stator core flux density	T
B_{disc}	Rotor disc flux density	T
B_{fund}, $\hat{B}$	Peak value of the fundamental flux density wave, magnetic loading	T
B_{rem}, B_r	Permanent magnet remanence	T
B_{tooth}	Tooth flux density	T
B_z	Axial flux density	T
c	Running clearance	m
c	Number of coils	
c'	Effective running clearance	m
d	Diameter	m
d_{bobbin}	Coil bobbin edge thickness	m
$D_{coil\ inner}$	Concentrated coil inner diameter	m
$D_{coil\ outer}$	Concentrated coil outer diameter	m
$d_{conductor}$	Conductor diameter	m
$d_{conductor}$	Slot depth available for conductors	m

D_i	Core inner diameter	m
$D_{i,mag}$	Magnet inner diameter	m
D_m, D_{mean}	Core mean diameter	m
D_o	Core outer diameter	m
$D_{o,mag}$	Magnet outer diameter	m
d_{slot}, d_s	Slot depth	m
d_{turn}	Diameter of a turn	m
d_{wire}	Wire strand diameter	m
D_{wire}	Wire diameter	m
E	EMF	V
E_{ph}	EMF per phase	V
$E_{coil,\,n}$	EMF per coil, *nth* harmonic	V
F	Force	N
f	Frequency	Hz
f_{elec}	Electrical frequency	Hz
f_{mech}	Mechanical frequency	Hz
F_{total}	Total closing force between rotor discs	N
g_{eff}	Air-gap effective length	m
$g_{eff,end}$	Effective gap of the end winding	m
H	Magnetic field intensity	A/m
h	Surface heat transfer coefficient	$W/m^2.^oC$
$\boldsymbol{H}$	Magnetic field intensity	A/m
H_a	Magnetic field intensity in air	A/m
H_m	Magnetic field intensity in the permanent magnet	A/m
H_{yn1}	Magnetic field intensity in the y direction in region 1, *nth* harmonic	A/m
H_{yn2}	Magnetic field intensity in the y direction in region 2, *nth* harmonic	A/m
i	Instantaneous current	A

I	Current	A
I_{rated}	Rated current	A
I_{slot}	Total slot current	A
$I_{slotted}$	Rated current in a slotted TORUS	A
I_{TORUS}	Rated current in an air-gap wound TORUS	A
J	Current density	A/m^2
$\bar{J}$	Magnet equivalent current density	A/m^2
k	Heat transfer coefficient	$W/m.^oC$
k_l	Flux enhancement (leakage) factor	
k_{bobbin}	Plastic bobbin heat transfer coefficient	$W/m.^oC$
k_c	Running clearance modulator	
$k_{campbell}$	Core diameter ratio	
k_{carter}	Carter coefficient	
k_{copper}	Copper heat transfer coefficient	$W/m.^oC$
k_{dn}	*nth* winding distribution factor	
k_{fill}	Fill factor	
$k_{insulation}$	Insulation heat transfer coefficient	$W/m.^oC$
k_{loss}	Power loss factor	
K_n	Linear current density	A/m
k_{slot}	Slot depth to slot width ratio	
k_{tooth}	Tooth to slot ratio	
$k_{winding}$	Wound conductors heat transfer coefficient	$W/m.^oC$
l	Length	m
L	Coil inductance	H
l_{eff}	Core effective length	m
$L_{end,\ n}$	Coil self inductance in the end winding region, *nth* harmonic	H
L_{gap}	Gap leakage inductance per slot	H
$L_{gap\ leakage}$	Gap leakage inductance per pole per phase	H

$L_{main,\ n}$	Coil self inductance in the main winding region, *nth* harmonic	*H*
l_{phase}	Length of a phase conductor	*m*
$L_{self,phase}$	Phase self inductance (measured)	*H*
L_{slot}	Slot leakage inductance per slot	*H*
$L_{slot\ leakage}$	Slot leakage inductance per pole per phase	*H*
L_{syn}	Synchronous inductance	*H*
$L_{syn/coil}$	Synchronous inductance contribution per coil	*H*
l_{turn}	Length of a mean turn	*m*
m	Number of phases	
m_{core}	Stator core mass	*kg*
$M_{end,\ n}$	Coil mutual inductance in the end winding region, *nth* harmonic	*H*
$M_{main,\ n}$	Coil mutual inductance in the main winding region, *nth* harmonic	*H*
m_{stator}	Stator total iron mass	*kg*
m_{teeth}	Stator teeth mass	*kg*
N	Turns per pole per phase	
n	Rotational speed	*RPM*
$N_{/slot}$	Turns per slot	
N_{coil}	Number of turns per concentrated coil	
$n_{parallel}$	Number of parallel strands	
$n_{slots/pole/phase}$	Number of slots per pole per phase	
$n_{strands}$	Number of strands per conductor	
P	Power	*W*
p	Poles	
P	Permeance	*Wb/At*
$P_{density}$	Power density	W/m^3
P_{eddy}	Conductor eddy loss	*W*

pf	Power factor	
P_{I2R}	I^2R power loss	W
P_{in}	Power input	W
P_{iron}	Stator core iron loss	W
P_{loss}	Power loss	W
P_{out}	Power output	W
R	Resistance	Ω
$R_{conductor}$	Thermal resistance of slotted conductor	$W/^oC$
R_{core}	Thermal resistance of the stator core heat transfer path	$W/^oC$
$R_{core+tooth}$	Thermal resistance of a heat transfer path comprising stator core and tooth	$W/^oC$
R_{inner}	Inner radius	m
R_{liner}	Thermal resistance of a slot liner	$W/^oC$
r_m	Coil mean radius	m
R_{outer}	Outer radius	m
R_{phase}	Phase resistance (measured)	Ω
R_{slot}	Slot thermal resistance	$W/m.^oC$
$R_{surface\ HT}$	Surface heat transfer equivalent thermal resistance	$W/m.^oC$
R_{tooth}	Thermal resistance of a tooth	$W/^oC$
R_w	Phase winding resistance	Ω
T	Temperature	^oC
T	Torque	Nm
t_a	Winding thickness	m
t_{copper}	Axial depth of copper in an air-cored coil	m
t_{core}	Stator core thickness	m
t_{disc}	Rotor disc thickness	m
$t_{insulation}$	Conductor insulation thickness	m
$t_{insulation(core)}$	Core insulation thickness	m
t_{liner}	Slot liner thickness	m

t_m, Y_m	Magnet thickness	m
t_{ring}	Stator supporting ring thickness	m
t_{core}	Stator core thickness	m
t_{stator}	Stator overall thickness	m
V	Terminal voltage	V
V_{core}	Stator core volume	m^3
V_{reg}	Voltage regulation	$(\%)$
w	Coil width	m
$w_{conductor}$	Slot width available for conductors	m
w_{slot}, w_s	Slot width	m
$w_{slots\ total}$	Total slot width per pole per phase	m
w_{tooth}	Tooth width	m
$w_{tooth\ inner}$	Tooth width at the inner core diameter	m
X_L	Inductive reactance	Ω
X_{mutual}	Reactance from mutual inductance component	Ω
X_{self}	Reactance from self inductance component	Ω
X_{syn}	Synchronous reactance	Ω
Y_1	y-coordinate of current sheet	m
Y_2	Gap between iron boundaries	m
Z	Complex impedance	Ω
α	Pole arc to pitch ratio	
α	Temperature coefficient of resitivity	$\Omega m/^oC$
γ	Coil displacement angle	*radians*
δ	Power angle	*degrees*
δS	Elemental cross sectional area	m^2
ΔT	Temperature difference	^oC
η	Efficiency	$(\%)$
θ_c	Electrical angle between coils	*Radians*
θ_p	Electrical angle between magnet poles	*Radians*

λ	Wavelength	*m*
λ	Flux linkage in air	*Wb*
λ_0	Coil bore flux linkage in air	*Wb*
λ_1	Coil flux linkage within coil radii, in air	*Wb*
μ_o	Permeability of free space, $4\pi \times 10^{-7}$	*H/m*
μ_r, μ_{rec}	Magnet recoil permeability	
ρ_0	Resistivity at 0°C	*Ωm*
ρ_{core}	Stator core density	kg/m^3
ρ_T	Resistivity at T°C	*Ωm*
σ	Mean coil spread	*electrical degrees*
σ_{Di}	Coil spread at inner diameter	*electrical degrees*
τ_m	Pole arc	*m*
$\tau_{p(m)}$	Pole pitch	*m*
$\tau_{p(rad)}$	Pole pitch	*radians*
τ_s	Slot pitch	*m*
φ	Power factor angle	*degrees*
φ	Flux	*Wb*
φ/m	Flux per metre	*Wb/m*
φ_{core}	Stator core flux	*Wb*
φ_{disc}	Rotor disc flux	*Wb*
$\varphi_{main,\ n}$	Working flux in the main winding region, *nth* harmonic	*Wb*
$\varphi_{pp,n}$	Flux per pole, *nth* harmonic	*Wb*
ψ	Flux linkage	*Wb*
$\psi_{coil,\ n}$	Coil flux linkage, *nth* harmonic	*Wb*
ω	Angular frequency	*rad/s*

Chapter 1. Introduction

Recent advances in permanent magnet materials and power electronic devices have reawakened interest in alternative electrical machines, facilitating the development of novel, application-specific topologies, some with interesting characteristics and significant advantages over the traditional genres. Permanent magnet axial flux machines are particularly appropriate for use in compact engine-generator sets, and the development of machines specifically for this application was the subject of Brown's doctoral thesis, [1]. High electric and magnetic loadings are possible and the correspondingly high reaction torque achievable, coupled with a convenient geometry, make permanent magnet axial flux machines suitable candidates for other direct-drive applications such as low speed wind turbines, [2], and in-wheel motors, [3].

Conventional machines such as the synchronous generator and the induction motor, upon which the modern world is heavily reliant, are well understood and methods of design and analysis of these machines are sophisticated and highly developed. By contrast, machines that have been devised more recently pose new challenges to understanding and scientific methodology. The purpose of this thesis, therefore, is to describe, verify, and benchmark a range of methods and techniques specifically for the design and analysis of permanent magnet axial flux machines for certain direct-drive applications so as to build up a body of expertise for further research in this area.

This thesis focuses particularly on electromagnetic Finite Element Analysis (FEA) as a major tool in the process. The MEGA software, [4], developed by the Applied

Magnetics research group at the University of Bath, is used extensively, and its application to the various machines considered is described in detail throughout the work. In particular, electromagnetic FEA is used to:

- Evaluate the assumptions used in analytical methods, particularly the 2D approximations applied in electromagnetic field analyses
- Verify the predictions of analytical methods both in terms of the magnitudes and characteristics of electromagnetic fields, and the resultant equivalent circuit parameters
- Predict the electromagnetic performance of a range of machines
- Corroborate the results of experimental tests and assist with interpretation and understanding
- Illustrate the electromagnetic fields present in a range of permanent magnet axial flux machines, thereby aiding understanding of the mode of operation of these machines as well as the nuances of design and analysis
- Perform virtual tests that may not be carried out in the laboratory owing to practical limitations

This work was generously funded by the Engineering and Physical Sciences Research Council (EPSRC), as well as a Collaborative Award in Science and Engineering (CASE) arising from a long-established partnership between the School of Engineering at the University of Durham, and Newage-AVK-SEG. As a consequence of this CASE, the foundation of the thesis is the derivation, verification and benchmarking of a range of methods and techniques specifically for the design and analysis of the air-gap wound TORUS machine of Spooner and Chalmers, [5], a version of which is now being trialled by Newage-AVK-SEG as part of a new generation of compact engine-generator sets. Any improvements to such a generator

in terms of size, mass, efficiency, or cost are potentially of great interest in this application, and so the methods and techniques developed are then extended to the investigation of permanent magnet axial flux machines having a slotted stator winding.

Furthermore, as this work unfolded, a number of mechanical engineering firms expressed an interest in permanent magnet axial flux machines for use as direct-drive generators in small scale Vertical Axis Wind Turbines (VAWTs). There is currently significant interest in the development of VAWTs for the urban environment, [6], although suitable generators are not readily available. Firms with neither electrical machine manufacturing expertise nor appropriate facilities are frequently forced down the route of using a standard induction machine and gearbox arrangement, but this has a number of disadvantages and a purpose built direct-drive synchronous machine operating at variable speed is a strong alternative candidate. A TORUS prototype was subjected to field tests by such a firm and certain problems emerged, leading to Bumby's development of a novel permanent magnet axial flux topology having concentrated coils and an ironless stator. The topology could easily be realised by a mechanical engineering workshop with no previous experience of electrical machines manufacture and is the subject of an international patent, [7].

The emergence of this new topology facilitates the extension and further development of the methods and techniques for the design and analysis of permanent magnet axial flux machines for direct-drive applications forming the subject of this thesis. Finally, the methods and techniques thus far developed are extended to further VAWT generators involving different pole shapes and larger specifications, as well as the application of the topology as an in-wheel motor for a solar powered car.

The permanent magnet axial flux machines considered in this thesis were conceived with simplicity, economy, and ease of assembly and manufacture in mind; these are overarching principles of the research here described. In summary, the thesis contains proven methods and techniques of design and analysis which were used in the development of a range of novel machines for direct-drive applications, and will be of use in the course of further research in this field.

1.1. Thesis outline

Chapter 2 is a literature review, giving an overview of relevant developments in axial flux machines. Chapter 3 and Chapter 4 then serve as a full exposition of the analytical, FEA, and experimental methods used in the analysis and test of two prototype machines along the lines of the TORUS design of Spooner and Chalmers, [5]. This facilitates benchmarking of the basic equations and approaches upon which the remainder of the thesis builds. Two analytical approaches to the electromagnetic analysis are outlined: a general field solution as described by Bumby et al, [8], and a more simple approach utilising magnetic circuit analysis. Conventional techniques are extended to the calculation of loss in the machine, thermal analysis, and performance prediction based on the synchronous machine equivalent circuit. The analytical predictions are then verified by the FEA and experimental test of the two prototype machines. Notably, no FEA of axial flux machines had previously been undertaken at Durham and so Chapter 4 focuses particularly on the development of FEA models in order to benchmark this type of analysis. Experimental verification also provided the author with practical experience in the operation of this genre of machine as well as the experimental methods used in this field.

Following the development of a range of basic techniques, Chapter 5 describes the first steps towards utilising these for new designs through the modification of an existing TORUS design so as to place the stator winding in slots. Alternative designs are drawn up and the analytical and FEA techniques are extended to the analysis of two modified machine designs. Comparison between the original TORUS design and its slotted counterparts is made.

In Chapter 6 a new design for a 40kW, 4500RPM prototype machine with a slotted stator winding is drawn up for comparison with a 40kW TORUS prototype, [9]. The previous work concerning slotted variants of the basic TORUS machine is utilised, but a more independent design is described. A general design procedure for slotted machines is developed and analytical expressions for the loss mechanisms in the new slotted design are derived along with a more sophisticated thermal model so that the entire design process can be implemented in a spreadsheet. The chapter concludes with an analytical comparison between the TORUS and the new slotted design.

In Chapter 7, attention is turned specifically to axial flux machines for small-scale wind turbine applications. During the course of this research, a design was conceived by Bumby, [7], which addresses the problems highlighted by the transfer of the TORUS to VAWTs and capitalises on the natural suitability of axial flux machines to this application. The novelty of the new design arises from the specification of an ironless stator with concentrated, bobbin-wound coils, conceived with simplicity and ease of manufacture in mind. In this way it complements the designs so far considered, expanding the family of axial flux machines to which the analyses are extended. The construction and analysis of a prototype is described with particular focus on FEA and experimental tests.

Finally, Chapter 8 details three further machines having ironless stators and concentrated coils. Each of the three offers something new in terms of either a particular design nuance, extension to a new application, or the FEA approach required as a result of these advances. The first is a specification for larger version of Bumby's novel machine, [7], having different pole and coil numbers; this leads to the use of linear (translating) dynamic FEA. The second is a prototype motor for a solar-powered car. The increased importance of a lightweight machine with the maximum power density achievable in this application led to the use of trapezoidal magnets and coils. Modified analytical methods are described and compared with FEA and the results of some initial experimental tests. Finally, the third design presents a combination of the principles outlined previously in the chapter, namely a move to a significantly larger machine for the VAWT application which utilises trapezoidal poles and coils much like the motor designed for the solar-powered car; in this case, analytical and FEA predictions are compared for a 10kW, 140RPM design.

1.2. Original contributions to the advancement of knowledge

The author claims the following to be original contributions to the advancement of knowledge:

- The benchmarking of the unified 2D approach to the analytical solution of the electromagnetic fields arising from permanent magnets and phase currents in permanent magnet axial flux machines of Bumby et al, [8], with the results of FEA and experimental tests, and a conventional magnetic circuit analysis.
- The extension of the unified 2D approach of Bumby et al, [8], to permanent magnet axial flux machines with a slotted stator winding.
- The benchmarking of the unified 2D analytical solution for permanent magnet axial flux machines with a slotted stator winding alongside the results of FEA and a conventional magnetic circuit analysis.
- The derivation of a design procedure using the unified 2D analytical solution for permanent magnet axial flux machines with a slotted stator winding
- The design of a new 40kW, 4500RPM generator for a diesel engine generator set using this approach.
- The FEA and experimental test of Bumby's novel permanent magnet axial flux generator for a VAWT, [7].
- The FEA and experimental test of Bumby's novel permanent magnet axial flux motor for a solar-powered car, [7].

Chapter 2. Axial flux machines in the literature

2.1. The origins of axial flux machines

In 1831 Michael Faraday produced DC current using what was the first electrical generator, consisting of a copper disc that rotated in an axial field, [10]. The device later became known as the *"homopolar generator"* and the concept has been used to some extent in more modern times, for example in the work of Bumby on superconducting DC machines, [11]. Although Faraday's work represents a huge milestone in the understanding of electricity and magnetism, the generator concept and the axial flux orientation did not gain wide popularity.

However, soon after Faraday's demonstration Thomas Davenport of Brandon, Vermont built a radial flux machine along more conventional lines and took out a USA patent on the design in 1837, [12]. It was not until the 1970s that axial flux machines gained any popularity as a viable alternative. Notably, the work of Campbell, [13], which arose from new developments in permanent magnet material technology, significantly renewed interest in machines with axially-oriented flux, opening up a field of research that is still advancing today.

2.2. Axial flux machines defined

For the purpose of this thesis, axial flux machines are defined as rotating electrical motors/generators in which magnetic flux crossing the gap between the rotor(s) and stator(s) does so predominantly in the axial direction. As a result, such machines tend to be disc-shaped, having a relatively large diameter and a short axial length by

comparison with the more conventional radial flux machines, which tend to be cylindrical. This distinction is illustrated, Figure 2.1.

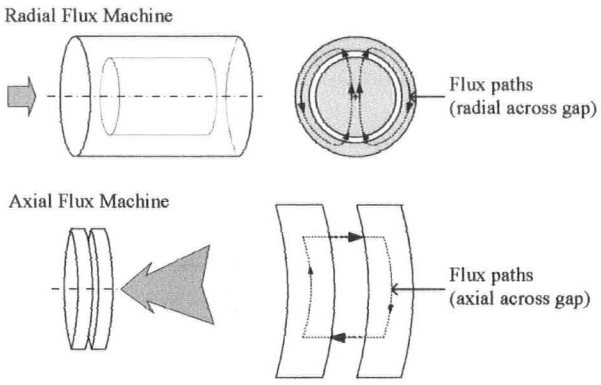

Figure 2.1: Basic distinction between axial and radial flux

Alternatively, a radial flux machine may be transformed into an axial flux machine as follows. Consider a simplified radial flux machine, having a permanent magnet rotor and a stator with a distributed winding, Figure 2.2.

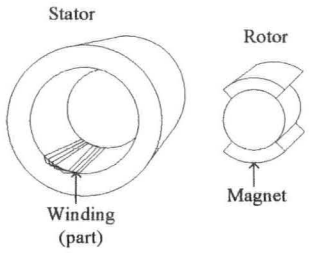

Figure 2.2: Simplified radial flux machine

Consider unwrapping the stator and rotor components and viewing each in a linear format, Figure 2.3

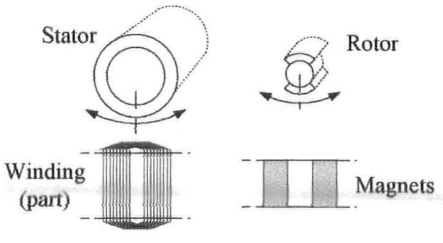

Figure 2.3: Unwrapped stator and rotor

Now consider rewrapping the linear components in a new orientation, Figure 2.4.

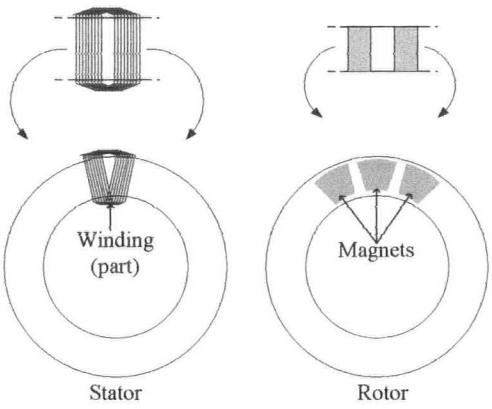

Figure 2.4: Reoriented stator and rotor

This reorientation has yielded a format where the magnetic flux passes between stator and rotor in the axial direction, and where the machine is effectively annular with an active area framed by inner and outer diameters. In fact, it is the requirement for axial mounting of the rotating part that creates disc-type components. Compare this with the radial flux machine where both the diameter and the axial length of the air-gap determine the active area. This decoupling of the active area from the axial length is a significant feature of axial flux machines and is fundamental to the application of this concept. Another significant feature is the arc-shape of each magnet, commonly implemented as a trapezium.

Also, the axial flux configuration is naturally suited to high pole numbers since increasing the number of poles in an electrical machine reduces the flux per pole and hence the back iron requirement in the stator and rotor components. In a radial flux machine, much of the rotor could be under-utilised in such circumstances but an axial flux machine can simply have a shorter axial length.

2.3. Orientations of axial flux machine

Before exploring axial flux topologies beyond the primitive reorientation shown in Figure 2.4 it would be useful to consider a 2D simplification. In radial flux machines it is straightforward to assume infinite length in the axial direction and so consider a 2D cross-section as shown, Figure 2.5.

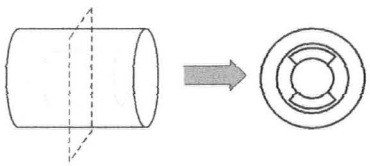

Figure 2.5: 2D radial flux

In the axial flux arrangement a 2D simplification is less obvious since it is not clear that any dimension could be considered infinitely long. It may be the case that such a machine is inherently 3D and must be analysed as such. Consider the active length of the axial flux orientation of Figure 2.4 to be infinitely long in the radial dimension and hence consider the geometry of the machine its mean radius. Then, consider viewing the annular stator and rotor of Figure 2.4, looking radially inwards toward the centre from a point beyond the outer diameters of these components. If the annuli are unwrapped, i.e. reversing Figure 2.4, whilst maintaining this radial viewpoint, a 2D realisation occurs as illustrated in Figure 2.6.

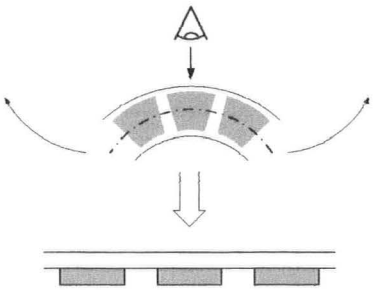

Figure 2.6: 2D axial flux

The early machines described by Campbell, [13], were brushed DC motors having only a single stator disc with permanent magnets, an ironless rotor with a distributed winding not unlike that shown in Figure 2.4, and a stationary element of back-iron on the far side of the armature. The 2D development of this is shown, Figure 2.7.

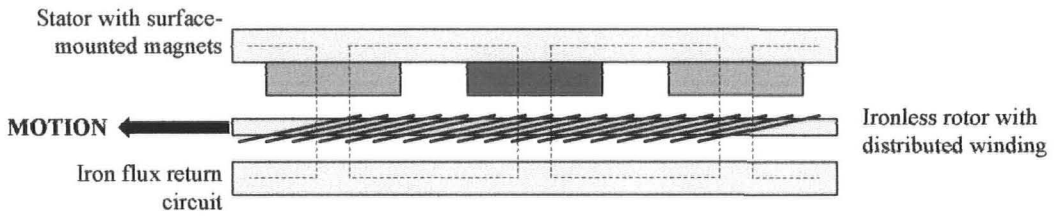

Figure 2.7: 2D development of a basic brushed DC motor

The iron flux return component is static with respect to the field, hence limiting the potential for eddy loss in the iron components. However, the effective air-gap is large since rare-earth magnets have permeability close to that of free space and the rotor is ironless, such that the magnetic flux density experienced by the armature winding is likely to be weak. A natural extension of this topology is therefore to increase the volume of rare-earth magnet material using a more symmetric design with a pair of stator magnet arrays. Neglecting the winding for the moment, this yields the excitation field setup shown in Figure 2.8.

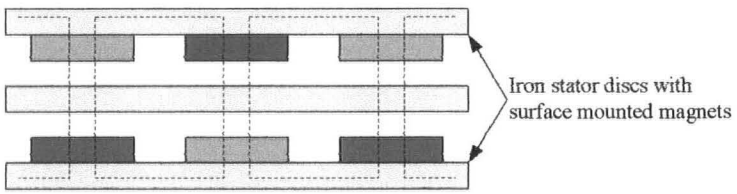

Figure 2.8: "Shine-through" axial flux arrangement

In the arrangement illustrated by Figure 2.8, north poles face south poles and the flux may simply be considered to "shine through" the rotor; this "shine-through"

arrangement is one of two generic types of permanent magnet axial flux machine considered in this thesis.

The other generic machine type considered was devised by Spooner and Chalmers, [5], but is related to the earlier work of Evans and Eastham, [14]. It utilises circumferential flux paths in the central component, as shown in Figure 2.9. In this case, north poles face north poles in the axial direction and, if the central component is ferromagnetic, flux takes an axial path across the air-gap but travels circumferentially for a distance equal to a pole pitch, and finally turns once more to cross the gap and complete the circuit.

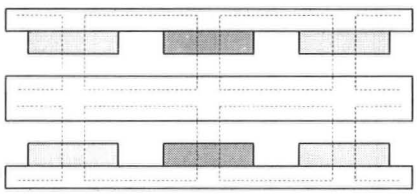

Figure 2.9: Axial flux arrangement with circumferential paths

The work of Spooner and Chalmers, [5], applied this arrangement in the generating mode, whereby the components upon which the magnets are mounted rotate in tandem either side of a central stator with a polyphase winding. The winding itself is much simpler than that of Campbell, [13], since it is toroidal in nature; thus spatial distribution is automatically achieved as the winding progresses around the stator core in the manner of a spiral. Although flux crosses the air-gap in the axial direction, it is actually travelling circumferentially when it links the turns of the winding, as shown in Figure 2.10. Spooner and Chalmers called this arrangement the TORUS, [5], and its investigation is the starting point of this thesis. It is interesting to note that the excitation field in this arrangement is split symmetrically between

each rotor and therefore that the stator core could be formed in two isolated pieces joined at the axial centre of the machine.

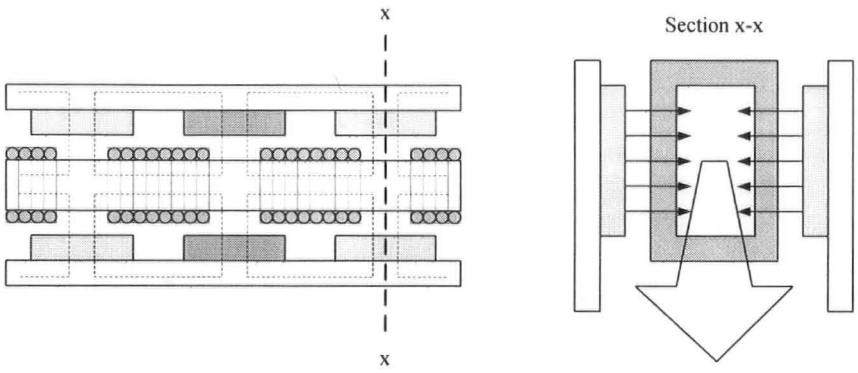

Figure 2.10: TORUS arrangement

Comparison should be made with the double-disc alternator with AC-side excitation devised by Evans and Eastham, [14]. Although this machine has a wound field mounted around (but not rotating with) a central hub, the flux does cross the air-gap axially and the novel field arrangement gives rise to circumferentially travelling excitation flux which links the toroidal winding. Figure 2.11 shows the concept.

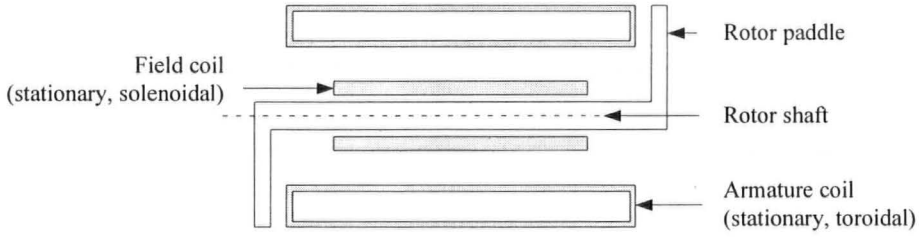

Figure 2.11: Rough concept of the machine of Evans and Eastham, [14]

A wound field arrangement along similar lines has been combined with a permanent magnet TORUS-type machine in the novel topologies of Haydock and Brown, as described in Brown's doctoral thesis, [1].

It should be noted that Campbell's early motor designs, [13], were of the brushed DC variety. Hence the rotor(s) carried the winding and therefore also required slip rings

and a commutator. Developments in power electronics over more recent years have facilitated widespread use of the so-called brushless DC arrangement. In this case, the rotor(s) can carry the magnets and the winding can be accommodated by the stator, allowing for a much simplified construction. This arrangement has much in common with the synchronous generator, in terms of its topology and mode of operation, such that a single machine can now be operated as a synchronous generator and a brushless DC motor. The machines considered by the author during the course of this research have stationary windings and permanent magnet rotors, and are mostly considered to operate as synchronous generators although some references are made to operation in the brushless DC mode.

Having established the two generic types of permanent magnet axial flux machine to be considered in this thesis, namely the "shine-through" arrangement and the TORUS machine, a more detailed review of the literature is presented.

2.4. Literature review

A survey of the literature on axial flux machines indicates a few themes that have been consistently presented and which may be used to classify work in the field. It is acknowledged that much of the literature follows more than one theme and that a number of different influences have made the advancement of knowledge in this area to be somewhat haphazard. However, all of the literature encountered by the author in this field takes up at least one of these themes and so this review attempts a thematic presentation.

2.4.1. Applications of axial flux machines

The literature describes axial flux machines in a range of applications that are often unusual; having unconventional geometric requirements to which the axial flux topology is naturally suited.

Firstly, Campbell, [13], [15], acknowledged the potential applications of a cooling fan motor for an automobile radiator, and an electric vehicle traction motor. Specifically, Campbell described a traction motor for a bicycle wheel, [15] and Campbell et al described the design of an axial flux motor for use in an electric wheelchair, [16].

In 1987, Chan presented a general survey of axial flux machines, [17], describing high frequency inductor alternator applications and highlighting the potential of single phase machines in small domestic applications.

The seminal paper of Spooner and Chalmers, [5], in which the TORUS machine was first described, outlined the particular suitability of this machine in portable engine-generator sets, citing the following advantages:

- *A light, compact mechanical configuration well suited to integration with an engine unit*
- *A short axial length allowing direct mounting on the engine shaft and eliminating the need for separate bearings and couplings*
- *A large radius giving rise to a high moment of inertia such that the flywheel is redundant*
- *The possibility of operation as a brushless DC motor thereby eliminating the starter motor and its engagement mechanism*

This has given rise to a substantial corpus of work on engine integration of such machines, whether as standalone generator sets or as part of a hybrid vehicle arrangement. In particular, the TORUS topology has further been investigated by Bumby, Brown, Brooking et al, ([18] - [23]), and other axial flux arrangements have been used in this application by Coles, Hill-Cottingham, and Walker et al, ([24] - [26]).

Nakata et al described a brushless DC motor for a computer floppy-disk drive, [27], and Furlani mentioned low-torque servo and speed control applications, [28]. Proca et al described low power applications such as servomotors and alternators, [29], whilst Gu et al noted pumps, fans, wheels, and floppy-disk drives [30]. Schmidt and Patterson added a ceiling fan to the list of axial flux motor applications, [31], Eastham et al added an aircraft drive, [32], and Huang et al a submarine ship drive, [33].

A high speed axial flux machine has been developed at Imperial College, London over recent years and commercial production took place in 1999 at the Turbo Genset Company. Pullen et al described the application of these machines in automotive applications and in hybrid powertrains in conjunction with a gas turbine in particular, [34], utilising multistage machines having ratings between 12kW and 100kW at 60,000RPM. In the same paper the potential coupling of this machine, via a gearbox, to internal combustion engines in automotive applications was also discussed. In a later paper from the Turbo Genset Company, [35], Etemad described a modular, multistage 50kW machine coupled with a small gas turbine for the auxiliary power unit market, focusing on the construction as well as some starting and power conditioning issues. Also at Imperial College, Holmes et al described a generator for

a microfabricated axial flow micro turbine, reporting a generator outer diameter of 7.5mm generating 2.2mW at 30,000RPM, [36].

In 1996, Spooner and Williamson described a multipole radial field machine with permanent magnet excitation for use as a direct-coupled generator in a wind turbine, [37] and Spooner et al considered modular generator design in the wind turbine application, [38]. Although from a radial flux perspective, these papers pre-empted the work on simply-constructed axial flux machines for wind turbines described later in this thesis. Spooner and others successfully applied the TORUS-type design to direct-drive wind turbines later; notably Chalmers et al, [2], described a 5kW machine with the following advantages in this application:

- *A short axial length and a high power to weight ratio facilitating direct, compact integration with the wind turbine*
- *A natural fan action from the disc rotors and magnets providing good cooling even at low rotational speeds*
- *Low inductances arising from the slotless air-gap winding, and short end-windings of low resistance, the combined effect of which is a good voltage regulation characteristic*
- *A slotless winding limiting cogging torque, noise, vibration, and high-frequency rotor loss*

Muljadi et al described a modular axial flux machine in this application, [39], and Lombard and Kamper described the design, analysis and performance of a machine with an ironless stator for high efficiency applications such as flywheels, direct-drive wind turbines, and engine-generator sets, [40].

Owing to the fact that an axial flux motor can be integrated with a wheel, thereby eliminating almost all of the conventional transmission arrangements associated with internal combustion engines, the "wheel motor" has proved a particularly popular application of axial flux machines and this was developed by Zhang, Profumo, Cavagnino et al, ([41] - [46]). Hredzak and Gair et al also considered this application with a focus on the reduction of torque ripple by various means, [47], [48], whilst Johansen et al considered a wheel motor for a bicycle, [49]. Mendrela et al referred to the electric scooter application as the setting for their work on different stator structures, [50], and Marignetti and Scarano described designs for two-wheeled vehicles generally, [51], [52]. Bianchi et al described a motor design for an electric scooter, [53] whilst Terashimi et al described motor and controller arrangements in an electric vehicle with four in-wheel motors, [54]. Also, Tseng and Chen described the computer aided design and analysis of a wheel motor, [55].

Caricchi, Crescimbini, and Solero et al at the University *"La Sapienza"* in Rome, often in collaboration with other authors, published a range of papers on axial flux machines in a variety of applications, including vehicle wheel motors in general, [56] - [57], a motor drive for an electric scooter, [58], an adjustable speed pump, [59], an air-cored generator aboard ships, aircraft, or hybrid electric vehicles, [60], a modular motor for a ship propulsion drive, [61], a direct-drive elevator with a severe space constraint, [62], and a compact generator for hybrid vehicles, [63].

The suitability of permanent magnet axial flux machines as wheel motors is especially in evidence in the solar car application where high efficiency and low mass are of paramount importance. Patterson and Spee described some aspects of the design and development of axial flux motors for this application, [3], [64], and

Lovatt et al described a very high performance machine utilising a Halbach magnet array and an ironless air-gap winding, [65].

Thus the axial flux machine appears in a wide range of applications where its natural characteristics offer significant geometrical advantages over more conventional genres. In addition, a number of other characteristics of permanent magnet axial flux machines are alluded to, namely: high efficiency, high power density, low loss, and simplicity of construction. Clearly, not all these characteristics are unique to axial flux machines and some authors have made objective comparisons with radial flux machines.

2.4.2. Comparison with radial flux machines

Leung and Chan, [66], offered a geometric comparison between axial and radial flux topologies by considering ratios of flux and current between the two for the same specific magnetic and electric loadings, and deriving a power ratio as follows:

$$\frac{P_{axial}}{P_{radial}} = \frac{(D_o + D_i)^2 (D_o - D_i)}{4d^2 l} \qquad \text{Eq. 2.1}$$

In this equation, D_o and D_i are the outer and inner diameters of the axial flux machine armature core, whilst d and l are the diameter of the radial flux air-gap and the axial length of the radial flux machine respectively.

When considering direct-drive generators for wind turbines, Spooner and Williamson outlined a range of designs having diameters of approximately two metres, [37]. An axial flux topology was considered but discounted because of the practical problems of a predicted axial force of 155kN between the stator and each rotor disc, and the structural stability of the stator core.

At the Politecnico di Torino, Profumo et al presented a survey of axial flux machine types with particular reference to the electric car application, [42]. Comparison was made between axial and radial flux induction machines assuming a fixed performance and considering the motor rated power per cubic metre of machine volume. The resulting power density ratio was defined as follows:

$$\frac{P_{density(axial)}}{P_{density(radial)}} = \frac{p\left(1+\frac{\pi}{2p}\right)^2}{2\pi} \qquad \text{Eq. 2.2}$$

Note that this ratio is a function of the poles, p; that the ratio increases with p; and that axial flux induction machines appear to exhibit a larger power density than their radial flux counterparts in multipole configurations.

In a later paper from the same department, Cavagnino et al presented a full comparison between axial and radial flux structures for PM synchronous motors, [46]. The comparison was made in terms of electromagnetic torque developed, and the following remarks were made:

- *Radial flux machines are preferable where the axial length of the motor is long; as the pole number increases the torque capability improves to a point, but then decreases as iron losses increase*
- *Axial flux machines can deliver high torque if the axial length is very short, and if the pole number increases the torque density continues to increase even at high pole numbers i.e. the active weight decreases more than the electromagnetic torque as pole number increases*

It was concluded that axial flux machines are attractive for flat (i.e. axially short) geometries with high pole numbers.

Laithwaite's classic principle of electric machine goodness, [67], was extended to contemporary machines including permanent magnet axial flux motors by Brice and Patterson, [68]. The goodness factor of an axial flux machine was shown to be the same as that in the radial flux case and an argument for maximising the pole pitch was made.

Brown et al presented an idealised approach to the electromagnetic comparison by considering the magnetic and electric loadings to remain constant in each case, thereby reducing the analysis to geometrical considerations, [20]. Where a fixed volume of permanent magnet material was considered, it was concluded that for machines with pole numbers above ten the axial machine is potentially the smaller, but that the radial flux machine is significantly the smaller where very low pole numbers are used.

Finally, Huang et al considered electrical machine design as a system optimization where there are a variety of potential topologies and where the design task is more complicated than a simple sizing exercise, [69]. A general approach to sizing different machine topologies was derived and design guidelines were set out.

Although a range of opinion exists, it is commonly agreed that axial flux machines are capable of a performance and efficiency comparable with their radial flux counterparts, and in certain configurations, namely in small machines where the axial length is short and the pole number large, axial flux machines can make better use of the space available. This is in addition to the advantages that may be gained by using a machine with a large diameter and a small axial length.

2.4.3. Novel axial flux machines

Much research in this field utilises a small number of established topologies as a basis for analysis or optimization, extension to new applications, or slight modification. However, there are a number of publications presenting truly novel axial flux machines and these are outlined here.

In 1974, Campbell published *"principles of a permanent magnet axial-field DC machine"*, [13], which formalised his own prior work on "pancake-shaped" and "disc-armature" machines. Working in the brushed DC mode, these machines consisted of axially polarised permanent magnets on a stator disc with a second, flux return disc and a rotating, distributed armature as shown in Figure 2.8 Nakata et al described a similar machine, but in the brushless DC mode for a 3.5'' computer floppy-disk drive, [27]. In a later paper, [70], Campbell assessed the impact of an iron powder compact material in place of the previous laminated ring. Later still, Nafisi and Campbell described an investigation into the use of powdered iron wedges as teeth in the armature of an axial field DC machine, [71].

Alternative materials also featured in the work of Jensen et al, [72], who described a low-loss motor which has a TORUS-type topology but specifies a tape wound amorphous iron stator core, Cvetovski et al who described improvements to a disk motor through use of soft a magnetic iron composite material, [73], and Holmes et al who described laser micromachining of very small scale devices, [36].

In 1980, Leung and Chan published a paper entitled *"A new design approach for axial field electrical machines"*, [66], describing a "shine-through" arrangement where the armature/stator component consisted of isolated teeth made from separate

stacks of laminations. A follow up paper was published by Chan describing a single phase induction motor version of the machine, [17]. A similar design to that of Leung and Chan was described with a permanent magnet field by Lukaniszyn et al as a *"disk type motor with a co-axial flux in the stator"*, [74].

The work of Evans and Eastham has already been mentioned. These authors published a series of papers on a novel disc alternator with AC side excitation, [14], [75], [76] and the basic concept was illustrated in Figure 2.11. The field coil is concentric with the rotor shaft but does not rotate with it. The rotor paddles deliver a rotating field to the toroidally-wound stator core where flux travels axially between paddle and stator, and circumferentially around the core. This pre-empted the work on the TORUS and its slotted counterpart, and the stationary field winding concentric with the rotor hub was used much later by Brown, Mebarki, Novinschi et al, [1], [77] - [79].

The TORUS design of Spooner and Chalmers, [5], has already been described. Much of the literature utilises this topology and the design has been of great influence in the field of axial flux machines generally. In a later paper, Wu, Spooner and Chalmers considered the design of TORUS generators with a particular focus on reducing voltage regulation, [80].

In 1996, Caricchi et al described a permanent magnet axial flux machine having a number of novel features, [56], notably axially stacked components giving a multistage axial flux machine. In this arrangement, an *n-stage* machine would have *n* stators and *(n+1)* permanent magnet disc rotors. For large wheel motors, the authors proposed an ironless stator with a toroidal duct for forced or natural water cooling. A

further point of interest concerning this design was the specification of rhomboidal stator coils instead of the more usual trapezoidal shape in an attempt to increase the torque output per unit of I^2R loss. In a later paper the multistage approach was extended to a modular motor for ship propulsion drives, [61].

The design of an in-wheel motor for a solar-powered electric vehicle by Lovatt et al exhibited a number of interesting novel features, [65], and was claimed by the authors to be more efficient and lightweight than all other direct-drive motors. The authors specified an axial flux machine with an ironless air-gap winding and ironless rotors made possible by a Halbach array of magnets, shown in Figure 2.12.

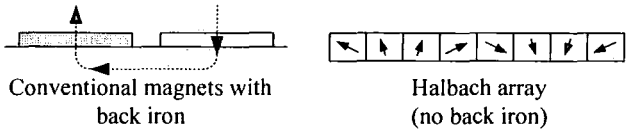

Figure 2.12: Halbach magnet array

In the design of a permanent magnet axial flux generator for a wind turbine, [39], Muljadi et al reversed the positions of stator and rotor with respect to the original TORUS design. The topology of the basic module has been referred to elsewhere in the literature as the *"internal rotor"* design but was, in all other respects, very similar to the TORUS and almost identical to the multistage TORUS of Caricchi et al, [61].

The machines developed at Imperial College and produced by the Turbo Genset Company also demonstrate a number of novel features. In particular, the topology described by Pullen et al, [34], and Etemad, [35], was designed to operate at a very high speed (60,000RPM). With a focus on the production of a lightweight, robust,

low cost machine, a multistage machine was described which utilised rare-earth, rotor-mounted magnets, and "shine-through" flux paths with an ironless stator.

In addition, this expertise with high speed axial flux machines was extended to a very small generator for a microturbine as part of a microelectromechanical system (MEMS), as described by Holmes et al, [36]. The axial flux geometry was argued to be particularly suitable for MEMS devices owing to the possibility of planar stator coils afforded by this orientation, and the ease of fabrication of such coils by comparison with solenoids. A prototype device with a diameter of 7.5mm was described. Being much smaller than other axial flux machines considered here, this device required a rather different approach to fabrication, and techniques such as silicon deep reactive ion etching (DRIE), multilevel electroplating, SU8 processing, and laser micromachining were referred to in the paper. The generator itself consisted of permanent magnets mounted on the central turbine rotor, with upper and lower stator components housing coils and a soft magnetic material flux return circuit. As such, this machine was also an internal rotor type with a "shine-through" flux orientation.

Cavagnino et al described a variant of the internal rotor design for more conventionally-sized machine that utilised permanent magnet poles sandwiched between stainless steel rings, [45]. This topology was effectively a slotted version of the TORUS which had been turned inside out, Figure 2.13.

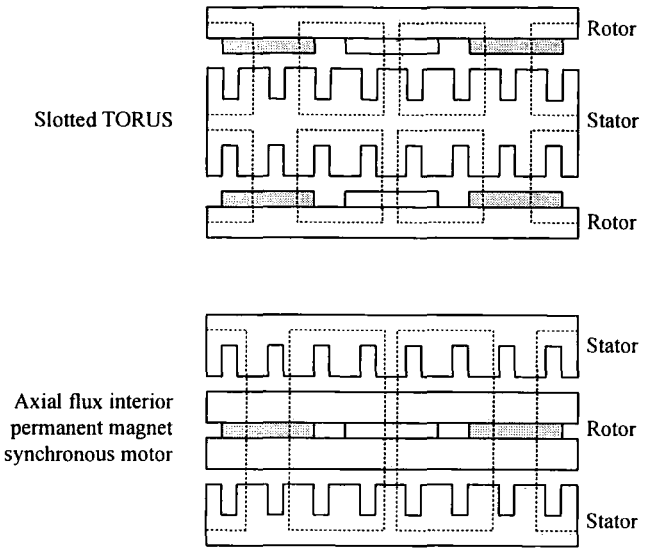

Figure 2.13: Comparison between a slotted TORUS and an interior rotor machine

Lastly, the work described by Brown in his doctoral thesis, [1], and in subsequent papers by Brown, Mebarki, Novinschi et al, ([77], [78], [79]) combined a number of ideas that were present in the literature so as to propose a novel machine for small scale engine driven generator applications having excitation control. Based on a TORUS machine with a slotted winding, the rotor hub also carried a static field coil much like the design of Evans and Eastham, ([14], [75], [76]) and thus facilitated some field control.

2.4.4. Methods of analysis and optimisation

In this final section on the literature, some of the literature having particular focus on analysis and/or optimisation is reviewed. Analytical methods for the calculation of flux per pole and EMF, taking radial and circumferential variations of flux density into consideration, were described in the early paper by Campbell, [13]. Two important points were made in the paper, which have informed successive work on axial flux machines. Firstly, it was stated that the pole arc to pole pitch ratio is an important parameter in the design and operation of such machines. Secondly, it was

stated that the ratio between the inner and outer radii of the active area are critical and can be simply optimised. By maximising the expression for armature power in terms of magnetic and electric loadings, Campbell, [13], showed the maximum armature power to occur where:

$$R_{outer} = \sqrt{3} R_{inner} \qquad \text{Eq. 2.3}$$

A similar paper by Campbell, published in 1975, described the numerical method of obtaining the magnetizing force at the winding planes in 3D, [15]. Circumferential and radial flux density results were shown as evidence of the 3D nature of the field, and as an argument for the necessity of a 3D solution. In 1981, Campbell et al described a procedure of design and optimisation of axial field permanent magnet motors, [16], using algorithms to determine the motor parameters from the minimum amount of input. D'Angelo et al described a 3D FEA of a permanent magnet axial field machine, [81], presenting a detailed description of finite element methodology that is now well established and readily available in software packages on the market.

Leung and Chan also presented an optimisation of the ratio between the core diameters, [66]. Campbell's result of a root three factor was quoted, but the authors here described a servo motor application where a low inertia of the rotating parts was a desired characteristic and so derived a new ratio. Some pole-shaping, incorporating a method of skewing the pole faces, was briefly described as a solution to the problem of cogging torque. Nakata et al presented a Poisson equation solution which assumed a square-wave magnetisation function and used iteration to converge on the magnetisation value in the pole piece, [27]. Takano et al used a second order approximation to the air-gap flux density arising from permanent magnets in a

brushless DC motor, [82] and Furlani published two papers describing a two dimensional field solution for axial field permanent magnet motors, [28], [83].

The paper by Gu et al of 1994 compared three methods of computing the field in a DC permanent magnet coreless disc machine, [30]. The paper described analyses of the field arising from the permanent magnets using finite element methods in two and three dimensions, as well as a magnetic circuit method.

In the paper of Caricchi et al where the multistage machine with water cooled, rhomboidal windings was introduced, some optimisation was carried out and a factor was determined to relate the torque of the design with that developed by an idealised machine, [56]. This showed that the machine with rhomboidal coils operating with a non-square wave flux density profile could achieve a maximum of 77% of the specific torque of the idealised square wave flux density machine with trapezoidal coils.

Following the original TORUS design of Spooner and Chalmers, [5], Chalmers et al described the modelling and simulation of the TORUS generator with particular focus on calculating the self inductance components by considering harmonic fluxes in a range of 2D reductions, [84]. A 2D solution to Laplace's equation was presented in a format so as to give an analytical expression for the flux entering the stator core and thus express the n^{th} harmonic for each self inductance component. This was the first instance in the literature of the application of an analytical field solution to axial flux machines where simplifying assumptions concerning flux waveforms were not required.

Lukaniszyn and Wrobel considered the influence of permanent magnet dimensions and stator core structure on the torque of a TORUS-type arrangement, [85]. The requirement for 3D FEA was argued by the authors who then described benchmarking of the results of 3D FEA predictions alongside experimental results for a slotless TORUS prototype. The use of a slotted core was evaluated where slots were achieved through the formation of teeth from ferromagnetic powder and synthetic resin composite. Skewing the stator teeth or the magnet edges was recommended as a method of reducing undesirable torque, and a FEA study of these effects was documented by Lukaniszyn et al in a later paper, [86]. A similar approach to the optimization of a shine-through disc motor was also described by Lukaniszyn et al, [74], [87].

Brown et al described 3D FEA of a TORUS and compared the predictions with an experimentally-obtained no-load waveform as well as inductance and voltage regulation characteristics, [18]. Marignetti and Scarano described the mathematical modelling of an axial flux PM motor wheel, [52], using a combination of analytical and 3D FEA (computational) methods. Similarly, Parviainen et al described a quasi-3D modelling approach which combined analytical methods with the results from a non-linear reluctance network analysis, [88].

Proca et al presented an analytical model for a radial flux machine with a slotted stator winding, [29], using Laplacian/quasi-Poissonian field equations to give the permanent magnet and armature conductor fields in 2D. Huang et al described the development of general purpose sizing and power density equations for axial flux machines, and compared a TORUS-type machine with an internal rotor machine as an illustration, [89]. In later papers by Aydin et al, these general purpose equations

were used for a comparison between slotted and air-gap wound TORUS machines, [90], [91]. Furthermore, FEA was used to demonstrate the effects of the recommended approaches on cogging and ripple torque.

2.4.5. Contributions to the literature

The work described in this thesis contributes to the field described in sections 2.4.1 to 2.4.4 as follows. Axial flux machines are described in a variety of applications, namely as a diesel engine driven generator, a vertical axis wind turbine generator (VAWT) and a solar car wheel motor. In particular, direct drive generators specifically for VAWTs have only recently appeared in the literature in the paper of Bumby and Martin, [6].

The unified analytical approach to the analysis of permanent magnet axial flux machines of Bumby et al, [8], is described and verified alongside experimental tests, FEA, and more conventional machine analyses derived here. The FEA aspect of this verification was described in a recent paper, [92]. In addition, the novel machine of Bumby, [7], is described and a prototype machine is the subject of experimental tests, analytical methods, and an FEA study described in this thesis.

Finally, the extensive use of FEA is a particular focus of this thesis. In addition to general analyses, FEA is used to verify assumptions and approximations used in a range of analytical methods, to illustrate the electromagnetic fields present in a variety of axial flux machines, and thereby to demonstrate the principles of operation and nuances of design and analysis.

Chapter 3. General analysis of the TORUS

The prototype air-gap wound machines and the slotted designs of the following chapters are based on the TORUS design of Spooner and Chalmers, [5]. The basic orientation of this machine was outlined in section 2.3 and illustrated in Figure 2.9 and Figure 2.10. In this chapter, equations and methods of analysing the basic TORUS design are presented so that they can be applied and extended to the prototypes and new designs later described.

There are two main components of the analysis: analysis of the electromagnetic behaviour, and analysis of the losses and thermal behaviour. The electromagnetic analysis is achieved by two separate approaches. Firstly the unified analytical approach utilising a field solution described by Bumby et al, [8], is outlined. For the purposes of verification a more simple approach is also described that utilises magnetic circuit analysis. Conventional techniques are extended to the calculation of loss in the machine, and the thermal analysis uses a simple lumped parameter model in order to predict the heat dissipation capability. Finally, an equivalent circuit uses calculated parameters to predict the performance of the machine.

3.1. Basic construction

The basic TORUS design has two rotor discs which rotate either side of a stator core. Each disc holds an array of axially polarised, trapezoidal permanent magnets about its periphery; hence the active area is framed by the magnet arrays and is therefore ring-shaped. The stator core is commonly made from strip-wound steel to limit loss arising from eddy currents induced by axially travelling flux. Conductor eddy loss is

limited by forming thick conductors from a number of parallel strands which are twisted in order to avoid circulating currents. The winding can be achieved with two continuous conductors per phase: one to wind the north poles, having a circumferential portion between coils at the outer diameter of the core, and one to wind the south poles similarly. Figure 3.1 shows the stator and rotors of a prototype TORUS machine with sixteen poles and three series-wound phases with the six output connectors.

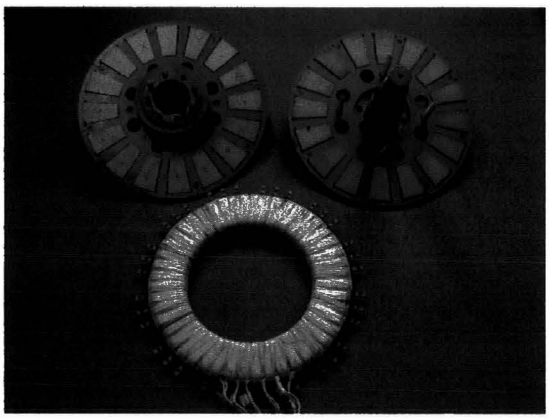

Figure 3.1: Stator and rotors of a TORUS machine

3.2. Applications

The TORUS was initially developed for portable generating sets which require a compact and lightweight machine with good heat dissipation characteristics, [5]. This topology has been commercialised by Newage-AVK-SEG in a compact, Variable Speed Integrated Generating Set (VSIG), [1], and similar designs have been used in conjunction with an internal combustion engine, [18] - [22]. If the machine is light enough and the axial length short enough an advantageous bearingless design can be realised, where the rotor discs are driven directly by the output shaft of the prime mover, and the stator core is suspended between the rotors from a supporting ring. This arrangement is shown in Figure 3.2.

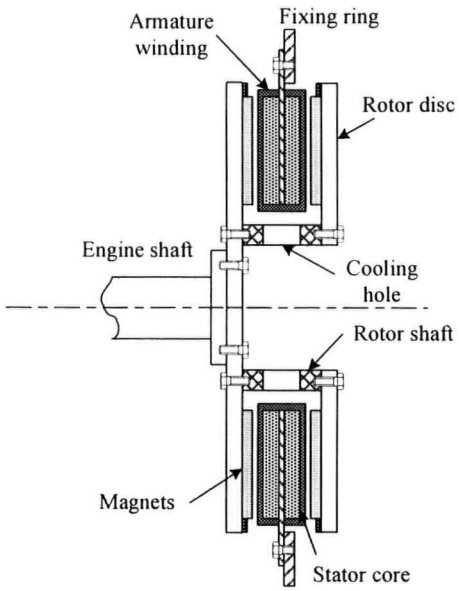

Figure 3.2: TORUS direct-drive arrangement

The direct-drive capability afforded by the high torque achievable in these machines has extended the application to direct-drive wind turbines [2] and in-wheel electric motors [3].

3.3. Mode of operation and equivalent circuit

The magnets on the rotor discs are arranged N-S around the periphery, and like poles face each other in the axial direction. In this arrangement, flux crosses the air-gap in the axial direction, splits into two in the stator to travel circumferentially around the core, and turns again to return to the same rotor one pole-pitch either side of the starting point. This is illustrated in Figure 3.3.

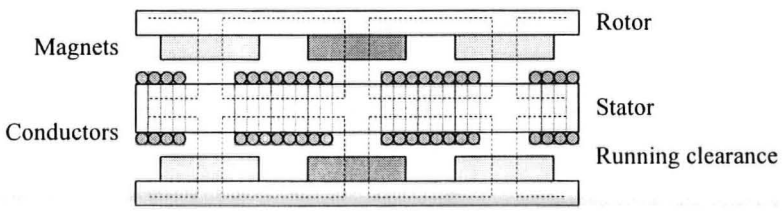

Figure 3.3: TORUS flux paths

With a polyphase AC winding, the machine operates as a permanent magnet synchronous generator and so the standard per-phase equivalent circuit of an EMF source in series with a resistance and a synchronous reactance can therefore be used. This is shown in Figure 3.4 alongside the associated phasor diagram.

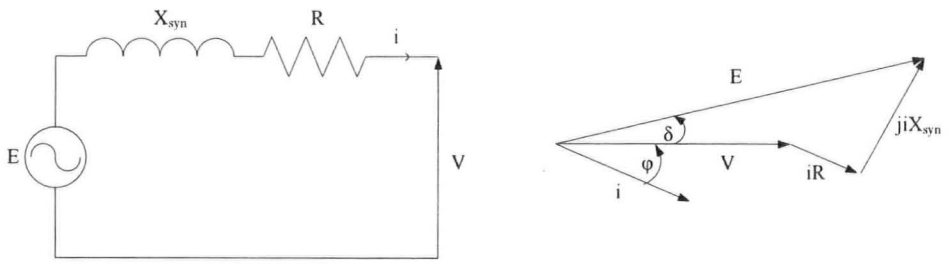

Figure 3.4: Equivalent circuit and phasor diagram

The main loss mechanism is I^2R loss in the conductors; other sources of loss are conductor eddy loss, stator iron loss (comprising eddy and hysteretic loss), and windage. Conductor eddy loss and stator iron loss act mechanically to retard the rotors and are therefore not considered in the electrical equivalent circuit. Any heat generated via these mechanisms must be considered in the thermal analysis however. Since this thesis is primarily concerned with electrical aspects of these machines, purely mechanical loss effects such as windage and pumping are neglected, and all efficiencies quoted are strictly electrical efficiencies.

3.4. Outline analytical model

3.4.1. Basic 2D model

In analysing the electromagnetic operation of the machine the geometry is approximated to a radial view into a circumferential slice through the machine at the mean diameter, as shown in Figure 3.3. The resulting *(z, θ)* coordinate system may be further simplified to Cartesian coordinate *(x, y)* respectively by ignoring

curvature. Boundary conditions may be applied to reduce the model further; these are illustrated in Figure 3.5.

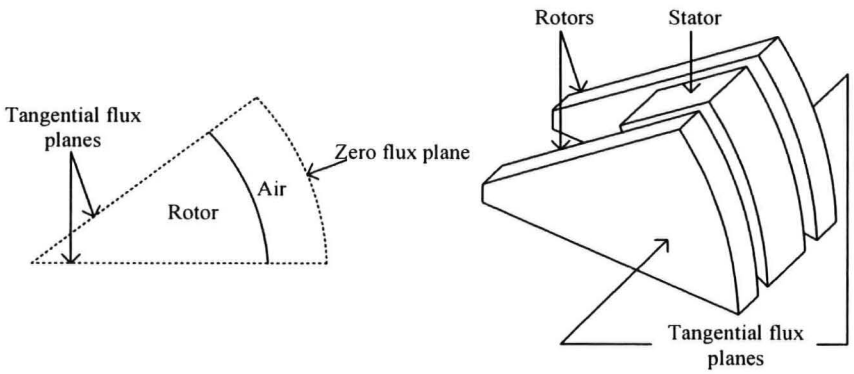

Figure 3.5: 3D boundary conditions

Also, an effective iron boundary exists at the axial centre of the machine; there is a tangential flux condition here and so the two sides of the machine can be considered to contribute separately to the fields under consideration. The analysis proceeds per unit length into the page, and the result is multiplied by two to take both sides into account and then modulated by an effective length to take account of the third dimension. Rotational symmetry may be exploited in separate analysis of the field arising from the magnets and the field arising from the phase currents under steady-state, no-load conditions using the units shown in Figure 3.6.

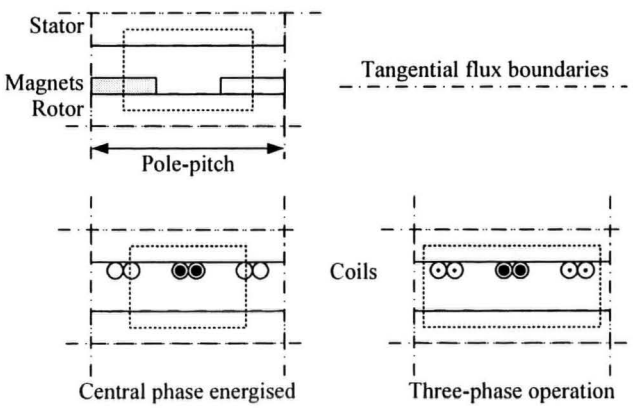

Figure 3.6: Tangential flux boundary conditions

Where the field around the core ends is considered, the same arguments may be applied. The 2D model consists of the core end windings on the stator iron surface with an unbounded region of air above. The mean radius of the core approximates to a tangential flux iron boundary and so only one core end need be considered.

3.4.2. Key geometrical parameters

The inner and outer diameters of the core frame the active area of the machine and are related by a factor $k_{campbell}$. One of the outcomes of Campbell's pioneering work in the field of axial flux machines was the optimisation of the ratio between these diameters by maximisation of the armature power, [13]. It was shown that the maximum power occurs when:

$$D_i = \frac{D_o}{\sqrt{3}} = 0.577 D_o \qquad \text{Eq. 3.1}$$

Hence Campbell's factor is defined:

$$k_{campbell} = \frac{D_i}{D_o} \qquad \text{Eq. 3.2}$$

In reality, the factor is often varied around the 0.58 mark in order to accommodate an extra turn, since the inner core diameter is a limiting factor in the winding design and maximum power may be realised by slight deviation from Campbell's precise value.

Where the magnets overhang the core, the effective core length is taken as:

$$l_{eff} = \frac{D_{o,mag} + D_o}{2} - \frac{D_{i,mag} + D_i}{2} \qquad \text{Eq. 3.3}$$

Where p is the number of poles, the pole pitch in electrical radians is given:

$$\tau_{p(rad)} = \frac{2\pi}{p} \qquad \text{Eq. 3.4}$$

Similarly in metres, taken at the mean diameter:

$$\tau_{p(m)} = \frac{\pi D_m}{p} \qquad \text{Eq. 3.5}$$

The magnet poles are assumed to occupy a proportional arc of the pole pitch, given by the pole arc to pole pitch ratio:

$$\alpha = \frac{\tau_m}{\tau_p} \qquad \text{Eq. 3.6}$$

In both of the electromagnetic analyses, the steel is assumed to be infinitely permeable and an effective air-gap is defined which takes the slightly increased permeability of the permanent magnets into account:

$$g_{eff} = \frac{t_m}{\mu_r} + c + t_a \qquad \text{Eq. 3.7}$$

The inner diameter is a critical parameter in the design of the winding, in that the circumferential space afforded the winding is at its most restricted here. The conductors are assumed to touch at the inner diameter, such that the coil spread here is given in electrical degrees as:

$$\sigma_{D_i} = \frac{180}{m} \qquad \text{Eq. 3.8}$$

Since the turns are not strictly radial but rather remain in contact with one another across the core face, the spread effectively reduces across the core face and the mean spread is used to determine the distribution factor:

$$\sigma = \sigma_{D_i} \frac{D_i}{D_m} \qquad \text{Eq. 3.9}$$

The mean diameter is given:

$$D_m = \frac{D_o + D_i}{2} \qquad \text{Eq. 3.10}$$

The N turns of each coil are assumed to be uniformly distributed over this mean spread angle; hence the *nth* harmonic of the mean distribution factor:

$$k_{dn} = \frac{\sin\left(\frac{n\sigma}{2}\right)}{\frac{n\sigma}{2}} \qquad \text{Eq. 3.11}$$

3.5. Field solution

3.5.1. Outline method

This method was published by Bumby et al, [8], and is based on a solution of Laplace's equation for the magnetic vector potential arising from a sinusoidal current sheet situated between two infinitely permeable boundaries. Current sheets are used to model the magnets and the phase currents such that this approach is a unified analysis. The basic building block shown in Figure 3.7 is used in both cases.

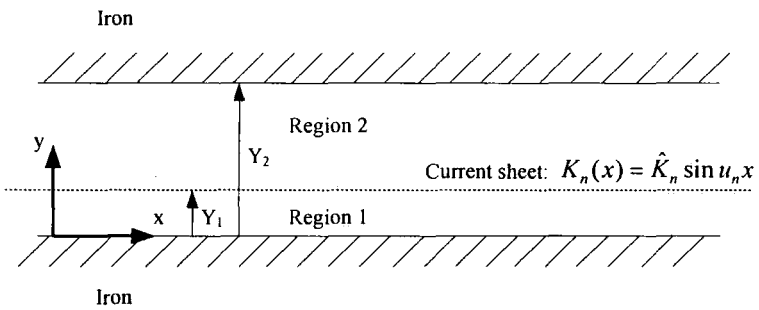

Figure 3.7: Current sheet model

Solution of Laplace's equation subject to boundary conditions at the iron surfaces and at the current sheet yields the vector potential and the normal component of magnetic field intensity in regions 1 and 2, where region 1 lies within the permanent magnet thickness and region 2 is air.

Region 1:

$$A_{zn1}(x) = -\frac{\hat{K}_n \mu_0}{u_n} \frac{\cosh u_n (Y_2 - Y_1)}{\sinh u_n Y_2} \cosh u_n y . \sin u_n x \qquad \text{Eq. 3.12}$$

$$H_{yn1}(x) = \hat{K}_n \frac{\cosh u_n (Y_2 - Y_1)}{\sinh u_n Y_2} \cosh u_n y . \cos u_n x \qquad \text{Eq. 3.13}$$

Region 2:

$$A_{zn2}(x) = -\frac{\hat{K}_n \mu_0}{u_n} \frac{\cosh u_n Y_1}{\sinh u_n Y_2} \cosh u_n (Y_2 - y) . \sin u_n x \qquad \text{Eq. 3.14}$$

$$H_{yn2}(x) = \hat{K}_n \frac{\cosh u_n Y_1}{\sinh u_n Y_2} \cosh u_n (Y_2 - y) . \cos u_n x \qquad \text{Eq. 3.15}$$

The constant u_n is defined where λ is the wavelength (equal to twice the pole pitch):

$$u_n = \frac{2\pi n}{\lambda} \qquad \text{Eq. 3.16}$$

3.5.2. Analysis of the field arising from the magnets

Figure 3.8 shows the overall model and the method of computing the magnetic linear current density distribution.

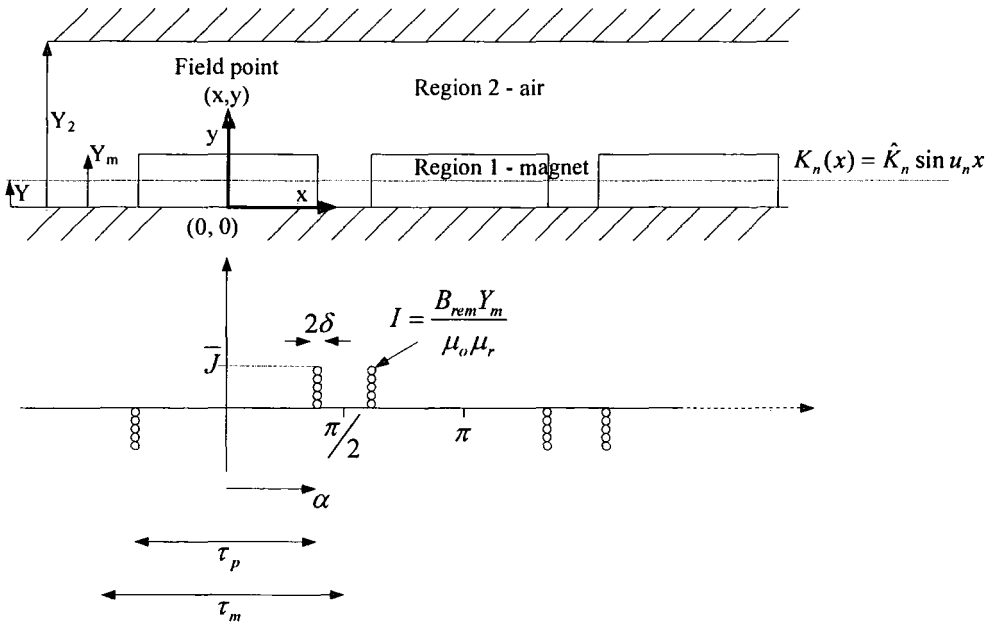

Figure 3.8: The magnetic field arising from the magnets

The magnetisation of the magnets is modelled as a current at the magnet edges:

$$I = \frac{B_r Y_m}{\mu_0 \mu_r} \qquad \text{Eq. 3.17}$$

This current assumed to flow in a vanishingly small thickness 2δ and the corresponding flux density, $\bar{J}$, is broken down into its constituent harmonics, with peak value given by:

$$\hat{J}_n = \frac{4}{\tau_p} \frac{B_{rem}}{\mu_0 \mu_{rec}} \sin\left(\frac{n\pi}{2} \frac{\tau_m}{\tau_p}\right) \qquad \text{Eq. 3.18}$$

The magnets are divided into a number of elemental current sheets in the y-dimension, each having linear current density:

$$K_n(x) = \hat{J}_n dy \sin u_n x \qquad \text{Eq. 3.19}$$

Finally, this is substituted into the general solution for region 2 (section 3.5.1) and integrated over the magnet thickness to obtain:

$$A_{zn2}(x) = -\frac{\hat{J}_n \mu_0}{u_n^2} \frac{\sinh u_n Y_m}{\sinh u_n Y_2} \cosh u_n (Y_2 - y) \sin u_n x \qquad \text{Eq. 3.20}$$

with:

$$B_{yn2}(x) = \frac{\hat{J}_n \mu_0}{u_n} \frac{\sinh u_n Y_m}{\sinh u_n Y_2} \cosh u_n (Y_2 - y) \cos u_n x \qquad \text{Eq. 3.21}$$

Two adjustments can be made to take the increased permeability of the magnet region into consideration, since the solution above assumes regions 1 and 2 to have permeability μ_o. Firstly, as shown in Figure 3.8, the equivalent magnet current takes account of μ_r. Secondly, the effective air-gap defined in section 3.4.2 may be used as length Y_2. The variation of B_y with x, taken at the stator core surface ($y = Y_2$) is of interest and is used later for comparison between results.

In the 2D model, the difference in vector potential between two points in the x-dimension is equal to the magnetic flux passing between the two points in the y-

dimension, per metre in the z-dimension. The flux entering the stator core per pole may thus be calculated by setting $y = Y_2$ and evaluating the difference in vector potential across a pole-pitch. This is multiplied by the effective core length defined in section 3.4.2 to give the flux per pole per rotor:

$$\hat{\phi}_{pp,n} = \frac{\hat{B}_n}{n\frac{p}{2}} D_m l_{eff} \sin\frac{n\pi}{2} \qquad \text{Eq. 3.22}$$

Noting that, at $y = Y_2$:

$$\hat{B}_n = \frac{\hat{J}_n \mu_0}{u_n} \frac{\sinh u_n Y_m}{\sinh u_n Y_2} \qquad \text{Eq. 3.23}$$

The flux per pole divides into two in the stator to travel circumferentially around linking the coils, but both sides of the machine contribute and so the core flux is equal to the flux per pole per rotor calculated above. The RMS values of the coil harmonic voltages are thus given:

$$E_{coil,n} = \sqrt{2}\pi n k_{dn} N f \hat{\phi}_{pp,n} \qquad \text{Eq. 3.24}$$

The total coil EMF is thus:

$$E_{coil} = \sqrt{E_{coil,1}^2 + E_{coil,2}^2 + \ldots + E_{coil,n}^2} \qquad \text{Eq. 3.25}$$

The induced voltage per phase depends on the coil interconnection, but series connected coils are assumed here so:

$$E = pE_{coil} \qquad \text{Eq. 3.26}$$

3.5.3. Analysis of the field arising from phase currents

In order to use the general expressions given in section 3.5.1, the conductors are represented as a current distribution that can be substituted directly. This is possible with single layer windings but multi-layer arrangements may require an approach

similar to the one used to model the magnets. Figure 3.9 shows the armature conductor model.

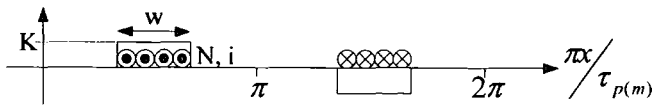

Figure 3.9: Phase conductor model

The coil width is taken at the mean diameter and is given:

$$w = \frac{\sigma D_m}{p} \qquad \text{Eq. 3.27}$$

Hence the linear current density:

$$K = \frac{Ni}{w} \qquad \text{Eq. 3.28}$$

Expressing these blocks of current density as a Fourier series:

$$K(x) = \sum \hat{K}_n \sin(u_n x) \qquad \text{Eq. 3.29}$$

The harmonic peak values are:

$$\hat{K}_n = \frac{4K}{n\pi} \sin\frac{n\pi}{2} \sin\frac{n\sigma}{2} = \frac{2}{\pi} \frac{Npk_{dn}}{D_m} \sin\frac{n\pi}{2} i \qquad \text{Eq. 3.30}$$

This current distribution is substituted into the general equations of section 3.5.1 to give the vector potential at the stator core surface *(y = 0)*:

$$A_{zn1}(x) = -\frac{\hat{K}_n \mu_0}{u_n} \frac{\cosh u_n (Y_2 - Y_1)}{\sinh u_n Y_2} \sin u_n x \qquad \text{Eq. 3.31}$$

Hence the flux density:

$$B_{yn1}(x) = \mu_0 \hat{K}_n \frac{\cosh u_n (Y_2 - Y_1)}{\sinh u_n Y_2} \cos u_n x \qquad \text{Eq. 3.32}$$

The difference in vector potential across a pole pitch gives the flux entering the core per unit length into the page. In the case of the main winding region, the length into

the page is the effective core length but the flux entering the core splits into two and so here:

$$\hat{\phi}_{n,main} = \left(A_{zn,x=-\tau/2} - A_{zn,x=\tau/2} \right) \times \frac{l_{eff}}{2} \qquad \text{Eq. 3.33}$$

If the winding is thin and can be assumed coincident with the stator surface without too much loss of accuracy, algebraic expressions can be derived as follows. Evaluating Eq. 3.33 for $Y_1 = 0$:

$$\hat{\phi}_{n,main} = \frac{4\mu_0 N k_{d,n}}{\pi n} l_{eff} \coth u_n g_{eff} i \qquad \text{Eq. 3.34}$$

The flux linkage is:

$$\hat{\Psi}_{coil,n} = \hat{\phi}_{n,main} N k_{d,n} \qquad \text{Eq. 3.35}$$

The coil self inductance is the flux linkage per amp current, hence in the main region:

$$L_{main,n} = \frac{4\mu_0 N^2 k_{d,n}^2}{\pi n} l_{eff} \coth u_n g_{eff} \qquad \text{Eq. 3.36}$$

The flux linking the adjacent coils can be found similarly, evaluating the flux between $(\gamma - \tau_p/2)$ and $(\gamma + \tau_p/2)$ where γ is the coil displacement, which is $\pi/3$ for a toroidal machine with 3-phases. Hence the mutual inductance:

$$M_{main,n} = \frac{4\mu_0 N^2 k_{d,n}^2}{\pi n} l_{eff} \coth u_n g_{eff} \cos u_n \gamma \qquad \text{Eq. 3.37}$$

In the case of the end winding region, Y_2 is set to a large value, since there is no rotor iron above the core end. The length into the page equals the stator thickness and again the flux entering the core splits into two, but conductors at the inner and outer radii both contribute hence the approach described gives the core flux. Thus the self inductance of this region is:

$$L_{end,n} = \frac{4\mu_0 N^2 k_{d,n}^2}{\pi n} t_{stator} \qquad \text{Eq. 3.38}$$

Also the mutual inductance:

$$M_{end,n} = \frac{4\mu_0 N^2 k_{d,n}^2}{\pi n} t_{stator} \cos u_n \gamma \qquad \text{Eq. 3.39}$$

In order to assimilate the synchronous inductance from the calculated values, the reciprocal property of mutual inductance is assumed to hold; hence the mutual inductances calculated above are equal to the mutual inductance of the coil under consideration arising from unit current in either of its adjacent coils. During 3-phase operation, a peak current of *i* in one coil would be accompanied by *–i/2* in each of the adjacent coils. The currents in the adjacent coils, although of negative polarity, set up fluxes that reinforce the flux of the central coil, and so the phase synchronous inductance is composed of the self inductance of a phase and a component of mutual inductance arising from current in each of the other 2 phases. Since the current is *i/2*, the contribution of each adjacent phase is *M/2*, and this applies to both the main winding and the end winding regions. There are p coils per phase connected in series and so the synchronous inductance is given:

$$L_{syn} = p\sum_n \left(L_{main,n} + L_{end,n} + M_{main,n} + M_{end,n}\right) \qquad \text{Eq. 3.40}$$

The synchronous reactance is therefore:

$$X_{syn} = j\omega L_{syn} = j2\pi f_{elec} L_{syn} = j\frac{\pi np}{60} L_{syn} \qquad \text{Eq. 3.41}$$

3.6. Magnetic circuit solution

3.6.1. Analysis of the field arising from the magnets

This is a more conventional method where the magnetic circuit law is applied to a closed loop in the main winding region. The magnetic field intensity and thus the flux density are assumed to remain constant across the effective air-gap. The steel in the circuit is assumed to be infinitely permeable and the flux density arising from the

permanent magnets is calculated. The flux paths and parameters are shown in Figure 3.10.

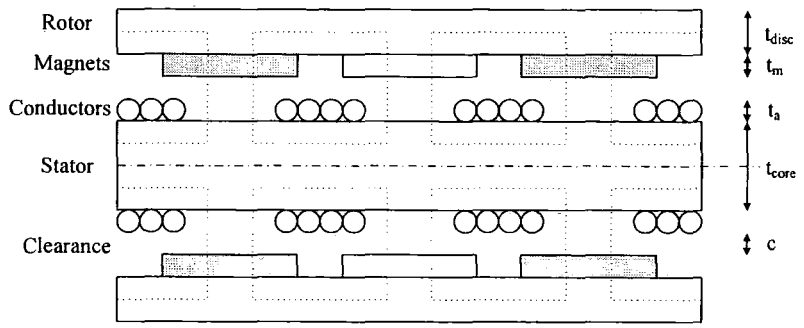

Figure 3.10: Flux paths and parameters

It is assumed that the permeability of the winding is equivalent to the permeability of free space. Considering the flux around one loop, the magnetic circuit law gives:

$$\oint H.dl = 2H_m t_m + 2H_a(t_a + c) = 0 \qquad \text{Eq. 3.42}$$

The flux density in air is:

$$B = \mu_o H_a \qquad \text{Eq. 3.43}$$

Assuming a linear magnet *BH* characteristic, the flux density in the magnet is:

$$B = B_r + \mu_o \mu_r H_m \qquad \text{Eq. 3.44}$$

These two flux densities must be equal, since the flux density must be continuous at the magnet/air interface. Substituting into Eq. 3.42 gives:

$$B = \frac{B_r \frac{t_m}{\mu_r}}{\frac{t_m}{\mu_r} + t_a + c} \qquad \text{Eq. 3.45}$$

The denominator is recognisable as the effective air-gap defined in section 3.4.2. A square profile may be assumed across the pole arc, and Fourier analysis shows the peak value of the fundamental to be:

$$B_{fund} = \frac{4B}{\pi} \sin\left(\frac{\tau_m}{2}\right) \qquad \text{Eq. 3.46}$$

More commonly, the circumferential variation of the flux density waveform can be approximated by a sinusoid, where the value of B given above represents the peak:

$$B(x) = B\sin(u_1 x) \qquad \text{Eq. 3.47}$$

Now this flux density is integrated to obtain the flux per pole. Consider the elemental area, δa, shown in Figure 3.11.

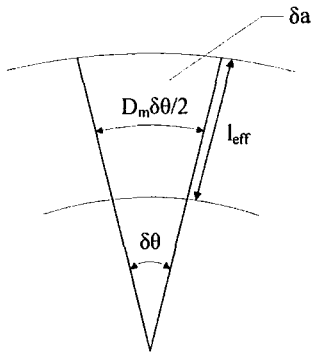

Figure 3.11: Elemental area of a pole

The area is given:

$$\delta a = l_{eff}\frac{D_m}{2}\delta\theta \qquad \text{Eq. 3.48}$$

To work in electrical radians it is necessary to divide by the number of pole pairs; the peak flux per pole can then be calculated by integrating between 0 and π:

$$\hat{\phi}_{pp} = \int B.da = \frac{l_{eff}D_m}{p}\int_0^{\pi} B\sin(\theta)\delta\theta = \frac{2Bl_{eff}D_m}{p} \qquad \text{Eq. 3.49}$$

This takes the same form as the first harmonic of the flux derived from the field solution, Eq. 3.22. Again, the flux per pole divides into two in the stator to travel circumferentially around linking the coils, but both sides of the machine contribute and so the core flux is equal to the flux per pole per rotor calculated above.

Assuming the coils experience a sinusoidal variation of this flux with time, the RMS induced voltage per coil is:

$$E_{coil} = 4.44 k_{d1} N f \hat{\phi}_{pp} \qquad \text{Eq. 3.50}$$

The induced voltage per phase with series connected coils is given by Eq. 3.26.

3.6.2. Analysis of the field arising from phase currents

The boundary conditions described in section 3.4.1 indicated that half the axial length of the machine, spanning one pole pitch and with the central of the 3 coils energised, would provide satisfactory representation for magnetic circuit analysis. Figure 3.12 shows this reduced segment along with a graph of the associated MMF distribution for the main winding region.

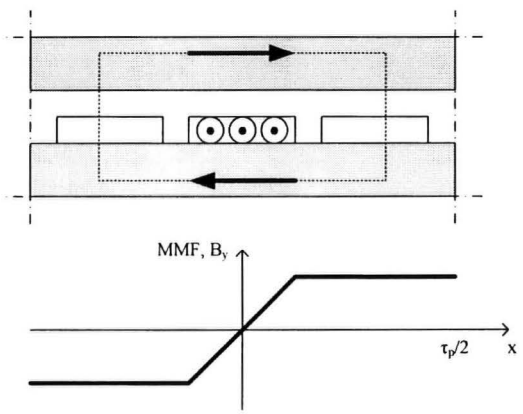

Figure 3.12: Inductance calculation: reduced model

The magnetic circuit law gives the peak value of flux density:

$$2Hg_{eff} = Ni \Rightarrow B = \frac{\mu_o Ni}{2g_{eff}} \qquad \text{Eq. 3.51}$$

Hence B is a trapezoidal waveform with wavelength $2\tau_p$ and peak value given above. Fourier representation gives:

$$B(x) = \sum_{n\_odd} B_n \sin\left(\frac{\pi n x}{\tau_p}\right) \qquad \text{Eq. 3.52}$$

Where:

$$B_n = \frac{4k_{dn}\left(\frac{\mu_o Ni}{2g_{eff}}\right)}{n\pi} \qquad \text{Eq. 3.53}$$

Since this is an approximate method, only the first harmonic of flux density is considered. Hence the variation of axial flux density with x at the stator surface is approximated to:

$$B_y(x) = \frac{2\mu_0 Nik_{d1}}{g_{eff}\pi}\sin\left(\frac{\pi x}{\tau_p}\right) \qquad \text{Eq. 3.54}$$

Integrating this between *0* and $\tau_p/2$ gives the contribution to the core flux per unit core length into the page:

$$\phi / m = \frac{2\tau_p \mu_0 Nik_{d1}}{g_{eff}\pi^2} \qquad \text{Eq. 3.55}$$

Taking both sides of the stator into account means that the core length into the page is $2l_{eff}$. The limits on the flux density integration imply that the flux per metre defined by Eq. 3.55 is the contribution to the core flux and not the flux per pole. The coil inductance is the flux linkage per amp hence the coil self inductance of the main winding region:

$$L_{main} = \frac{N\phi_1 k_{d1}}{i} = \frac{4\tau_p \mu_0 N^2 k_{d1}^2 l_{eff}}{g_{eff}\pi^2} \qquad \text{Eq. 3.56}$$

The same method is extended to the calculation of mutual inductance; the expression for flux density is now integrated between $\tau_p/3$ and $\tau_p/2$ to give the flux, and the resulting expression is:

$$M_{main} = \frac{2\tau_p \mu_0 N^2 k_{d1}^2 l_{eff}}{g_{eff}\pi^2} \qquad \text{Eq. 3.57}$$

Since this is based on the sinusoidal first harmonic of the flux density, the mutual inductance is exactly half the self inductance as expected. In three phase operation,

each of the adjacent coils contributes *M/2* to the synchronous inductance since they carry half the current. The synchronous inductance (per coil) is therefore:

$$L_{syn/coil} = L_{main} + 2\left(\frac{M_{main}}{2}\right) = \frac{3}{2}L_{main} \qquad \text{Eq. 3.58}$$

The magnetic circuit approach is difficult to apply in the case of the end-winding region; the effective gap is not easily defined now, owing to the absence of iron above the conductors. Perpendicular flux paths cannot be assumed and the magnetic field intensity and flux density will vary throughout the space above the winding. Alternatively, consider the expression for self inductance in the main winding obtained from the field solution, Eq. 3.36. Where the effective gap is much smaller than the pole pitch, the following simplification can be made:

$$\coth u_n g_{eff} \rightarrow u_n g_{eff} = \frac{\tau_p}{\pi g_{eff}} \qquad \text{Eq. 3.59}$$

Making this substitution and considering the 1st harmonic only gives the same as the solution obtained by magnetic circuit analysis, Eq. 3.55. Consider now the 1st harmonic of the end winding inductance obtained from the field solution, Eq. 3.38. This is similar to that for the main winding inductance obtained from the magnetic circuit analysis which includes a term representing the effective gap, g_{eff}. Replacing this with a new equivalent effective gap gives the expression for the end winding inductance, where this equivalent gap is:

$$g_{eff,end} = \frac{\tau_p}{\pi} \qquad \text{Eq. 3.60}$$

Thus a simple expression along the lines of the magnetic circuit approach can be used for the calculation of the end-winding inductance.

Again, where the first harmonic is considered the mutual inductance is equal to exactly half of the self inductance, hence:

$$L_{end} = \frac{4\tau_p \mu_0 N^2 k_{d1}^2 t_{stator}}{g_{eff,end} \pi^2} \qquad \text{Eq. 3.61}$$

$$M_{end} = \frac{2\tau_p \mu_0 N^2 k_{d1}^2 t_{stator}}{g_{eff,end} \pi^2} \qquad \text{Eq. 3.62}$$

The phase synchronous inductance from the magnetic circuit method is thus:

$$L_{syn} = p\left(L_{main} + L_{end} + M_{main} + M_{end}\right) \qquad \text{Eq. 3.63}$$

The reactance is again calculated using Eq. 3.41.

3.7. Losses and thermal analysis

3.7.1. Thermal analysis

In order to assess the heat dissipation capabilities of the machine, and hence evaluate the allowable loss and the current rating as described, a simple thermal model is devised. The thermal path of the heat through the copper and insulation is ignored and all the loss is assumed to originate at the surface of the winding and be dissipated from this surface according to the heat transfer coefficient $h = 150W/m^2/^oC$ obtained experimentally by Spooner and Chalmers, [5].

The conductors are assumed to touch at the inner diameter, and then appear rectangular when viewed in the axial direction. Hence, it is assumed that the area over which the heat loss is transferred is the surface of these coils across the main winding region of both sides, given:

$$a = \pi D_i \left(D_o - D_i\right) \qquad \text{Eq. 3.64}$$

The winding surface is assumed to be at an operating temperature appropriate to the material, and the difference between this temperature and the ambient temperature is assumed to be dropped in heat transfer to the air that is being naturally pumped across the winding in the radial direction. The heat transfer is proportional to the heat transfer coefficient, the temperature differential and the surface area across which heat is transferred:

$$P_{loss} = hA\Delta T \qquad \text{Eq. 3.65}$$

3.7.2. The stator winding

The types of conductors appropriate for this type of machine were described in section 3.1. Preformed conductors consisting of a number of parallel-connected twisted strands are considered here since they can be readily made in-house and are utilised in the prototypes described in the following chapter. Experimental work in the School of Engineering at the University of Durham, [9], has shown that conductors formed from 3, 7 or 9 twisted strands of wire work well, and that the overall diameter can be calculated:

$$d_{conductor} = \sqrt{\frac{n_{strands} d_{wire}^2}{0.62}} \qquad \text{Eq. 3.66}$$

Insulation tape adds to this diameter to give the diameter of an insulated turn.

$$d_{turn} = d_{conductor} + 2t_{insulation} \qquad \text{Eq. 3.67}$$

Only single-layer windings are considered, so the winding thickness is equal to the diameter of a turn and the inner and outer layers of core insulation, hence:

$$t_a = d_{turn} + 2t_{insulation(core)} \qquad \text{Eq. 3.68}$$

The resistivity depends on the operating temperature, a value of which is assumed, based on the properties of the materials used. Hence:

$$\rho_T = \rho_0(1+\alpha T) \qquad \text{Eq. 3.69}$$

The cross-sectional area of the conductor depends on the geometry of the strands and the number used:

$$a_{conductor} = n_{strands}\frac{\pi d^2{}_{wire}}{4} \qquad \text{Eq. 3.70}$$

In order to calculate the length of conductor per phase, the length of an average turn is considered. Figure 3.13 shows the cross section of the twin stator cores and supporting ring, with the winding region and a mean turn illustrated.

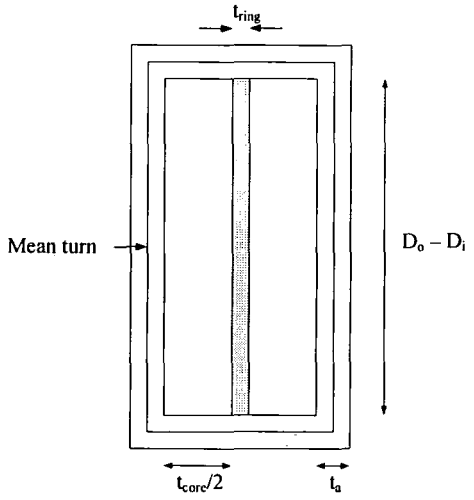

Figure 3.13: Mean turn

The length of the mean turn is given:

$$l_{turn} = 2\left(\frac{D_o - D_i}{2} + t_{stator} + 2t_a\right)$$

In this analysis, it is assumed that the coils are series connected and so each phase is wound separately, one coil at a time, such that a circumferential portion situated at the outer diameter of the core runs between coils of a given phase. The north coils of each phase are wound separately from the south coils, so the coil interconnection

length per phase is approximated by two outer circumferential lengths per layer. The conductor length per phase is thus approximated by all the turns and a length of conductor accounting for the interconnections:

$$l_{phase} = l_{turn} Np + 2\pi D_o \qquad \text{Eq. 3.71}$$

The phase resistance is then given:

$$R = \frac{\rho l_{phase}}{a_{conductor}} \qquad \text{Eq. 3.72}$$

3.7.3. Loss mechanisms and their analysis

The main source of loss in this type of machine is I^2R loss. This loss is easily calculated from the phase resistance and the operating current. The next most significant loss is that arising from eddy currents induced in the conductors. Since the winding is situated in the air-gap and not placed in slots, the conductors are exposed to the full excitation field. The power loss per metre length of circular conductor arising from induced eddy currents is calculated as set out by Carter, [93], pp. 254-256.

$$P_{eddy/m} = \frac{\pi}{4}\frac{d^4}{16}\frac{B^2\omega^2}{\rho} \qquad \text{Eq. 3.73}$$

Dividing to n strands reduces this factor from $(nd)^4$ to $n(d^4)$. The parallel connected strands must not permit circulating eddy currents and so they must be twisted in order to equalise the EMF induced in the individual strands. The eddy loss of a single strand is considered and then multiplied up by the number of strands per conductor, the number of conductors per coil, the number of coils per phase, and the number of phases. The resistivity used is that defined in section 3.7.2 at the operating temperature of the machine.

The frequency is the electrical frequency, which is related to the speed of rotation, *n (RPM)*, and the number of poles by:

$$f_{elec} = \frac{np}{120} \qquad \text{Eq. 3.74}$$

The flux density used is the peak value of the first harmonic, and the portion of the conductors equal to the effective length is assumed to generate this loss per side of the machine. Both sides of the core are taken into account and so the total conductor eddy loss is given:

$$P_{eddy} = mpNn_{strands} \frac{\pi}{4} \frac{d_{wire}^4}{16} \frac{\hat{B}_1^2 \omega^2}{\rho} 2l_{eff} \qquad \text{Eq. 3.75}$$

Finally, since the stator iron also experiences alternating flux, it is susceptible to iron losses, namely hysteretic and eddy loss. The manufacturer's quoted iron losses are 2.8W/kg at 1.5T, 50Hz, which Bumby and Spooner normalised to the relevant flux density and frequency, [9]. The total loss therefore depends on the mass of the core, which is given by:

$$m_{core} = V_{core} \rho_{core} = \pi \frac{(D_o^2 - D_i^2)}{4} t_{core} \rho_{core} \qquad \text{Eq. 3.76}$$

Thus the iron loss is given by:

$$P_{iron} = \left[\frac{f_{elec}}{50}\right]^{1.32} \left[\frac{B_{core}}{1.5}\right]^{1.97} m_{core} \qquad \text{Eq. 3.77}$$

3.7.4. Determination of the rated current

The thermal model of section 3.7.1 gives the total allowable loss, from which the iron and conductor eddy losses are subtracted to leave a remainder loss which is allocated to I^2R loss:

$$P_{I^2R} = P_{loss} - P_{eddy} - P_{iron} \qquad \text{Eq. 3.78}$$

The allowable operating current then depends on the phase resistance and the number of phases:

$$I = \sqrt{\frac{P_{I^2R}}{mR_{phase}}} \qquad \text{Eq. 3.79}$$

The current density in A/mm^2 is then given:

$$J = \frac{I \times 10^{-6}}{A_{conductor}} \qquad \text{Eq. 3.80}$$

The electric loading at the mean diameter is therefore:

$$A_{RMS} = \frac{INmp}{\pi D_m} \qquad \text{Eq. 3.81}$$

3.8. Performance calculations

Assuming unity power factor operation, the terminal voltage can be obtained:

$$V = \sqrt{E^2 - \left(IX_{syn}\right)^2} - IR_w \qquad \text{Eq. 3.82}$$

The terminal power is then:

$$P = mVI \qquad \text{Eq. 3.83}$$

The voltage regulation at rated current is given as a percentage:

$$V_{reg}(\%) = 100 \times \frac{E - V}{E} \qquad \text{Eq. 3.84}$$

Finally the efficiency is given by:

$$\eta(\%) = 100 \times \frac{P}{P + P_{loss}} \qquad \text{Eq. 3.85}$$

3.9. Discussion

Equations and methods of analysing the basic TORUS design have been presented so that they can be applied and extended to the prototypes and new designs later described.

Two approaches to the electromagnetic analysis have been described: one based on a general field solution and the other utilising magnetic circuit analysis. The methods have been shown to be related in the calculation of the flux per pole arising from the permanent magnets, and in the calculation of the inductance in the main winding region. The field solution for the end-winding inductance was compared with the magnetic circuit solution to the main winding inductance in order to derive an effective gap which allows evaluation of the end-winding inductance using a magnetic circuit solution.

The losses in the TORUS have been analysed and evaluation techniques described; an approximate thermal model has been described which may be used to estimate the total allowable loss in such machines and thereby determine the rated current. Using this information and the electromagnetic equivalent circuit parameters, the performance of TORUS machines can be predicted.

These techniques are used directly in the next chapter for comparison with the results of finite element analysis and experimental testing of two prototype generators. The techniques are then extended to the design and analysis of a range of different permanent magnet axial flux machines.

Chapter 4. FEA and experimental test of TORUS machines

In this chapter the analytical methods described in Chapter 3 are benchmarked with FEA, and both sets of predictions are verified by experimental testing of two prototype TORUS machines. No FEA of axial flux machines had previously been undertaken at Durham and so it was necessary to develop skills and methods in this area; hence there is a particular focus on this. Analyses were carried out with 2D and 3D, static and dynamic models using the MEGA software developed by the Applied Electromagnetics research group at the University of Bath, [4]. MEGA solves the low frequency (no displacement) subset of Maxwell's equations using the finite element method for a wide variety of 2D and 3D problems, including the following situations that were utilised here:

- 2D formulations based on $\boldsymbol{A}$ or $\boldsymbol{H}$
- Magnetostatics in 2D and 3D
- Steady state current in 2D and 3D
- Voltage or current forced wire-wound coils
- External circuit models
- Permanent magnets
- Combination of meshes using Lagrange multipliers, allowing separate meshing of the rotor and stator that can then be joined together and solved in different relative positions

Further to the electromagnetic analysis, the Strand7™ FEA software for mechanical engineering problems, [94], was used to simulate the steady-state thermal behaviour of the machines.

The predictions of the analytical methods of Chapter 3 are presented and compared with those obtained from FEA. Finally, a series of experimental tests carried out on two prototype machines in the laboratory is described and the results presented for comparison with the various predictions.

4.1. The prototype machines

Two prototype machines had previously been built at Durham based on the TORUS design of Spooner and Chalmers, [5]. The original application was diesel engine-generator sets and the machines are rated at 40kW at 4500RPM and 20kW at 3000RPM. The topologies are the same as that described in Chapter 3, (illustrated in Figure 3.1) and a view of the assembled unit is shown, Figure 4.1.

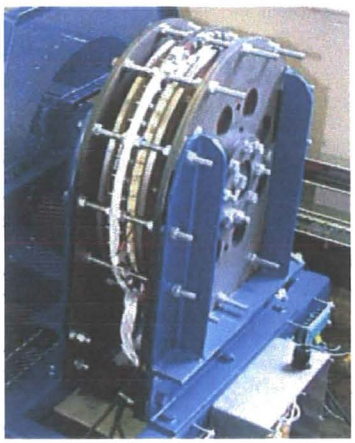

Figure 4.1: 40kW prototype fully assembled

The core dimensions are illustrated in Figure 4.2, and the outline parameters of the two prototypes are given, Table 4.1.

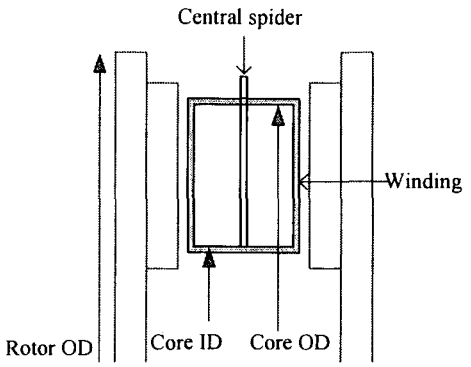

Figure 4.2: Rotor and core dimensions

	40kW machine	20kW machine
Number of poles per disc	16	12
Winding layers	1	2
Turns per armature coil	4	9
Magnet thickness (mm)	6	6
Magnet radial length (mm)	75	72.5
Magnet width –OD/ID (mm)	51/31	65/32
Magnet overhang – OD (mm)	6	5
Magnet overhang – ID (mm)	6.5	5
Pole pitch (mm)/(degrees)	62/22.5°	60/30°
Pole arc at mean diameter (mm)	41	48
Pole arc to pole pitch ratio	0.66	0.8
Gap (winding+mech.clear)(mm)	8	9
Gap+magnet thickness (mm)	14	15
Rotor disc thickness (mm)	10	10
Rotor OD (mm)	415	314
Core OD (mm)	378	290
Core ID (mm)	253	165
Core radial depth (mm)	62.5	62.5
Mean diameter (mm)	316	227.5
Core thickness (mm)	28.4	22
Overall machine axial length (mm)	74	73

Table 4.1: Summary of the prototype machines

Other than the outer diameter and the rating, the main differences are the ratio between the core diameters, the pole-arc to pole-pitch ratio, and the winding specification. In spite of these minor differences, the two prototypes are very similar to each other and so enabled solid benchmarking of the various analytical and FEA methods.

4.2. Analytical predictions

4.2.1. Field solution: excitation field

The field solution described in Chapter 3 was used to plot the circumferential variation of axial flux density arising from the permanent magnets at the stator core surface for both prototypes, Figure 4.3 and Figure 4.4.

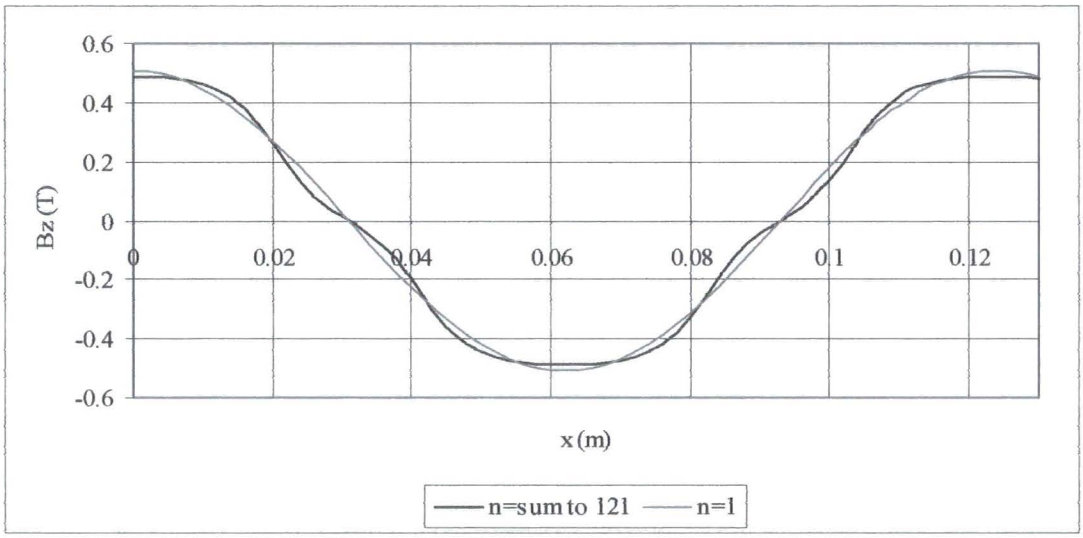

Figure 4.3: Excitation field flux density – 40kW prototype

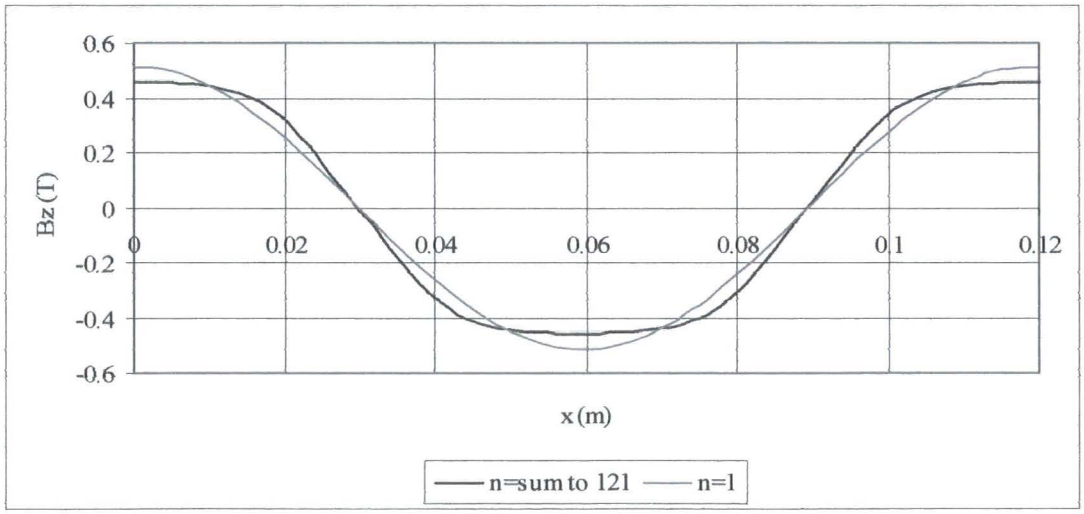

Figure 4.4: Excitation field flux density – 20kW prototype

The 20kW machine exhibits a more square overall profile, on account of the higher pole arc to pole pitch ratio, with a lower peak value on account of the increased effective gap. The harmonic values of the peak flux per pole and the induced EMF per coil were calculated for both prototype machines at their rated speeds, and are shown in Table 4.2.

	40kW, 4500RPM		20kW, 3000RPM	
n	φ_n	$E_{coil,\,n}$	φ_n	$E_{coil,\,n}$
1	1.38E-03	14.284014	1.32E-03	15.424650
3	-3.62E-06	-0.087481	5.25E-05	1.506162
5	-1.91E-05	-0.418748	9.31E-21	0.000000
7	-4.32E-06	-0.022098	-1.80E-06	-0.026488
9	1.39E-07	-0.002096	-7.19E-07	0.006193
11	4.20E-07	-0.010616	-1.94E-07	0.005285
13	1.20E-07	-0.002233	-3.47E-08	0.001070
15	-8.22E-09	-0.000003	1.32E-23	0.000000
17	-1.78E-08	-0.000341	3.30E-09	0.000018
19	-5.25E-09	-0.000132	1.73E-09	0.000044
21	5.77E-10	0.000008	5.70E-10	0.000018

Table 4.2: Harmonic values of the flux per pole and induced EMF per coil

The harmonic content affects the EMF profile as can be seen in Figure 4.5 and Figure 4.6.

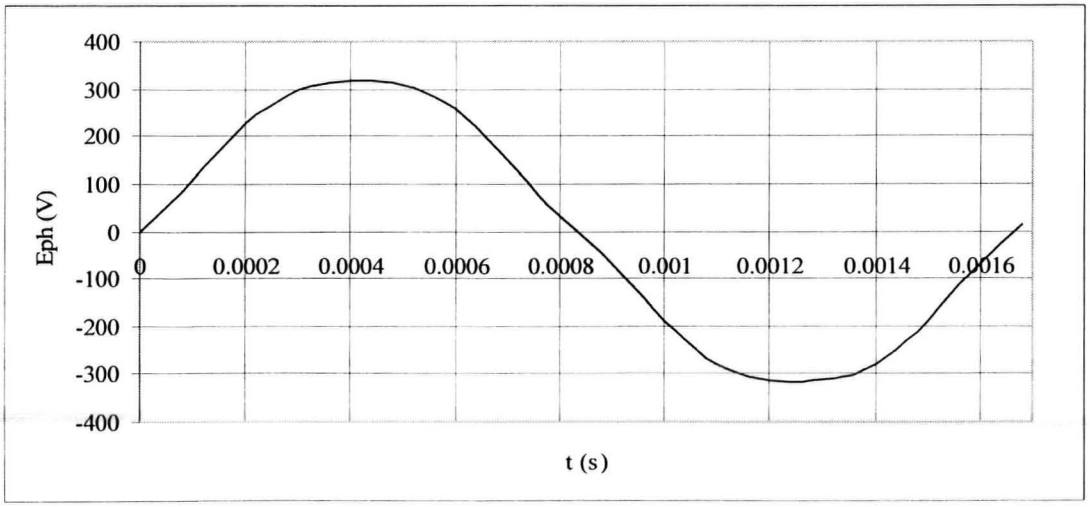

Figure 4.5: EMF induced in one phase at 4500RPM – 40kW machine

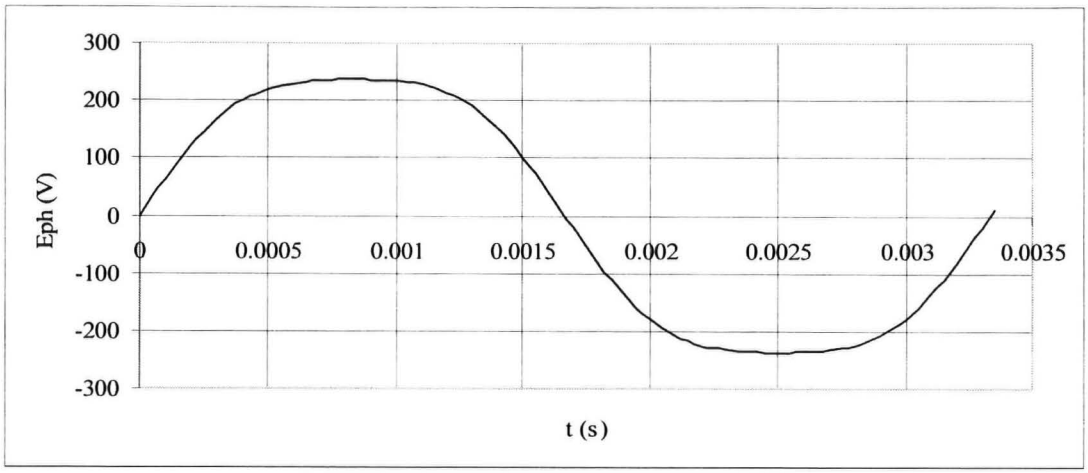

Figure 4.6: EMF induced in one phase at 3000RPM – 20kW machine

In summary, this analysis of the field arising from the permanent magnets yields the following results:

	40kW	**20kW**
Peak flux density, 1st harmonic (T)	0.509	0.515
Peak flux density, sum to 21 harmonics (T)	0.488	0.456
Peak flux per pole, 1st harmonic (mWb)	1.380	1.317
Peak flux per pole, sum to 21 harmonics (mWb)	1.353	1.367
$E_{phase\ RMS}$ 1st harmonic (V)	228.54	185.08
$E_{phase\ RMS}$ sum to 21 harmonics (V)	228.65	185.98

Table 4.3: Summary of excitation field analysis

4.2.2. Field solution: field arising from phase currents

The field solution described in Chapter 3 was used to plot the circumferential variation of axial flux density at the stator core surface arising from unit current in one phase with the permanent magnets demagnetised, Figure 4.7 and Figure 4.8. The 20kW prototype has more turns per pole per phase, which accounts for the higher flux density, but otherwise the graphs are similar in that the harmonic sum yields an approximately trapezoidal waveform that follows the MMF distribution of the phase conductors.

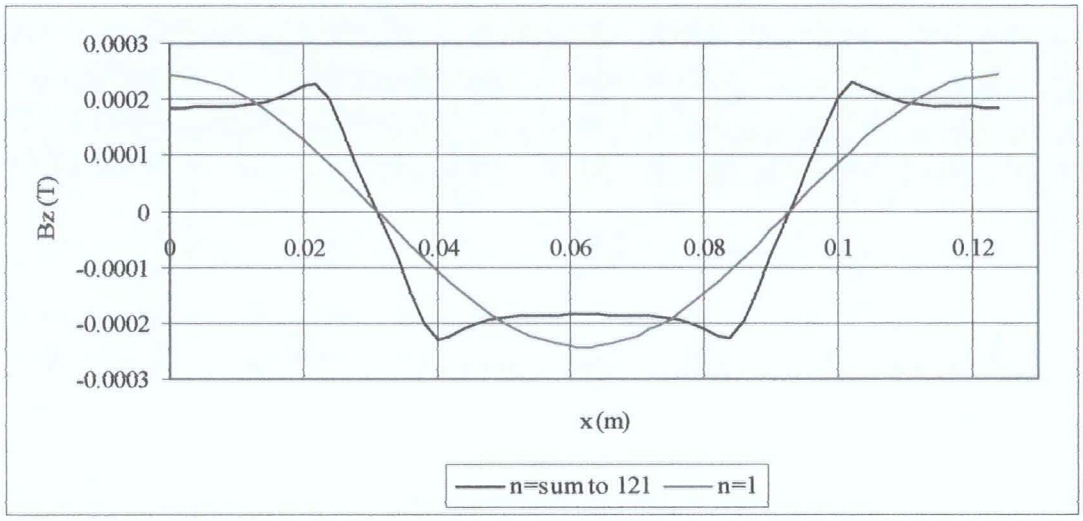

Figure 4.7: Phase current flux density – 40kW prototype

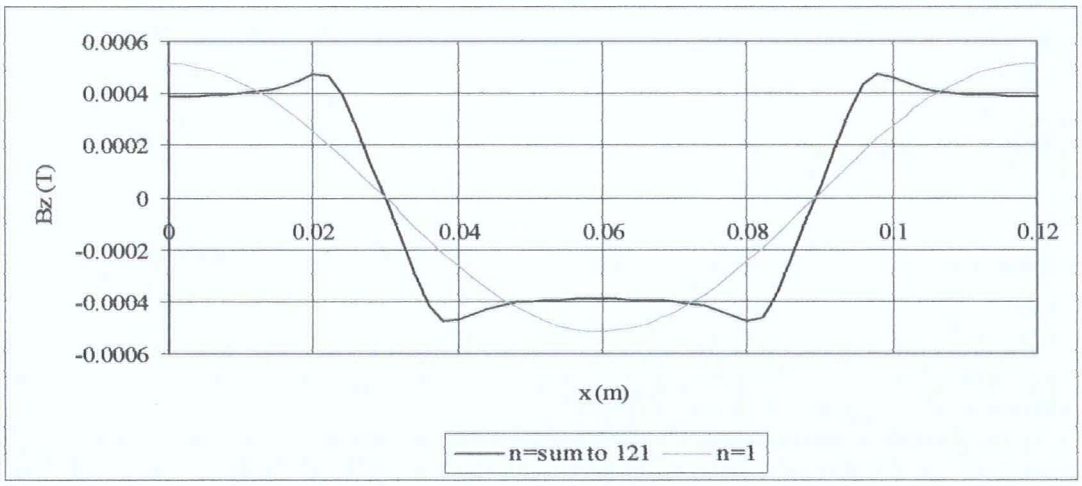

Figure 4.8: Phase current flux density – 20kW prototype

The flux density above the end-windings, situated at the inner and outer stator core ends, can similarly be plotted by setting the effective gap to a large value and adjusting the coil spread appropriately. The air-gap above the ends is effectively unbounded, and a large effective gap models this satisfactorily. The coils are touching at the inner radius of the core, so the electrical spread is 60^{o} there. The coils are "racetrack-shaped" as shown in Figure 4.9; therefore, they exhibit a rectangular profile when viewed in the axial direction and hence the spread reduces with

increasing radius. However, this analysis assumes that the difference between the inner and outer ends cancels and so an average spread is used for the plots below and for the ensuing calculation of the end-winding inductance.

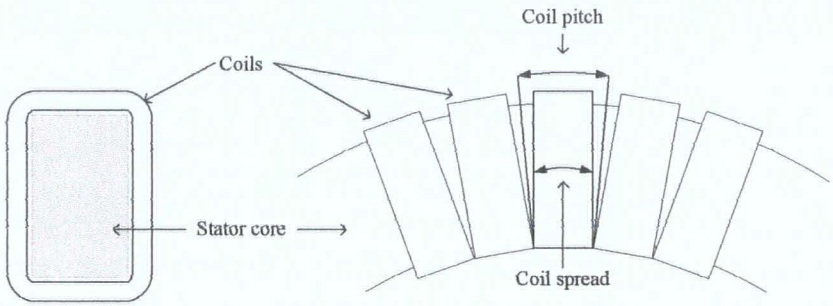

Figure 4.9: "Racetrack-shaped" coil definition

This time, the circumferential variation of radial flux density at the stator core surface arising from unit current in one phase with the permanent magnets demagnetised is shown, Figure 4.10 and Figure 4.11.

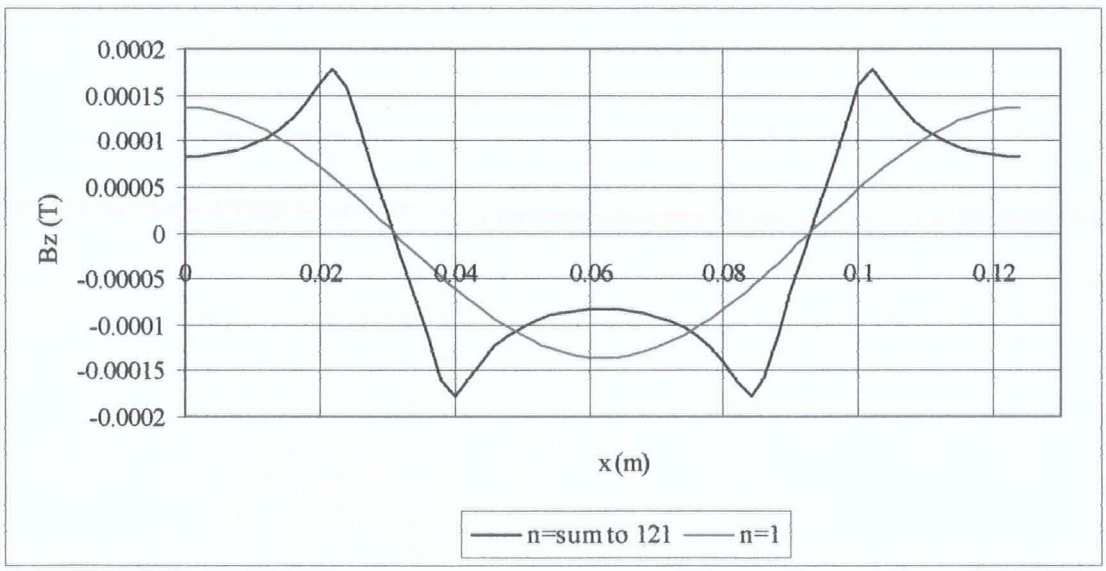

Figure 4.10: Phase current flux density – end-leakage – 40kW prototype

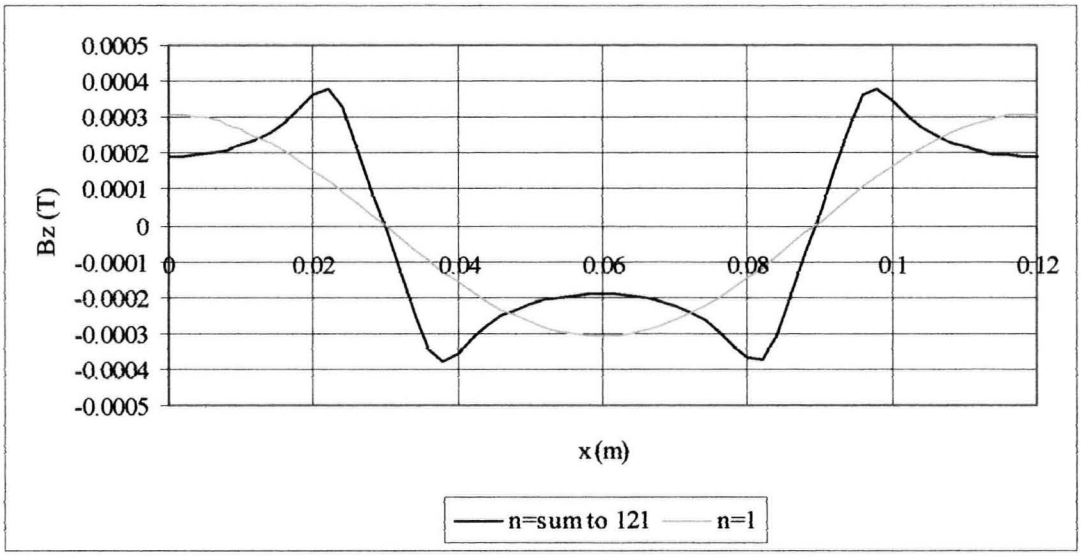

Figure 4.11: Phase current flux density – end-leakage – 20kW prototype

Since there is effectively no iron above the stator in these cases, the plots indicate flux densities that are at least an order of magnitude smaller than those encountered in the main winding region. The pronounced peaks and troughs are also indicative of a leakage field, as opposed to the small peaks indicating slight leakage effects superimposed on the otherwise regular field encountered in Figure 4.7 and Figure 4.8.

The results of the inductance calculations are given here for the main and end-winding regions of each machine, both per unit length in the 3rd dimension and also as modulated by the relevant length. The number of poles and the electrical frequency is factored in to finally give the per-phase synchronous reactance of each machine for operation at the appropriate rated speed. Since each of the inductances is calculated as a harmonic series, the value of the first harmonic and the sum to 121 harmonics is also given in each case. Table 4.4 shows the full set of inductance results.

		40kW	20kW
Per unit length	$L_{coil\ main,\ n=1}$ (H)	4.032E-05	1.908E-04
	$M_{coil\ main,\ n=1}$ (H)	2.016E-05	9.539E-05
	$L_{coil\ end,\ n=1}$ (H)	2.410E-05	1.235E-04
	$M_{coil\ end,\ n=1}$ (H)	1.205E-05	6.174E-05
	$L_{coil\ main,\ n=sum\ to\ 121}$ (H)	4.653E-05	2.273E-04
	$M_{coil\ main,\ n=sum\ to\ 121}$ (H)	1.559E-05	7.114E-05
	$L_{coil\ end,\ n=sum\ to\ 121}$ (H)	3.014E-05	1.594E-04
	$M_{coil\ end,\ n=sum\ to\ 121}$ (H)	7.634E-06	3.802E-05
Modulated by relative lengths	$L_{coil\ main,\ n=1}$ (H)	2.77E-06	1.29E-05
	$M_{coil\ main,\ n=1}$ (H)	1.39E-06	6.44E-06
	$L_{coil\ end,\ n=1}$ (H)	6.27E-07	3.06E-06
	$M_{coil\ end,\ n=1}$ (H)	3.13E-07	1.53E-06
	$L_{syn\ phase,\ n=1}$ (H)	8.161E-05	2.869E-04
	$X_{syn,\ n=1}$ (Ω)	0.308	0.541
	$L_{coil\ main,\ n=sum\ to\ 121}$ (H)	3.2E-06	1.53E-05
	$M_{coil\ main,\ n=sum\ to\ 121}$ (H)	1.07E-06	4.8E-06
	$L_{coil\ end,\ n=sum\ to\ 121}$ (H)	7.84E-07	3.95E-06
	$M_{coil\ end,\ n=sum\ to\ 121}$ (H)	1.98E-07	9.43E-07
	$L_{syn\ phase,\ n=sum\ to\ 121}$ (H)	8.409E-05	3.004E-04
	$X_{syn,\ n=sum\ to\ 121}$ (Ω)	0.317	0.566

Table 4.4: Summary of field-calculated inductance values

4.2.3. Magnetic circuit solution: excitation field

The magnetic circuit solution described in Chapter 3 was used to plot the circumferential variation of axial flux density arising from the magnets at the stator core surface for both machines. Figure 4.12 and Figure 4.13 compare the sine, square and first harmonic of the square wave approximations for each machine. The sine approximation is used for the 40kW machine, and the 1st harmonic of the square wave approximation is used for the 20kW machine on account of the increased pole arc to pole pitch ratio.

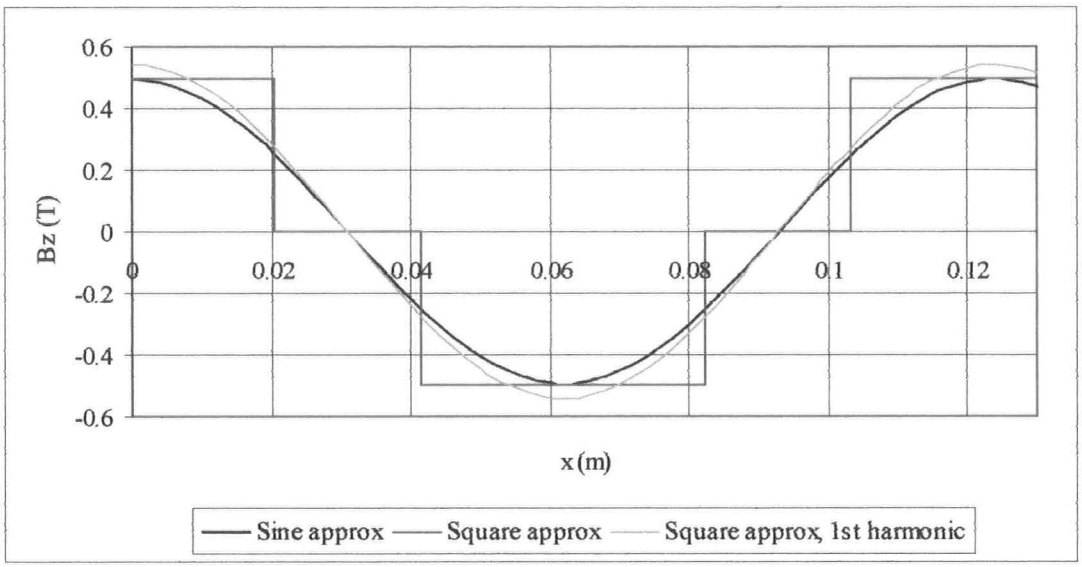

Figure 4.12: Excitation field flux density – 40kW machine

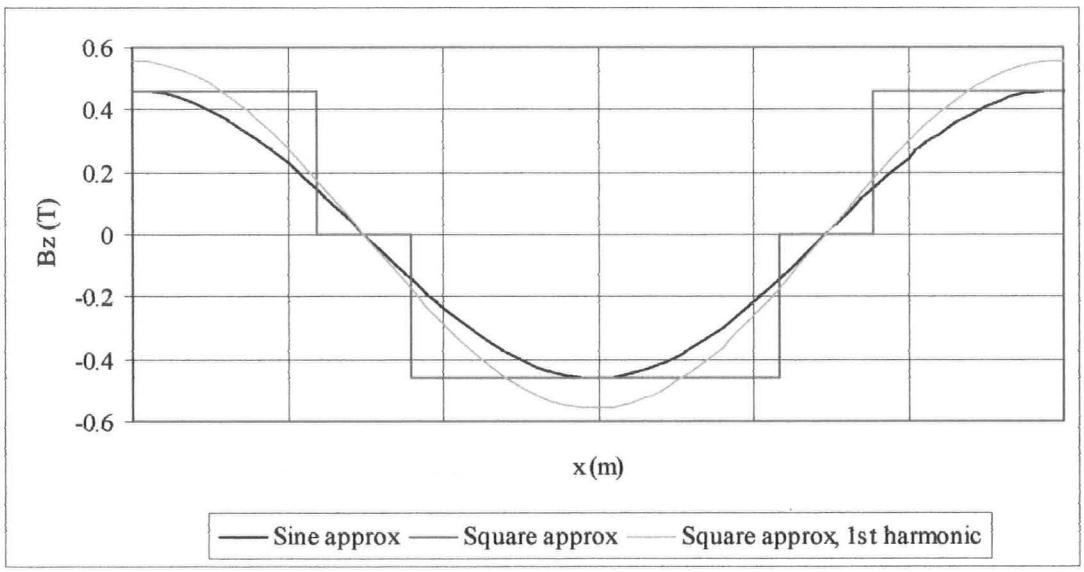

Figure 4.13: Excitation field flux density – 20kW machine

In summary, this analysis of the field arising from the permanent magnets yields the following results:

	40kW	**20kW**
Peak flux density (T)	0.494	0.558
Peak flux per pole (mWb)	1.341	1.428
$E_{phase\ RMS}$ (V)	221.92	200.47

Table 4.5: Summary of excitation field analysis

4.2.4. Magnetic circuit solution: field arising from phase currents

The magnetic circuit solution described in Chapter 3 was used to plot the circumferential variation of axial flux density at the stator core surface arising from unit current in one phase with the permanent magnets demagnetised. The trapezoidal profile for each machine is illustrated along with the first harmonic of each waveform which is used to calculate the inductance, Figure 4.14 and Figure 4.15.

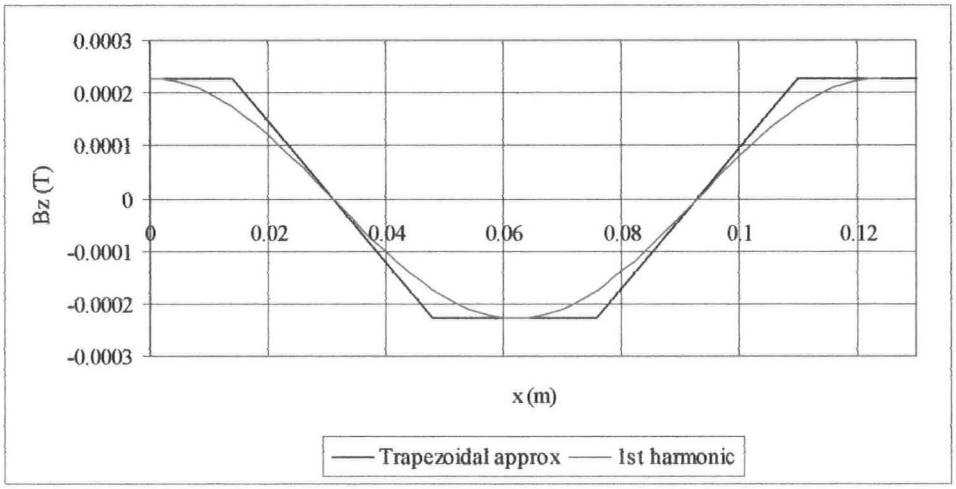

Figure 4.14: Phase current flux density – 40kW prototype

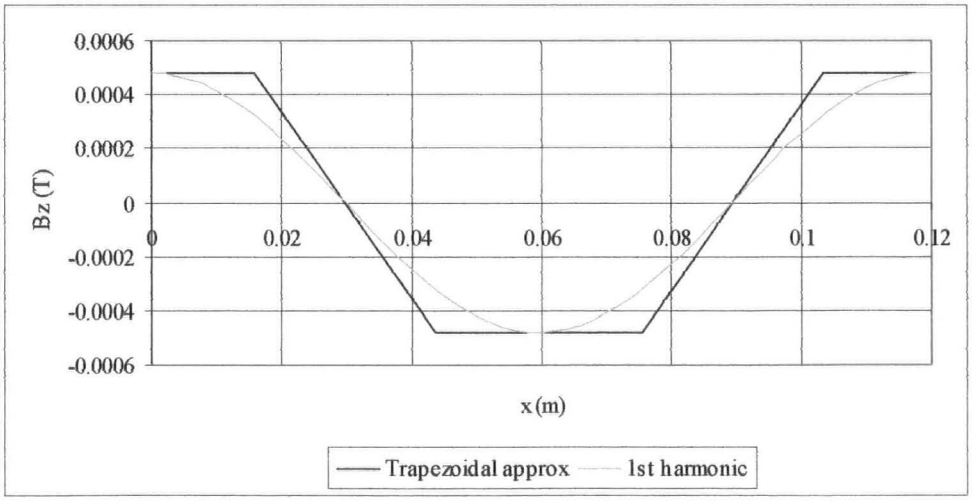

Figure 4.15: Phase current flux density – 20kW prototype

The results of the inductance calculations are given here for the main and end-winding regions of each machine, both per unit length in the 3rd dimension and also as modulated by the relevant length. The number of poles and the electrical frequency is factored in to finally give the per-phase synchronous reactance of each machine for operation at the appropriate rated speed. Table 4.6 shows the full set of inductance results.

		40kW	20kW
Per unit length	$L_{coil\ main}$ **(H)**	3.176E-05	1.484E-04
	$M_{coil\ main}$ **(H)**	1.588E-05	7.419E-05
	$L_{coil\ end}$ **(H)**	9.106E-06	4.537E-05
	$M_{coil\ end}$ **(H)**	4.553E-06	2.268E-05
Modulated by relative lengths	$L_{coil\ main}$ **(H)**	2.185E-06	1.002E-05
	$M_{coil\ main}$ **(H)**	1.093E-06	5.008E-06
	$L_{coil\ end}$ **(H)**	6.265E-07	3.062E-06
	$M_{coil\ end}$ **(H)**	3.133E-07	1.531E-06
	$L_{syn\ phase}$ **(H)**	6.749E-05	2.354E-04
	X_{syn} **(Ω)**	0.254	0.444

Table 4.6: Summary of magnetic circuit-calculated inductance values

4.2.5. Comparison of the analytical methods

Some brief comparisons are made between the field solution and the results of the magnetic circuit analyses. The magnetic circuit method serves simply as a rough verification of the field solution and could perhaps be more rapidly applied to the approximate design and analysis of this type of machine. The field solution is expected to be more accurate and the parameters obtained from this are used with the per-phase equivalent circuit model described in section 3.3 to predict the performance of the two prototypes for comparison with the experimental tests described in section 4.7.

Figure 4.16 compares the analyses of the circumferential variation of axial flux density in the 40kW machine arising from the permanent magnets. Figure 4.17 compares the analyses of the variation of flux density arising from unit current in one phase of the winding. The first harmonics compare very well, verifying the field solution as well as indicating a good level of accuracy achievable with the simpler magnetic circuit analysis.

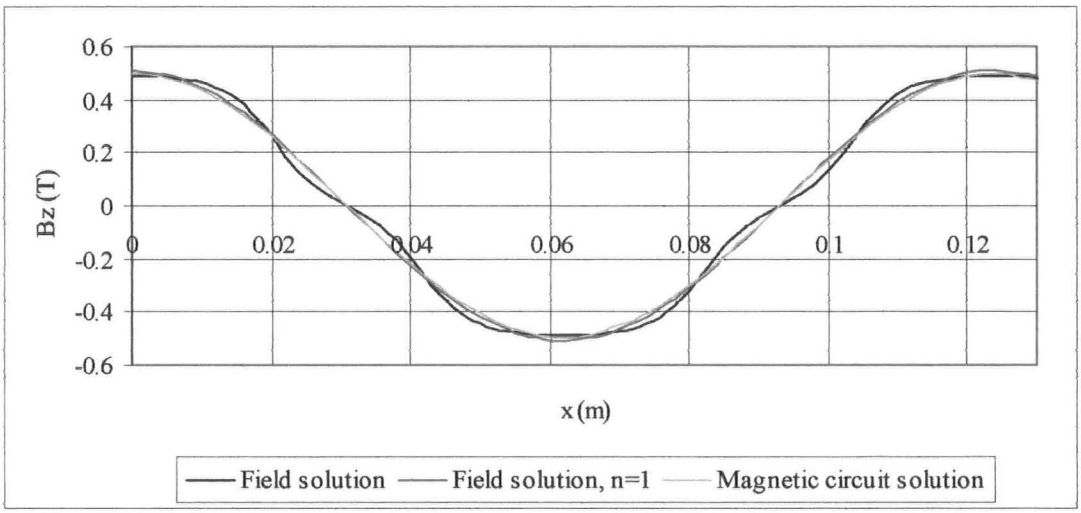

Figure 4.16: 40kW excitation field comparison

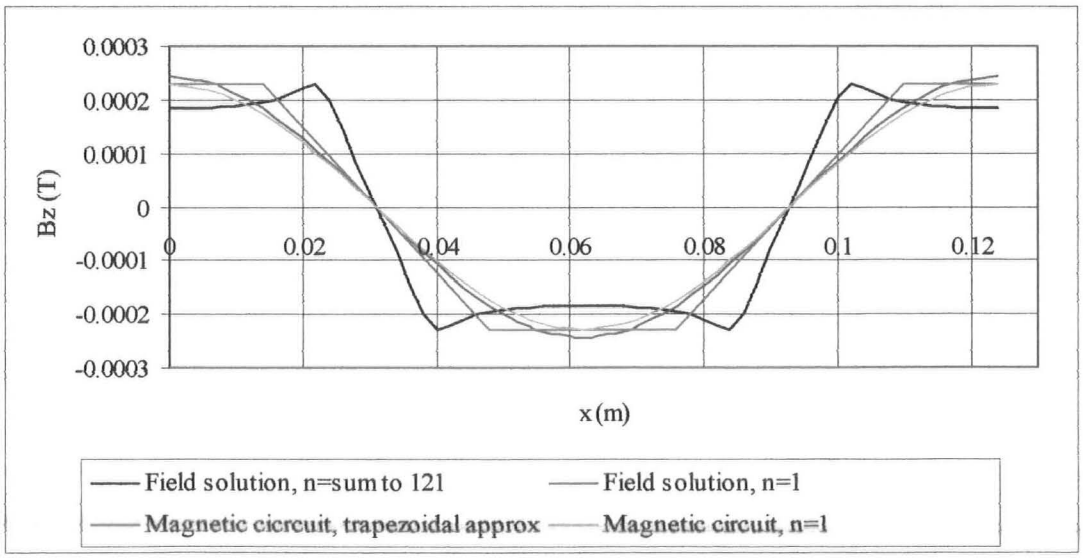

Figure 4.17: 40kW field arising from phase currents comparison

Table 4.7 summarises the results, showing the difference calculated between the magnetic circuit method and the more accurate field solution.

		Field solution	Magnetic circuit method	Difference (%)
40kW	**B_{pk} (T)**	0.488	0.494	1
	φ_{pp} (mWb)	1.353	1.341	1
	E (V_{RMS})	228.65	221.92	3
	X_{syn} (Ω)	0.317	0.254	20
20kW	**B_{pk} (T)**	0.456	0.461	1
	φ_{pp} (mWb)	1.367	1.428	4
	E (V_{RMS})	185.98	200.47	8
	X_{syn} (Ω)	0.566	0.444	22

Table 4.7: Summary and comparison of analytical predictions

The results compare well, particularly in the calculation of the excitation field. The magnetic circuit calculation of the open-circuit EMF, *E*, in the 20kW machine is slightly higher than that of the field solution. This is attributed to the fact that this method requires either a sinusoidal or a square approximation to the flux density waveform. Since the pole arc to pole pitch ratio is relatively high in the 20kW machine a square wave assumption was applied, and the first harmonic of that assumption was used for the calculation of flux per pole and then EMF. As shown by the field solution plot, Figure 4.4, the waveform is quite flat-topped, but certainly not a perfect square since not all the flux crosses the gap in a perpendicular fashion. However, the sinusoidal approximation gives an even greater discrepancy in this case and so the square wave was assumed to be the best available choice in that simple analysis. The method could be enhanced by a flux reduction factor of less than unity to account for this, obtained from FEA or by comparison with the field solution if required.

The calculation of the synchronous reactance is less accurate. The field arising from phase currents is much richer in harmonics and therefore the 1st harmonic approximation of the magnetic circuit method is not quite sufficient. Again, the assumption that all the flux crosses the gap perpendicularly contributes to the inaccuracy; the field solution plot of this field, Figure 4.7 and Figure 4.8, indicates a large amount of air-gap leakage flux. This is attributed to extra, parallel flux paths of lower reluctance that are ignored in the magnetic circuit analysis. These paths reduce the overall reluctance and, since the inductance is inversely proportional to the reluctance of the flux path, the synchronous reactance increases.

Although the magnetic circuit analysis predicts a significantly reduced synchronous reactance by comparison with the field solution, the absolute values are very small and the effects on the equivalent circuit calculations are negligible. If greater accuracy of the magnetic circuit method were required, a flux leakage factor greater than unity could be applied to account for this leakage reactance.

4.2.6. Predictions of the simple thermal analysis

The thermal analysis described in Chapter 3 was applied to each of the prototype machines. The winding parameters of each are shown along with the predictions of the analyses in Table 4.8.

This completes the analytical predictions for the two prototypes since all the equivalent circuit parameters are defined. In section 4.8, the predicted performance of the prototypes according to equivalent circuit analysis using these parameters is compared with the actual performance measured in the laboratory.

	40kW	20kW
Strand outer diameter (m)	0.001075	0.001075
Number of strands	3	3
Conductor diameter (m)	0.002365	0.002365
Insulation thickness (m)	0.000880	0.000880
Turn diameter (m)	0.004125	0.004125
Winding thickness (m)	0.005805	0.00700
Operating temperature (^{o}C)	160	160
Resisivity of copper at 0^{o}C (Ωm)	1.55E-08	1.55E-08
Temperature coefficient of resistance	0.004260	0.004260
Resisivity at operating temperature (Ωm)	2.61E-08	2.61E-08
Strand copper diameter (m)	0.001000	0.001000
Conductor cross sectional area (m^2)	2.36E-06	2.36E-06
Length of mean turn (m)	0.200	0.200
Length of phase conductor (m)	15.2	23.7
Phase resistance (Ω)	0.168	0.262
Eddy loss (W)	549	233
Iron loss (W)	110	30
Area for heat dissipation (m^2)	0.12	0.08
Ambient temperature (^{o}C)	20	20
Temperature difference (^{o}C)	140	140
Power dissipation (W)	2603	1876
I^{2}R loss allowance (W)	1944	1613
Rated current (A)	62.11	45.29
Current density (A/mm^2)	26.36	19.22
Electric loading (A/m)	12031	20529

Table 4.8: Summary of the winding parameters and thermal analysis

4.3. Electromagnetic FEA: general introduction

FEA is used here for a number of reasons, all concerning the modelling and analysis of the electromagnetic properties of the prototype machines. Firstly, close replications of the 2D geometry analysed in section 4.2 are solved in order to verify the results of the analytical approaches described in that section. Secondly, 3D FEA models are solved in order to check the application of the various 2D scenarios to what is essentially a 3D problem. Further to this, the illustrations of the magnetic fields in the machine that can be obtained from FEA studies give valuable insight into the operation of the machine as well as the nuances of the design and analysis.

Also, since the impedances of the machines are naturally small by comparison with more conventional machines, a short-circuit test is impossible in reality, but a virtual test may be carried out by FEA. There are other practical ways to determine the synchronous reactance and these are described with the experimental tests, but it is interesting that a virtual test may be carried out where its practical equivalent is impossible to implement. In fact, the overall visualisation and calculation of the electromagnetic properties and parameters of the machines can be carried out in much more detail and with illustrative techniques that far surpass anything that could be practically achieved in the laboratory, and so FEA is a very powerful tool in all aspects of electromagnetic design and analysis.

All the models described here assume a linear BH characteristic throughout. This makes significant savings in processing time since a non-linear solution performs multiple iterations in order to home in on the appropriate point on the relevant BH curve. Since the machines analysed are at the prototype stage the use of material is not optimal and the specification of rotor and stator back iron errs on the side of caution. Nevertheless, the flux density levels in the various components were monitored throughout the FEA in order to ensure that the linear solver was appropriate.

As with most electrical machines, the air-gap is an area of significant interest in this analysis and is generally at least an order of magnitude smaller than the overall machine size. This places considerable constraints on the FEA model since the rate at which the density of mesh elements can change through a model is finite: abrupt density changes across a mesh can result in awkwardly shaped elements that may compromise the calculations. This must be balanced with a pressing need for

variation in the density and hence size of the elements, since the number of simultaneous calculations and therefore the number of elements allowed is limited, i.e. the regularity of the mesh must be balanced with the need for coarseness of the mesh in non-critical regions in order to devise an appropriate mesh within the capabilities of the processing resource.

Furthermore, the most appropriate method of forming 3D models in the FEA program used for this analysis is by extrusion of a base plane. The base plane is perpendicular to the axial dimension and is therefore extruded along the axis of the machine. The levels of element boundaries in this z-direction are thus dictated by the thickness of the rotor discs, magnets, stator core, winding, and running clearance. The running clearance is of the order of a couple of millimetres and, when a 3D dynamic model is created, the sliding interface between the rotor and stator meshes is defined at the centre of this running clearance. For the best results at least two layers of air elements either side of the interface should be used, which implies element dimensions of the order of half a millimetre in the z dimension at this level. This dimension must be contrasted with the radial and circumferential dimensions of the largest elements on the base plane, since this approach could result in elements with unwieldy aspect ratios that will again compromise the results.

In order to overcome these problems, boundary conditions were exploited in most of the analyses. This reduced the size of the model, allowing for increased mesh refinement and improved regularity. The application of boundary conditions to this problem was described in Chapter 3. The axial symmetry consists of a tangential flux plane perpendicular to the axis which effectively allows modelling of only half of the machine, namely one rotor disc and half of the stator core. In fact, the construction of

the stator in two halves with its central spider support further underlines the fact that the two sides of the machine are uncoupled. The outer planes of the rotor discs that are similarly perpendicular to the axis of the machine can also be given a tangential flux boundary condition; this effectively bounds all the flux within the axial length of the model. In the case of 2D modelling, the coils are simply implemented as elements of the mesh, and so these conditions reduce the model by half in the axial direction as well as taking care of the axial ends of the machine. The same can be said for the analysis of the excitation field in the 3D model, but the implementation of coils is a different matter. In this case the coils are modelled as separate entities which must reside in a region of air. The *"automatic cut"* and *"reduced scalar"* commands within the MEGA program, [4], identify the air elements that contain the coils, convert these elements to regions of reduced scalar potential in order to implement the appropriate current density, and make appropriate cuts if holes appear in the conductor regions. These coils and the resulting reduced scalar regions effectively straddle the axial centre of the machine in the 3D representation which can cause problems, so the full axial length is modelled in this case. Tangential flux symmetry boundaries at the outer planes of each rotor are still applied, however.

Since high pole numbers are typically encountered in such machines, rotational symmetry in the circumferential direction can be exploited. In the case of the excitation field, half a pole pitch is sufficient representation and reduces the model by a factor of 32 or 24 for the 40kW and 20kW machines respectively. The visualisation afforded by such a minimal model is not ideal however, and the field arising from the phase currents cannot fully be analysed with that approach. In order to achieve good visualisation and a full analysis of both fields with a single model and consistent boundary conditions, a rotational span of one pole pitch was used.

Each rotor modelled carries half a north and half a south permanent magnet pole, so tangential flux conditions at the edges of the model apply. With a three phase machine, the fields arising from energisation of the central coil, or from energisation of all three coils (assuming 120^{o} displaced sinusoidal currents with the central coil at a maximum or minimum value) both exhibit the same symmetry, and so the tangential flux conditions at the sides are equally applicable.

Whether the tangential flux or the periodic boundary conditions are applied at these radial edges of the model, or their 2D equivalent, the flux conditions are satisfactory for the scenarios described above. Although the Biot-Savart formulation is used to calculate the field arising from phase currents, the commonly used technique of a fractional mesh with the full array of coils is not required where the arrangement of magnets, coils and symmetry conditions are exactly as described here.

The boundary conditions described thus far are complete and have been detailed and illustrated previously in section 3.4.1, Figure 3.5 and Figure 3.6. If a reasonable portion of air beyond the outer diameter of the machine is modelled then it is appropriate to apply zero scalar potential conditions to the nodes and elements across this curved plane. This effectively confines all the flux within the 3D model and is sufficient for full and unique specification of the problem. Figure 4.18 illustrates a sample reduced 3D model. The permanent magnets are shown in blue and pink, and have a remanance of 1.2T and a recoil permeability of 1.07. The steel appears in red and is assumed to have a linear BH characteristic with a relative permeability of 2000, a common value for electrical steel. The coils are shown in grey.

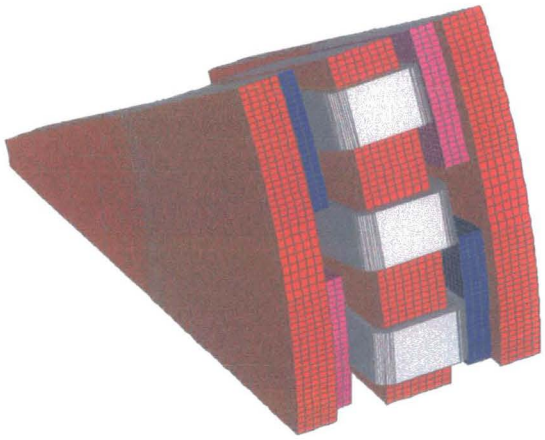

Figure 4.18: Sample 3D FEA mesh

The electromagnetic FEA now proceeds with separate analyses of the fields arising from permanent magnets and phase currents for comparison with the field distributions and equivalent circuit parameters obtained by analytical methods in section 4.2. The development of FEA models of the 40kW machine are described and illustrated. The exact approach was used for the analysis of the 20kW machine, and the results of both analyses are presented. For the analysis of the field arising from the magnets, a static 2D model is first described that facilitates visualisation of the field and calculation of the variation of the excitation flux density at the stator core surface. The flux per pole can also be calculated from this model, and these results serve to verify the predictions of the analytical methods.

A static 3D model is then described which gives good visualisation of the field variation and again enables calculation of the flux density waveforms, the flux per pole, and calculation of the per-phase induced EMF, verifying the predictions of the analytical methods and checking the validity of the 2D approximation.

The development of dynamic 3D models that simulate an open-circuit test and return the resulting 3-phase voltage waveforms for direct comparison with the experimental test is finally described. Periodic or symmetry boundaries may not be implemented in a dynamic model where the sliding interfaces are disc-shaped and so the full machine must be modelled. This places considerable strain on the mesh since the available processing power is only just sufficient for a fractional model, and the results are somewhat variable. In order to overcome this, a linear dynamic 3D model is described which ignores the curvature present in the machine and considers the geometry at the mean diameter. The field is compared with the results of the disc-shaped model for verification of the linear approach. Since the sliding interface is rectangular in a linear model the boundary conditions may be exploited and the resulting EMF predictions are more consistent.

4.3.1. 2D magnetostatic FEA

Figure 4.19 shows the FEA mesh of the 2D reduced model described above alongside the same model with calculated contours of magnetic vector potential (effectively flux lines.

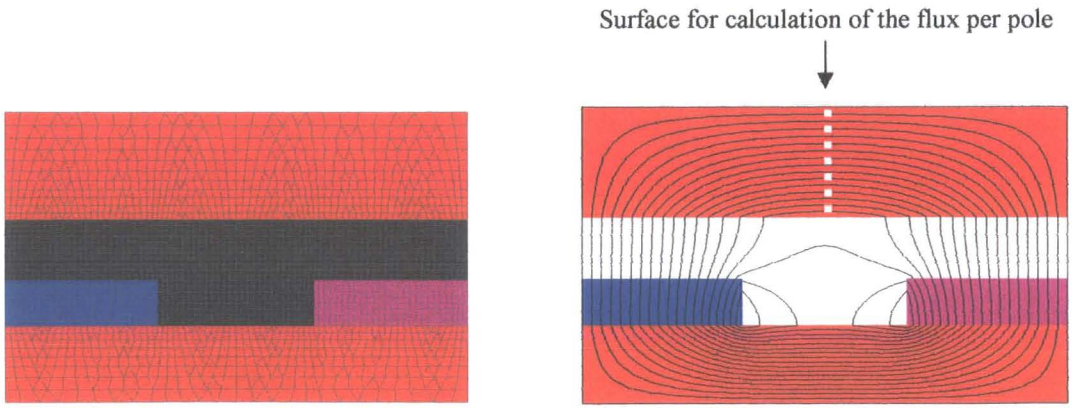

Figure 4.19: 2D FEA of the 40kW machine

The axial flux density is obtained at the centroid of the air elements at the stator core surface; this gives a waveform for comparison with the analytical prediction, shown in Figure 4.20.

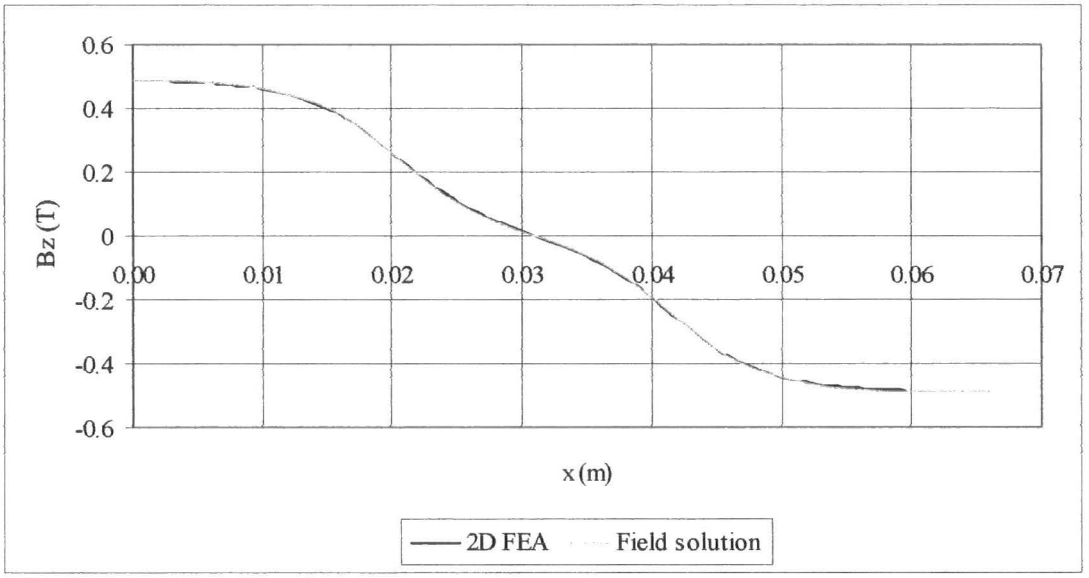

Figure 4.20: Excitation field flux density comparison

This flux density gives an indication of the flux entering the stator core and the waveform can be numerically integrated using Matlab, for example, to give the peak flux per pole. Alternatively, a surface may be defined in the FEA model across which the flux density can be integrated. An axially directed slice into the core is taken as shown in Figure 4.19; the flux passing here is the contribution of one side of the machine to the peak flux per pole per unit length into the page and, when normalised appropriately, gives a value of 1.354mWb, which compares well with the field solution of 1.353mWb. In order to normalise the result per unit length into the page, the effective core length defined in section 3.4.2 was used; the validity of this approach is verified now by 3D FEA.

4.3.2. 3D magnetostatic FEA

The 3D model consists of the full axial length of the machine, comprising both rotors and the stator, and spans one pole pitch, namely 22.5 mechanical degrees. The mesh is made from 154,082 elements with 159,215 nodes, thus requiring 159,215 equations to be solved. There are 4 regions: air, iron, and two orientations of permanent magnet. No coils have been modelled yet, and the mesh is shown in Figure 4.21, with the coordinate system.

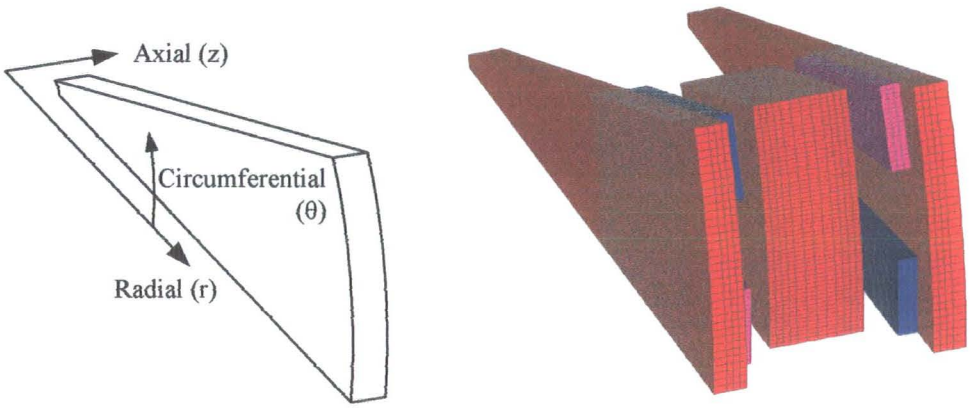

Figure 4.21: 40kW 3D FEA mesh

Again, the variation of flux density at the stator core surface is of interest, and the 3D model yields information about this across that entire plane as a 3D Cartesian flux density vector at the centroid of each element, along with the 3D Cartesian coordinate of that centroid. The values are exported to MS Excel where the data is organised; the axial flux density (B_z) is of interest, and the (x, y) coordinates within the plane are required whereas the z coordinate is constant across the plane. A Matlab program (see Appendix 1) was devised to organise this data and facilitate the 3D surface of flux density and the circumferential and radial variations of the field at these points, Figure 4.22, Figure 4.23, and Figure 4.24. It should be noted that the Matlab coordinate system in Figure 4.22 is (x, y, z), but that the (r, θ, z) system is illustrated for comparison with the mesh of Figure 4.21.

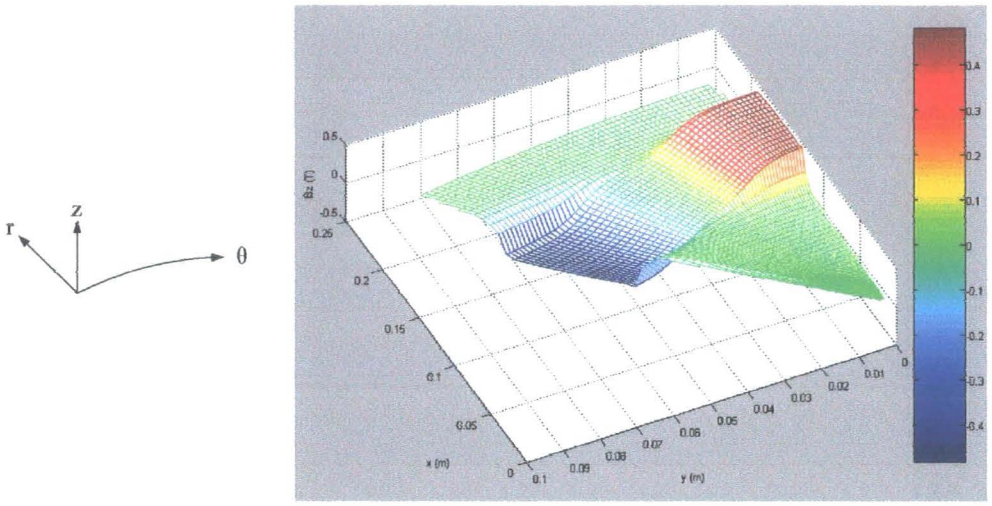

Figure 4.22: 3D surface of axial flux density in the air-gap

Of the 2D comparisons, the circumferential variation is taken at the mean radius and is compared with the 2D FEA result, whereas the radial variation is taken across the centre of a pole and gives an appreciation of the end effects.

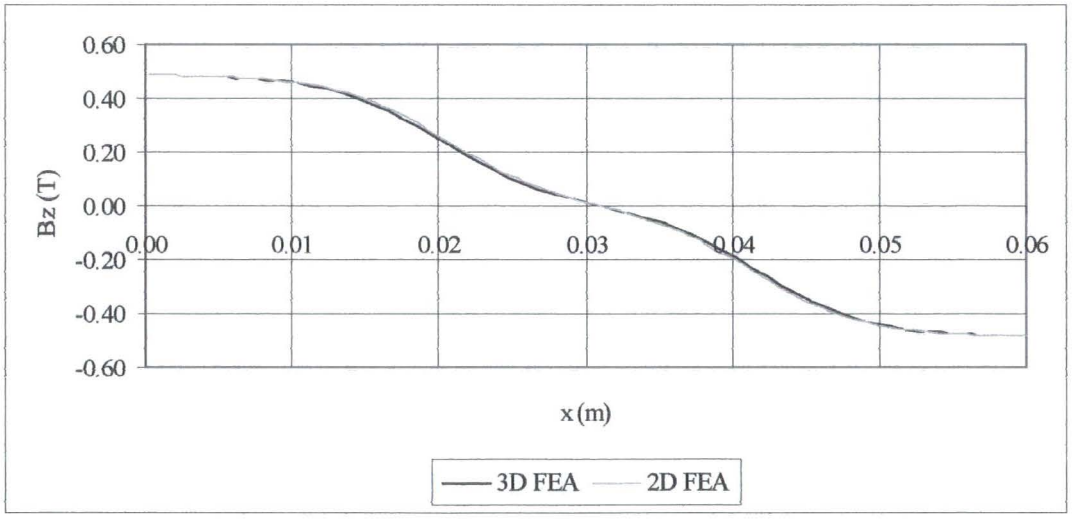

Figure 4.23: Circumferential variation of axial flux density in the air-gap

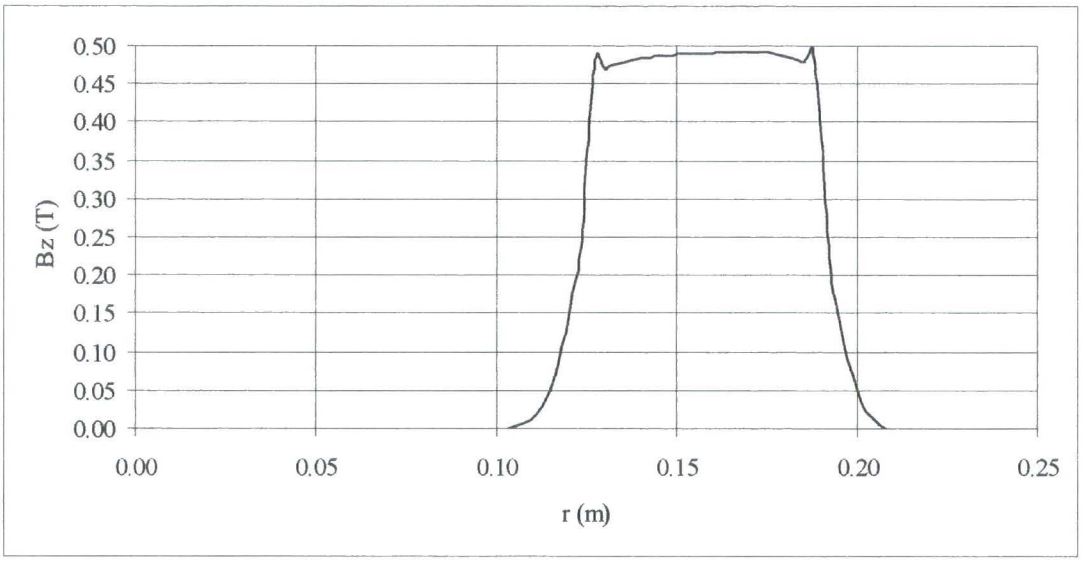

Figure 4.24: Radial variation of axial flux density in the air-gap

In order to illustrate this radial variation, gain an appreciation of the end effects, and evaluate the assumption of infinite length in the radial dimension which is made in 2D approaches, Figure 4.25 shows the process of taking a radial slice into a similar model which spans two pole pitches and consists of only half the axial length of the machine.

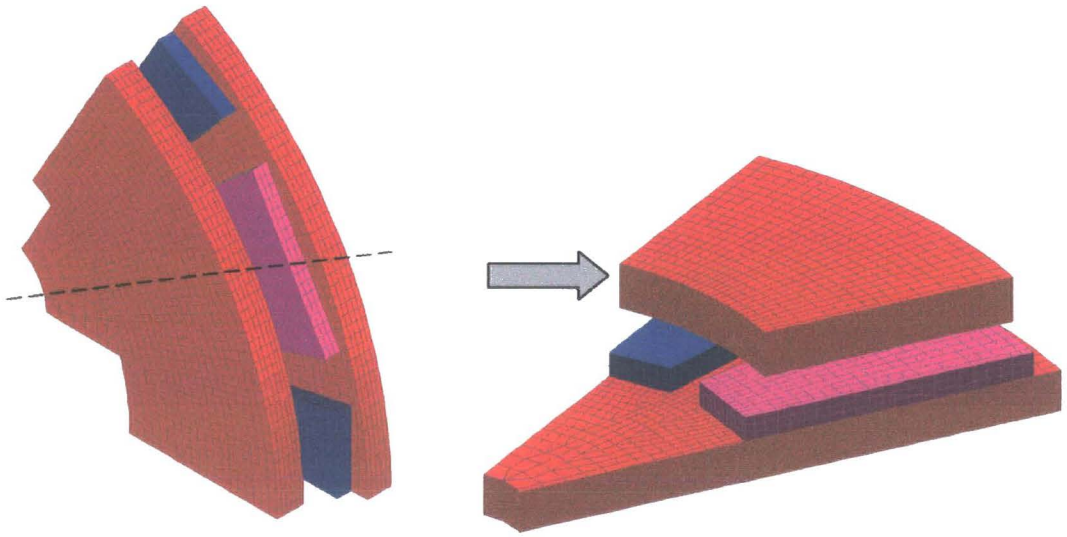

Figure 4.25: The process of taking a radial slice into the 3D FEA mesh

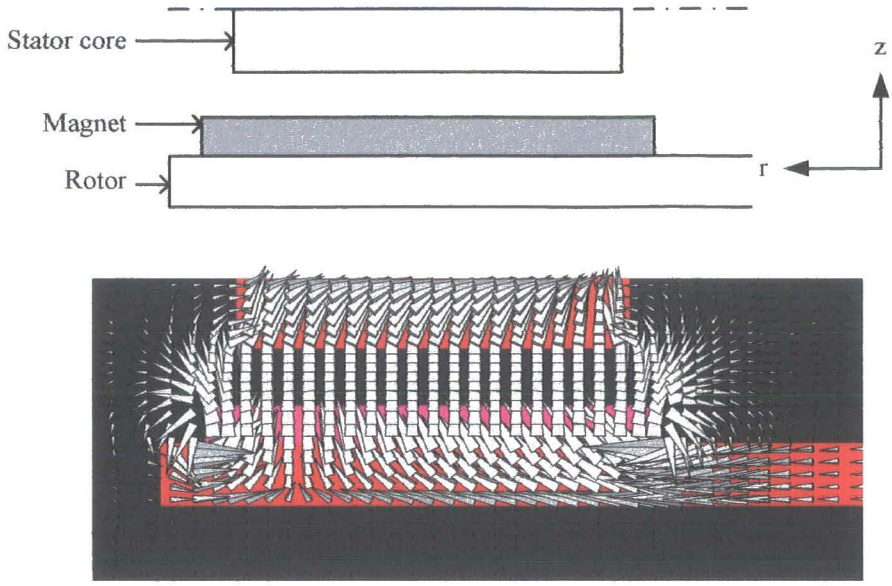

Figure 4.26: 3D FEA illustration of the radial end effects

Figure 4.26 shows this section face on, which can be related to the radial plot of flux density shown in Figure 4.24. This indicates that a 2D reduction whereby a section at the mean diameter is considered representative of the radial length should give a reasonable appreciation of the flux density across the radial depth of the stator core. However, some end effects at the inner and outer diameters are clearly in evidence. In particular, leakage flux around the edges of the magnet and a certain amount of flux entering the stator core ends are in evidence. To some extent, both of these phenomena are attributed to this particular design whereby the rotor magnets overhand the stator core edges to some extent in an attempt to make better use of this region. Although not considered here, this aspect of the FEA could provide a basis for evaluation of this design nuance.

The flux per pole can be determined in the same way as it was from the 2D model, namely by defining a plane in the stator core across which to integrate the flux density in order to obtain the peak value of the circumferentially travelling flux; this

principle is illustrated in Figure 4.27, which shows a sample model of only half the axial length of a machine.

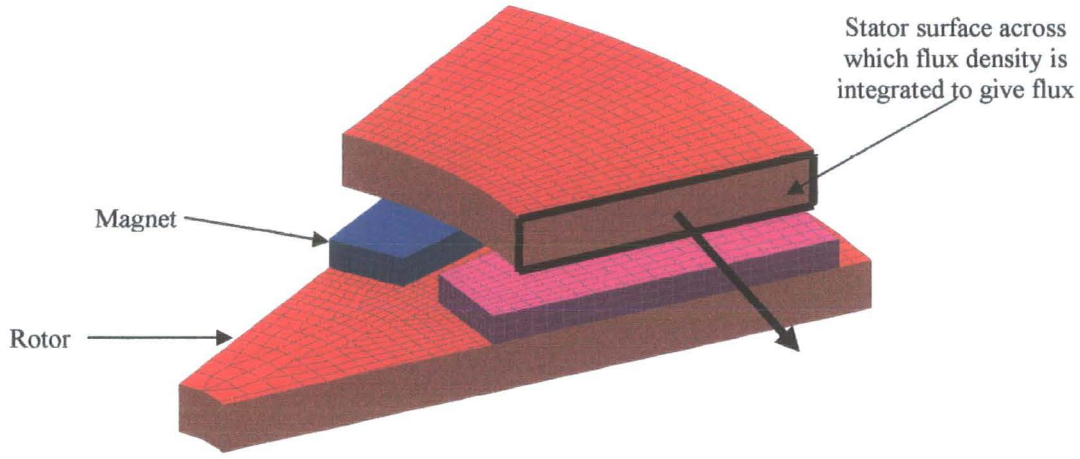

Figure 4.27: Integration surface to give the core flux

Since the model used (shown in Figure 4.21) is in 3D and comprises the full axial length of the machine, no modulation of the result by any effective length factor is required. The integral gives a peak flux per pole of 1.342mWb which compares well with the 2D analytical and FEA results of 1.353mWb and 1.354mWb respectively. The end effects indicated by the graph of the radial variation of flux density, Figure 4.24, and the FEA illustration, Figure 4.26 are noticeable and interesting, but are minimal in this case. The effective length approach described in section 3.4.2 is verified and the 2D approach is accurate to within 1% of the 3D FEA in terms of the peak core flux evaluation.

The magnetostatic FEA solution can also be used to plot the variation of circumferentially travelling core flux with angle around the stator core. Points on the curve at any angle can be obtained as per the peak flux per pole prediction, and the phase displacement of the 4 turns per coil of the 40kW machine can be included to obtain the coil induced EMF by superposition. This method is appropriate in the case

of the air-gap wound TORUS machine since the spatial variation of flux around the stator core is the same as the temporal variation of flux in the stator core at a fixed angle, owing to the fact that the stator surface is smooth and the rotors effectively rotate a field that is otherwise constant with respect to the stator. A sinusoidal approximation to the stator core flux is made from the analytical prediction of the peak core flux; this is compared with the actual core flux variation obtained from the FEA, Figure 4.28.

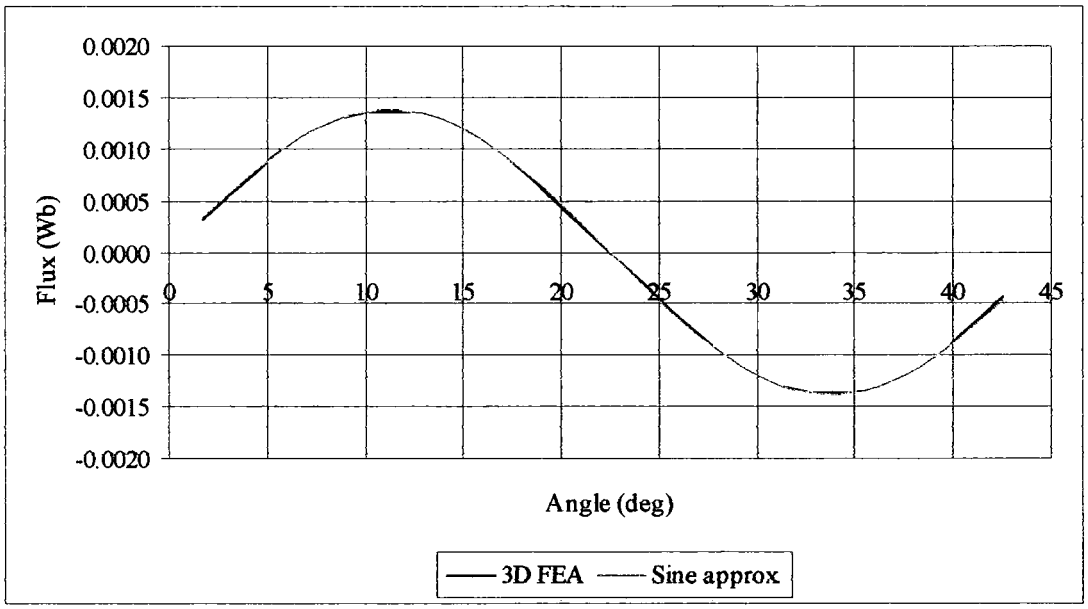

Figure 4.28: Angular variation of the circumferentially-travelling core flux

A simple conversion factor is used to give the variation of core flux with time experienced at a fixed location in the stator core. Since the location of each turn of the phase winding is known, the EMF induced in each turn of a coil can be plotted. This is shown in Figure 4.29 for operation at 1500RPM, since the analysis was originally undertaken for comparison with a test result at that speed.

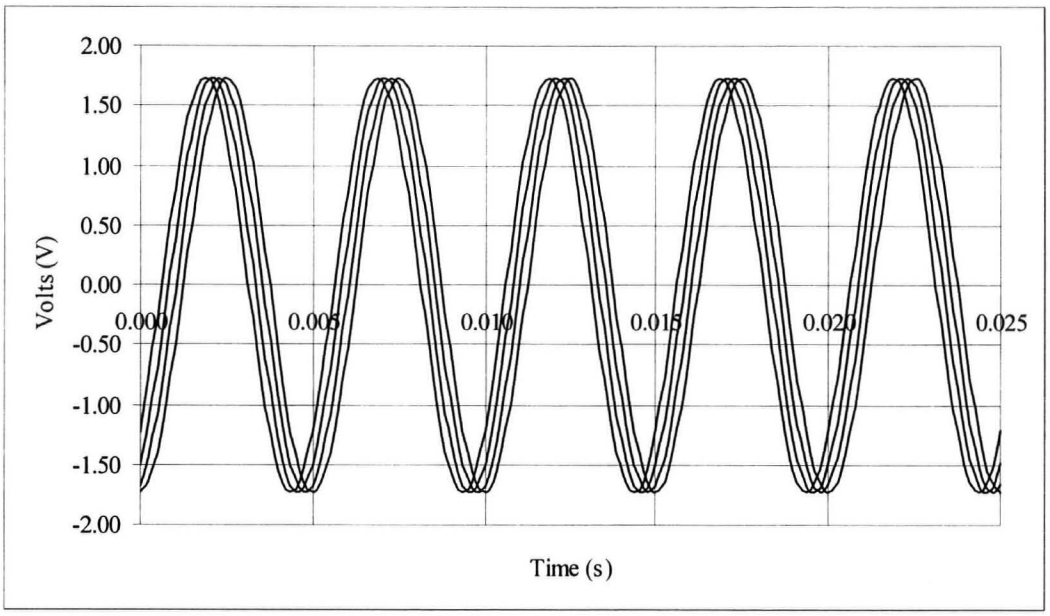

Figure 4.29: Induced EMF per turn at 1500RPM

Further to this, the EMF waveform per coil can be obtained by superposition, and the coils per phase can be factored in to generate a predicted 3-phase waveform, shown in Figure 4.30. This indicates an RMS value of 74.8V per phase, which equates to 224.5V at 4500RPM. Comparing the analytical result of 228.7V indicates accuracy to within 2%.

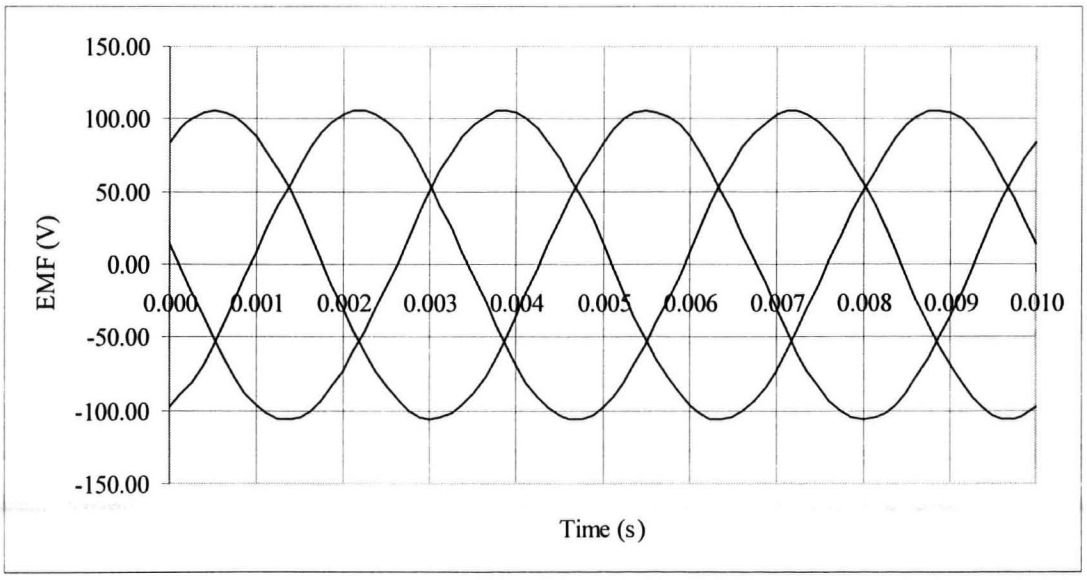

Figure 4.30: Induced EMF per phase at 1500RPM

4.3.3. 3D dynamic FEA

The methods of calculating the open circuit induced EMF by FEA that have been outlined so far both make certain approximations: the flux is assumed to vary sinusoidally with time, and the coil spread is assumed to be constant at the value obtained at the mean diameter of the machine. In order to check the validity of this approach, and perhaps calculate the open circuit induced EMF more accurately, it is possible to run a dynamic 3D FEA from which EMF waveforms are returned directly, without recourse to further assumptions and calculations. This section describes the development, verification, and results of 3D dynamic FEA models of the 40kW prototype machine.

Since disc-shaped sliding interfaces required to connect multiple parts of a mesh that require relative movement may not be implemented alongside periodic boundary conditions, it is necessary to model the entire machine for this analysis. This places considerable constraints on the resolution of the mesh, as described in section 4.3, and consequently may compromise the accuracy of the results. Therefore a static solution of the entire model is first obtained for verification purposes. The FEA mesh consists of 96,000 elements with 94,505 nodes and equations, and is shown with and without the element outlines in Figure 4.31.

"Racetrack-shaped" coils are now added to the stator core and these accurately represent the winding of the TORUS machine since the coils are rectangular when viewed from the axial direction, almost touching at the inner diameter and keeping parallel sides between the inner and outer diameter such that the coil spread reduces with increasing diameter. Figure 4.32 shows how the coil geometry is defined in the FEA program, alongside the stator mesh with its full complement of coils.

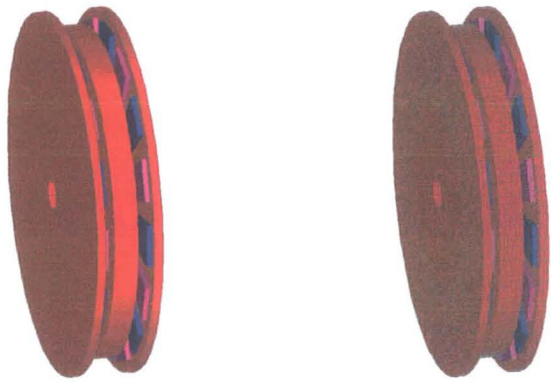

Figure 4.31: Full disc 3D dynamic FEA model

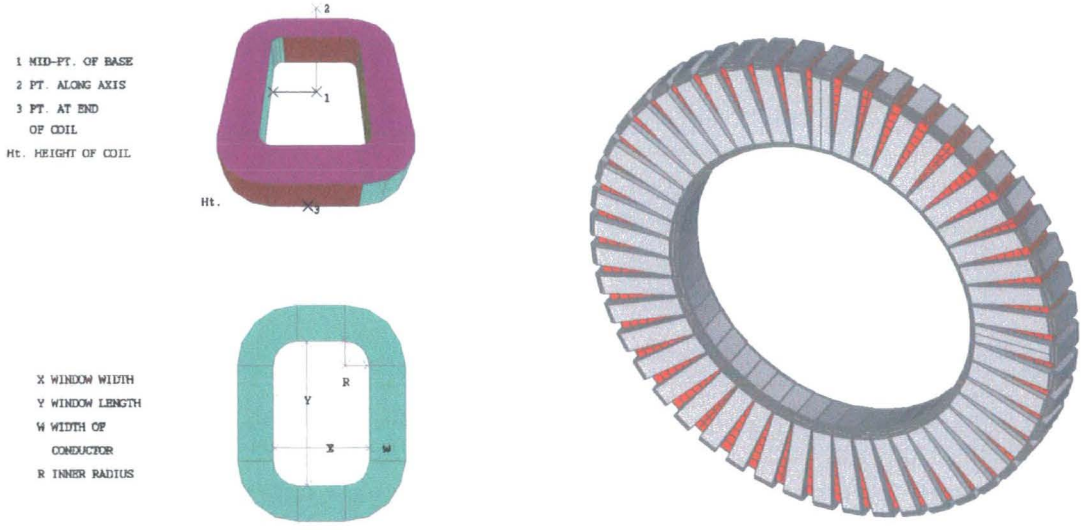

Figure 4.32: Coil definition and stator mesh with coils

Firstly the model is solved in the static state with a zero current forced in the coils; the analysis of the field arising from the magnets described for the fractional model in section 4.3.2 is repeated in order to obtain the 3D plot of the field and the circumferential and radial flux density variations for comparison. The results and comparisons are shown in Figure 4.33; two angles on the 3D plots are shown for clarity.

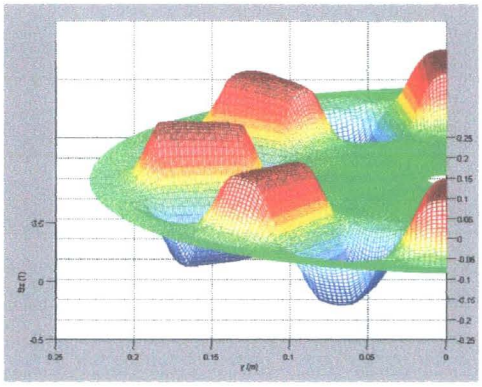

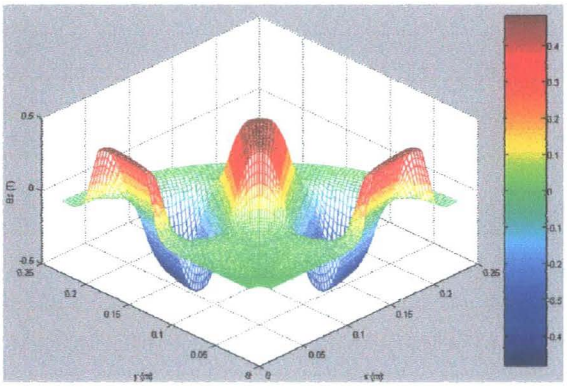

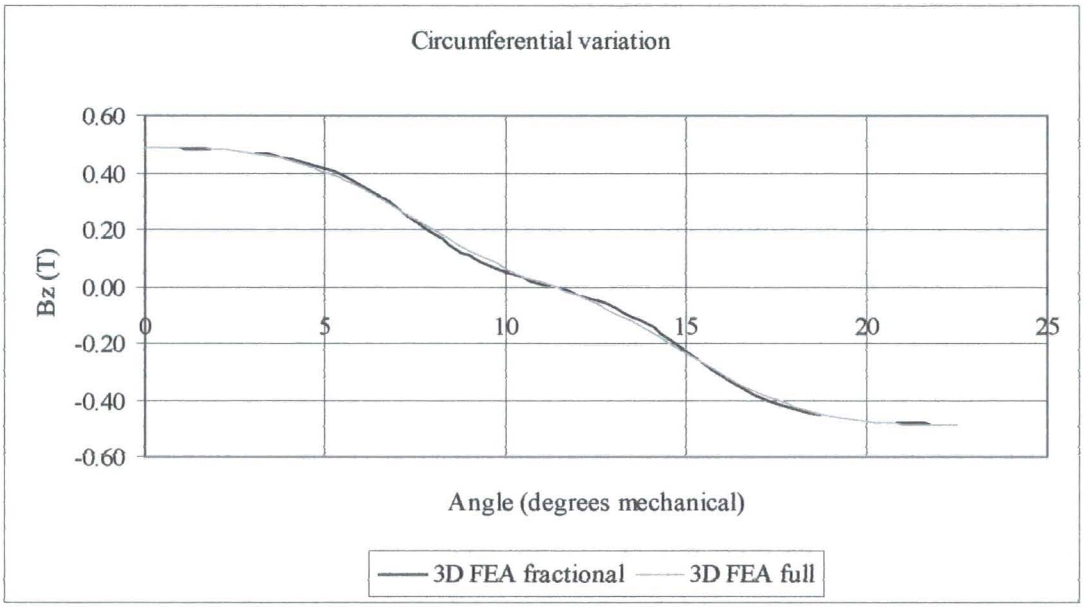

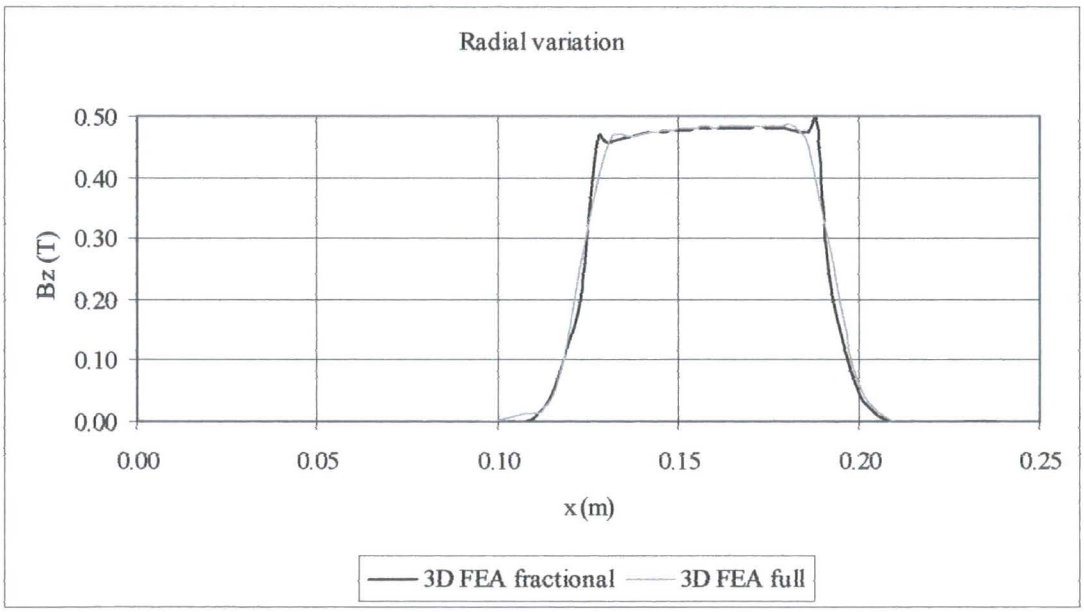

Figure 4.33: Field plots and comparisons from the 3D FEA of the full machine

Although there are some discrepancies between the waveform obtained by the more refined fractional model and the coarse full model, notably the detail around the radial ends of the machine, the results are still in good agreement and give confidence in the EMF prediction of the full 3D dynamic model.

In order to form the dynamic model, the static model of the machine is reduced into three components: two rotors and a stator section, separated at the centre of each running clearance. In the formulation of each model, the full machine file is first opened, and the necessary levels in the axial dimension are deleted; in this way the coordinate system is consistent and the components do not require rotation or reorientation when they are reconnected to form the dynamic model. When the components are read, the first rotor file is read in. The *"read yet another model"* command is used to read the stator file, which is declared to be a moving component. The Lagrange interface menu automatically appears and the interface between the two components is defined as a plane perpendicular to the axial direction, with a set distance from the origin. The second rotor is read in similarly, declared to be a static component, and the second Lagrange interface defined. Only relative movement is required between the stator and rotors, so the stator moves since it is easier to define one moving component than two.

Since the phases are open-circuited, no current flows and so the coils do not contribute to the magnetic field present. Therefore it is sufficient to only model one coil. However, six coils were modelled here with two of each phase (north and south) connected in series, so that the phase angle and the connection procedure can be checked. The coils are given a set number of turns and are connected to ports at their individual input and output. A port can be either set neutral, connected to ground, or

have a forced current specification. For example, the two coils of a given phase are connected as follows: one is connected between a forced current of zero amps and a neutral; the other is connected between ground and the neutral respectively. This yields a series connection between the coils and the coils would have opposing polarities if current flowed. Since the electrical angle between the coils is 60°, one of the phases is reversed in order to preserve a 120° phase angle output, i.e. the six coils appear in this sequence: A-BB-C-AA-B-CC. The ports are defined as shown in Table 4.9.

Port	Specification
AIN	Current forced, I=0
AON	Neutral
AOUT	Grounded
BIN	Current forced, I=0
BON	Neutral
BOUT	Grounded
CIN	Current forced, I=0
CON	Neutral
COUT	Grounded

Table 4.9: Coil port specifications

The coils are set up as shown in Table 4.10 to achieve the connections described above.

Coil number	Phase/polarity	Input	Output
1	AA	AOUT	AON
2	B	BIN	BON
3	CC	COUT	CON
4	A	AIN	AON
5	BB	BOUT	BON
6	C	CIN	CON

Table 4.10: Coil connections

The simulation is set up for dynamic movement at a constant speed of 4500RPM with a simulation length to give two full electrical cycles. A time-step appropriate to

the simulation length is specified and the solver returns graphs of voltage with time for both coils and ports where required. As a quick initial check, the voltage measured across coil 1 should be half that measured at port AIN, since AIN should be a sum of the two series-connected coils. The waveforms are imported to MS Excel and the resulting three phase waveform for the full machine (all 16 poles) is shown in Figure 4.34.

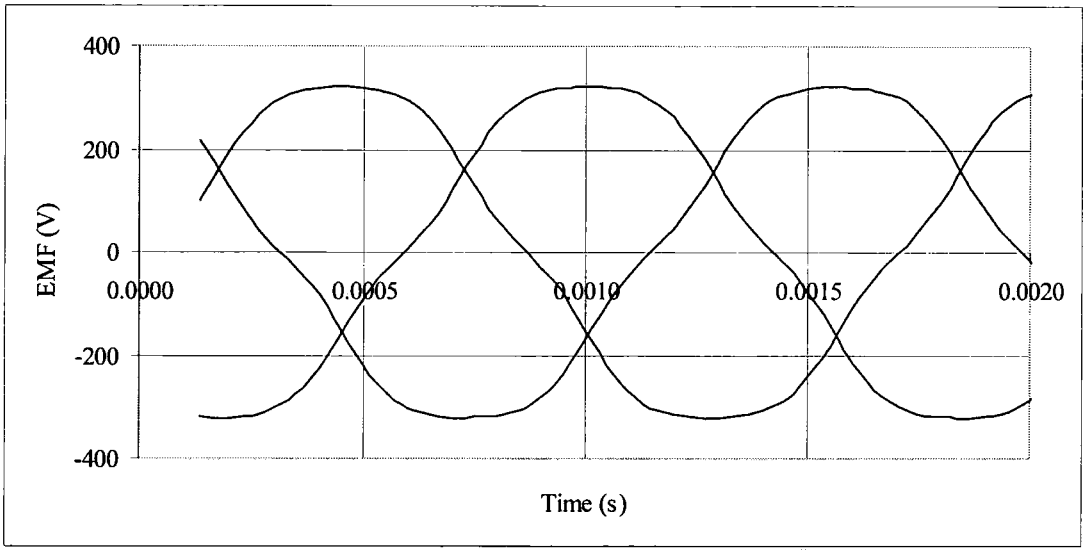

Figure 4.34: EMF prediction at 4500RPM from the full 3D dynamic FEA

The waveforms have a peak value of 320V indicating an RMS of 226V, comparing well with the analytical value of 228.7V and the FEA result of 224.5 obtained by the more circuitous route described in section 4.3.2.

In calculating the RMS values it is assumed that the voltage waveform is sinusoidal. In a final check on this dynamic model, the waveform obtained for one phase is compared with the first harmonic obtained by considering the peak flux per pole given by the static FEA. Figure 4.35 shows the comparison.

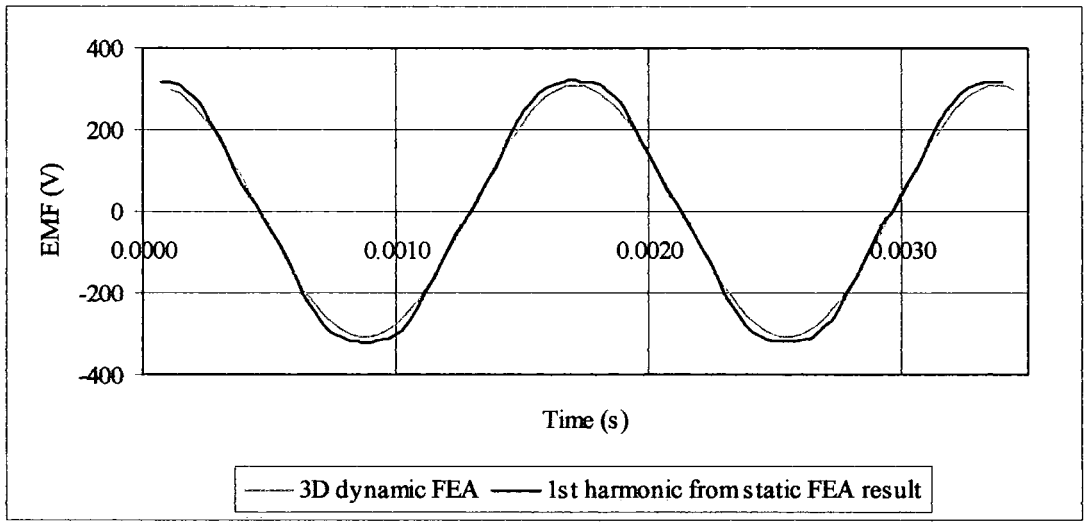

Figure 4.35: Comparison of EMF calculation by 3D dynamic and static FEA

4.3.4. 3D linear dynamic FEA

Where the computational resources constrain the accuracy of the full 3D dynamic model considerably, an alternative approximation may be made in the form of a linear model that ignores the curvature and represents the machine according to the geometry at the mean diameter. Such a model is described here, verified alongside the refined 3D static model, and solved in the dynamic state for comparison with the full 3D disc model.

The reason for making the linear approximation is that the sliding interface is rectangular and hence periodic boundary conditions may be used to facilitate the exploitation of symmetry. This enables the solution of a more refined mesh shown in Figure 4.36, along with a 3D plot of the axial flux density arising from the permanent magnets, as evaluated at the stator core surface.

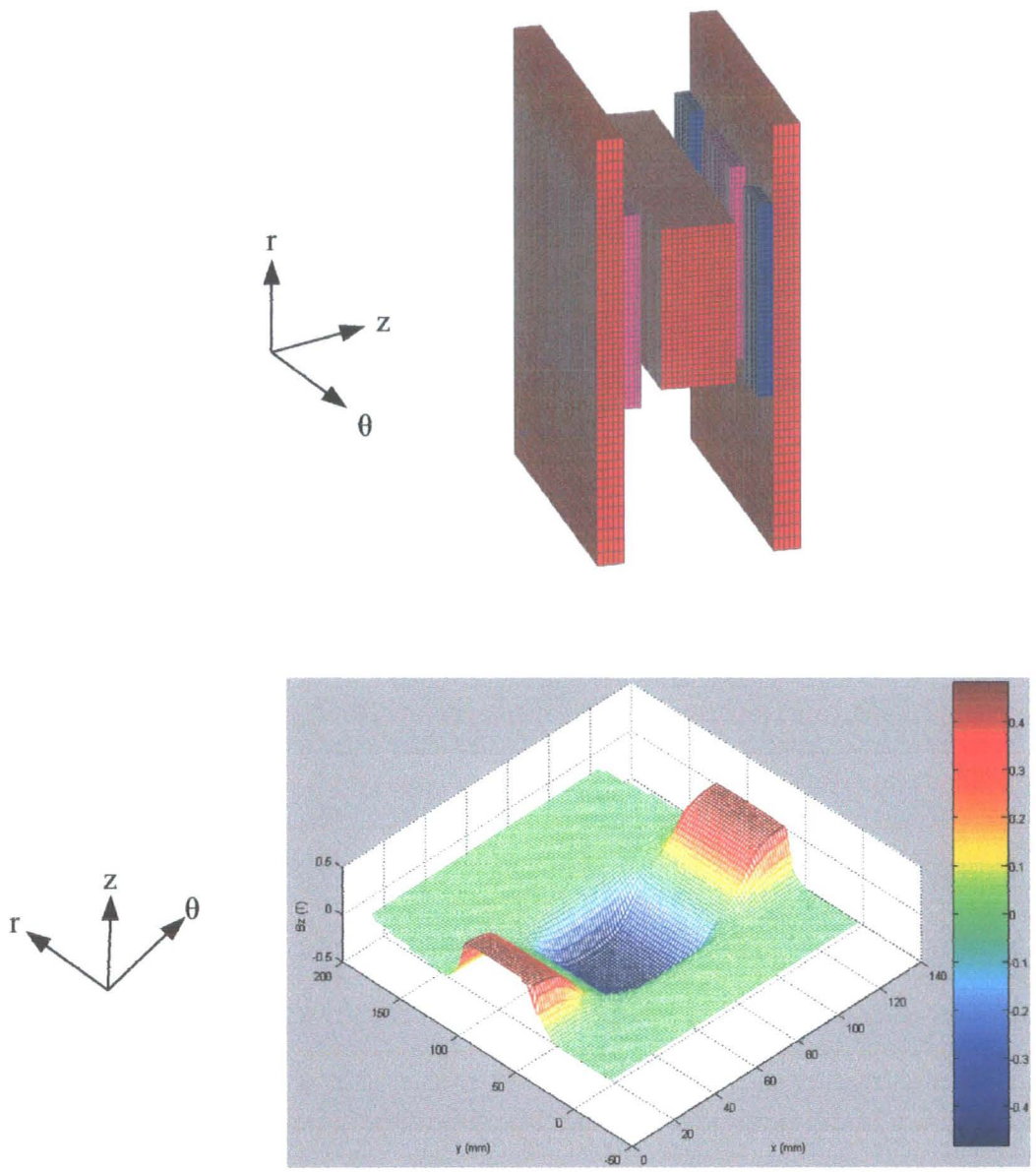

Figure 4.36: 3D linear FEA model and 3D plot of the field arising from the magnets

The Matlab interpolation program outlined in Appendix 1 was used to obtain the circumferential and radial variations of this field which are compared with the results from the accurate disc-shaped model of section 4.3.2, shown in Figure 4.37.

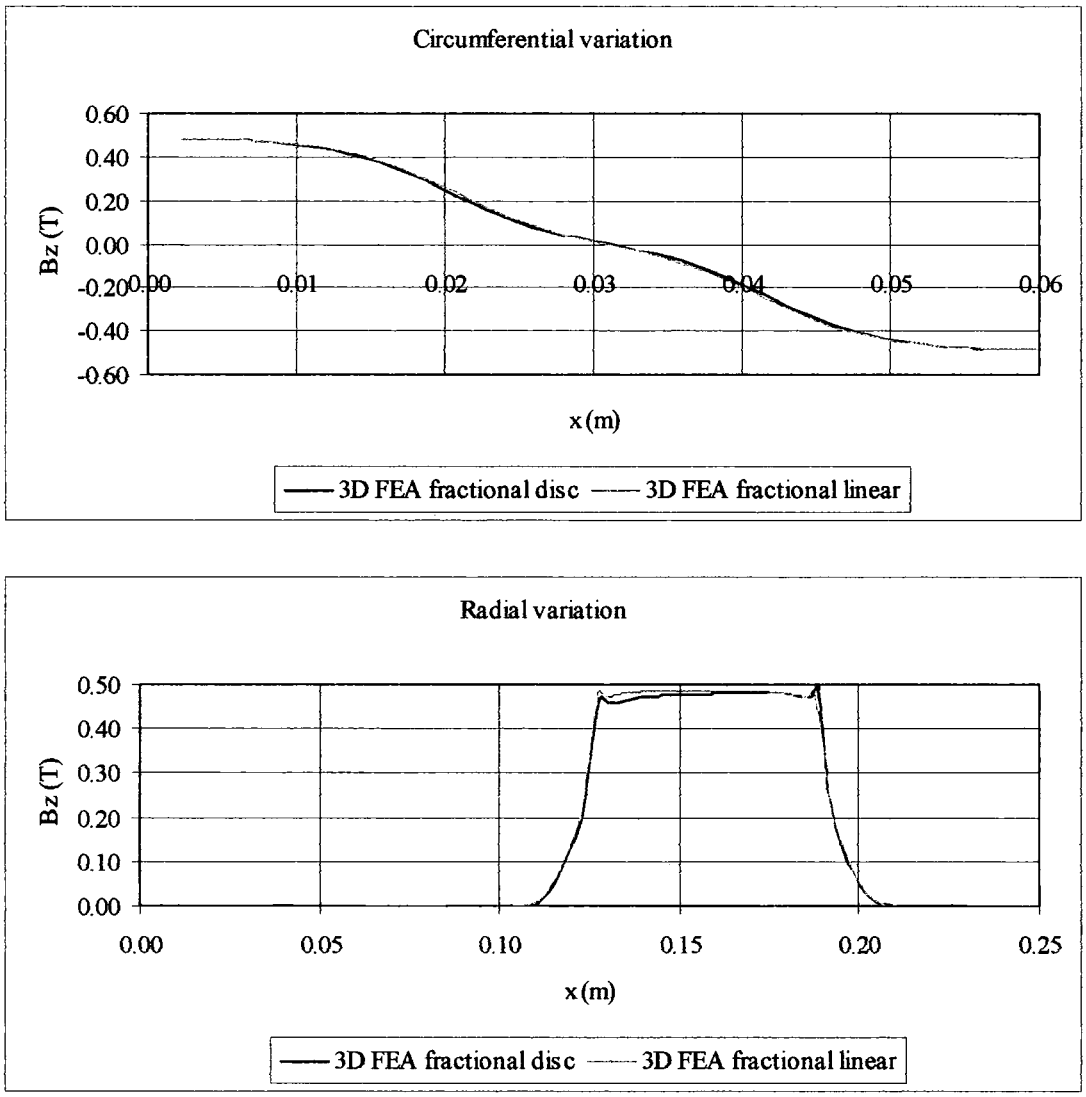

Figure 4.37: 3D FEA excitation field results and comparisons

The linear approximation shows good agreement with the accurate fractional disc-shaped model, which gives confidence for further application of the linear approach. The plots of the circumferential variation of flux density are almost identical and, since the linear mesh is refined, it picks up the end effects in the radial variation that were missed by the rough disc-shaped mesh of the full machine. The very slight difference in these end-effects between the inner and outer core radii is obviously not highlighted by the linear solution since a geometry consistent with the mean diameter is assumed across the radial length of the model; the difference is very slight and so the linear model is now solved for the dynamic case.

The full model is divided into three separate entities that are then reassembled with the appropriate Lagrange interfaces and periodic boundaries. The coils are connected exactly as before; the movement is dynamic and defined as a translation now, converted by $v = \omega r$ from 4500RPM at the mean diameter of the machine. The time period and time-step lengths are set as before and the resultant waveform of a single phase is compared with the static FEA calculation and the result of the coarsely meshed full disc dynamic FEA, Figure 4.38

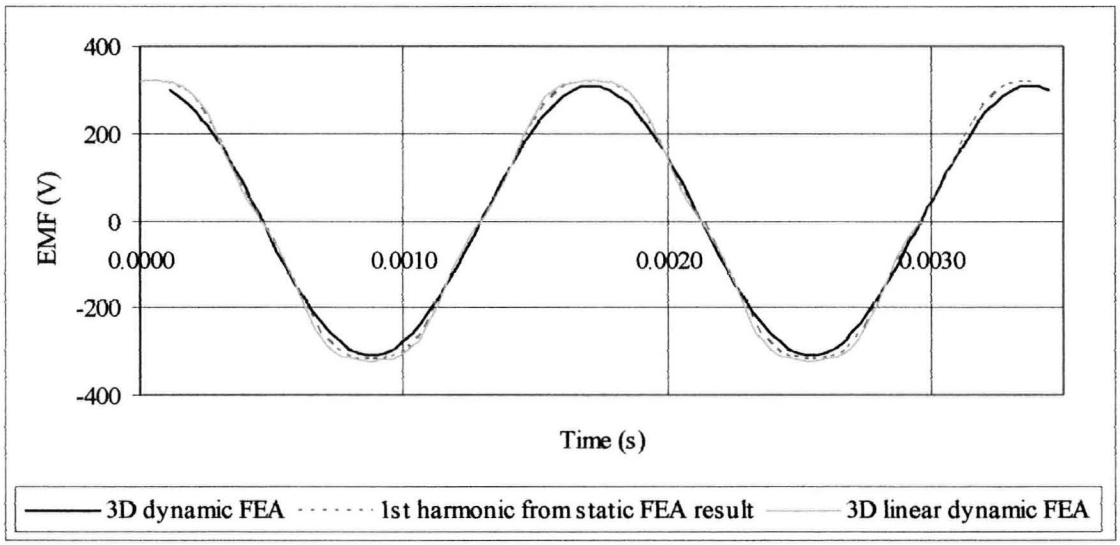

Figure 4.38: Comparison of FEA EMF predictions

The phase RMS value is 227V, comparing well with the full disc model (226V), the analytical prediction (228.7V) and the static FEA calculation (224.5V). The waveforms compare nicely, indicating an almost exact match between the 1st harmonic from the static FEA result and the 3D linear FEA result. The slight difference between the disc-shaped dynamic FEA and the other two waveforms is attributed to inaccuracy encountered owing to the coarseness of the mesh.

4.4. FEA: field arising from phase currents

The analysis of the field arising from phase currents follows a similar format to the analysis of the excitation field in that 2D models are first described and used to check the analytical results, and 3D models are then developed to validate the application of the 2D approach used by the analytical results. Once again, the FEA facilitates good visualisation of the fields which enhances the understanding of the design and operation of the machine. In addition, the synchronous reactance (X_{syn}) is obtained from the analysis of the field arising from phase currents for use in the equivalent circuit model. In all cases, the remanance of the permanent magnets is deactivated but the relative permeability of the magnet regions remains.

Two different states of energisation are considered: firstly, the field arising from current in just one phase of the machine is calculated. This was the situation analysed by the analytical methods, and the phase self and mutual inductance components can be obtained from this and then combined to give the synchronous inductance. Secondly, an instant in normal operation with 3-phase sinusoidal currents can be replicated by forcing a current of iA in phase B and $-i/2A$ in phases A and C; since this sets up the full stator MMF, the synchronous inductance may be obtained directly. The boundary conditions described for the analysis of the excitation field, section 3.4.1, hold for both of these states of energisation and the reasoning behind this was fully detailed in that section.

The usual experimental tests for inductance involve an open circuit test as per the dynamic FEA described in section 4.3.3, which gives the open-circuit EMF, E, a DC resistive test which gives the phase resistance, R, and finally a short-circuit test. By short circuiting a phase the resultant current is limited only by the internal impedance

of the machine, namely the resistance (known) and the synchronous reactance, X_{syn}, (unknown). Simple equivalent circuit analysis with the known value of E returns X_{syn}, but reduction of this into the self, mutual and leakage components is not possible. This may be replicated by FEA, but would require a full 3D dynamic model with all the coils implemented and connected. The complexity and size of the model would doubtless compromise the resolution of the mesh and hence accuracy of the results; the model would be time-consuming to build and solve, and the results would be limited.

Instead, a FEA approach was used that is similar to the short-circuit test used in the laboratory but is possible with a static model and can be arranged so as to yield separate components of self and mutual inductance. This is possible since the field arising from a forced AC (RMS) current in a single phase or all three can be calculated; further to this, the back EMF induced in a given coil or phase can be obtained directly. If a known current is forced in one phase, the resulting back EMF across that phase is solely attributable to the inductive reactance of that phase and yields the phase self inductance directly. Similarly, the back EMF measured across the adjacent phases may be directly related to their mutual inductance and the results combine to give the synchronous reactance as described in section 3.5.3. Both the self and mutual inductance components include a certain amount of air-gap leakage inductance which is difficult to separate out but is minimal. The 2D analysis works by separation of the main and end-winding components and so indicates the relative magnitude of the leakage and working flux components. Analysis of the field arising from 3-phase forced AC (RMS) currents can yield the synchronous reactance directly, since the back EMF measured across a phase with a forced current of 1A is

equal to the impedance of that phase, which is the synchronous reactance under those circumstances.

4.4.1. 2D magnetostatic FEA

The 2D model for the analysis of the field arising from phase currents is a simple modification of that used for the analysis of the excitation field, the difference being the presence of three coils that are implemented by altering the characteristics of the elements in the relevant regions. Thus the coils in a 2D model are part of the mesh, and the result is shown, Figure 4.39; for direct comparison with the analytical solution, the three phase conductors are concentrated at a distance of half the winding thickness away from the stator core, and the field is evaluated at the stator core surface.

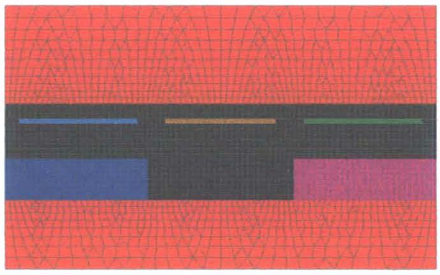

Figure 4.39: 2D FEA mesh with coils

The new regions are defined as coil ports, representing wire-wound coils having zero conductivity and a specified number of turns; these are connected to ports in a single pole version of the scheme described in section 4.3.3. Flux lines arising from a forced current of 1A in the central coil are shown in Figure 4.40. The resulting flux density variation is also shown in comparison with the analytical prediction. The plots compare well and the slight discrepancy is ascribed to the fact that the current placement and field evaluation was imprecise in the FEA owing to the discrete nature of the mesh.

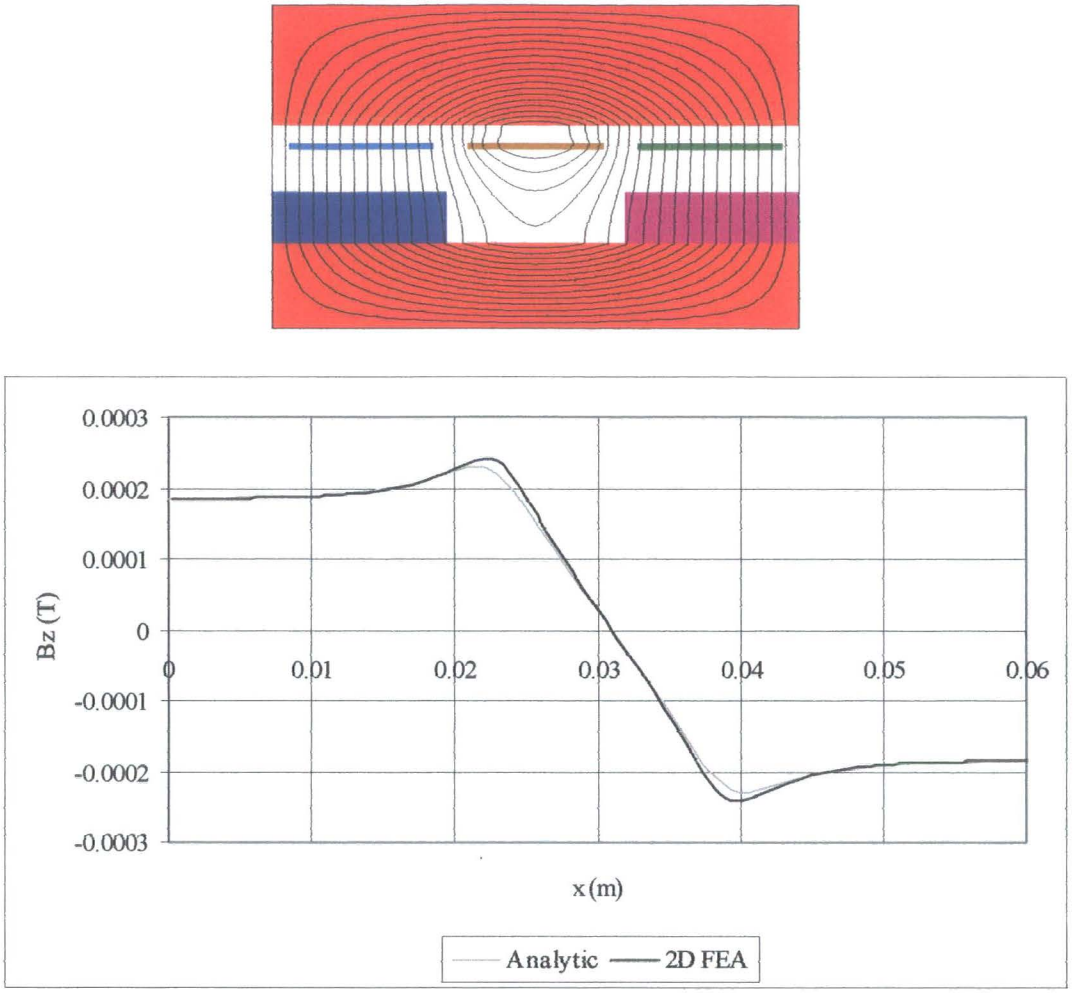

Figure 4.40: Field arising from phase currents: 2D FEA and analytical comparison

The same model can be modified further for the analysis of the end-winding regions by removing the rotor material and extending the air region. Since the field consists entirely of leakage flux, more air is included to ensure that the zero magnetic vector potential boundary condition holds at the top of the model. The model and resulting flux lines are shown in Figure 4.41; this is oriented to show an axially-directed view of the end-winding at the outer diameter of the stator core but the spacing of the coils is arranged so as the give the average geometry that would be encountered at the mean diameter in reality. Clearly there are no end-windings at the mean diameter, but the geometry here is assumed to give a satisfactory average representation of the inner and outer end effects.

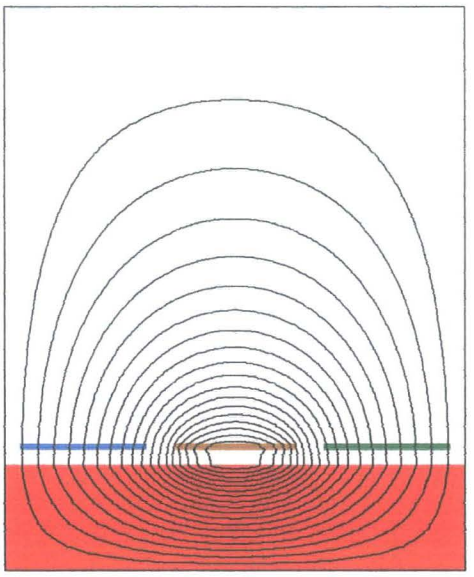

Figure 4.41: Flux distribution in the end-winding region from 2D FEA

The variation of flux density entering the core at its surface, arising from unit current in the central coil, is obtained from the FEA and compared with the analytical prediction which was obtained from the design spreadsheet by setting the effective air-gap to a large value (effectively removing the rotor). Since this is the end-winding region, Figure 4.42 shows the circumferential variation of radially directed flux.

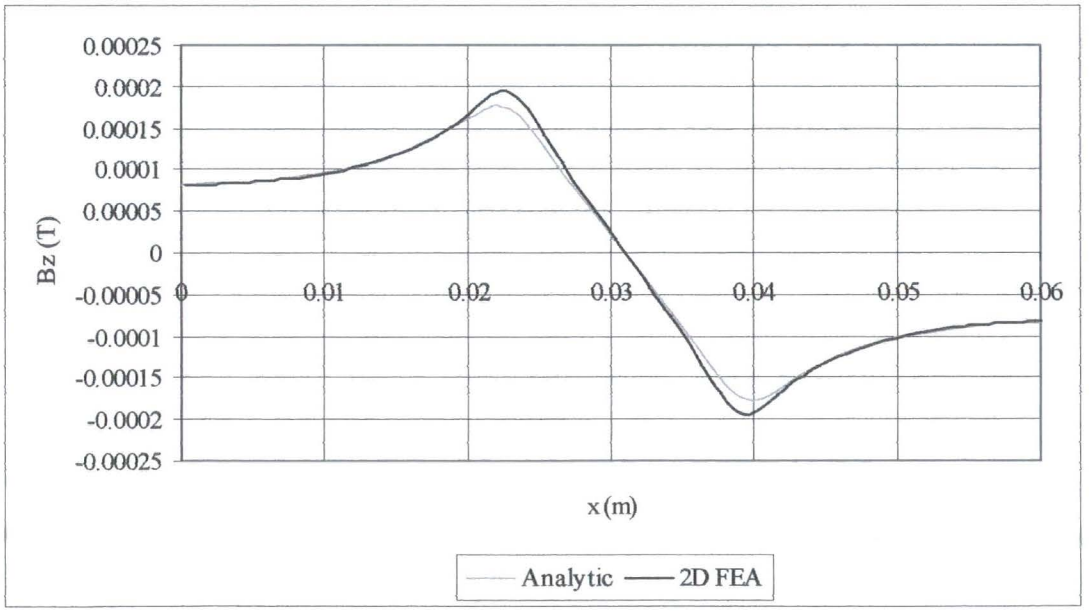

Figure 4.42: End leakage flux density comparison

Again, the slight discrepancy between the analytical prediction and the FEA result is attributed to imprecision in the location of the winding and the field evaluation points. In any case, the magnitude of the flux density is so low in this region and the low number of turns that is a characteristic of both prototype machines results in an almost insignificant end-winding leakage inductance in both cases.

The self and mutual inductances were evaluated from similar models for the main and end-winding regions by the forced AC current method described above. Since the analytical field solution assumes the conductors to reside in a sheet of negligible thickness at the stator core surface for the calculation of inductance (see section 3.5.3), the 2D FEA models were altered accordingly. The new FEA meshes are shown, Figure 4.43, and the results are shown in comparison with the full field analytical solution, both per unit effective length and also modulated by the twice the core length in the case of the main winding region, and twice the core thickness in the case of the end-winding region, Table 4.11.

The results compare well; the end-winding inductances are so small that their slight inaccuracy has a small effect on the overall accuracy. The analytical prediction of the synchronous reactance agrees with the 2D FEA result to within 2%. The 2D FEA and the analytical results show satisfactory agreement overall; the next step is to extend the FEA to 3D in order to validate the 2D approximation. This is particularly interesting in the case of the end-winding field, since the coil spread is of the same order of magnitude as the core thickness, and so the infinite length assumption is somewhat tenuous in the case of the end-winding analysis; it is likely that the end-winding field is dominated by further end effects.

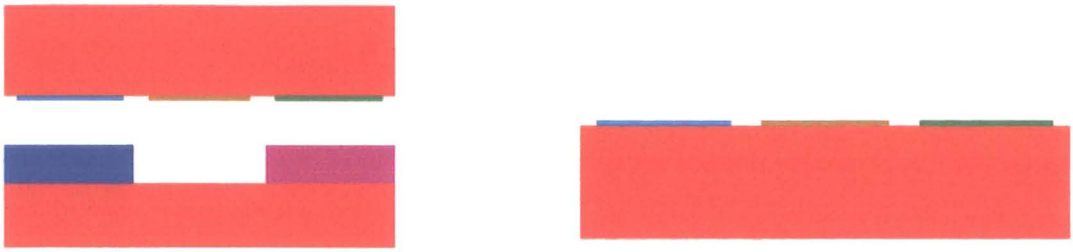

Figure 4.43: 2D FEA models for the main and end-winding inductance calculation

		Analytical	2D FEA	Error (%)
Per unit length	$L_{coil\ main}$ (H)	4.65E-05	4.57E-05	1.8
	$M_{coil\ main}$ (H)	1.56E-05	1.58E-05	1.4
	$L_{coil\ end}$ (H)	3.01E-05	2.93E-05	2.9
	$M_{coil\ end}$ (H)	7.63E-06	7.72E-06	1.1
Modulated by relative lengths	$L_{coil\ main}$ (H)	3.201E-06	3.14E-06	1.8
	$M_{coil\ main}$ (H)	1.072E-06	1.09E-06	1.4
	$L_{coil\ end}$ (H)	7.836E-07	7.62E-07	2.9
	$M_{coil\ end}$ (H)	1.985E-07	2.01E-07	1.1
	$L_{syn\ phase}$ (H)	8.409E-05	8.31E-05	1.2
	X_{syn} (Ω)	0.317	0.313	1.2

Table 4.11: 2D FEA inductance results compared with the analytical predictions

4.4.2. 3D magnetostatic FEA

The 3D model used for the analysis of the excitation field (section 4.3.3) was modified slightly for the analysis of the field arising from phase currents. The magnet remanance was de-activated, although their relative permeability remained, and the coils were implemented as per the dynamic model of section 4.3.3. Only three coils were required in the single pole model, and the coil connections were similar to those of the dynamic model, with the exception that phase B was energised with 1A for field plotting and inductance calculations as described for the 2D analysis, section 4.4.1. Figure 4.44 shows the FEA model with coils, and the field plot for 1A phase B excitation.

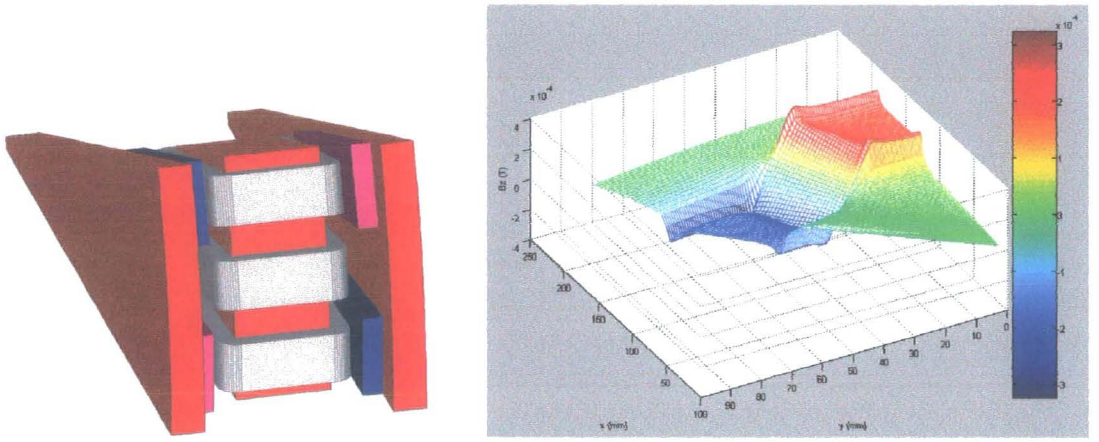

Figure 4.44: 3D FEA model with coils and flux density surface with 1A in phase B

The radial variation in axial flux density is appreciable from the 3D surface plot shown, and clearly exhibits end-effects at the core inner and outer radii. The circumferential variation was extracted from this data and is compared with the 2D FEA result and the analytical solution, Figure 4.45. The comparison between the 2D and 3D FEA results is good, and both compare well with the analytical prediction as described in section 4.4.1.

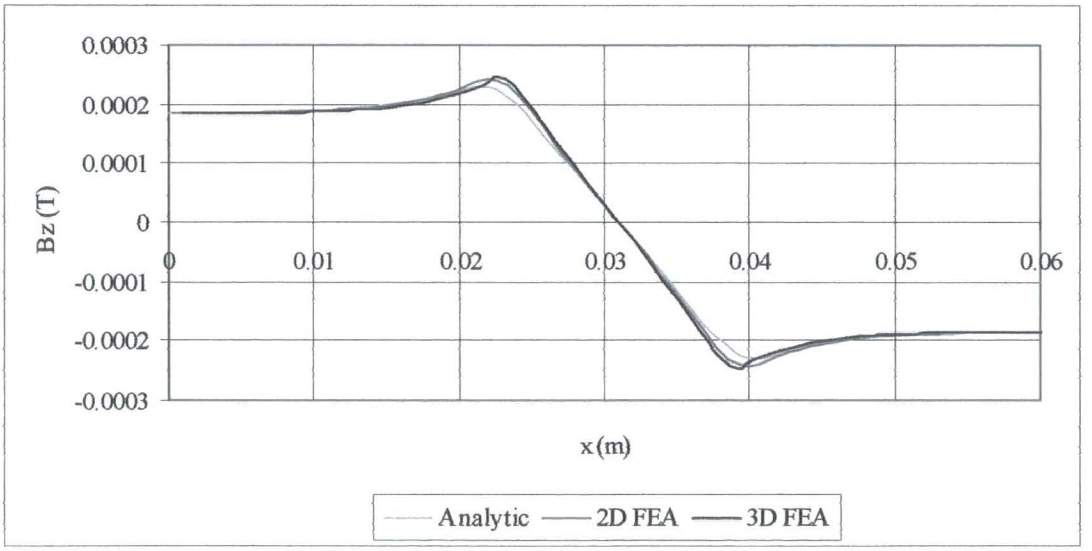

Figure 4.45: Comparison of the field arising from phase currents

Figure 4.46 shows flux density vectors in the end-winding region from the 3D FEA for comparison with Figure 4.41, and Figure 4.47 shows the full end-leakage comparison: namely the circumferential variation of radially-directed flux. The 2D FEA and analytical variations are given for the mean diameter equivalent, but in reality the end-windings only exist at the inner and outer diameters. For this reason, the 3D FEA results are plotted at the inner and outer diameters, with the x-scaling modulated to the mean diameter. The end-effects obtained by 3D FEA are similar at the inner and outer diameters; both are in reasonable agreement with the 2D results and, given the overall effect of the end-leakage inductance indicated in section 4.4.1, the results are satisfactory.

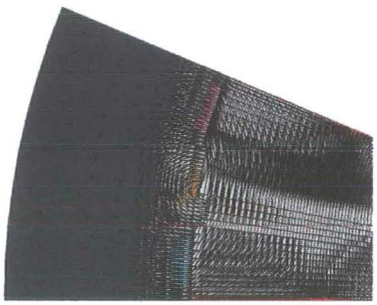

Figure 4.46: End leakage flux density vector plot from 3D FEA

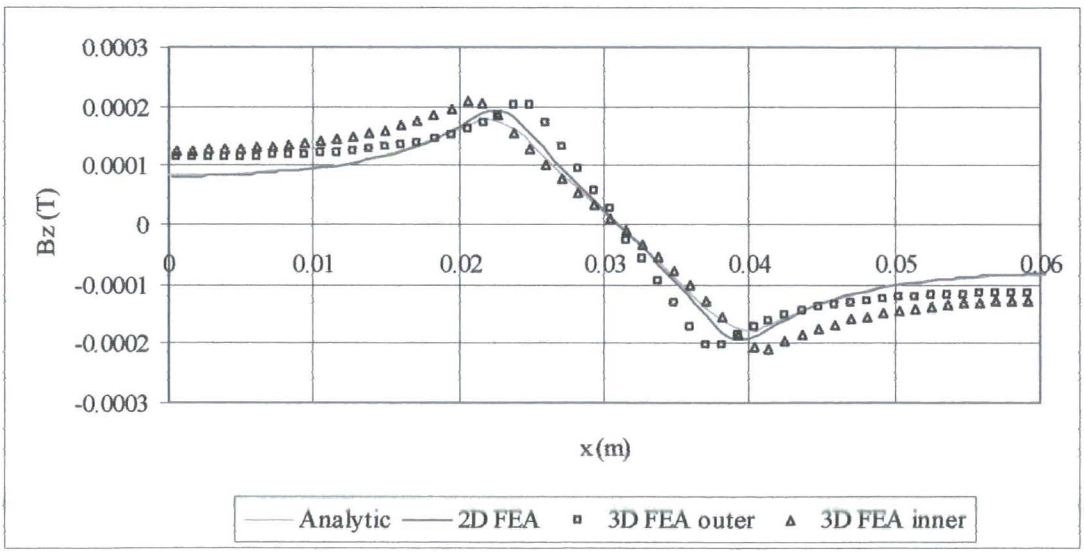

Figure 4.47: End leakage flux density illustration and comparison

The self and mutual inductances were calculated using the forced AC method previously described. Since the 3D FEA incorporates the combined effects of the main and end-windings the respective quantities are inseparable and values of inductance per metre are no longer meaningful. Table 4.12 compares the end results of self, mutual and synchronous inductance obtained from the analytical method, 2D FEA and 3D FEA, and quotes errors relative to the 3D FEA results.

	3D FEA	2D FEA	Error (%)	Analytical	Error (%)
L_{coil} (μH)	3.85	3.91	1.5	3.98	3.5
M_{coil} (μH)	1.46	1.29	11.8	1.26	13.0
$L_{syn\ phase}$ (μH)	85.0	83.1	2.2	84.1	1.0
X_{syn} (Ω)	0.32	0.31	2.2	0.32	1.0

Table 4.12: Full inductance comparison between the FEA and analytical predictions

The results compare well, particularly in the case of the self inductance. There is some difference between the 3D FEA mutual inductance result and the values obtained by the 2D analyses. The fact that the 2D analyses are consistent with each other indicates that this discrepancy is concomitant with the infinite length, winding thickness and coil location assumptions used in the 2D cases.

On the whole, the inductance values are small and the mutual inductance has a limited effect, with the result that the overall predictions of synchronous reactance of the three methods agree to within 3%. For an additional check of this approach, the synchronous reactance of one coil was measured directly from the 3D FEA model by forcing $i = 1A$ in phase B and $i = -0.5A$ in phases A and C. With unit current, the back EMF measured across phase B is the impedance, namely pure reactance in this case, and can be multiplied up by the pole number to give the synchronous reactance. The result of 0.32Ω agrees with the previous calculation.

For completion and further verification of the dynamic model used in section 4.3.4, the inductance calculations were performed using the linear 3D FEA model. The coil self inductance was 3.80μH and the mutual inductance was 1.44μH; these results agree with the 3D FEA disc-shaped model results quoted in Table 4.12 to within 2%, verifying the models and indicating that the inaccuracy in the mutual inductance predictions from the 2D analyses is attributable to the 2D approximations. The linear model yields a synchronous reactance of 0.32Ω, as per the disc-shaped model.

4.5. Summary of electromagnetic FEA

Sections 4.3 to 4.4 were an exposition of the finite element analysis techniques that form the basis of much of the analysis of the machines described in the forthcoming chapters. The FEA results were benchmarked alongside the analytical field calculations, with the equivalent circuit values of E and X_{syn} agreeing to within 3% across a range of finite element studies. In addition, the electromagnetic fields in the 40kW machine have been illustrated in a number of ways. The remainder of the chapter deals with thermal FEA and experimental verification of the above.

4.6. FEA of the thermal behaviour

Although the majority of this work concentrates on the electromagnetic analysis of axial flux machines, the performance of any electrical machine is dictated to some extent by its thermal properties and so some idea of the thermal behaviour is required. Only the 40kW prototype is analysed; it is assumed that rough verification of the simple analytical method can satisfactorily be obtained from this. The approach taken is to assume the analytical calculation of the loss magnitudes and the

rated current holds, and to model the dissipation of these losses in order to check that the temperature rise in the model is approximately as specified.

The analytical method described in section 3.7.1 utilised the surface heat transfer coefficient $h = 150W/m^2/^oC$ obtained experimentally by Spooner and Chalmers, [5], and made an approximation to the heat transfer mechanism in order to predict the allowable loss in the machine. The accurate calculation of the heat transfer coefficient is a thermo-fluids problem beyond the scope of this project but in this section the approximation to the heat transfer mechanism within the machine was verified by a simple, steady-state, thermal FEA.

The Strand7™ program, [94], was used to accurately replicate the iron loss, conductor eddy loss, and I^2R loss as sources of heat in a 2D section of one coil pitch at the mean diameter on one side of the machine. Again, the rotors were ignored and all the heat dissipation was assumed to occur between the stator and the outside air with the surface heat transfer coefficient $h = 150W/m^2/^oC$ obtained experimentally by Spooner and Chalmers, [5]. The analytical method assumed all the losses to be concentrated at the winding surface and considered only the direct heat transfer path to air. The aim of this FEA was to see how accurately that approximation represents the actual case, by including the following more realistic complications. Firstly, the iron loss actually originates in the stator core and is assumed to be uniformly distributed through this region for the FEA; the conductor eddy and I^2R losses originate in the conductors and were modelled as such. Secondly, the actual coil consists of four turns and these were modelled separately in the FEA along with the appropriate insulation. This ignores the twisted strand construction, but is still more realistic than the simple analytical method. Heat transfer by conduction is assumed to

occur within the stator components according to their various thermal conductivities. Finally, heat transfer is assumed to occur to the surrounding air from the exposed steel of the stator and from the outer surfaces of the insulation. Table 4.13 shows the material properties used in the model.

Component	Colour	Material	Thermal conductivity ($W/m^2/^oC$)
Stator	Blue	Steel	150
Conductor	Green	Copper	380
Insulation	Red	Nomex tape	0.5

Table 4.13: Materials used in the thermal FEA

All the heat transfer arising from the previously calculated losses is assumed to occur by the mechanisms represented in this model. The losses are included in the model as heat sources and are thus input in units of W/m^3. The I^2R loss is easily obtained in this format, according to:

$$P\left(/m^3\right) = J^2\rho \qquad \text{Eq. 4.1}$$

The current density is obtained from the rated current, and the resistivity is assumed to take the value calculated analytically for the maximum operating temperature. Were the FEA to indicate temperatures at odds with this then it would be necessary to iterate the solution. The masses of the copper and stator steel were calculated in order to obtain the iron loss and conductor eddy loss per cubic metre of material.

Figure 4.48 shows the model and the resulting temperature contours returned by the solver. No further processing of the result is required: although the mesh is a 2D membrane the power sources are in W/m^3 implying unit length into the page. The heat dissipation is also per unit into the page, and so the resulting temperatures hold for any depth of model. The maximum temperature recorded on the contour plot is 119°C, which is a temperature rise, and this compares with the specified 140°C rise

allocated in the spreadsheet, based on assumed ambient conditions and the maximum allowed temperature according to material properties. The simplified loss mechanism used in the spreadsheet thus agrees with this FEA to within 18% which indicates adequate accuracy in this case. It is reassuring that the spreadsheet design appears to err on the side of caution, particularly since the heat transfer in the end-winding regions of the actual machine is likely to be less favourable than that of the main winding region.

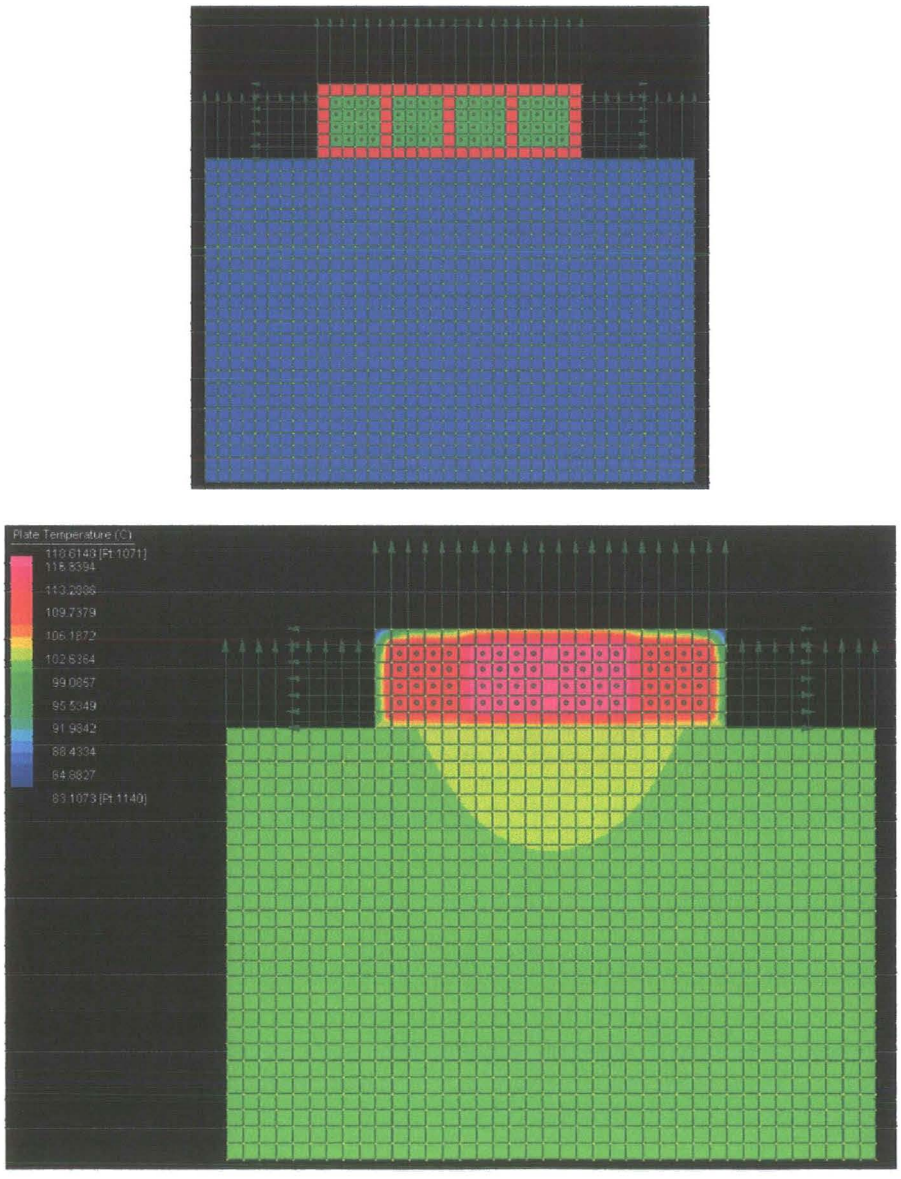

Figure 4.48: Thermal FEA model and temperature contours

4.7. Experimental work: static and dynamic tests

In this section a series of experimental tests on the prototype machines is described. Although a full range of load tests was not carried out, the equivalent circuit parameters previously calculated by analytical methods and FEA techniques were measured and thus provide verification of the analysis.

A range of static tests were performed in order to obtain the phase resistance, R, and synchronous reactance, X_{syn}. Conventionally, X_{syn} is obtained from a combination of open-circuit, short-circuit, and resistance tests but in the case of the air-gap wound toroidal generator the phase impedances are so small that a short-circuit test is impossible to carry out. Instead, a static experiment was derived for this.

Open-circuit tests were performed using a Ward-Leonard test rig to run the generators up through a range of speeds, measure the EMF induced across each phase, and capture some waveforms using a digital oscilloscope. Furthermore, three concentrated test coils having 5, 10, and 10 turns of narrow gauge wire were wound on the stator core; the EMF waveform generated across these was then used to derive the flux wave.

The open-circuit test of the 20kW machine was performed at a speed of only 300RPM. This was to assess the suitability of the machine for a direct-drive wind turbine application following a request from a manufacturer of a vertical axis wind turbine for a suitable lightweight generator with a short axial length and direct-drive capability.

Owing to a failure in the test-rig equipment it was not possible to take a full range of standard load tests, but the experimental procedures described here are sufficient to verify the equivalent circuit parameters predicted by the design spreadsheet and by the FEA.

4.7.1. Static test set-up and inductance analyser results

The inherently low inductance of these machines makes accurate measurement difficult. The standard short circuit tests can only be conducted at low speeds where reactance is negligible, so an alternative method is required. Static AC tests on the fully assembled machine induce eddy currents in the rotor iron and magnets, giving a poor representation of actual operating conditions where the rotor and stator field are in synchronism. In order to overcome this, static tests were carried out on the machine prior to assembly, with spare strip-wound stator cores used in place of the rotors to eliminate eddy currents and permanent magnet interference. Non-magnetic spacers were used to separate the iron surfaces. The gap between the stator and rotor is a sum of the winding thickness, t_a, the running clearance, c, and the magnet thickness, t_m. Wooden spacers of thickness equal to $c + t_m$, were made and an inductance analyser was used to measure the resistance and inductance of each phase for a range of frequencies from 20Hz to 1kHz. It is common practice to either quote inductance values for a standard frequency e.g. 1kHz, or for the frequency corresponding to the operating conditions of the machine in question. Table 4.14 shows the results for the 40kW machine.

	Phase A		Phase B		Phase C	
f (Hz)	R_{phase} (Ω)	$L_{self, phase}$ (μH)	R_{phase} (Ω)	$L_{self, phase}$ (μH)	R_{phase} (Ω)	$L_{self, phase}$ (μH)
20	0.1290	68.0	0.1320	68.0	0.1320	66.0
25	0.1290	70.0	0.1315	70.0	0.1320	70.0
30	0.1290	72.0	0.1315	72.0	0.1320	72.0
40	0.1290	73.0	0.1315	73.0	0.1320	72.0
50	0.1290	73.0	0.1315	73.0	0.1320	72.0
60	0.1290	73.0	0.1320	73.0	0.1320	72.0
80	0.1290	72.0	0.1320	73.0	0.1320	72.0
100	0.1295	72.0	0.1325	72.0	0.1325	71.0
120	0.1300	71.5	0.1330	72.0	0.1330	71.0
150	0.1305	71.5	0.1335	71.5	0.1335	70.5
200	0.1315	71.0	0.1345	71.2	0.1340	70.2
250	0.1325	70.6	0.1355	70.6	0.1350	69.8
300	0.1335	70.2	0.1365	70.2	0.1360	69.6
400	0.1350	69.6	0.1385	69.6	0.1375	69.0
500	0.1365	69.2	0.1400	69.2	0.1390	68.6
600	0.1385	68.8	0.1420	68.8	0.1405	68.2
800	0.1415	68.4	0.1450	68.2	0.1435	67.8
1000	0.1445	68.0	0.1485	67.8	0.1465	67.4

Table 4.14: Inductance analyser results for the 40kW machine

The results obtained from the inductance analyser appeared to vary slightly with the frequency in the case of the 40kW and the 20kW machines. The electrical frequencies at the rated speeds of 4500RPM and 3000RPM are 600Hz and 300Hz respectively, and Table 4.15 summarises the phase average impedance results from the inductance analyser test on both machines.

	20kW	40kW
R_{phase} (Ω)	0.1942	0.1403
$L_{self, phase}$ (μH)	223	68.6

Table 4.15: Summary of the inductance analyser results

4.7.2. Static AC impedance test

As a further check on these values a variable voltage AC supply (Variac) was connected to each phase in turn for an AC impedance test. With a sinusoidal current of known magnitude and frequency in one phase, the voltage across the energised phase gave the impedance and the voltage induced across the non-energised phases gave an indication of the mutual inductance. Various ways of measuring voltage were investigated. The most consistent method used a Voltec power analyser connected to the energised phase which measured the voltage, current, and power factor, from which impedance, reactance and hence inductance were calculated. In addition, a Fluke™ multimeter was used to measure the voltage induced in the adjacent (non-energised) phases, allowing calculation of the mutual inductance. For example, with phase A energised:

$$Z_a = \frac{V_a}{I_a} \qquad \text{Eq. 4.2}$$

The power factor angle is given:

$$pf = \cos(\varphi) \Rightarrow \varphi = \cos^{-1}(pf) \qquad \text{Eq. 4.3}$$

Hence the inductive reactance:

$$X_L = Z_a \sin(\varphi) \qquad \text{Eq. 4.4}$$

Hence the phase self-inductance:

$$|L| = \frac{X_L}{\omega} \qquad \text{Eq. 4.5}$$

Also resistance:

$$R = Z\cos(\varphi) \qquad \text{Eq. 4.6}$$

Similarly, the phase mutual inductance:

$$|M| = \frac{E_b}{\omega I_a} \qquad \text{Eq. 4.7}$$

Table 4.16 shows the results obtained from the 40kW prototype machine.

Energised Phase	V_a (V)	V_b (V)	V_c (V)	I (A)	pf	Z (Ω)
A	0.611	0.040	0.036	4.94	0.98	0.124
B	0.041	0.633	0.042	5.03	0.98	0.126
C	0.034	0.040	0.615	4.83	0.98	0.127
Energised Phase	**X (Ω)**	**R (Ω)**	**L (μH)**	**M (μH)**	**M (μH)**	**M (μH)**
A	0.023	0.121	74.2		25.9	22.9
B	0.024	0.124	75.7	26.0		26.3
C	0.023	0.125	74.4	22.6	26.5	

Table 4.16: AC impedance test results – 40kW prototype

The results for both machines are summarised, Table 4.17.

	20kW	40kW
R_{phase} (Ω)	0.183	0.123
$L_{self,\ phase}$ (μH)	241	74.8
M_{phase} (μH)	78.6	25.0

Table 4.17: Summary of the static AC test results

There is a significant discrepancy between the results of the AC static test and the inductance analyser measurements. A more conventional approach is to calculate the inductance from the impedance measured in the AC static test and the resistance obtained from a static DC test or the impedance analyser. This is impossible since the resistance measured by the analyser is slightly greater than the AC impedance measurement. This serves to highlight the fact that a calculation of the difference between two very similar results obtained by different methods is likely to be error prone. With this in mind, the inductance analyser results for the resistance, R, and the self-inductance, *L*, are assumed to be the most accurate, with the AC static test useful for an indication of the mutual inductance, *M*, only. However, it is clear that the inductance values are minimal: this is attributed to the low number of turns and the large effective gap.

4.7.3. Dynamic flux measurements

In order to take an accurate measurement of the excitation flux wave in the machine, three concentrated test coils having a small number of turns were wound at natural indentations occurring between the thick turns of the main winding on the stator of the 40kW machine so as to avoid any obstruction protruding into the running clearance. The machine was spun up to 1500RPM and the EMF induced across the test coils was measured using a Fluke™ multimeter. The results are shown, Table 4.18.

Coil number	Number of turns	Induced EMF at 1500RPM (V_{RMS})
1	5	6.063
2	10	12.062
3	10	12.323

Table 4.18: Test coil induced EMF results for the 40kW prototype

The average RMS voltage per turn is 1.217 and V, assuming a sinusoidal flux wave, the peak value of excitation flux is given:

$$\hat{\phi} = \frac{E_{RMS}\sqrt{2}}{N\omega} \qquad \text{Eq. 4.8}$$

The resulting value was 1.370mWb. Also, an oscilloscope was used to capture the EMF induced in each of the test coils and Figure 4.49 shows the traces. A Matlab trapezoidal integration routine was used to obtain the flux wave from one of the EMF waveforms, according to:

$$E = -N\frac{d\phi}{dt}$$
$$\therefore \phi = -\frac{1}{N}\int E dt \qquad \text{Eq. 4.9}$$

Although the induced EMF waveform exhibits considerable harmonic content, the flux waveform obtained by this integration method is more sinusoidal and is shown, Figure 4.50.

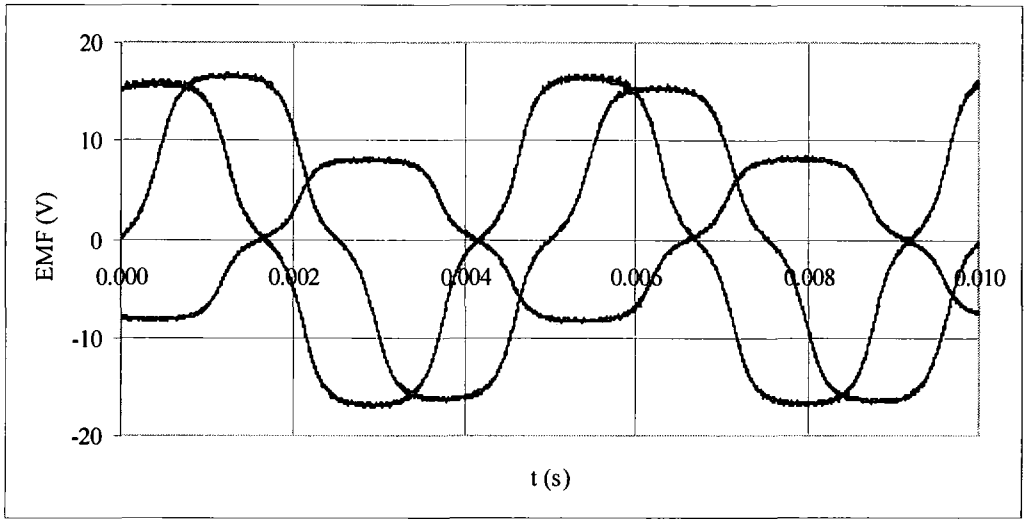

Figure 4.49: Oscilloscope traces of the test coil EMF

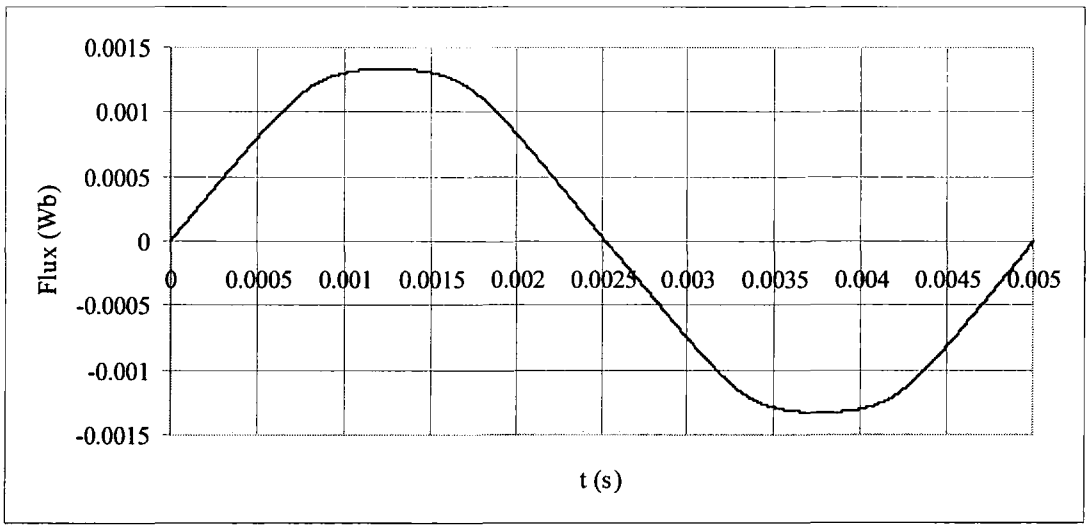

Figure 4.50: Flux waveform in the 40kW prototype

The integration was performed on each of the waveforms and the average value of peak flux obtained was 1.34mWb, which agrees with the more direct calculation from the Fluke™ measurement to within 3%. The direct calculation from the Fluke™ measurement is expected to be less accurate than the integration approach,

owing to the sinusoidal assumption used in obtaining the peak flux value from an RMS result. Owing to difficulties encountered in positioning the test coil, this test was only carried out on the 40kW prototype.

4.7.4. Dynamic phase EMF measurement

Open-circuit tests were conducted on both machines in order to measure the per-phase induced EMF. Figure 4.51 shows the oscilloscope trace of the 40kW machine at 1500RPM and Figure 4.52 shows that for the 20kW machine at 300RPM. These indicate 50.69V_{RMS} (40kW) and 62.2V_{RMS} (20kW) per phase per 1000RPM.

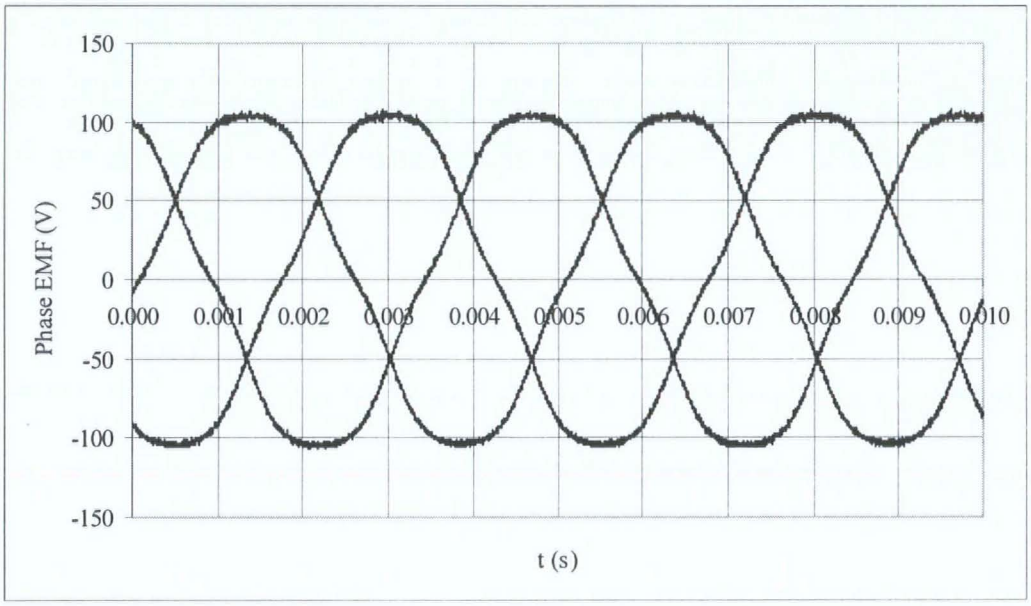

Figure 4.51: 40kW prototype machine phase EMF at 1500RPM

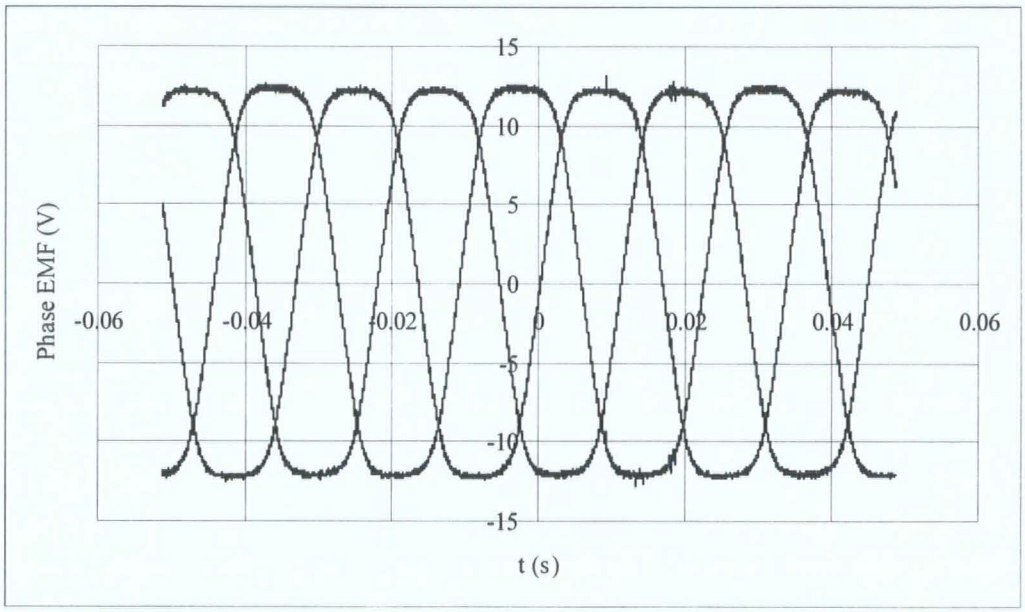

Figure 4.52: 20kW prototype machine phase EMF at 300RPM

4.8. Comparison between the predictions and test results

Some comparison between the magnetic circuit and field solution analytical methods has already been presented, section 4.2.5, and the field solution has been acknowledged as the most accurate analytical method used. The differences between the two methods and the implications of the various assumptions on the respective sets of predictions were discussed throughout section 4.2. For the purpose of comparison between the analytical results and the experimental test results then, the predictions obtained from the field solution in the form of the most accurate harmonic sums available are used here.

Similarly, the FEA techniques were built up through 2D and 3D static and dynamic models and the differences between the results were accounted for during the development of the models. The most accurate FEA predictions of the flux and synchronous reactance are those obtained from the disc-shaped 3D static model; the linear 3D dynamic model provides the most accurate EMF predictions, and so these

are used for comparison with the experimental test results. Table 4.19 compares the analytic, FEA, and test results quoting errors as a percentage of the test results. The values shown in this table are for operation at the rated speeds of the two machines.

	40kW machine @ 4500RPM				
	Test result	**Analytical**	**Error (%)**	**FEA**	**Error (%)**
φ_{pk} **(mWb)**	0.134	0.135	1.0	0.134	0.1
E_{RMS} **(V)**	228	229	0.4	227	0.4
R_{ph} **(Ω)**	0.140	0.111	20.7	N/A	N/A
L_{ph} **(μH)**	68.6	63.7	7.1	61.6	10.2
M_{ph} **(μH)**	25.0	20.3	18.8	23.4	6.4
X_{syn} **(Ω)**	0.353	0.317	10.2	0.320	9.3
	20kW machine @ 3000RPM				
	Test result	**Analytical**	**Error (%)**	**FEA**	**Error (%)**
φ_{pk} **(mWb)**	N/A	1.367	N/A	1.360	N/A
E_{RMS} **(V)**	187	186	0.5	186	0.5
R_{ph} **(Ω)**	0.194	0.174	10.3	N/A	N/A
L_{ph} **(μH)**	223.0	231.0	3.6	229.0	2.7
M_{ph} **(μH)**	68.6	68.9	0.4	61.6	10.2
X_{syn} **(Ω)**	0.569	0.566	0.5	0.586	3.0

Table 4.19: Full comparison of the numerical predictions and results

The resistance was measured at room temperature and without knowing the exact wire temperature it is difficult to make an appropriate analytical prediction; the quoted analytical predictions of resistance were calculated for 20°C but take no account of the length of the leads, the resistance of which was included in the experimental test. This results in an analytical under-prediction in comparison with the measured results. The 20kW prototype has longer phase conductors since it has more turns and a double-layer winding, meaning that the resistance of the leads is less likely to contaminate the measurement than in the case of the 40kW prototype. The accuracy of the 20kW resistance prediction is accordingly superior to the 40kW

prediction and it is expected that the analytical predictions would be accurate for a known operating temperature.

Otherwise the predictions and the measured results are in good agreement, particularly in the case of the peak excitation flux and the phase induced EMF. The inductance values are very low in these machines, which makes accurate measurement difficult but also means that a high level of accuracy is not so important. In equivalent circuit terms, a 10% error in the prediction of X_{syn} for these two machines has a negligible effect on the accuracy of the performance prediction.

Further to the numerical results, oscilloscope traces obtained from the dynamic testing of the 40kW machine can be compared directly with the analytical predictions and the results of the FEA. Firstly, the flux waveform obtained by numerical integration of the EMF induced across the test coils is compared with the analytical prediction and the results of the 3D static FEA. In the case of the FEA, a number of surfaces were defined within the stator core of the model across which the flux density was integrated in order to obtain the circumferential variation of flux; this approach was described in section 4.3.2. Secondly, the phase EMF waveform obtained directly from the practical test is compared with the result obtained directly from the dynamic 3D FEA, and with the analytical prediction. Both of these comparisons are shown in Figure 4.53 and indicate an excellent level of agreement between the practical test, the analytical predictions, and the FEA results.

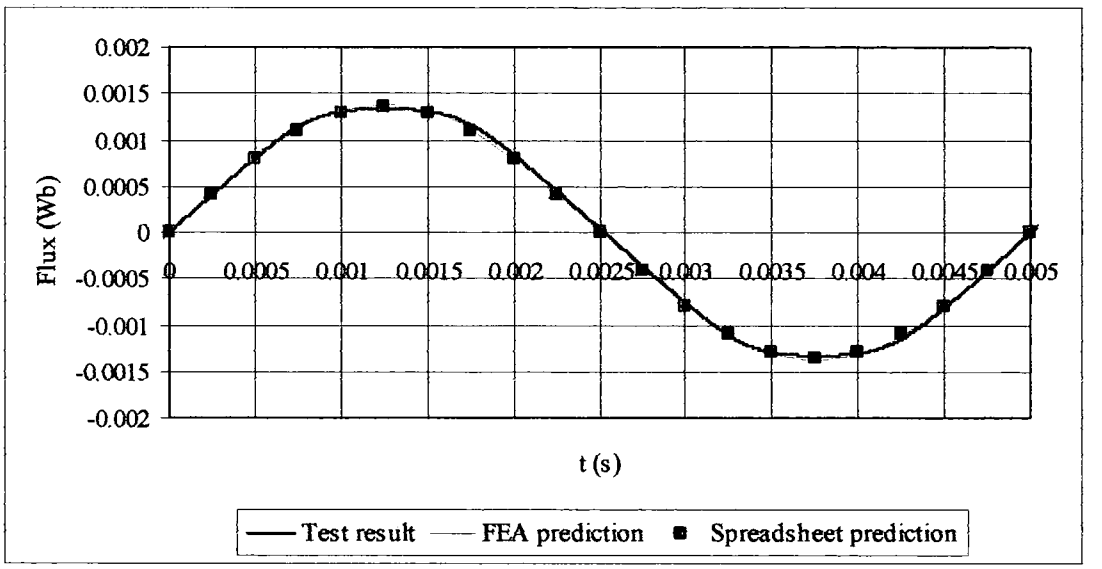

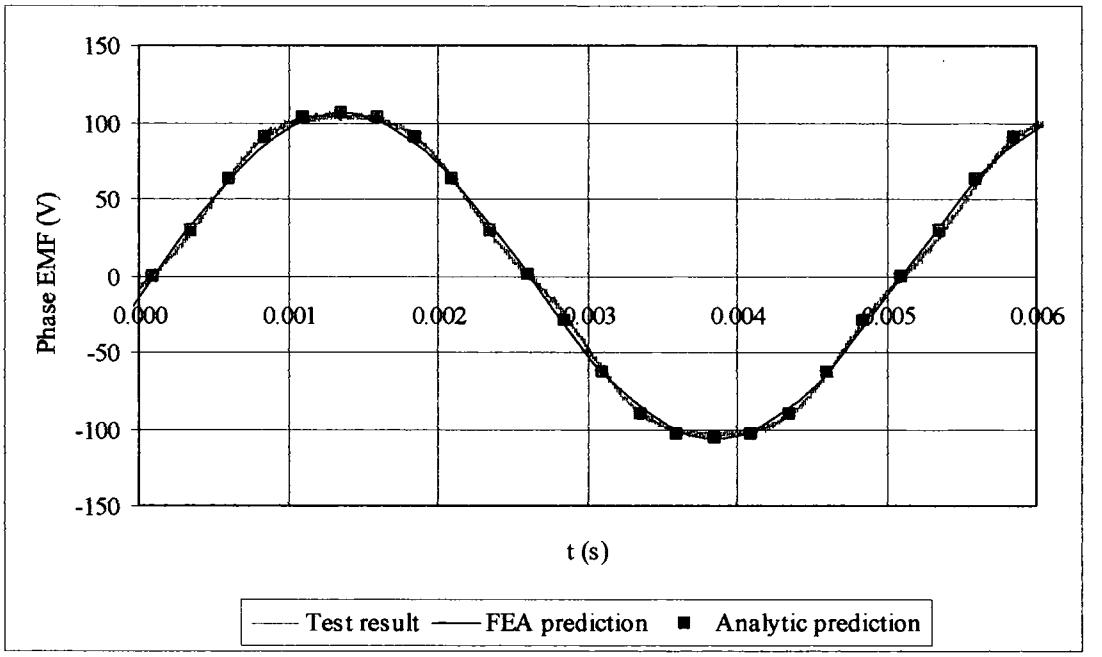

Figure 4.53: Stator core flux and EMF comparisons for the 40kW machine

4.9. Discussion

In this chapter the analytical methods developed in Chapter 3 were applied to two prototype axial flux generators with toroidal air-gap windings. The results of the magnetic circuit method and the field solution were compared and contrasted in the different modes of the electromagnetic analysis, and the main differences between

the two approaches were illustrated and accounted for. In addition, analytical methods for the prediction of the losses generated in the machines and the loss dissipation characteristics were briefly described.

Further to this, a range of electromagnetic FEA techniques were described and the results of the FEA were compared directly with the analytical predictions for the benchmarking of the two approaches. The analytical methods use a 2D approximation, and the FEA was carried out in both 2D and 3D in order to verify the analytical predictions and check the applicability of the 2D approach to a 3D problem. The field solution shows excellent agreement with the FEA, particularly in 2D where the results are almost identical. Comparison with the 3D FEA results shows up some inaccuracy in the 2D approach, but not a significant amount; the predictions concerning the field arising from the magnets agree, with the slight inaccuracy being confined to the case of the field arising from phase currents. In that case, the inductance values are so slight that highly accurate prediction is difficult and also not of great importance. In summary, the FEA was carried out in order to predict the electromagnetic equivalent circuit parameters E and X_{syn} for comparison with the analytical predictions, and the results obtained from the two methods agree to within 3% which gives confidence in further application of both approaches to this type of machine.

The thermal characteristic of the machine are somewhat more difficult to predict, but further a FEA was performed in order to check the validity of some of the simplifying assumptions made in the analytical approach to this. The analytical method is conservative and this is reflected in the fact that the FEA predicts a temperature rise of 119°C in the machine compared with the 140°C limit used for the

calculations. One difficulty encountered in this aspect of the analysis was the assignment of a suitable heat transfer coefficient, *h*. The value obtained by Spooner and Chalmers, [5], was used in lieu of an experimentally determined value for this particular machine but this is far from ideal and research into the thermal behaviour of these machines is an important area of study beyond the scope of this thesis.

Finally, a series of laboratory tests were described that allow experimental determination of the equivalent circuit parameters. These confirmed the accuracy of the analytical and FEA approaches with both predictions of E agreeing to within 1% of the test result for both machines, the 20kW predictions of X_{syn} agreeing to within 3% of the test result and the 40kW to within 11% owing to the very small overall value of inductance. In the case of the 40kW machine the measured value of X_{syn} exceeded the predictions, indicating that the source of error is likely to be stray inductance owing to the leads and connections which were not considered in the analyses but are significant in actuality, owing to the small values involved. Measurement of the phase resistances was also detailed but these results contrasted slightly with the analytical predictions owing to temperature uncertainty.

In order to illustrate the level of agreement achieved between the analytical predictions and the test results, on-load performance predictions are shown here in comparison with performance predictions using the equivalent circuit values obtained by experimental test. Ideally, the direct results of load tests should be compared but equipment failure prohibited the collection of these results. However, these comparisons facilitate some validation and the graphs are shown,

Figure 4.54.

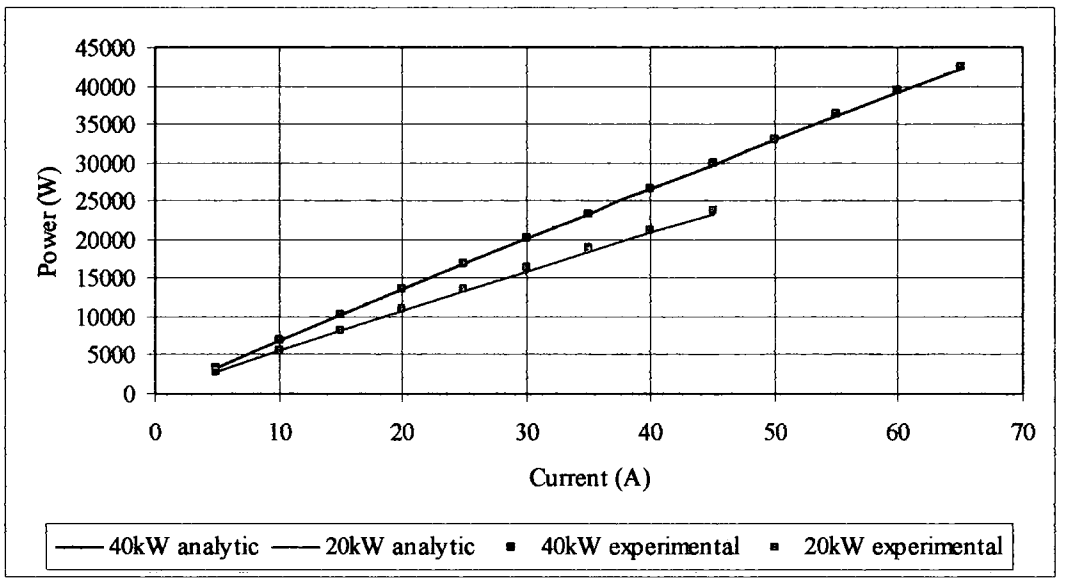

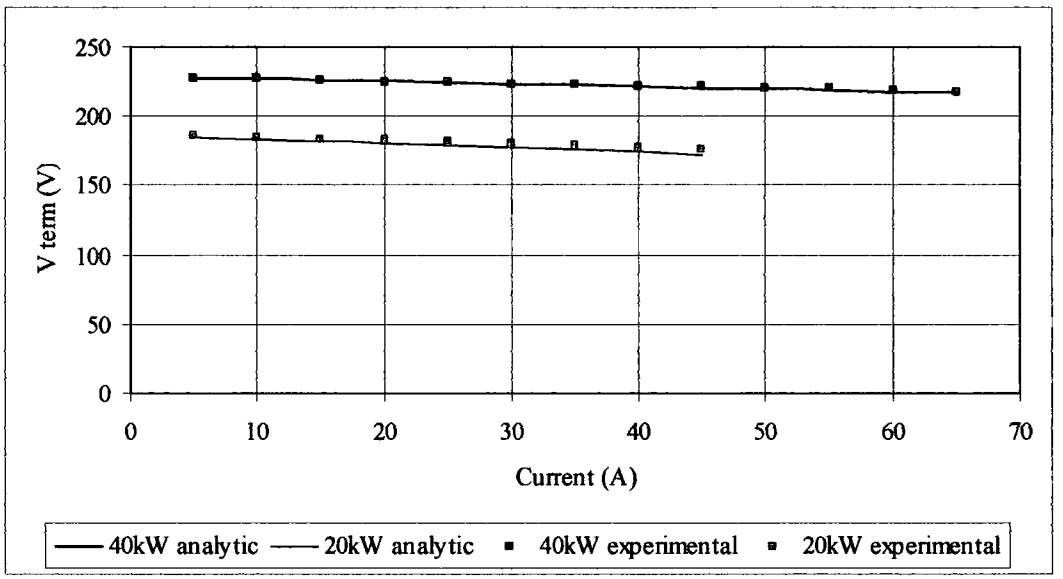

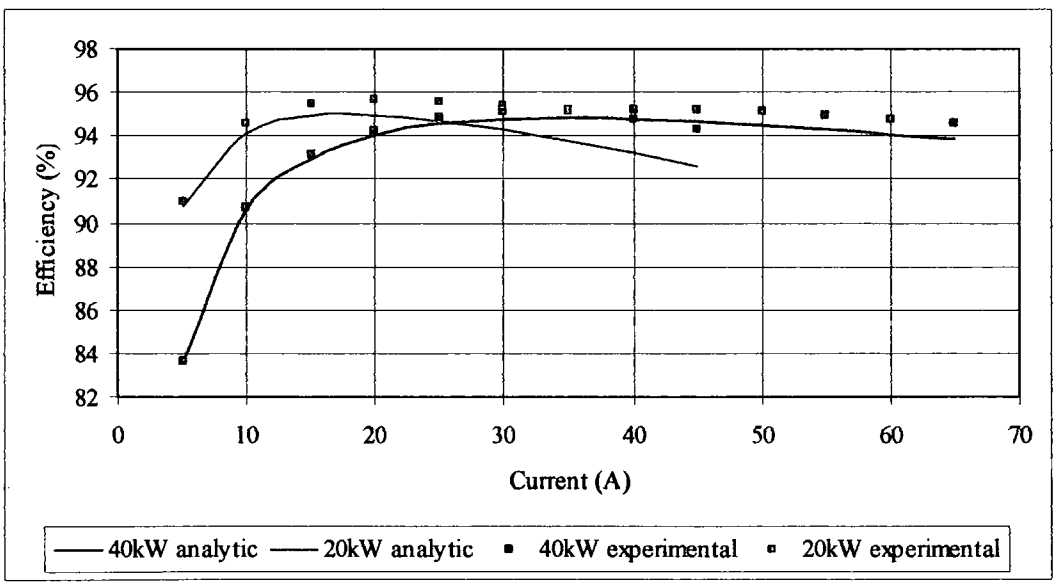

Figure 4.54: Performance prediction comparisons

The comparisons are good, the main difference being between the efficiency plots owing to the disparity between the analytical predictions of resistance at the assumed operating temperature and the room temperature measurement.

In summary, the work described in this chapter pulls the analytical predictions, FEA results, and experimental test results together in order to benchmark the calculation and measurement of the equivalent circuit parameters E and X_{syn} in particular. The machines analysed and tested are prototypes that have previously been built along the standard lines of the TORUS design, [5], and this work provides a foundation for the investigation of modifications to the design and of new machines which is the aim of the following chapters; the good results obtained here give confidence in the successful application of the methods described to these different cases.

Chapter 5. Modification of the 40kW TORUS to a slotted stator winding arrangement

The initial aim of this thesis was to develop analytical, FEA, and experimental techniques specifically for permanent magnet axial flux machines, which would then facilitate the design, analysis, and test of a range of novel machines. The previous chapters included an introduction to axial flux machines, an exposition of various analytical methods for the analysis of the TORUS-type machine, a comprehensive account of the author's approach to the electromagnetic analysis of such machines using the MEGA FEA program, and the experimental test of two existing prototype machines. Hence the development of a range of basic techniques is complete and the first steps towards utilising these for new designs are described in this chapter.

To begin with, the concept of modifying an existing design to give the stator a toothed structure by slotting the conductors is considered. The aim is to keep the design as close as possible to the 40kW TORUS prototype whilst realising a slotted winding. In this way, the effects of a slotted winding may be investigated with all other things kept constant as far as possible. One effect slotting has in this case is to decrease the effective air-gap since the conductors are removed from this region, thereby increasing the excitation flux density. Hence the back-iron required to carry this flux in the stator and rotors increases accordingly. With the exception of the winding design and this back-iron requirement, the other parameters are kept constant and the analytical and FEA techniques previously developed are extended to two such modified machines. Since the FEA and experimental approaches were shown to agree well in the previous chapter, it is assumed that FEA will give accurate predictions of the electromagnetic behaviour of the modified machines.

Significant simplifications must be made to the analytical methods, however, and a further aim of this investigation is to assess the impact of these simplifications by comparison of analytical predictions and those from FEA models representing the actual geometries more precisely.

It is shown that the analytical methods are still sufficiently accurate even when adapted to slotted machines, thus affirming the validity of the application of these to further slotted designs. A comparison between the 40kW TORUS and its slotted counterparts shows that there are advantages to slotting, but that these are perhaps not fully realised by the modified designs; Chapter 6 then goes on to consider an original design to take this further.

5.1. Introduction to slotted windings

5.1.1. Comparison between air-gap and slotted windings

It is usually desirable to minimise the air-gap of an electrical machine in order to maximise the useful flux for a given MMF, and to minimise the leakage flux by channelling the flux to where it is required. Since copper conductors have permeability close to that of air, positioning conductors in the air-gap means that their thickness contributes to the effective air-gap. To avoid this, conventional machines commonly utilise a tooth and slot structure for distributed windings, or a salient structure with some kind of pole-face for concentrated windings. These approaches both allocate space for the copper whilst keeping the air-gap as small as possible; they provide favourable flux paths in order to maximise the useful flux and minimise the leakage. Figure 5.1 illustrates the two methods.

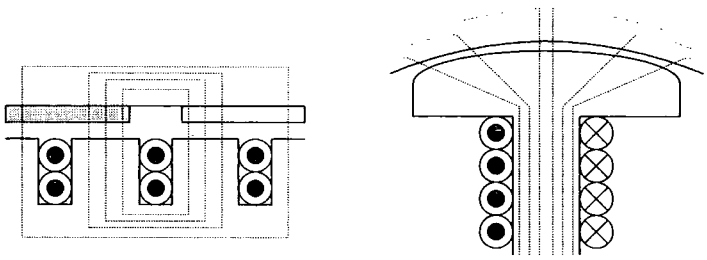

Figure 5.1: Slotted and salient structures

Conventional machines may use either or both of these methods and air-gap windings tend to be rare exceptions usually encountered where a physical consideration takes precedence over the maximisation of the flux. Examples include large DC machines, where commutation is improved by utilisation of the more even spread of a slotless winding, [95], and very small machines. On these occasions, it has tended to be the case that an air-gap winding has been a modification made to a standard machine. This is not the case where axial flux machines are concerned; these have been built with a range of unusual winding configurations. The early design by Campbell, [13], originally had an air-cored arrangement whereby a distributed winding was embedded in an epoxy construction. The TORUS design of Spooner and Chalmers, [5], was a milestone in the development of axial flux machines and is the basis of the air-gap wound designs considered in this thesis so far; its winding was conceived directly as an air-gap type design for its simplicity, for the good cooling afforded, and also since the strong, rare-earth magnets used to provide the excitation can give significant flux density levels even with a large effective gap.

Taking a very general approach to the electromagnetic properties, it can be shown that torque in rotating electrical machinery arises from shear stress, which can simply be thought of as the product of magnetic and electric loadings (this is described in

more detail in Chapter 6). High air-gap shear stress within a favourable geometry results in a compact machine capable of producing a large reaction torque. All machines balance the effects of magnetic and electric loading for best performance given the restraints of geometry, cooling, application, and general principle of operation. The TORUS machine exhibits high torque since good cooling enables high electric loading, but slotting the stator may realise a more advantageous combination of these loadings.

Slotting offers significant advantages with respect to the TORUS arrangement; principally, the reduction of the effective air-gap results in a higher magnetic loading, or reduced magnet requirement for a given magnetic loading. Slotting also removes the conductors from the main field, meaning that much of the copper is exempt from eddy current loss. Slots give greater mechanical location, support and protection for the conductors: this could facilitate multi-layer windings, potentially increasing the amount of conducting material without increasing the air-gap. In summary, a slotted machine is likely to exhibit a higher power density and therefore be more compact.

However, slotted conductors exhibit poor cooling compared with an air-gap winding, which is likely to decrease the rated current. The alternating permeability of the tooth and slot regions results in slot harmonics in the flux and EMF waveforms, which can cause cogging torque as well as extra eddy current losses from high frequency components. The flux density levels in the teeth are likely to be high, giving extra iron loss and the higher magnetic loading means more back iron is required in the stator and rotors, resulting in a longer and heavier machine. The extra leakage flux associated with slots will act to increase the leakage reactance, and the shorter air-

gap will give increased forces of attraction between the rotors and stator making assembly more difficult. On the whole, a slotted machine is more complicated and this is reflected in the cost and the level of manufacturing difficulty.

5.1.2. Implementation of a slotted toroidal winding

Recalling the basic construction of TORUS machines described in Chapter 3, the stator is commonly made from strip-wound steel, resulting in a coil-like construction that effectively presents a laminated structure to axially-directed flux. In order for this initial study to yield designs that are as similar to the air-gap wound design as possible, the same strip-wound steel is stipulated for use in the slotted modifications.

This means that there are two ways to implement a slotted winding: add material to the core to make teeth, or remove material from the core to make slots. Added tooth material would be highly susceptible to iron losses since flux levels are often at their most concentrated in tooth regions and since laminated teeth would be difficult to effect. One approach would be to use solid tooth material of soft-iron composite; previous work by Lukaniszyn and Wrobel [85], indicated that teeth having a relative permeability in the region of 5.0 result in a significant increase in the electromagnetic torque developed by the machine without the disadvantage of prohibitive levels of cogging torque, which is examined later in this chapter. This approach would be awkward to implement and is a significant departure from the TORUS idea. Performance enhancement of axial flux machines by the use soft iron composites is an interesting area of study but would perhaps confuse this investigation. The removal of material from a standard strip-wound core is more in-line with the aim to modify the existing TORUS design, and so that approach is considered here.

There are two obvious methods of removing material from strip-wound steel so as to produce a slotted stator core. Firstly, it is possible to simply mill the material from a pre-wound core. This does present a few difficulties, since the effective laminations are not as easy to mill as a solid material would be, and the potential for shorting laminations together is high. It is also a rather crude approach that may only be used for open slots and for slots and teeth of appropriate size having structural integrity sufficient to withstand the mechanical forces subjected by this method. However, this has been achieved by Newage-AVK-SEG in the construction of prototype HBH machines, [77], and is ideally suited to the manufacture of prototypes. The second option is more refined and places less mechanical stress on the structure, although it would require significant investment in manufacturing equipment and is therefore more suited to higher levels of production. This approach consists of punching slots in the steel prior to winding the cores. Some form of indexing would be required since the slot pitch varies with radius, but this method is far superior since the laminations are less likely to be shorted, the core is not subjected to high mechanical stresses, the whole process could be automated, and the production of semi-closed slots would be possible. It is envisaged that any significant level of manufacture would utilise this option but since this is merely an early design study which would require verification through prototype testing were further investigation required, open slots formed by milling a pre-wound core are stipulated.

5.2. Slotted versions of the 40kW prototype machine

5.2.1. Design approach

The electric loading is already high in the air-gap wound machine owing to the good cooling afforded by the location of the conductors directly in a stream of cool air that is naturally pumped through the machine by the permanent magnets acting as crude

fan blades. Placing the conductors in slots may increase the amount of conducting material that can fit into a given portion of the stator, but the allowable current density may decrease on account of the poorer cooling available, particularly to those conductors at the bottom of the slot. With this in mind, striving to increase the electric loading by packing conductors deep in the stator away from the natural cooling effect is potentially risky without the specification of additional cooling. This would also require a much thicker stator which would make the machine axially longer and heavier, and could rule out the attractive single-bearing design option currently used with the air-gap wound machine on engine-generator sets. Therefore, the initial aim of this study was to investigate the effect of using slotted conductors to increase the magnetic loading, whilst endeavouring to keep the electric loading as close to the value obtained in the air-gap wound machine as possible by utilising the same conductors and opting for shallow slots.

5.2.2. Different options for slotting the existing winding

With the above points in mind, the modifications to the prototype will endeavour simply to specify slotted versions of the 40kW TORUS prototype, keeping the same number of turns, poles, and phases, and aiming to increase the magnetic loading whilst maintaining the high electric loading as far as possible. The machine has three phases and 16 poles, with one coil/pole/phase resulting in 48 coils overall, each with 4 turns. Figure 5.2 shows the air-gap winding and five theoretically possible slot arrangements of these conductors.

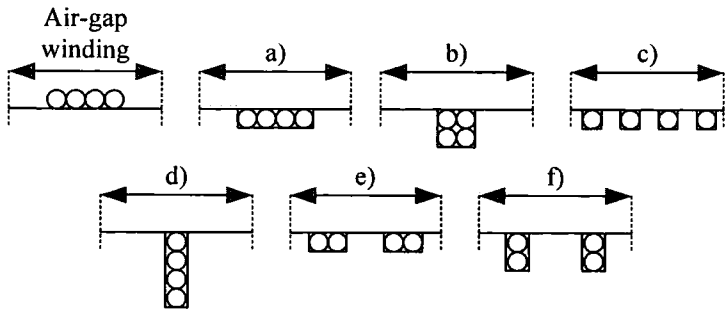

Figure 5.2: Slot arrangements

The possibilities are:

a. 1 slot/pole/phase, 1 conductor deep

b. 1 slot/pole/phase, 2 conductors deep

c. 4 slots/pole/phase, 1 conductor deep

d. 1 slot/pole/phase, 4 conductors deep

e. 2 slots/pole/phase, 1 conductor deep

f. 2 slots/pole/phase, 2 conductors deep

Parallel slots in a toroidal stator give rise to trapezoidal teeth; hence the inner section of the tooth becomes a limiting factor in the design. Option a) effectively slots the coils as they are, and would result in a very narrow tooth at the inner radius. This design would be mechanically weak, difficult to manufacture, and highly susceptible to saturation. Options c) and e) are very similar to this and hence can also be discounted.

Options b) and f) give roughly a 1:1 tooth:slot ratio at the inner circumference (an acceptable value); both appear to be mechanically feasible by inspection and offer a good compromise between maximising the tooth:slot ratio and minimising the slot depth. Option d) gives a better tooth:slot ratio, but this advantage is not worth the extra material and larger overall size required for slots twice as deep. Again, deeper

slots may compromise cooling. Therefore, options b) and f) are sized up using simple analytical methods, and the resulting designs are analysed using FEA techniques previously developed.

5.2.3. General modifications to the analytical methods

This effective gap was defined for the TORUS machine in Chapter 3, and consists of the magnet thickness (modulated very slightly by the recoil permeability of the magnets), the running clearance, and the winding thickness which is assumed to have unit relative permeability. Where the winding is in slots, it is likely that the effective gap is diminished since the winding thickness no longer contributes. However, the presence of slots, particularly open slots, presents a magnetic circuit of increased reluctance and this can be accounted for in the analysis by an appropriate extension of either the effective gap or the running clearance.

The analytical methods are derived from those presented in Chapter 3, with a few modifications to take the slotted nature of the winding into account. The variable permeability of the teeth and slots is not accounted for in detail, but a Carter coefficient is used to extend the air-gap to an effective gap length, which takes the general effect of the slots into consideration. It is therefore expected that these approaches will accurately capture the overall magnitude of the flux density as well as the general shape of the respective flux density waveforms, but that the slot harmonics will be neglected.

Figure 5.3 shows the geometry of the main winding region, along with the various parameters included in the analysis. The effective gap is like that of the TORUS, but without the winding thickness and with the running clearance, c, modified to c' by a

Carter coefficient as described by Say, [96]. This method uses empirical data to give an effective running clearance, taking the presence of slots into account.

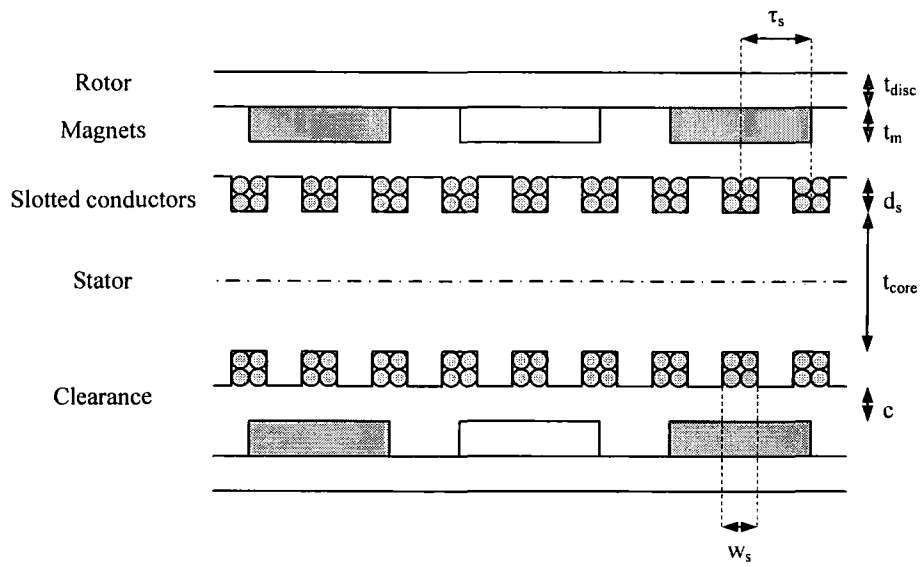

Figure 5.3: The geometry of the slotted design (main winding region)

The slot pitch is defined as:

$$\tau_s = \frac{\pi D_m}{pmn_{slots/pole/phase}} \qquad \text{Eq. 5.1}$$

The Carter coefficient is obtained from empirical data:

$$k_{carter} = f\left(\frac{w_{slot}}{c}\right) \qquad \text{Eq. 5.2}$$

The clearance is thus increased by a factor k_c:

$$c' = k_c c \qquad \text{Eq. 5.3}$$

Where:

$$k_c = \frac{\tau_s}{\tau_s - k_{carter} w_{slot}} \qquad \text{Eq. 5.4}$$

In the case of the main winding, the field solution model of a current sheet between two flat, infinitely permeable boundaries described in section 3.5 is clearly inaccurate. Methods such as the Schwartz-Christoffel equation can be used to transform polygonal boundaries into an infinite straight line, for example, where the standard solution can be applied. Such analytical solutions can be used to represent slotted structures in machines and are the source of Carter's coefficient described previously. The methods are described by Binns et al, [97], and certain assumptions are made, notably that the slot width is large compared with the air-gap, and that the slot can be treated as infinitely deep with the current at the bottom. In this instance, since the magnets add to the effective gap and running clearances are not quite as tight as could be encountered in a conventional radial flux machine, the slot width is of the same order of magnitude as the gap and may even be smaller than it. Also, since a large axial length is undesirable here, the assumption of infinite depth is tenuous. In both the magnetic circuit and the field solution methods then, the conductors are assumed to have zero thickness and lie on the surface of an un-slotted stator core, thus allowing direct application of the solutions derived in Chapter 3 for the air-gap wound machine with the new effective gap, g_{eff}, taking the slots into some consideration by use of the Carter coefficient defined previously.

Although the thickness and exact placement of the winding is ignored in both the magnetic circuit model and the field solution, the spread of the winding is retained and effective air-gap is again used in both analyses. This results in the phase conductor model depicted in Figure 5.4.

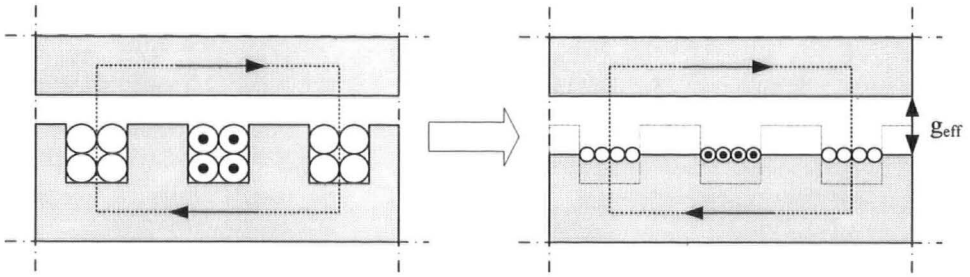

Figure 5.4: Phase conductor model

The end-winding in a slotted machine is similar to that in the air-gap wound machine, since it would be difficult and rather pointless to slot these sections of the stator; therefore, the end-winding leakage is analysed as it was for the fully air-gap wound machine. Since the conductors would be likely to spread across the core ends to some extent, they are assumed to spread uniformly over the entire coil pitch for ease of analysis. This approach represents those designs having only one slot per pole per phase most accurately but is expected to provide satisfactory results for alternative designs, particularly since the magnitude of the end-winding inductance is likely to be very small.

The winding distribution factor is also changed by the presence of slots. Where there is only one slot per pole per phase the same approach as for the air-gap wound machine can be applied, with the slot width used in place of the coil spread. Where there is more than one slot per pole per phase, the coil in each slot is assumed concentrated and a distribution factor based on the vector sum of the contribution of each slot is applied.

5.3. Analysis of the excitation field

5.3.1. Magnetic circuit solution

The TORUS magnetic circuit analysis gave the following expression for flux density:

$$B = \frac{B_r \frac{t_m}{\mu_r}}{\frac{t_m}{\mu_r} + t_a + c} \qquad \text{Eq. 5.5}$$

The denominator corresponds to the effective air-gap which is modified for slotted machines as described in section 5.2.3 to give:

$$g_{eff} = \frac{t_m}{\mu_r} + c' \qquad \text{Eq. 5.6}$$

This is substituted back into the equation for flux density to give a revised expression:

$$B = \frac{B_r \frac{t_m}{\mu_r}}{\frac{t_m}{\mu_r} + c'} \qquad \text{Eq. 5.7}$$

Since the conductors are now in slots, the effective gap is reduced and the flux density profile is better represented as a square profile covering the pole arc, shown in Figure 5.5.

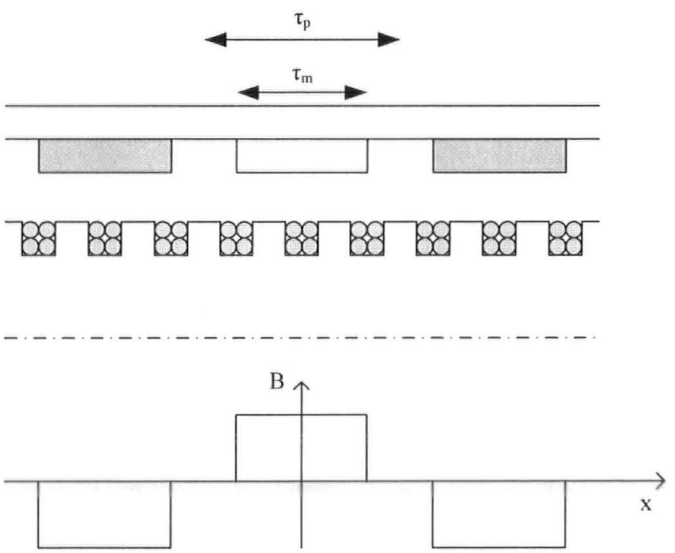

Figure 5.5: Flux density profile

Fourier analysis gives the peak value of the fundamental, where τ_m is the magnet pitch in electrical radians:

$$B_1 = \frac{4B}{\pi}\sin\left(\frac{\tau_m}{2}\right) \qquad \text{Eq. 5.8}$$

The fundamental peak flux per pole is calculated as per the TORUS, noting that the effective core length is simply:

$$l_{eff} = \frac{D_o - D_i}{2} \qquad \text{Eq. 5.9}$$

This is arises because the magnets are not intended to overhang the stator core in the case of slotted machines, and so the effective core length is equal to the actual radial depth of the core. Thus the peak flux per pole can be expressed:

$$\hat{\phi}_{pp} = \frac{B\left(D_o^2 - D_i^2\right)}{p} \qquad \text{Eq. 5.10}$$

This can also be calculated more simply, since the flux density can be considered constant across the magnet face in accordance with the square wave approximation:

$$\hat{\phi}_{pp} = \int B.da_{pp} = B\tau_m\left(D_o - D_i\right) \qquad \text{Eq. 5.11}$$

With 1 slot/pole/phase, the conductor spread within the individual slot is considered and so the slot distribution factor is defined:

$$k_{d,n} = \frac{\sin\left(\frac{n\pi w_{slot}}{2\tau_p}\right)}{\frac{n\pi w_{slot}}{2\tau_p}} \qquad \text{Eq. 5.12}$$

With more than 1 slot/pole/phase, the distribution factor can be calculated as follows. The coils are assumed uniformly spread over electrical angle σ, which is equal to π radians where there are three phases. The appropriate distribution factor is then:

$$k_{d,n} = \frac{\sin\left(\frac{n\sigma}{2}\right)}{\left(\frac{n\sigma}{2}\right)} \qquad \text{Eq. 5.13}$$

Also, the number of turns/pole/phase is related to the number of turns per slot and the number of slots/pole/phase:

$$N = n_{slots/pole/phase} N_{/slot} \qquad \text{Eq. 5.14}$$

The RMS induced voltage per coil (i.e. per pole, per phase) can be calculated as it was for the TORUS and considering only the first harmonic:

$$E_{coil} = 4.44 k_d N f \hat{\phi}_{pp} \qquad \text{Eq. 5.15}$$

Assuming all the coils of each phase to be wound in series, the induced voltage per phase is given:

$$E_{phase} = pE_{coil} \qquad \text{Eq. 5.16}$$

5.3.2. Field solution

The more accurate analytical solution proceeds in a similar fashion but using the equations for magnetic vector potential and flux density derived in section 3.5.2, that is:

$$A_{zn2}(x) = -\frac{\hat{J}_n \mu_0}{u_n^2} \frac{\sinh u_n Y_m}{\sinh u_n Y_2} \cosh u_n (Y_2 - y) \sin u_n x \qquad \text{Eq. 5.17}$$

and:

$$B_{yn2}(x) = \frac{\hat{J}_n \mu_0}{u_n} \frac{\sinh u_n Y_m}{\sinh u_n Y_2} \cosh u_n (Y_2 - y) \cos u_n x \qquad \text{Eq. 5.18}$$

Y_2 becomes the equivalent gap, g_{eff}, described above. The variation of B_y with x, taken at the stator core surface ($y = Y_2$) is of interest and is used for comparison with the predictions of the magnetic circuit method. Again, where the magnets are the same length as the core (i.e. there is no radial magnet extension to exploit the core ends), the flux per pole is:

$$\hat{\phi}_{pp,n} = \frac{\hat{B}_n}{n\frac{p}{2}} D_m (D_o - D_i) \sin \frac{n\pi}{2} \qquad \text{Eq. 5.19}$$

Noting that, at $y = Y_2$:

$$\hat{B}_n = \frac{\hat{J}_n \mu_0}{u_n} \frac{\sinh u_n Y_m}{\sinh u_n Y_2} \qquad \text{Eq. 5.20}$$

This approach is accurate enough to warrant consideration of higher order harmonics, and so the *nth* harmonic of RMS induced voltage per coil (i.e. per pole, per phase) is given:

$$E_{coil,n} = \sqrt{2}\pi n k_{dn} N f \hat{\phi}_{pp,n} \qquad \text{Eq. 5.21}$$

The total coil EMF by this method is thus:

$$E_{coil,n\_sum} = \sqrt{E_{coil,1}^2 + E_{coil,2}^2 + \ldots + E_{coil,n}^2} \qquad \text{Eq. 5.22}$$

The voltage per phase is then given by Eq. 1.16.

5.3.3. Analytical predictions for the two slotted designs

With respect to the excitation field analysis, the TORUS parameters shown in Table 5.1 remain the same in both slotted variants.

Number of poles per disc	16
Number of phases	3
Magnet thickness (m)	0.006
Running clearance (m)	0.0022
Magnet radial length (m)	0.076
Rotor outer diameter (m)	0.410
Core outer diameter (m)	0.380
Core inner diameter (m)	0.250
Magnet outer diameter (m)	0.392
Magnet inner diameter (m)	0.240
Pole arc to pole pitch ratio	0.66
Turns per pole per phase	4
Strand outer diameter (m)	0.1075
Number of strands per conductor	3
Conductor diameter (m)	0.02365

Table 5.1: Constant parameters in the TORUS and slotted variants

The geometries of the two slotted variants are as shown in Figure 5.6.

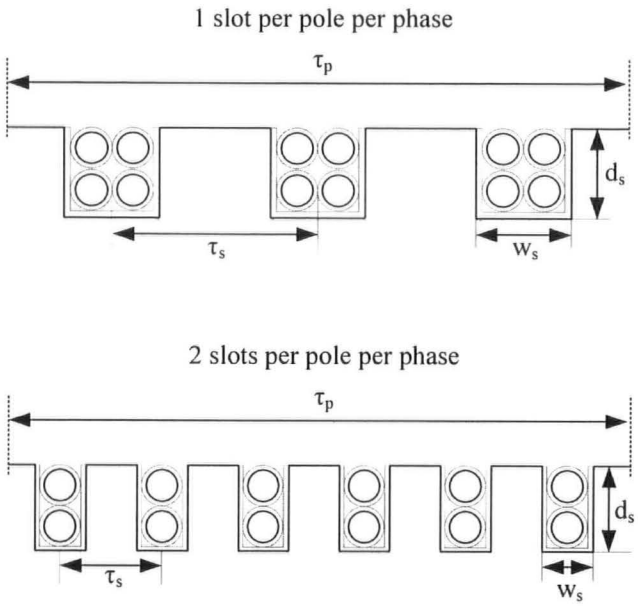

Figure 5.6: Geometry of the slotted variants

Incorporating a rough allowance for insulation tape and slot lining material, these geometries are compared with the TORUS design in Table 5.2; this also shows the effective gaps (calculated using a Carter coefficient where appropriate), and a value of excitation flux density for each design, obtained using the simple magnetic circuit formulation given by Eq. 5.17.

	TORUS	**1 slot**	**2 slots**
Slots per pole per phase	N/A	1	2
Slot pitch - τ_s (m)	N/A	0.021	0.010
Slot width - w_s (m)	N/A	0.008	0.004
Slot depth - d_s (m)	N/A	0.006	0.006
Carter coefficient - k_{carter}	N/A	0.425	0.253
Running clearance modulator – k_c	1	1.197	1.108
actual running clearance – c (m)	0.0022	0.0022	0.0022
Modulated running clearance – c' (m)	0.0022	0.0026	0.024
Effective gap – g_{eff} – (m)	0.0140	0.0082	0.0080
Flux density (T)	0.494	0.823	0.836

Table 5.2: Comparison of the TORUS and slotted variants

Figure 5.7 and Figure 5.8 show the circumferential variation of excitation flux density waveforms taken at the mean radius for the two slotted designs. The field solution waveforms shown are the fundamental and the sum to 21 harmonics. The magnetic circuit solution waveforms shown are the fundamental and a square wave approximation obtained from Eq. 5.17.

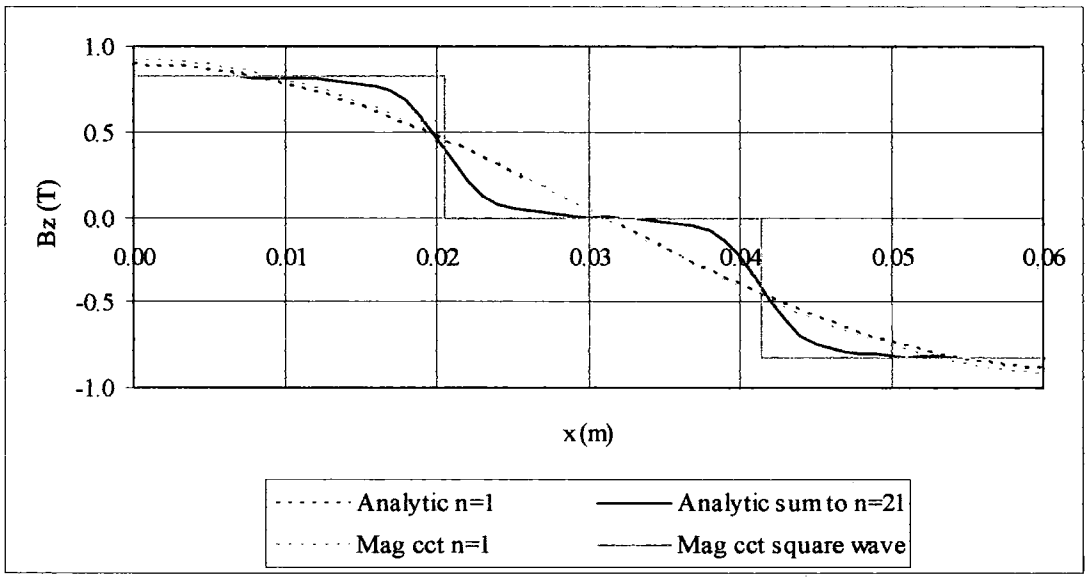

Figure 5.7: Circumferential variation of flux density (1 slot per pole per phase)

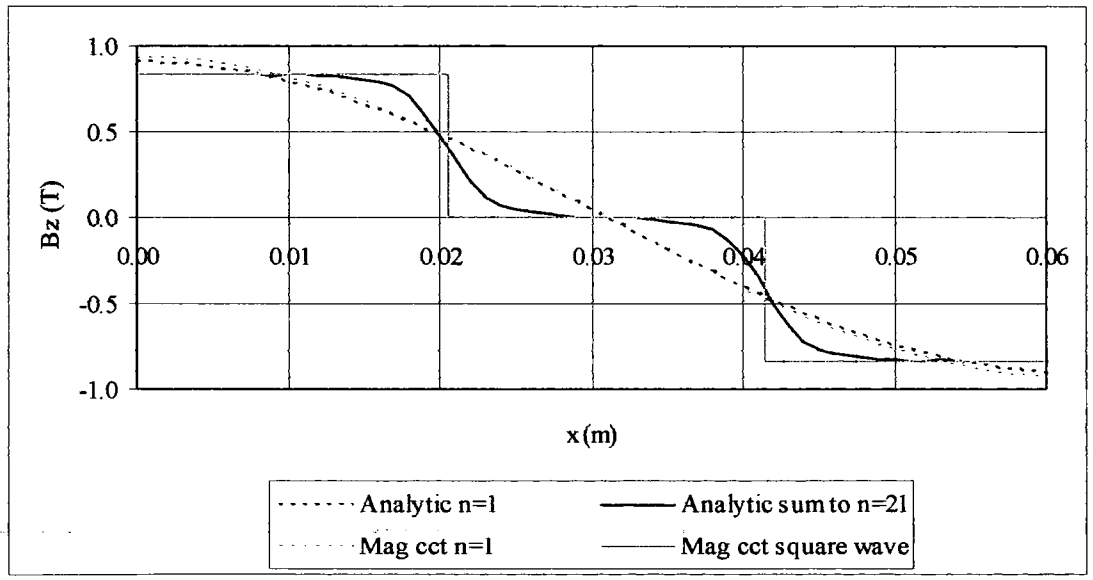

Figure 5.8: Circumferential variation of flux density (2 slots per pole per phase)

In both cases, comparison between the square wave approximation and the field solution harmonic sum shows good agreement, indicating that the square wave approach is preferable to the sine-wave approximation used in the TORUS analysis. This is a consequence of the reduced effective air-gap realised by the slotted geometry. Furthermore, the fundamental waveforms obtained by the field solution and the magnetic circuit solution are very similar in both cases. Finally, comparison of the waveforms between the 1 slot and 2 slots per pole per phase variants indicates very little differentiation. This is because the machines are similar and the tooth to slot ratio is similar in both cases. The 2 slot variant exhibits a slightly higher flux density since the geometry results in a slightly smaller effective gap when a Carter coefficient is determined according to the slot width and pitch.

Figure 5.9 compares the analytically derived first harmonic flux density waveform for the TORUS as well as the two slotted variants.

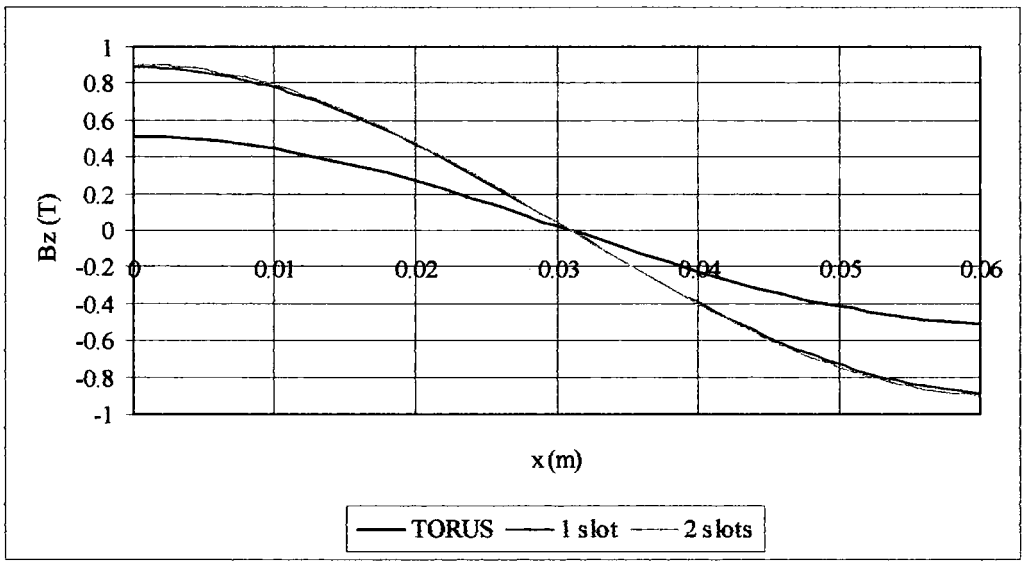

Figure 5.9: Circumferential variation of flux density – comparison of fundamentals

The waveforms of the slotted variants are of similar magnitude, both being significantly larger than that of the TORUS. The peak of the fundamental is roughly 0.9T for the slotted variants compared with 0.5T for the TORUS, i.e. slotting has resulted in an 80% increase in magnetic loading. This can be corroborated by a rough calculation: the TORUS has an effective gap consisting approximately of 6mm magnet, 2.2mm clearance and 5.8mm winding. Removal of this winding space from the gap diminishes the gap to 8.2mm, i.e. a 41% reduction. The new gap is therefore 58% of the old, and so a flux density increase of $(1 - (0.58)^{-1}) = 70\%$ might be expected, since the flux density is inversely proportional to the gap in the simple magnetic circuit formulation. Considering that the decreased gap also reduces inter-magnet leakage resulting in a more square-shaped flux density waveform, the 80% predicted increase seems reasonable.

Using the analytical methods described, the flux per pole and the induced EMF for rotation at 1500RPM were calculated and the results are tabulated for the three machines, Table 5.3. The speed of 1500RPM was chosen for consistent comparison with the experimental test result for the TORUS prototype machine.

	TORUS	**1 slot**	**2 slots**
Effective gap (m)	0.0136	0.0082	0.0080
Magnetic loading (T)	0.509	0.890	0.906
Peak flux per pole (mWb)	1.341	2.179	2.215
EMF at 1500RPM (V_{RMS})	76.22	129.95	125.86

Table 5.3: Comparison of the excitation fields

The effect of the increased magnetic loading achieved in the slotted variants on the magnitude of the peak flux per pole and the open-circuit induced EMF is clear and the slotted machines give values of EMF approximately 70% higher than the

TORUS. Of the slotted machines, the 2 slots variant exhibits a slightly higher magnetic loading and hence peak flux per pole owing to the slot geometry, but the 1 slot variant exhibits a slightly higher EMF owing to the higher distribution factor achieved with a more concentrated winding design. The EMF values given for the slotted variants are the RMS magnitudes of the sum to 21 harmonics taken from the field solution. A time-varying EMF waveform can be constructed from these harmonics and Figure 5.10 compares the waveforms predicted for rotation at 1500RPM.

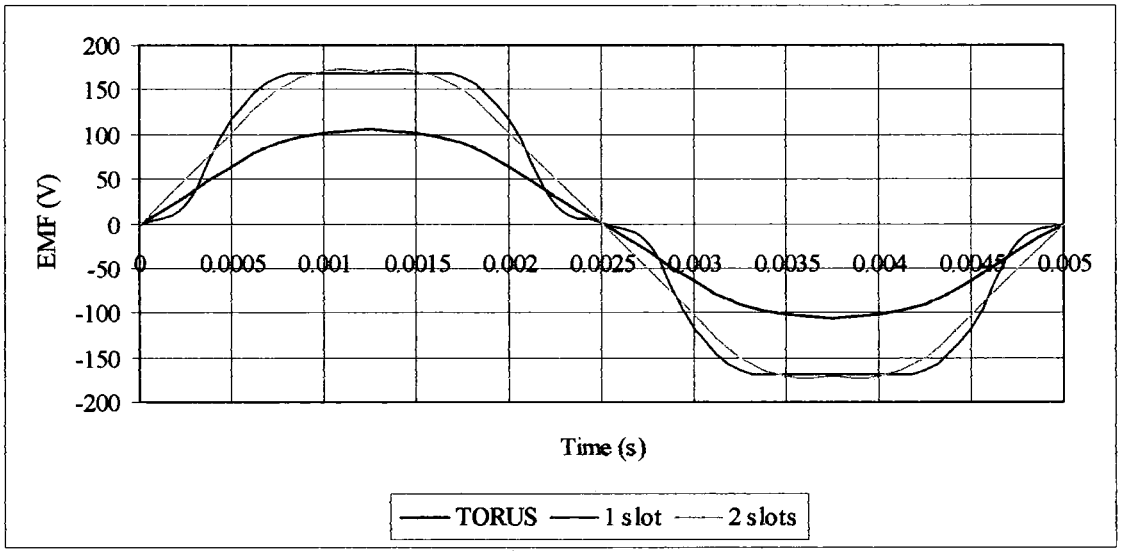

Figure 5.10: Analytical EMF predictions at 1500RPM

5.4. Rough sizing of the slotted machines

5.4.1. Rotor sizing

The peak flux per pole calculated above is the same as the peak core flux, since the flux contributed by each magnet divides into two upon entering the core, but magnets on both sides of the core contribute. Considering the flux in the rotor discs, Figure 5.11 shows that the peak flux per pole splits into two upon entering each disc.

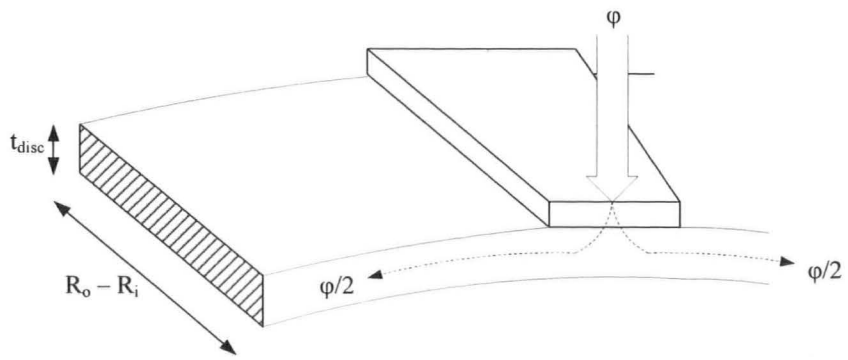

Figure 5.11: Rotor flux

Hence the peak disc flux will be roughly equal to a half of the peak flux per pole, although inter-magnet leakage flux (also carried by the rotors) is not accounted for in the peak flux per pole. The disc thickness is therefore calculated by taking a conservative estimate of the operating flux density in the rotors, and using this to determine a minimum thickness by considering the rotor flux and the area shown hatched in Figure 5.11. The actual disc thickness can be increased by a sensible amount to cater for the aforementioned leakage flux. The peak rotor flux is given:

$$\hat{\phi}_{disc} = \frac{\hat{\phi}_{pp}}{2} \qquad \text{Eq. 5.23}$$

Assuming a peak rotor flux density of B_{disc} = 1.2T, an appropriate working flux density based on the manufacturer's data, the minimum recommended thickness of the rotor is given:

$$t_{disc} = \frac{\hat{\phi}_{disc}}{B_{disc}(R_o - R_i)} \qquad \text{Eq. 5.24}$$

The outer diameter of the rotor is increased beyond the outer diameter of the magnets to allow for some form of magnet location and retention. Also, being a solid disc, the rotor has an inner diameter only to provide attachment to the driveshaft which is thus much smaller than the magnet D_o used in Eq. 1.24. Therefore the actual area for flux traversal is much larger than indicated by the hatched portion of Figure 5.11 anyway.

5.4.2. Stator sizing

The peak stator flux is equal to the peak flux per pole:

$$\hat{\phi}_{core} = \hat{\phi}_{pp} \qquad \text{Eq. 5.25}$$

Assuming a flux density in the stator, the core thickness can be found:

$$t_{core} = \frac{\hat{\phi}_{core}}{B_{core}(R_o - R_i)} \qquad \text{Eq. 5.26}$$

The manufacturer's data indicates that a flux density level of 1.4T can be achieved in the stator core without saturation. The core of the TORUS is divided axially into two segments which sandwich a central ring from which it is supported from the outside. Assuming a similar construction in the case of the slotted variants, the overall axial length of the stator is thus:

$$t_{stator} = t_{core} + t_{ring} + 2d_{slot} \qquad \text{Eq. 5.27}$$

5.4.3. Calculation of the phase resistance

The phase resistance of the slotted variants is calculated in the same way as that of the TORUS, described in section 3.7.2, using:

$$R = \frac{\rho l_{phase}}{a_{conductor}} \qquad \text{Eq. 5.28}$$

An operating temperature is assumed, based on the properties of the materials in use, and the resistivity of the copper is calculated according to this temperature and its own material properties. The cross-sectional area of the conductor is calculated according to the geometry of the strands and the number of strands used. In order to calculate the length of conductor per phase, the length of an average turn is considered. It is assumed that the conductors spread at the core ends to lie flat, 1 conductor deep. Figure 5.12 shows the cross section of the stator, illustrating such an average turn.

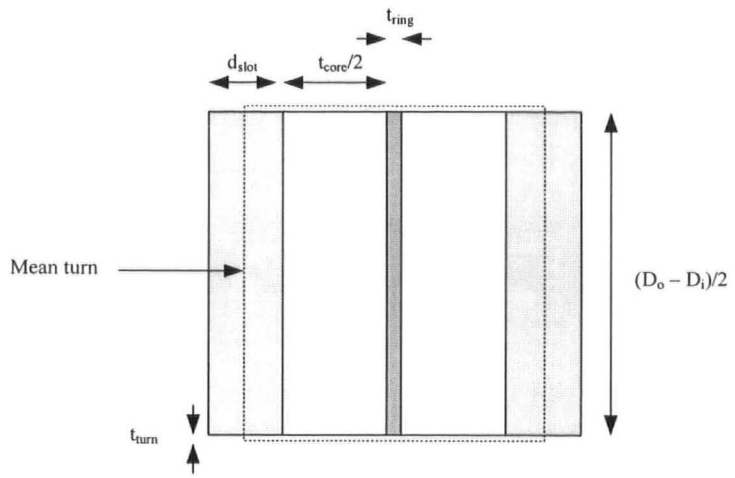

Figure 5.12: Average turn

The length of this turn is thus:

$$l_{turn} = 2\left(\frac{D_o - D_i}{2} + t_{cond} + t_{core} + t_{ring} + d_{slot}\right) \qquad \text{Eq. 5.29}$$

As per the TORUS, each phase is wound separately, one coil at a time, such that a circumferential portion situated at the outer diameter of the core runs between coils of a given phase. The north coils of each phase are wound separately from the south coils, so the coil interconnection length per phase is approximated by two outer circumferential lengths per layer. The conductor length per phase is thus approximated by the length of the average turn multiplied by the number of turns, added to a circumferential length of conductor accounting for the interconnections:

$$l_{phase} = l_{turn} Np + 2\pi D_o \qquad \text{Eq. 5.30}$$

The phase resistance can then be calculated by application of Eq. 5.28.

5.4.4. Comparison of the machine sizing results

Once the rotor and stator core thicknesses have been calculated, the resistance calculation follows since the lengths of the phase conductors are partly determined by the dimensions of the core. These calculations complete the sizing of the machine and the results are tabulated for comparison, Table 5.4.

	TORUS	1 slot	2 slots
Rotor thickness (m)	0.010	0.014	0.014
Stator core thickness (m)	0.026	0.024	0.024
Total axial length of the stator (m)	0.028	0.038	0.039
Length of an average turn (m)	0.190	0.200	0.200
Phase resistance (Ω)	0.17	0.17	0.17

Table 5.4: Comparison of the axial length and resistance parameters

Owing to the presence of slots, the total axial lengths of the slotted stators are significantly greater than that of the TORUS stator since the increased flux levels have increased the back iron requirement and the slot depth added to the stator exceeds the depth of the previous air-gap winding. However, the comparison is flawed since the stator core thickness of the actual TORUS prototype appears to be oversized when the equations of section 5.4.2 are applied. This is credited to either a cautious initial design decision or simply to the convenient availability of set core sizes.

A quick calculation of the stator core thickness actually required in the case of the TORUS, according to the same criteria as the slotted machines, provides figures for comparison. The peak core flux is 1.38mWb and, assuming levels of 1.4T in the core, this requires a thickness of 0.016m resulting in a total stator axial length of 0.019m. Adding the winding thickness of 0.058m for both sides would result in a stator of length 0.031m, compared with 0.038m and 0.039m for the 1 slot and 2 slots machines respectively. Considering the running clearance, the magnet thickness, and the rotor thicknesses, the total axial lengths of the machines are: 0.065m (TORUS), 0.083m (1 slot), and 0.084m (2 slots). Hence the 70% increase in the open circuit EMF achieved with slots has an associated 30% increase in axial length.

5.5. Analysis of the field arising from phase currents

5.5.1. Components of inductance

Having considered the excitation field in the slotted machines, and the resulting increase in axial length required to accommodate the increased flux that slotting facilitates, this rough comparison exercise now considers the fields arising from phase currents. As described in Chapter 3, this consideration leads to the evaluation of the various inductances present in such machines and ultimately quantifies the synchronous reactance.

Since the number of turns is low and the effective air-gap is large in comparison with more conventional machines, the magnitude of the synchronous reactance is likely to have a limited effect on the performance of the equivalent circuit described in Chapter 3. However, the principal reason for the calculation of this parameter here is to enable further benchmarking of the analytical methods with the results of more accurate FEA so that the methods can later be extended to machines where the synchronous inductance could potentially be more considerable.

The synchronous inductance is the per-phase inductance used in the equivalent circuit and the definition used here is that this inductance is equal to the total flux linkage experienced by a given phase, per amp current in that phase. A phase may link flux either arising from its own current (self inductance), or from current in adjacent phases (mutual inductance).

The slotted portion of the conductors (main winding) produces a field that forms a magnetic circuit through the rotor linking the permanent magnets; this is referred to

as working flux. There will be some leakage flux in the air-gap region as well as some slot leakage flux; these can be estimated separately.

The axial portion of the conductors (end-winding) is assumed to produce leakage flux only, since it is unlikely that any of this flux will interact with the rotor field. This conductor region is not slotted and is similar to the TORUS end winding. The components of the synchronous inductance are therefore assumed to be:

Main winding:

- Self inductance
  - Working flux
  - Air-gap leakage flux
  - Slot leakage flux
- Mutual inductance
  - Working flux

End winding:

- Self inductance
  - Leakage flux
- Mutual inductance
  - Leakage flux

The analysis proceeds in 2D, tackling the main-winding and end-winding regions separately by assuming infinite length in the radial and axial directions, and considering the inductance components per pole per phase. The results are then modulated by the core length and the stator thickness respectively. The slot leakage and the air-gap leakage are evaluated separately and finally the components are combined to give the synchronous inductance, taking the number of poles into account.

Once again, a simple magnetic circuit analysis is carried out alongside a more accurate method involving the solution to Laplace's equation described in Chapter 3. In both cases, the components of inductance are calculated when current is passed through one phase only. The general simplifications to the analytical approaches were described in section 5.2.3: the conductors are assumed to have negligible thickness; they are assumed to lie on the surface of an un-slotted stator core; they are assumed to be spread across an effective coil pitch according to the distribution factors calculated in section 5.3.1; and the Carter coefficient previously calculated is used to give an effective gap, g_{eff}, upon which the calculations are based.

5.5.2. Magnetic circuit solution

The boundary conditions applied in the analysis of the TORUS are also true for the slotted variants since the field orientations are the same; hence a reduced model of 1 pole pitch is considered again. The central phase is considered energised and the flux linking that phase and also the adjacent phases is calculated. Leakage is ignored at this stage; all the flux is assumed to travel in defined loops crossing the gap twice, and a trapezoidal MMF profile roughly corresponding to the spread of the conductors is assumed to accurately represent the flux density profile. This profile is assumed to remain constant across the gap and the iron is assumed infinitely permeable. The effective gap calculated previously takes the slots into consideration although the stator surface is assumed flat. Figure 5.13 shows the model and assumed flux profile with 1 slot/pole/phase.

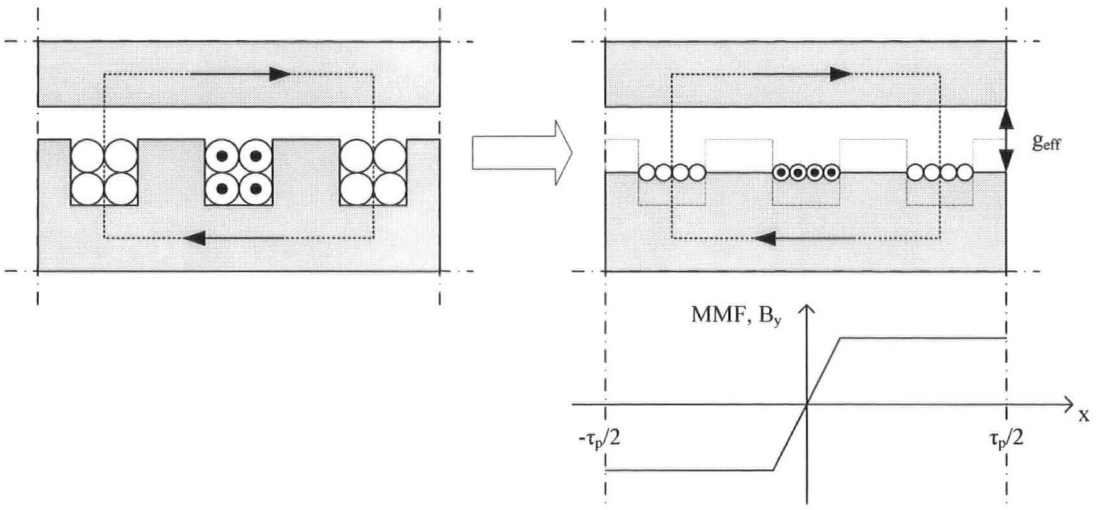

Figure 5.13: Magnetic circuit and assumed flux density profile

The effective gap is as before:

$$g_{eff} = \frac{t_m}{\mu_r} + c' \qquad \text{Eq. 5.31}$$

The magnetic circuit law gives B:

$$2Hg_{eff} = Ni \Rightarrow B = \frac{\mu_o Ni}{2g_{eff}} \qquad \text{Eq. 5.32}$$

The Fourier representation of the trapezoidal flux density assumption is:

$$B(x) = \sum_{n\_odd} B_n \sin\left(\frac{\pi n x}{\tau_p}\right) \qquad \text{Eq. 5.33}$$

Where:

$$B_n = \frac{4k_{d,n}\left(\frac{\mu_o Ni}{2g_{eff}}\right)}{n\pi} \qquad \text{Eq. 5.34}$$

Considering only the fundamental, the variation of axial flux density (B_y in this 2D model) with x at the stator surface is approximated to:

$$B_1(x) = \frac{2\mu_0 Nik_{d,1}}{g_{eff}\pi} \sin\left(\frac{\pi x}{\tau_p}\right) \qquad \text{Eq. 5.35}$$

Integrating this between *0* and $\tau_p/2$ gives the flux entering the stator core per unit core length into the page:

$$\phi_1 / m = \frac{2\tau_p \mu_0 N i k_{d,1}}{g_{eff} \pi^2} \qquad \text{Eq. 5.36}$$

Taking both sides of the stator into account means that the core length is simply the difference between the core inner and outer diameters. The coil inductance is the flux linkage per amp and each pole has *N* series turns per phase in this case. Hence the first harmonic of the self inductance:

$$L_{main} = \frac{N\phi_1 k_{d1}}{i} = \frac{4\tau_p \mu_0 N^2 k_{d,1}^2}{g_{eff} \pi^2} \frac{(D_o - D_i)}{2} \qquad \text{Eq. 5.37}$$

The same method is extended to the calculation of mutual inductance. The same state of energisation is assumed and the flux linking the turns of an adjacent (non-energised) phase is considered. The expression for flux density is now integrated between $\tau_p/3$ and $\tau_p/2$ to give the flux, and the resulting first harmonic of the mutual inductance is given:

$$M_{main} = \frac{2\tau_p \mu_0 N^2 k_{d,1}^2}{g_{eff} \pi^2} \frac{(D_o - D_i)}{2} \qquad \text{Eq. 5.38}$$

The end-winding is effectively air-gap wound in the format considered here and so the formulae derived in Chapter 3 for the TORUS are assumed to hold. The following equations for the first harmonics of the self and mutual inductances of the end windings were obtained from the field solution by considering an effective gap at the end windings. Since there is no rotor iron opposite the ends, this gap is merely an approximation to the length of the leakage flux paths in these regions. The TORUS analysis of section 3.6.2 is repeated with a slight modification to take some account of the contribution of the slot depth towards the effective core length.

The self inductance is thus given:

$$L_{end,1} = \frac{4\tau_p \mu_0 N^2 k_{d,1}^2}{g_{eff,end}\pi^2}(t_{stator} + d_{slot}) \qquad \text{Eq. 5.39}$$

When considering the first harmonic, the spatial displacement of the coils implies that the mutual inductance is half the value of the self inductance:

$$M_{end,1} = \frac{2\tau_p \mu_0 N^2 k_{d,1}^2}{g_{eff,end}\pi^2}(t_{stator} + d_{slot}) \qquad \text{Eq. 5.40}$$

The effective gap of the end-winding region was defined in Chapter 3 as:

$$g_{eff,end} = \frac{\tau_p}{\pi} \qquad \text{Eq. 5.41}$$

5.5.3. Magnetic circuit solution: main winding leakage inductances

Since the slot geometry is neglected in the above analysis, leakage in the main winding region was not taken into account and so is considered here in a simplified version of the method outlined by Carter [93], pp. 217-221. Carter divides slot leakage into 3 components: a) flux that links only some of the conductors in the slot; b) flux that links all of the conductors in the slot; and c) tooth tip leakage flux. In the case of fully open slots, the conductors are assumed to occupy the slot right up to the tooth tip. Any flux crossing the slot beneath the tooth tip will link some or all of the conductors, and is described by fluxes a) and b), above: this is slot leakage. c) is thus flux crossing above this, namely air-gap leakage flux. Slot and air-gap leakage self inductances are thus evaluated separately here. Since the magnitudes are likely to be small and the methods are very approximate, mutual effects are not considered.

5.5.4. Slot leakage inductance

All the slot leakage flux in this analysis is assumed to link some or all of the conductors by traversing the conductors themselves. The reluctance of the iron is ignored, and the fluxes are assumed to traverse the slot in straight lines perpendicular to the edges of the slot. The conductors are all grouped together to give an effective slot current which is uniformly distributed over the full slot depth. The simplification is illustrated in Figure 5.14.

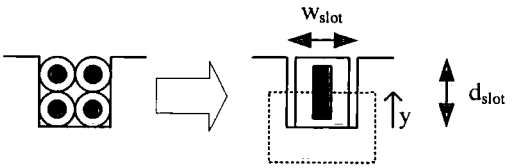

Figure 5.14: Slot leakage flux

The slot current is given in terms of the rated current and the number of series wound conductors per slot. Since the conductors occupying the slot in these variants are a specified array of thick, stranded turns, the number of conductors per slot is equal to the product of the width and the depth of the slot by number of conductors. Hence the slot current can be expressed:

$$I_{slot} = I_{rated} d_{slot(conductors)} w_{slot(conductors)} \qquad \text{Eq. 5.42}$$

The flux path crossing the conductor at position y is linked with current $I_{slot}y/d_{slot}$, where the slot dimensions are now given in metres, not by number of conductors. By the magnetic circuit law, the magnetic field intensity at this position is obtained from:

$$Hw_{slot} = \frac{I_{slot} y}{d_{slot}} \qquad \text{Eq. 5.43}$$

Hence the flux density:

$$B = \frac{\mu_0 I_{slot} y}{w_{slot} d_{slot}} \qquad \text{Eq. 5.44}$$

The radial length of this portion, considering both sides of the stator, is $(D_o - D_i)$ and hence the flux in the layer between y and $(y + \delta y)$ is given:

$$\delta\phi = \frac{\mu_0 I_{slot} y (D_o - D_i)}{w_{slot} d_{slot}} \delta y \qquad \text{Eq. 5.45}$$

This flux links all the current between itself and the bottom of the slot, hence the flux linkage:

$$\psi = i\delta\phi = \frac{\mu_0 I_{slot}^2 y^2 (D_o - D_i)}{w_{slot} d_{slot}^2} \delta y \qquad \text{Eq. 5.46}$$

Hence the slot leakage inductance can be found by summation over the slot depth:

$$L_{slot} = \frac{1}{I_{slot}^2} \sum \psi = \frac{\mu_0 (D_o - D_i)}{w_{slot} d_{slot}^2} \int_0^{d_{slot}} y^2 \delta y = \frac{\mu_0 d_{slot} (D_o - D_i)}{3 w_{slot}} \qquad \text{Eq. 5.47}$$

The slot leakage inductance per pole per phase is finally given:

$$L_{slot\_leakage} = n_{slots/pole/phase} L_{slot} \qquad \text{Eq. 5.48}$$

5.5.5. Air-gap leakage inductance

Air-gap leakage flux is termed tooth-tip leakage flux by Carter, [93], and its calculation here follows the method Carter prescribes. The flux path assumed for this component of leakage is shown in Figure 5.15.

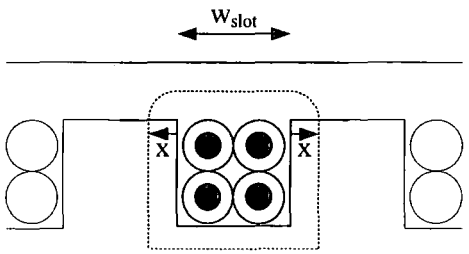

Figure 5.15: Air-gap leakage flux path

This flux path surrounds the whole conductor, and so the magnetomotive force (MMF) is equal to the slot current as defined by Eq. 5.17. This MMF is equal to the product of the air-gap leakage flux per slot and the reluctance of its path, since the

iron is assumed infinitely permeable. Where the permeance, P, is the reciprocal of reluctance, the flux can be expressed:

$$\phi = \mathrm{P} I_{slot} \qquad \text{Eq. 5.49}$$

Recalling that the air-gap leakage inductance per slot is, by definition, the flux linking the slot current divided by the slot current itself:

$$L_{gap} = \mathrm{P} \qquad \text{Eq. 5.50}$$

The elemental permeance of a flux path having length, l, and cross section, δS is given:

$$\delta \mathrm{P} = \frac{\mu_o \delta S}{l} \qquad \text{Eq. 5.51}$$

According to Figure 5.15, the length of the flux path is composed of the slot width flanked by two quadrants each of length $\pi x/2$. The total permeance can then be evaluated by integration, but the upper integration limit requires some consideration. Carter argues that flux emerging at the point where x is equal to the gap will just graze the rotor surface and so the upper limit should equal the gap. In the machines considered here, however, it is not inconceivable for the gap to be of the same order of magnitude as the tooth width. If the gap exceeded the tooth width, the assumed flux path would be invalid where x is greater than the tooth width. Hence the upper limit used here is equal to the tooth width. Where there is more than one slot per pole per phase the result is multiplied up. Hence:

$$L_{gap} = \mathrm{P} = \mu_o \int_0^{w_{tooth}} \frac{dx}{\pi x + w_{slot}} = \frac{\mu_o}{\pi} \ln\left(\frac{\pi w_{tooth} + w_{slot}}{w_{slot}}\right) \qquad \text{Eq. 5.52}$$

And:

$$L_{gap\_leakage} = n_{slots/pole/phase} L_{gap} \qquad \text{Eq. 5.53}$$

5.5.6. Field solution

The equations developed for the TORUS utilising the field solution are used again here with some slight modification. The field solution cannot be applied to the calculation of the air-gap leakage inductances in line with the above analysis, so it is only extended to the main and end-winding components of the self and mutual inductances. The air-gap leakage components obtained by magnetic circuit analysis can be utilised with the field solution in the assimilation of the synchronous reactance shown later.

Since the slotted conductors are assumed to be spread evenly across the pole pitch, the phase conductor current density model is now as illustrated in Figure 5.16.

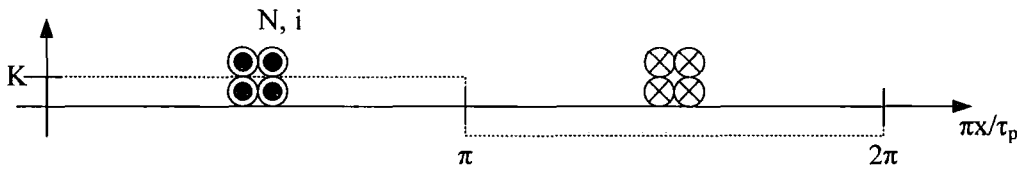

Figure 5.16: Phase conductor current density model

What was previously termed the coil width is now simply the pole pitch; this is concomitant with the coil spread being π radians:

$$w = \frac{\sigma D_m}{p} = \frac{\pi D_m}{p} = \tau_p \qquad \text{Eq. 5.54}$$

The same formulae can still be used, however, with the final result being the following expressions. Firstly, the coil self-inductance in the main winding region:

$$L_{main,n} = \frac{4\mu_0 N^2 k_{d,n}^2}{\pi n} l_{eff} \coth u_n g_{eff} \qquad \text{Eq. 5.55}$$

Similarly, the mutual inductance:

$$M_{main,n} = \frac{4\mu_0 N^2 k_{d,n}^2}{\pi n} l_{eff} \coth u_n g_{eff} \cos u_n \gamma \qquad \text{Eq. 5.56}$$

Again, for the evaluation of the end leakage inductance, the TORUS analysis of section 3.5.3 is repeated with a slight modification to take some account of the contribution of the slot depth towards the effective core length. Hence:

$$L_{end,n} = \frac{4\mu_0 N^2 k_{d,n}^2}{\pi n}(t_{stator} + d_{slot}) \qquad \text{Eq. 5.57}$$

And:

$$M_{end,n} = \frac{4\mu_0 N^2 k_{d,n}^2}{\pi n}(t_{stator} + d_{slot})\cos u_n\gamma \qquad \text{Eq. 5.58}$$

As before, these equations may be obtained from those derived for the main flux region (Eq. 5.39, 5.40) by considering the first harmonic and using the end-winding effective gap defined by Eq. 5.41.

5.5.7. Synchronous reactance

The synchronous reactance is the parameter used in the equivalent circuit described in Chapter 3. It is related to the synchronous inductance as follows:

$$X_{syn} = j\omega L_{syn} = j2\pi f_{elec} L_{syn} = j\frac{\pi np}{60} L_{syn} \qquad \text{Eq. 5.59}$$

The synchronous inductance is composed of inductances contributed by the various flux paths analysed separately in the above sections under three-phase operation. In the case of the magnetic circuit solution, the synchronous inductance is a simple sum of the main, end-leakage, slot-leakage and gap-leakage components of self inductance, and the main and end-leakage components of mutual inductance:

$$L_{syn} = p(L_{main} + L_{end} + L_{slot\_leakage} + L_{gap\_leakage} + M_{main} + M_{end}) \qquad \text{Eq. 5.60}$$

In the case of the field solution, the main and end winding components of self and mutual inductance are formed from a sum of their harmonic components, and the leakage components obtained from the magnetic circuit approach are added to the total.

Hence:

$$L_{syn} = p\sum_{n}\left(L_{main,n} + L_{end,n} + M_{main,n} + M_{end,n}\right) + p(L_{slot\_leakage} + L_{gap\_leakage}) \qquad \text{Eq. 5.61}$$

5.5.8. Results of the analysis of the field arising from phase currents

The various components of inductance calculated for the three machines using the methods derived in the preceding sections are presented below, Table 5.5. It should be noted that these values are per pole; the assimilation of the synchronous inductance from these components takes the number of poles into consideration as described in section 5.5.7. Firstly, as has already been discussed, the magnitudes of all these components are small. This is because of the large effective air-gap and the relatively small number of turns per pole per phase. Since the permanent magnet thickness is considerable, the effective air-gaps of even the slotted machines are still large by comparison with more conventional geometries.

Comparison between the first harmonics of the magnetic circuit and field solutions indicates good agreement. This is particularly true of the end-winding values, but this is not surprising since the magnetic circuit solution is effectively derived by simplification of the field solution. The main winding values agree to within 15% in the case of the TORUS and to around 5% in the slotted variants. This apparent improvement in the accuracy of the magnetic circuit solution is attributable to the increased suitability of the flux density profile used. A trapezium is more accurate in the case of the slotted machines than in the TORUS owing to the reduced effective air-gap.

	TORUS	1 slot	2 slots
Magnetic circuit solution (n = 1)			
L_{main} (H)	2.41E-06	3.98E-06	3.74E-06
M_{main} (H)	1.20E-06	1.99E-06	1.87E-06
L_{end} (H)	6.27E-07	7.65E-07	7.00E-07
M_{end} (H)	3.14E-07	3.83E-07	3.50E-07
Total (H)	4.55E-06	7.12E-06	6.66E-06
Field solution (n = 1)			
L_{main} (H)	2.78E-06	4.21E-06	3.94E-06
M_{main} (H)	1.39E-06	2.11E-06	1.97E-06
L_{end} (H)	6.27E-07	7.65E-07	7.00E-07
M_{end} (H)	3.14E-07	3.83E-07	3.51E-07
Total (H)	5.11E-06	7.47E-06	6.96E-06
Field solution (sum to n = 21)			
L_{main} (H)	3.20E-06	5.78E-06	4.24E-06
M_{main} (H)	1.07E-06	1.64E-06	1.70E-06
L_{end} (H)	7.84E-07	1.44E-06	8.18E-07
M_{end} (H)	1.99E-07	2.10E-07	2.46E-07
Total (H)	5.26E-06	9.08E-06	7.01E-06
Leakage associated with slots			
L_{slot} (H)	N/A	4.08E-08	8.17E-08
$L_{slot\ leakage}$ (H)	N/A	4.08E-08	1.63E-07
L_{gap} (H)	N/A	7.13E-07	7.13E-07
$L_{gap\ leakage}$ (H)	N/A	7.13E-07	1.43E-06
Total (H)	N/A	1.51E-06	2.38E-06

Table 5.5: Analytically obtained inductance components (all values per pole)

Inclusion of higher order harmonics in the field solution differentiates this result from the magnetic circuit solution more noticeably. These harmonics act to increase the self inductance of the main and end-winding regions, and to decrease the mutual inductances. Since the slotted machines have smaller effective air-gaps, it is probable that flux would be more confined within the region of the excited phase and less likely to spread to adjacent phases causing mutual effects. The extra harmonics included in the full field solution capture this detail.

Comparison between the TORUS and the slotted variants indicates that the inductance components of the slotted machines are generally larger; this is once more attributed to the reduced effective gap. The extra leakage components analysed will further increase the synchronous inductance of the slotted machines above that of the TORUS. There is also some difference between the two slotted variants themselves. Looking particularly at the total of the field solution (sum to $n = 21$), the 1 slot machine has an inductance per pole of approximately 9μH compared with 7μH for the 2 slot machine: a difference of some 25%. The principle reason for this is the different winding distribution factors used. The 1 slot variant is a special case where the winding can be assumed to spread only as far as the slot width. This implies that the winding is considerably more concentrated than might otherwise be the case. By the analysis described above, machines with two or more slots per pole per phase are assumed to have a winding spread which covers all the space available, namely the pole pitch divided by the number of phases. It is therefore likely that the inductance of the 1 slot machine is more accurate, and that the predicted inductance of the 2 slots machine is under-estimated owing to this harsh assumption concerning the spread.

There are few comparisons to be made in the case of the slot leakage flux predictions since these are rough approximations and only apply to the slotted variants which are, as yet, unrealised beyond this study. One general observation concerns the total magnitude of these leakage components: the 1 slot machine seemingly has less leakage inductance than the 2 slots machine. This is expected, since the slot width in the 1 slot machine is larger and, owing to the relative magnitudes of the slot and the effective gap, flux would be less likely to prefer the leakage path over the main flux path than in the 2 slots machine. One further observation is that the total of these slot

leakages are between 15% and 35% of the total inductance obtained from the field solution for both machines; this is a credible proportion. Since the magnitudes are small and that the synchronous reactances will be assimilated from a number of these small components, there is little more to be gained from such comparisons in this instance. Table 5.6 shows the final results of the synchronous inductances and reactances obtained from the magnetic circuit solution *(n = 1)*, and the field solution *(sum to n = 21)*, both incorporating the results of the slot leakage calculations. These values indicate the general trend and will be compared with the results of FEA in a later section. It should be noted that reactances are quoted for the rotational speed of 1500RPM for consistency with the work in previous chapters.

	TORUS	**1 slot**	**2 slots**
Magnetic circuit solution			
L_{syn} (H)	7.28E-05	1.38E-04	1.45E-04
X_{syn} (Ω)	0.0915	0.1736	0.1818
Field solution			
L_{syn} (H)	8.41E-05	1.69E-04	1.50E-04
X_{syn} (Ω)	0.1057	0.2128	0.1888

Table 5.6: Synchronous reactance comparison

In general, the slotted machines exhibit higher inductances. The analysis of the components indicated that the 1 slot machine has higher main inductance components owing to the more concentrated nature of the winding, but that the 2 slot machine has higher slot leakage components owing to the smaller slot width. This confuses the comparison shown in Table 5.6 since the magnetic circuit underestimates the main inductance components by only utilising the first harmonic. However, the methods agree reasonably well and the results of both confirm the predicted differences between air-gap wound and slotted machines as described in section 5.1.1.

5.6. Electromagnetic FEA of the slotted variants: excitation field

5.6.1. 3D magnetostatic FEA

Following the reasoning set out in Chapter 4 concerning the general FEA of the TORUS machine, this section analyses the slotted variants using similar techniques. Firstly, 3D magnetostatic models facilitating visualisation and quantification of the fields set up in the slotted variants as a result of the presence of the permanent magnet excitation are described. Axial and rotational symmetry are exploited so that two pole pairs of a single rotor and half a stator could be used in conjunction with tangential flux and periodic boundary conditions to accurately represent the whole machines. The mesh of the 1 slot/pole/phase machine is shown, Figure 5.17, where again the iron components are shown in red and the North/South permanent magnets are shown in pink and blue.

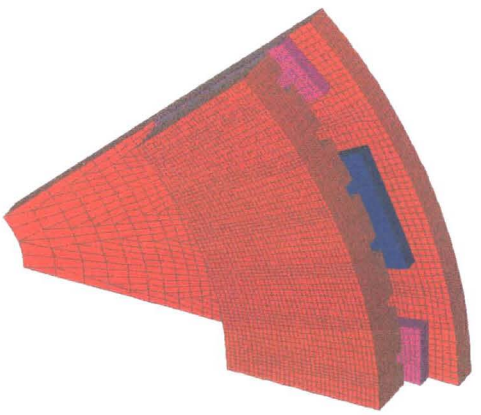

Figure 5.17: 3D FEA mesh of the 1 slot variant

The axial (working) excitation flux density was evaluated in the air elements just above the stator or tooth surface. The surfaces in Figure 5.18 illustrate the nature of these fields in the different machines.

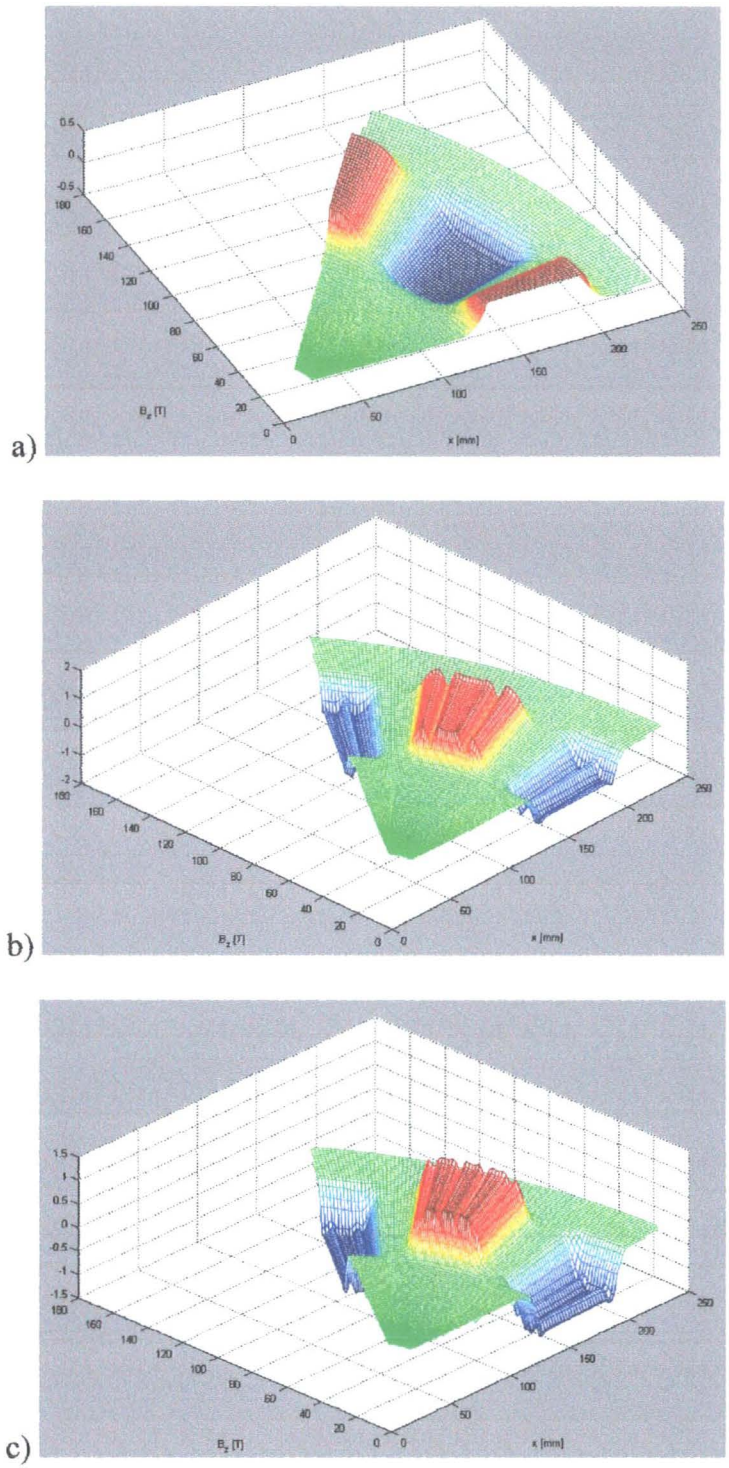

Figure 5.18: B_z stator surface for a) TORUS, b) 1 slot variant, c) 2 slots

Figure 5.19 compares the circumferential and radial variations of axial excitation flux density more clearly, showing 2D characteristics at the mean diameter and across the centre of a pole respectively. These show the increased magnetic loading possible with slotted conductors. The circumferential variation highlights the

markedly different flux density characteristic present in the slotted variants which exhibit an almost square profile with superimposed slot ripple. This indicates the existence of slot harmonics, and the associated effects are investigated later in this chapter.

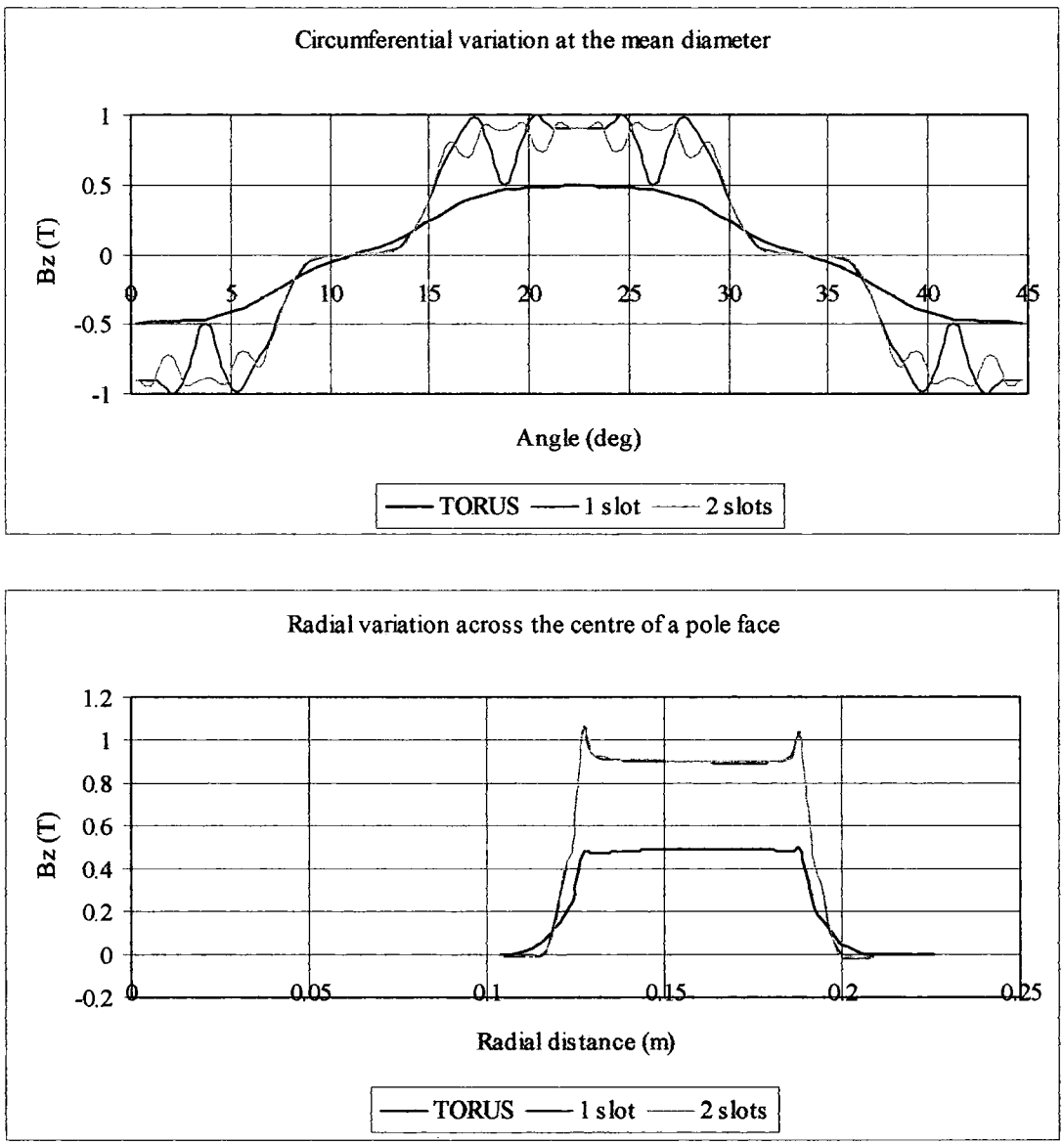

Figure 5.19: Excitation field flux density at the stator core from 3D FEA

The graphs in Figure 5.20 compare the analytical predictions with the FEA results for the circumferential flux density variation. Equivalent comparisons for the TORUS machine were made in section 3.4.

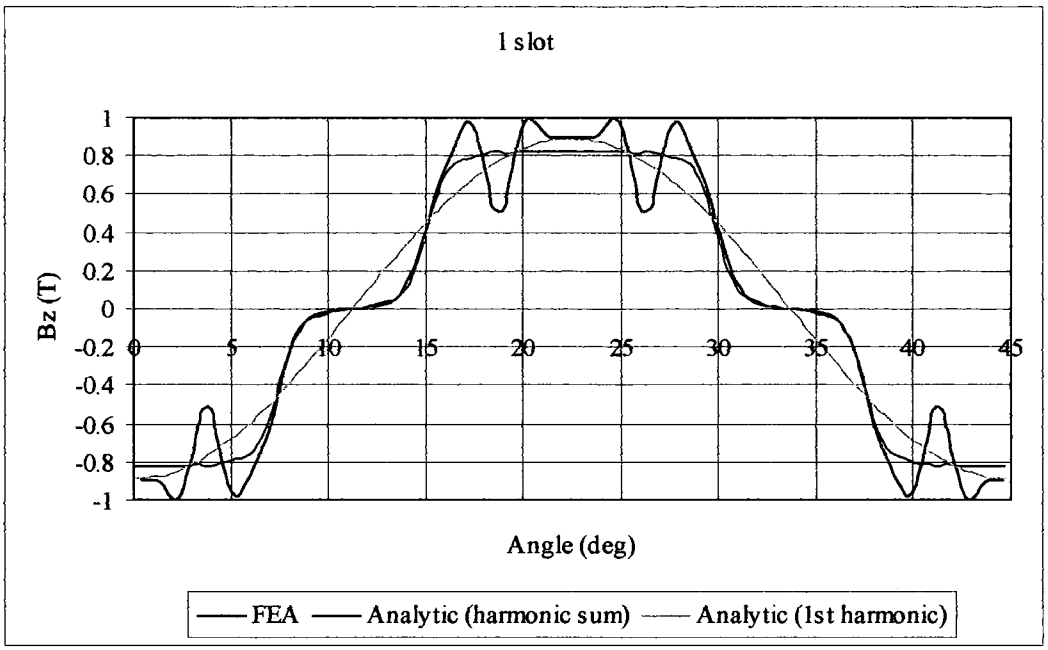

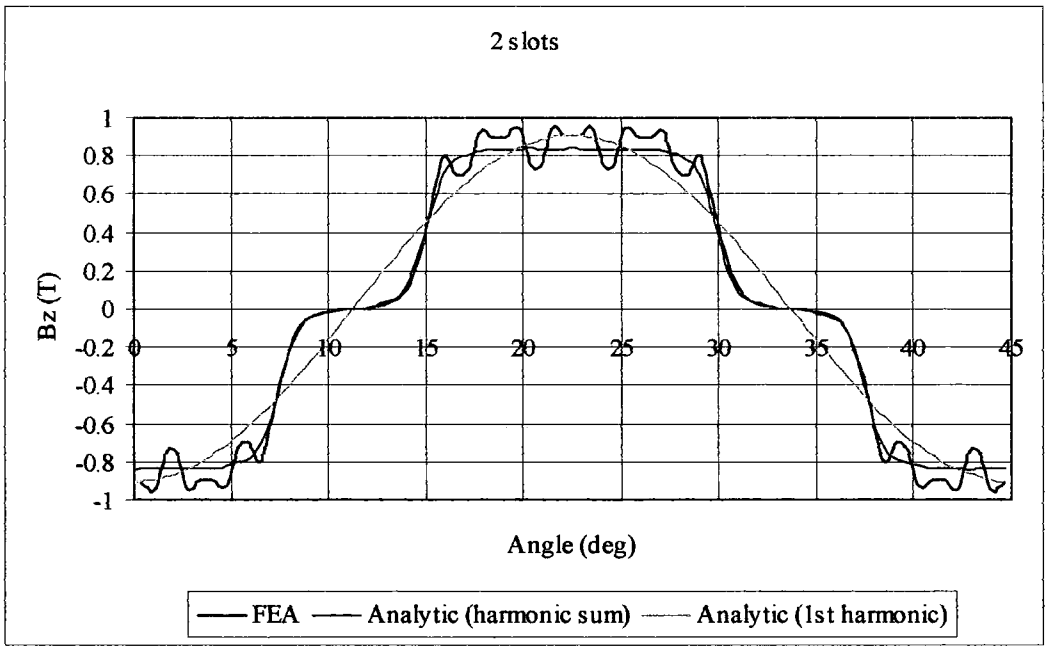

Figure 5.20: Circumferential B_z comparisons for the slotted variants

The comparisons show the expected similarities and differences between the analytical predictions and the FEA results. Since a Carter coefficient was used in the analytical solution, the overall shape and magnitude of the flux density variation agrees well with the FEA result in both cases. The difference arises from a superimposed slot ripple resulting from the variable reluctance presented by a tooth

and slot structure; this is picked up by FEA but was ignored in the analytical procedure.

In section 3.4, the spatial variation of the circumferentially-travelling core flux was obtained for the TORUS. Since the TORUS stator presents an approximately constant reluctance to the excitation field, the angular variation of core flux in the static case has the same waveform as the temporal variation of core flux at a fixed angle in the static case. Therefore it was possible to deduce the time-varying core flux and use this to establish the open-circuit EMF for a given winding specification. In the case of slotted machines this equivalence between the spatial and temporal flux waveform does not hold true, since the variable reluctance of the stator surface affects the excitation field significantly. However, the variation of core flux with angle was obtained for the slotted variants in the static state and is show in comparison with that of the TORUS, Figure 5.21.

Although the slotted waveforms are not to be used directly for the calculation of EMF, Figure 5.21 clearly shows an increased core flux when compared with the TORUS. Furthermore, Figure 5.22 shows the slotted core fluxes with spatial variations obtained from FEA converted to temporal variations by a factor equal to the time taken for a rotation equal to a pole pitch, in seconds, divided by a pole-pitch in metres. Comparison is made with the first harmonic of the core flux derived analytically in section 5.3 for the calculation of the open-circuit EMF.

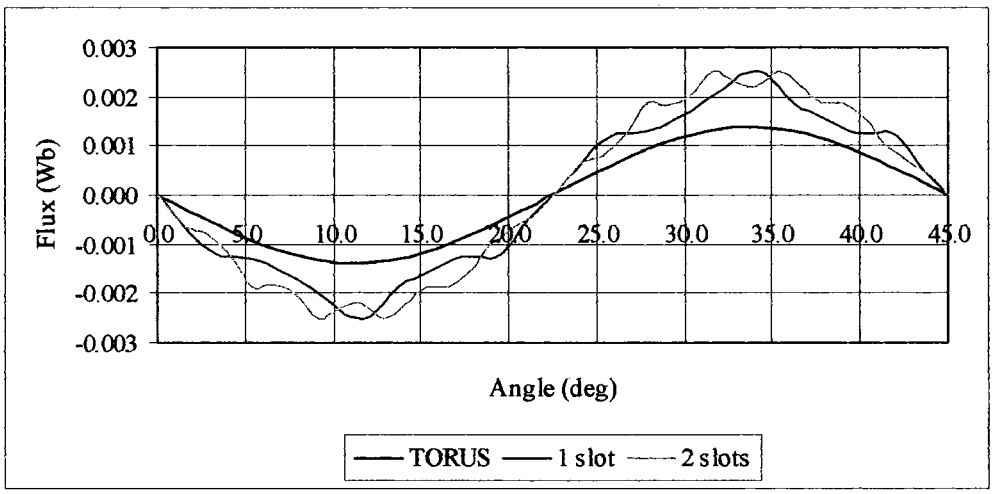

Figure 5.21: Circumferential variation of core flux in the static case

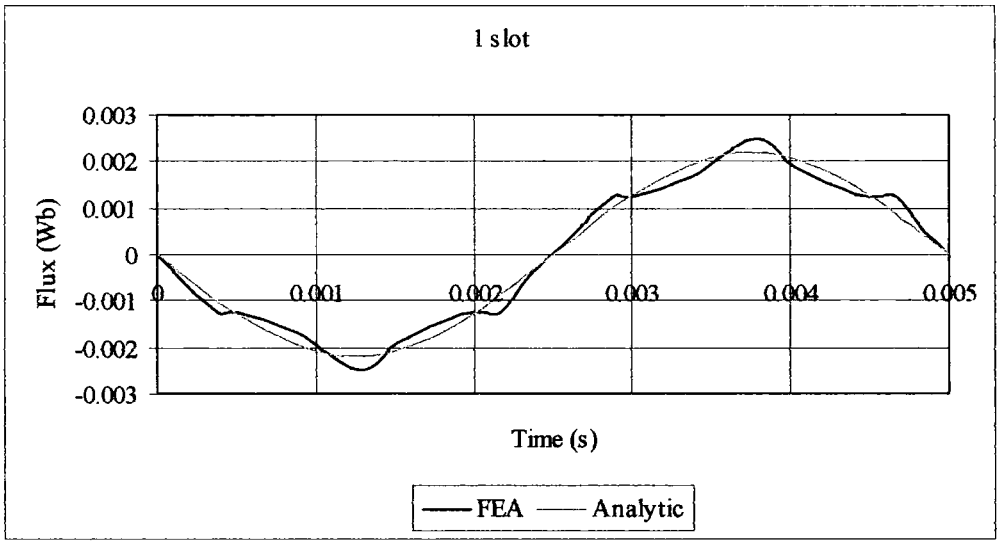

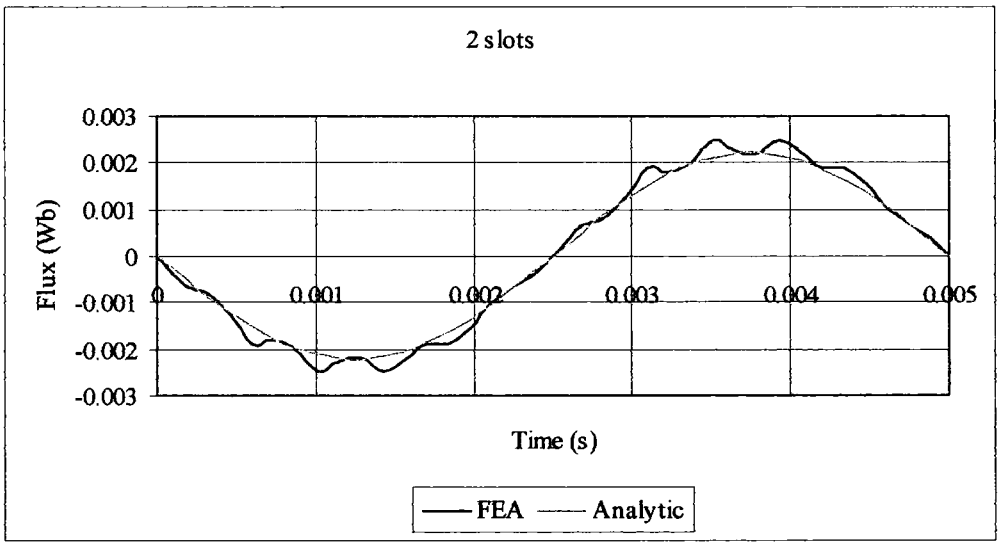

Figure 5.22: Temporal variations of core flux

The FEA and analytically-obtained waveforms shown in Figure 5.22 compare well; however, the FEA result may not be used directly for the calculation of EMF for the reasons set out above. An approximation could be achieved by fitting a sine-wave to the FEA waveform but there would be no benefit in this given the good agreement shown in Figure 5.22. Instead, the next section describes a more direct method of obtaining the induced EMF for the slotted machines by using dynamic FEA.

5.6.2. 2D dynamic FEA

3D dynamic FEA was described in section 4.3.3 for the evaluation of the open circuit EMF of the basic TORUS machine. In order to save modelling and processing time, 2D dynamic FEA is investigated here. Firstly, this approach is benchmarked by the construction of a 2D dynamic model of the TORUS. The approach is very similar to the 2D static approach described in section 4.3.1. Coils are no longer implemented by defining their geometry (such as a racetrack coil) and relying on an automatic cut resource in the software to generate appropriate reduced scalar regions; instead, conductors are defined directly within the mesh using the *"Edit Region"* facility where parameters such as the port connections and number of turns are specified for particular regions of the mesh. The sliding interface and movement specifications are similar to the 3D case, and symmetry is exploited in the axial and circumferential dimensions. The resulting 2D model is relatively small, consisting of a single rotor and half the stator core, spanning one pole pair. In the case of the TORUS, an equivalent machine length equal to the mean of the magnet and core lengths was applied to scale the model in the radial (3^{rd}) dimension. Figure 5.23 shows the EMF results obtained directly from 2D and 3D FEA models in comparison with the experimental test results from Chapter 3.

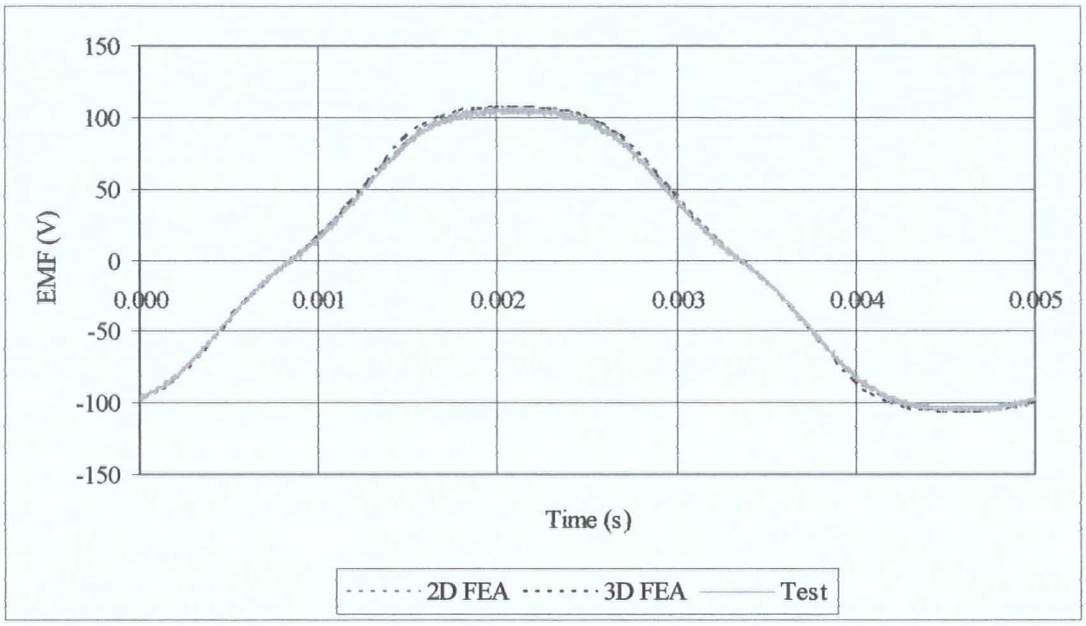

Figure 5.23: Open circuit EMF at 1500RPM: TORUS dynamic FEA benchmarking

These show good agreement, indicating that the 2D approximation is likely to be sufficiently accurate in the dynamic analysis of the slotted variants. In fact, owing to the reduced effective gap, the 2D approximation is more appropriate in the case of slotted machines since flux is less likely to make use of the relatively longer paths linking the end-windings.

Similar models of the slotted variants were therefore constructed and analysed in the same manner. By way of illustration, Figure 5.24 shows a static model of the 2 slots variant with magnetic vector potential contours arising from the permanent magnet excitation.

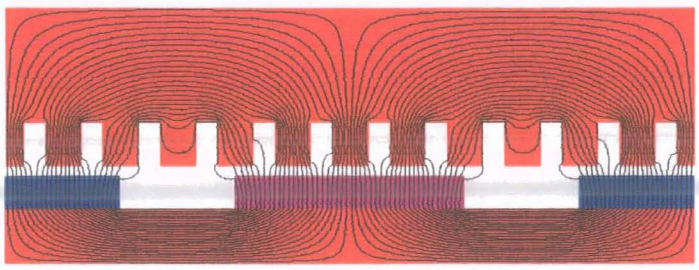

Figure 5.24: 2D FEA of the 2 slots variant

The contours shown are flux lines, in effect, and frames from the solution to the dynamic model are shown in Figure 5.25 as relative movement occurs between the stator and rotor. The effects of the variable reluctance the stator presents to the rotor field can clearly be seen.

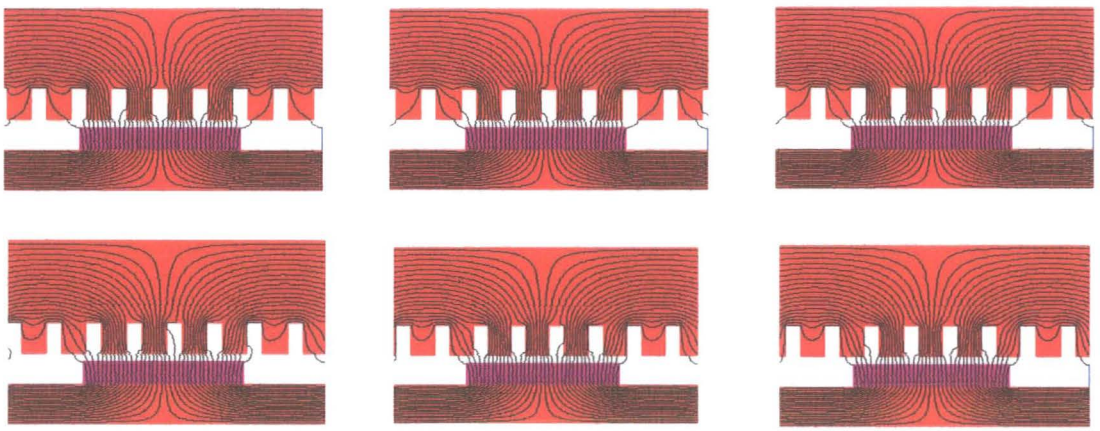

Figure 5.25: Frames from 2D dynamic FEA of the 2 slots variant

The induced EMF was measured at the coil ports for both slotted variants, and is shown in comparison with that of the TORUS for simulated operation at 1500RPM, Figure 5.26.

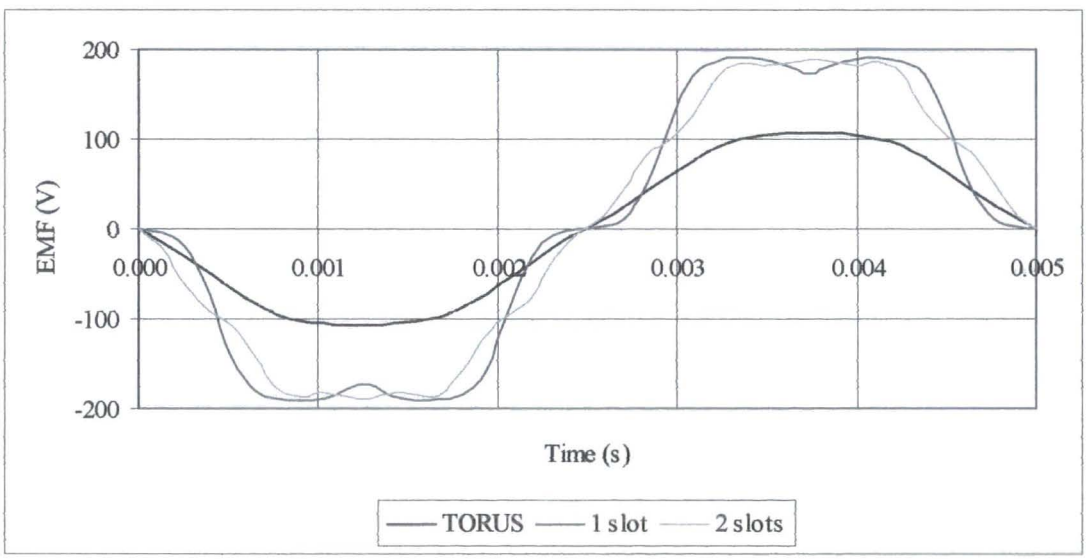

Figure 5.26: Induced EMF per phase at 1500RPM from 2D dynamic FEA

The main benefit of slotting is clearly in evidence here: the magnitude of the EMF induced in both slotted variants is approximately 75% higher than that of the TORUS, in line with the analytical predictions. However, the previously mentioned slot harmonics are clearly in evidence in the EMF predictions with both slotted variants exhibiting ripple and an approximately square or trapezoidal profile. The one-slot machine is evidently particularly prone to harmonics, having pronounced ripple, a definite point of inflexion, and an almost square profile. The waveform for two-slot machine, by comparison, shows that EMF becomes more sinusoidal as the number of slots per pole per phase increases. Ignoring the presence of ripple and the nuances of the waveforms, the overall magnitudes of the EMF induced in the slotted machines are compared with the analytical predictions, again at 1500RPM, Figure 5.27.

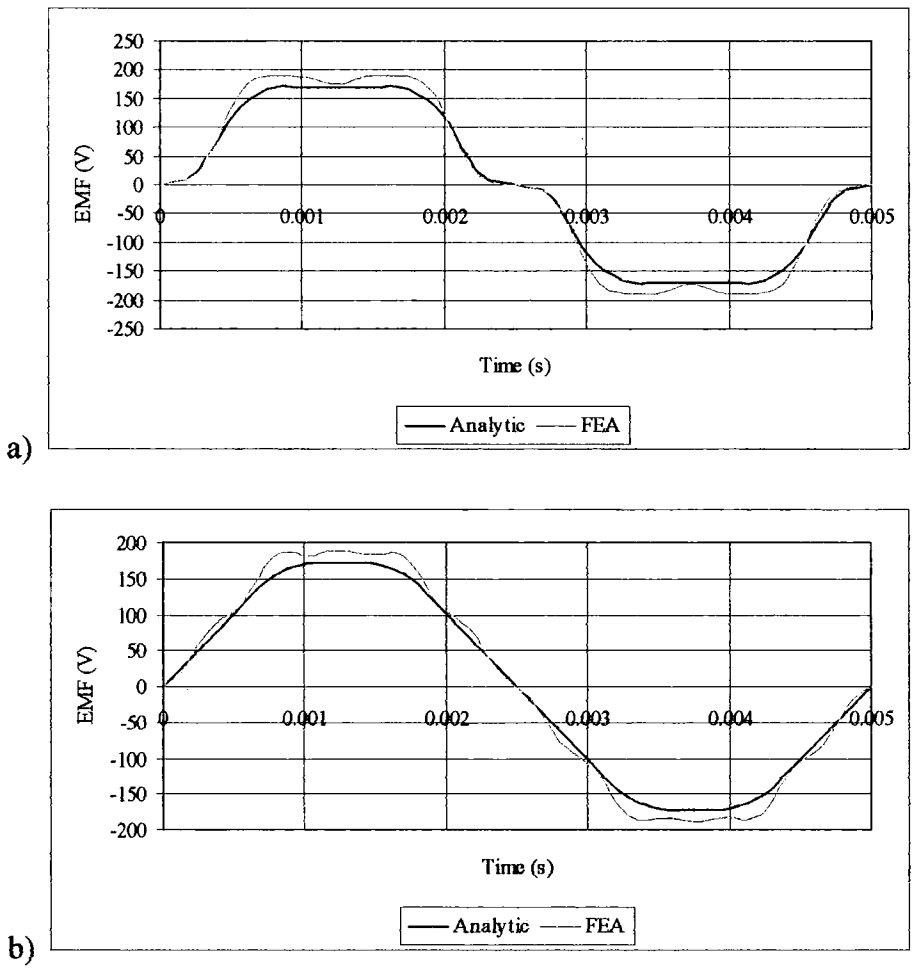

Figure 5.27: Analytical and 2D dynamic FEA comparison for a) 1 slot, b) 2 slots

The FEA and analytical results agree well overall, with the analytical predicting slightly less EMF in both cases (within 5%) and capturing the general waveform but omitting the nuances caused by slot harmonics.

The 2D dynamic FEA shows good agreement with the analytical results overall, and provides a clear illustration of the relative merits of slotted and air-gap wound machines as first described in section 5.1.1. The results give confidence in the analytically-derived first harmonic of EMF for use in equivalent circuit calculations.

5.7. Electromagnetic FEA: field arising from phase currents

5.7.1. Plotting the field arising from single phase excitation

The axial flux density resulting from phase currents in the stator winding was evaluated by implementing the winding as a series of racetrack coils in much the same way as for the TORUS, described in section 3.4.3. Figure 5.28 shows the FEA mesh of the 2 slots variant with its winding.

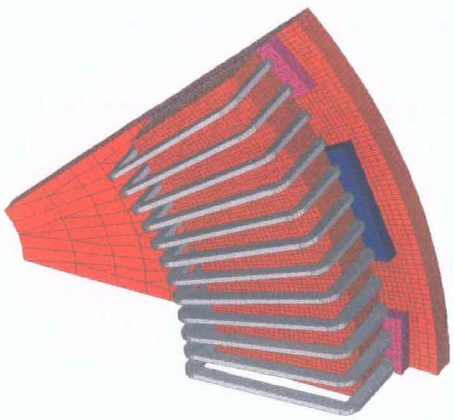

Figure 5.28: 3D FEA mesh of the 2 slots variant with coils

The remanence of the permanent magnet material was deactivated, leaving only regions of very slightly increased permeability to represent the magnets. A known current (5A in this case) was forced into a single phase and the resulting field was

illustrated and quantified in the main and end-winding regions. This facilitated comparison with the TORUS machine, both in terms of the shapes of the obtained waveform and the magnitude of the respective flux density profiles. The magnitude of the field resulting from phase currents determines the various inductances and ultimately the synchronous reactance of the respective machines. Since the number of turns per pole per phase is the same for the TORUS and the two slotted variants under consideration, the values of synchronous reactance will be approximately in proportion to the magnitude of the field evaluated here. Thus the field evaluation gives an indication and some verification of the synchronous reactance used in the equivalent circuit. Recalling the predictions of synchronous reactance in section 5.5.8, the FEA might be expected to yield field predictions for the slotted variants having magnitudes of around twice that of the TORUS in the main winding regions. The graphs in Figure 5.29 and Figure 5.30 compare the fields at the stator core surface arising from single phase excitation with 5A.

A number of observations can be made from these field plots which corroborate some of the assumptions made in the analytical approach to the calculation of the inductance components. Firstly, the magnitudes of the flux densities in the main winding region of the slotted machines are almost twice those of the TORUS as predicted above in line with the analytical prediction for the synchronous reactance. Secondly, the circumferential variations in the main winding region exhibit significant ripple in the case of the slotted machines; this is evidence of the leakage flux associated with slotted windings.

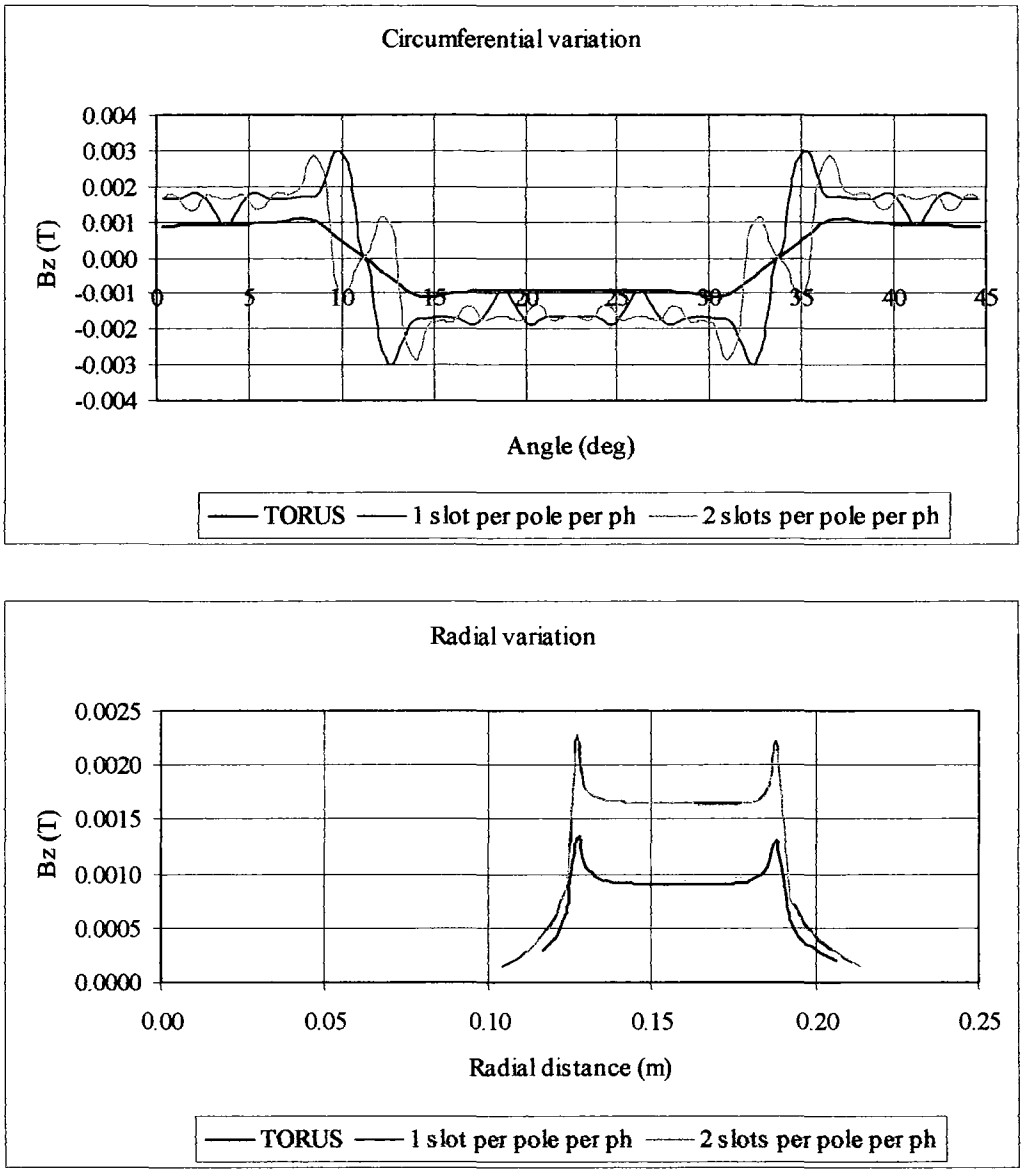

Figure 5.29: Axial flux density at the stator core surface – main winding region

Turning to the end-winding characteristics, it is clear that the difference between the TORUS and slotted variants is much less pronounced. This is because the ends of the slotted machines are air-gap type windings and are thus very similar to the TORUS. The slight differences are attributable to fringing at the core edges and to the different core thicknesses used in the slotted machines. These results affirm the analytical approach which modelled the end-windings of the slotted machines in much the same way as those of the TORUS. Given that the magnitude of the end-winding field does not appear to change in slotted machines, and that the magnitude

of the main winding field almost doubles, the relevance of this parameter in the slotted machines is less; the effects of leakage fluxes associated with the slots in the main winding region are perhaps more worthy of consideration.

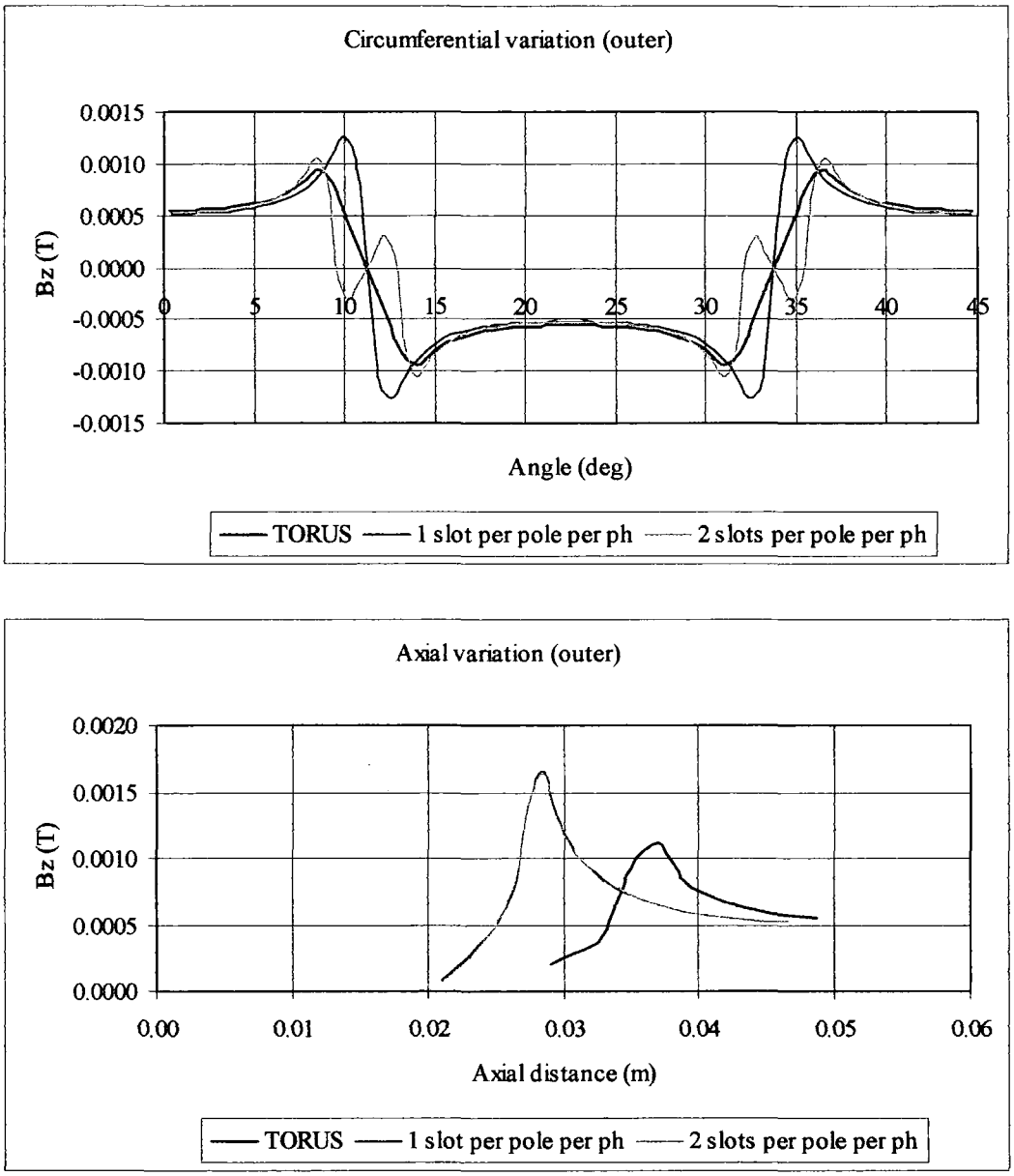

Figure 5.30: Radial flux density at the stator core surface – end-winding region

5.7.2. Determination of the synchronous reactance

The self and mutual inductances were calculated from the 3D magnetostatic model with the coils in place, using the forced AC method described in section 3.5. Since the effects of end-leakage, slot and air-gap leakage, and the main inductance are less easily separable using FEA techniques for the slotted variants the full 3D results are quoted outright. The results were obtained by combining self and mutual components of inductance with only one phase energised, and checking this against a simulated instant in synchronous operation by forcing 1A in phase B and -0.5A in phases A and C. In the latter case, the back EMF measured across phase B is attributable to the synchronous reactance directly. Table 5.7 compares the FEA results where L_{syn} is the synchronous inductance obtained by self/mutual combination, and L_{syn}* directly.

		TORUS	1 slot	2 slots
FEA	L_{phase} (µH)	66.33	130.4	114.6
	M_{phase} (µH)	22.49	34.7	35.7
	L_{syn} (µH)	88.82	165.2	150.3
	L_{syn}* (µH)	88.96	165.5	150.8
Analytical	L_{phase} (µH)	63.74	115.52	80.93
	M_{phase} (µH)	20.30	29.60	31.14
	$L_{slot\ leakage}$ (µH)	(N/A)	24.16	38.08
	L_{syn} (µH)	84.16	169.28	150.15

Table 5.7: FEA inductance predictions

The slotted machines demonstrate an increased inductance of approximately 80% by comparison with the TORUS, which agrees well with the increased magnitude of the field resulting from phase currents as described. Furthermore, these results agree well with the analytical predictions of synchronous inductance, giving further confidence in the application of the analytical methods to the design of slotted machines and the prediction of their performance. It should be noted that the slot leakage inductance is

a separate component in the analytical solution, whereas it is inseparable from L_{phase} and M_{phase} in the FEA results. The L_{syn} totals are directly comparable, however.

Since equivalent circuit parameters for E, R, and X_{syn} have now been obtained analytically and the values of E and X_{syn} verified with FEA, the equivalent circuit of the three machines under consideration can now be analysed. However, one further aspect of the slotted machines is first investigated using FEA, namely the existence and correction of cogging torque.

5.8. Electromagnetic FEA: investigation of cogging torque

5.8.1. Cogging torque in axial flux machines

In contrast to the TORUS machine, the stator utilised in slotted machines presents a variable reluctance to excitation flux originating from the permanent magnet field; the variation is particularly pronounced owing to the fact that the slots are open. This may yield stable rotor positions in the static case, where the magnet edges are more or less aligned with the edges of the teeth and the rotors demonstrate a resistance to motion. Conversely, there may also be unstable positions where the variable reluctance of the teeth results in a torque of alignment. The fields resulting from magnet edges being aligned and misaligned with the slots can be seen in the various frames of the dynamic 2D FEA shown in Figure 5.25. Where a tooth fully faces the magnet, the field lines are generally short and perpendicular to both surfaces. Conversely, when a tooth faces the edge of a magnet, the flux lines appear to stretch out, rather like elastic bands, illustrating the alignment torque.

When the rotors are in motion, the combined effects of stable and unstable positions manifest themselves as a continuous torque ripple which is superimposed upon the

electromagnetic torque developed by the machine. The ripple is known as cogging torque and it is detrimental since it causes uneven motion, resulting in vibration and associated noise and loss. Also, the resistance to rotation may prohibit the use of the generator in applications with low staring torque; the cogging torque may even be so large as to overpower the total electromagnetic torque developed, rendering the machine useless.

Alternatively, it is possible to consider this effect in terms of a modulation of the excitation field resulting in extra high frequency harmonic components. In addition to the mechanical effects described, this may result in extra eddy loss in both the magnet and the stator. As was shown in section 5.6.2, these harmonics also pervade the flux density and EMF waveform, and would similarly cause loss in the eventual electrical output of the generators.

5.8.2. FEA calculation of cogging torque in the slotted version

In order to gain a feel for the magnitude of cogging torque present in the slotted machine under consideration, the 2D dynamic FEA model of the machine with 2 slots per pole per phase was analysed. With the rotor in a range of static positions, the Maxwell Stress in the air-gap resulting from the permanent magnet excitation alone was evaluated across a single pole. As might be expected, the force is cyclical, having a period covering the dimension of a slot pitch. The model consists of only a single rotor with half a stator and the tangential force per pole resulting from this cogging effect is illustrated, Figure 5.31.

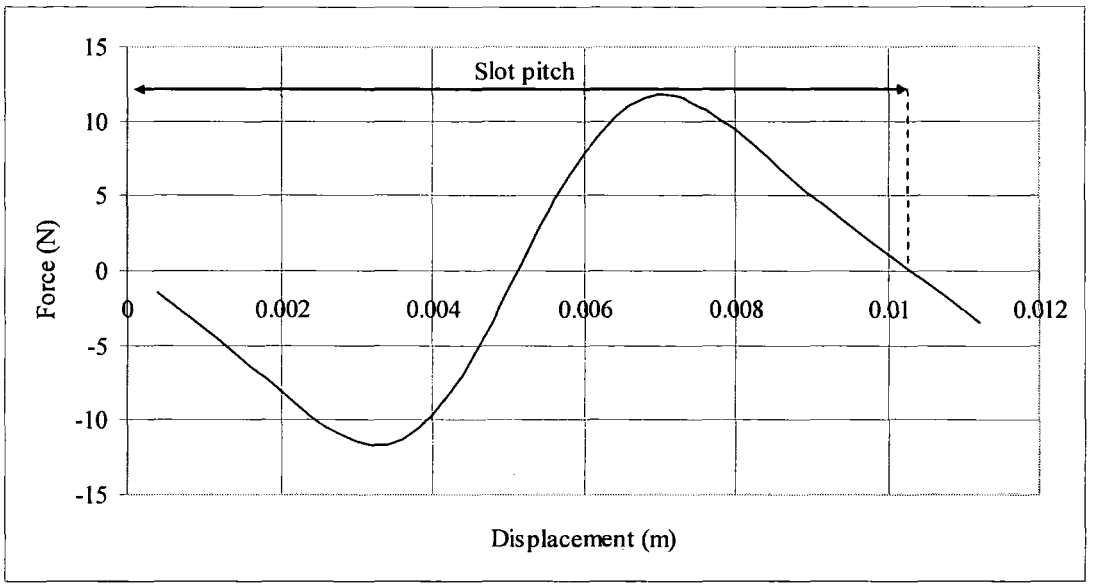

Figure 5.31: Tangential cogging force per pole per side (2 slots/pole/phase machine)

With 2 sides, 16 poles, and a mean radius of 0.158m, this indicates a peak cogging torque of 61Nm. The TORUS rating of 40kW at 4500RPM indicates the development of an electromagnetic torque of 85Nm. Clearly, the cogging torque ripple is of a similar magnitude to the electromagnetic torque; this is unacceptable. Owing to the dimensions of the slots, it is expected that the 1 slot machine would exhibit cogging torque of a higher magnitude with a longer period.

5.8.3. Reduction of cogging torque

A number of proven methods exist for the elimination of slot harmonics in axial flux machines, [86], usually implementing some form of relative skew between the two sides of the machine either by introducing offset between the rotors, or between the slots on either side of the stator. Offsetting the slots could make the winding process difficult and so it is envisaged that offsetting the rotors would be the easiest approach.

Rotor skew was modelled by considering both sides of the machine and altering the position of the magnets on one side such that the cogging torque contributed by the two sides cancel each other to some extent resulting in a smoothing effect. The skew required for this effect is equal to half the length of the cogging torque wave itself, and is therefore equal to half a slot pitch. The cogging torque characteristic will generally not be an exact sinusoid and cannot be fully eliminated by this cancellation process. Figure 5.32 shows the results for the 2 slots/pole/phase variant, namely a force (cogging torque) reduction of 75%.

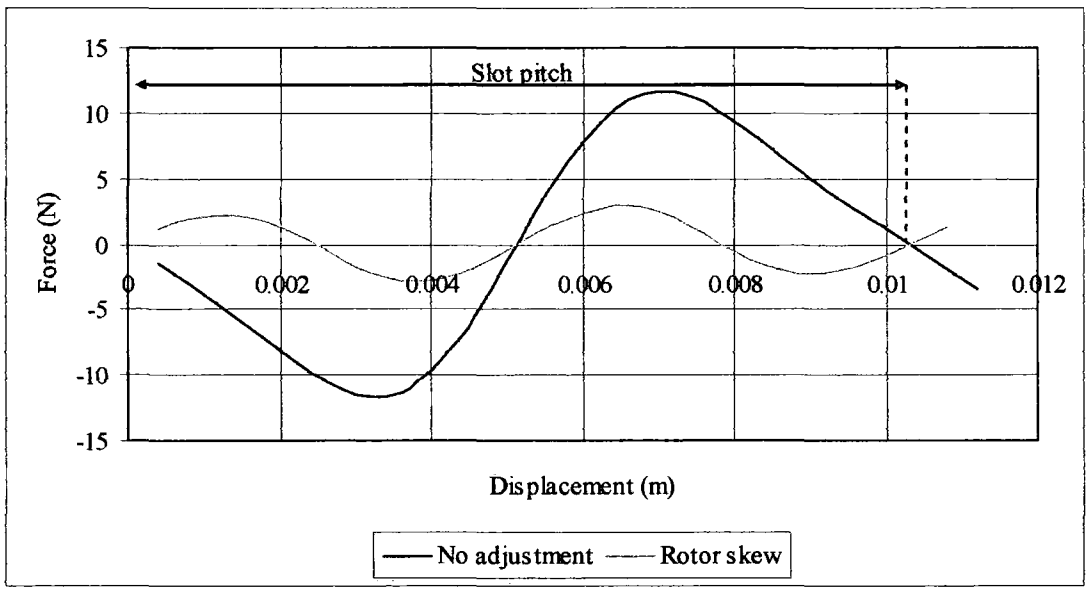

Figure 5.32: Cogging force per pole per side showing the effect of rotor skew

The resultant peak cogging torque is 15Nm, still a significant proportion of the total electromagnetic torque of 85Nm (18%). However, it must be remembered that this FEA is carried out in 2D under the assumption that the full magnet and slot edges are parallel in the radial dimension of the machine. This need not be the case: another relatively simple way to reduce cogging torque would be to shape the magnets such that the edges are not parallel with the slot edges; this approach is analogous to skewing the rotor bars of an induction motor. Furthermore, optimisation of the

dimensions of the magnets and slots has also been shown to help minimise cogging, [86], as has the use of powdered iron wedges to close the slots after winding. Iron powder composite teeth that attach onto the strip wound core have also been investigated, [85]. The teeth have a relative permeability of around 5, but have been shown to increase the electromagnetic torque considerably without introducing large amounts of cogging torque. Increasing the permeability of the teeth further is predicted to increase cogging torque but have a decreasing effect on electromagnetic torque; hence a relative permeability of 5 is thought to be an optimum value.

With the open slots specified at this stage of machine design, some cogging torque is likely to be present, but the modelling described above shows that much of it can be reduced by the relatively simple approach of rotor offset. Skewing the magnet edges and taking care over the specification of the magnet and slot parameters to avoid inherently stable positions could also be applied to the design without much difficulty. The conclusion drawn at this stage is that cogging torque can be a problem, and it is something the designer of such machines should keep in mind, but that it can be easily minimised in this type of machine.

5.8.4. The effect of cogging torque on the induced EMF

The same 2-sided dynamic modelling was used to predict the EMF with rotor skew for both slotted machines, and compare the results with those obtained without skew. Rotor skewing evidently attenuates the EMF slightly, giving a fundamental RMS value of 134.6V per phase compared with 139.1V before skewing for the 1 slot type, with 135.7V reducing to 134.8V for the 2 slots; the difference is more marked in the 1 slot/pole/phase machine on account of the greater skew angle required. However, both variants show a markedly improved waveform with rotor skew.

a)

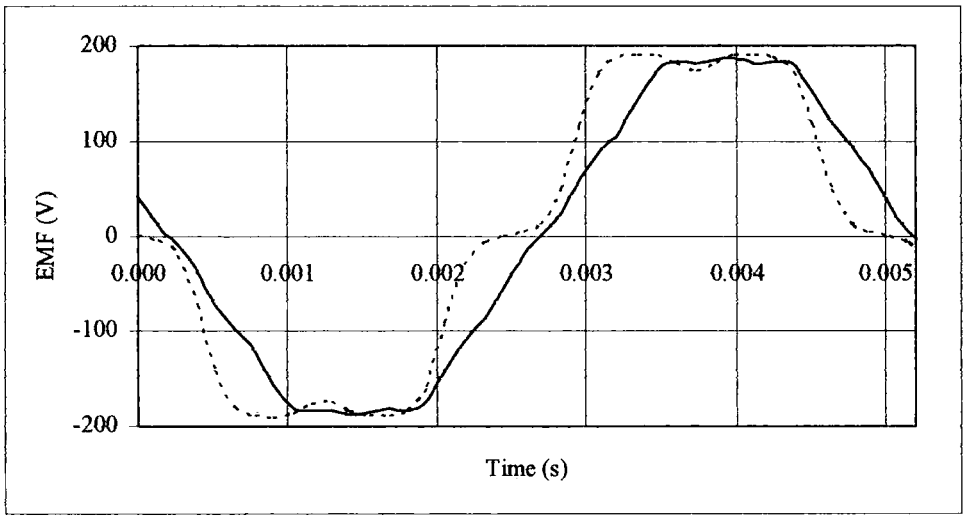

b)

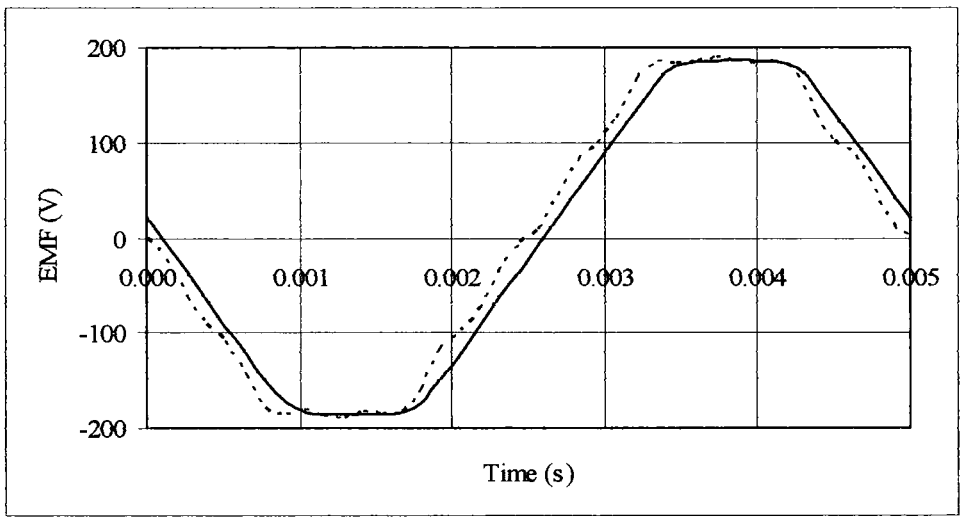

Figure 5.33: EMF prediction for 1500RPM with rotor skew (solid line) and without (dashed line) for a) 1 slot/pole/phase, and b) 2 slots/pole/phase

5.9. Thermal FEA of the TORUS and slotted versions

The aim of the investigation of the slotted variants so far has been to increase the magnetic loading above that of the TORUS whilst maintaining the already high electric loading. The air-gap winding of the TORUS is well cooled since the conductors sit in a stream of forced air cooling brought about by the natural pumping action of rotating discs and enhanced by the paddle-like presence of the magnets. Burying the conductors in slots will reduce this cooling effect and, whilst the design

aim was to keep the electric loading high, some reduction in electric loading will be necessary and is quantified here.

Strand7, [94], was used in section 4.6 and shown to give predictions of the thermal behaviour of the TORUS that agreed reasonably well with the simple analytical method. A 2D model of one coil pitch taken at the mean radius was constructed here for similar analysis of the slotted variants. Again, the rotors were ignored and all the heat dissipation was assumed to occur between the stator and the outside air according to the coefficient $h = 150W/m^2/^oC$ obtained by Spooner and Chalmers [5], and the windings were assumed to be the only sources of heat loss. The resulting meshes are shown, Figure 5.34, and Table 5.8 shows the material properties used in the model.

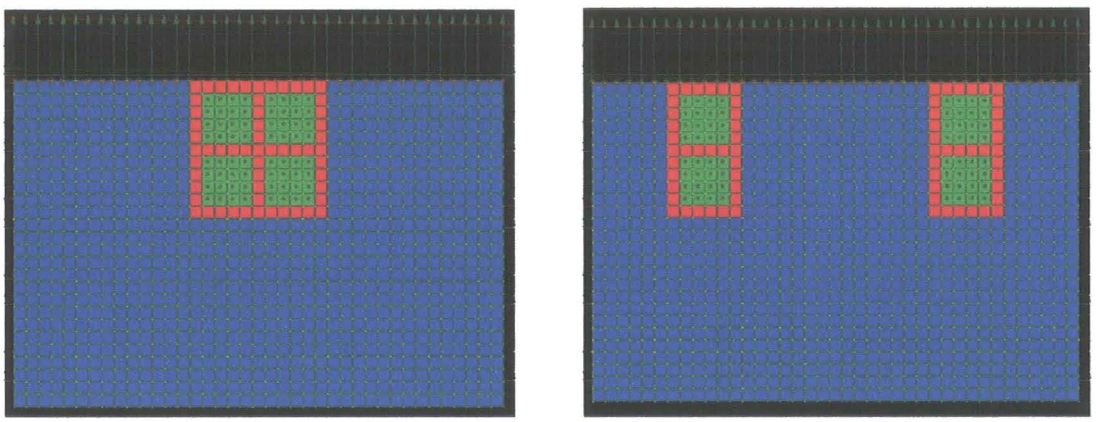

Figure 5.34: Heat transfer meshes of slotted machines

Component	Colour	Material	Thermal conductivity ($W/m^2/^oC$)
Stator	Blue	Steel	150
Conductor	Green	Copper	380
Insulation	Red	Nomex tape	0.5

Table 5.8: Materials used in the thermal FEA

The solution was obtained for the same heat source power density as the TORUS, and then the heat source was reduced gradually by trial and error until the solution a temperature rise of around 140°C as specified by the TORUS design. It should be noted that an ambient temperature of 20°C was set in these models, so solutions show temperatures in excess of 20°C (ambient) + 140°C (rise) = 160°C. The resulting solutions are shown, Figure 5.35.

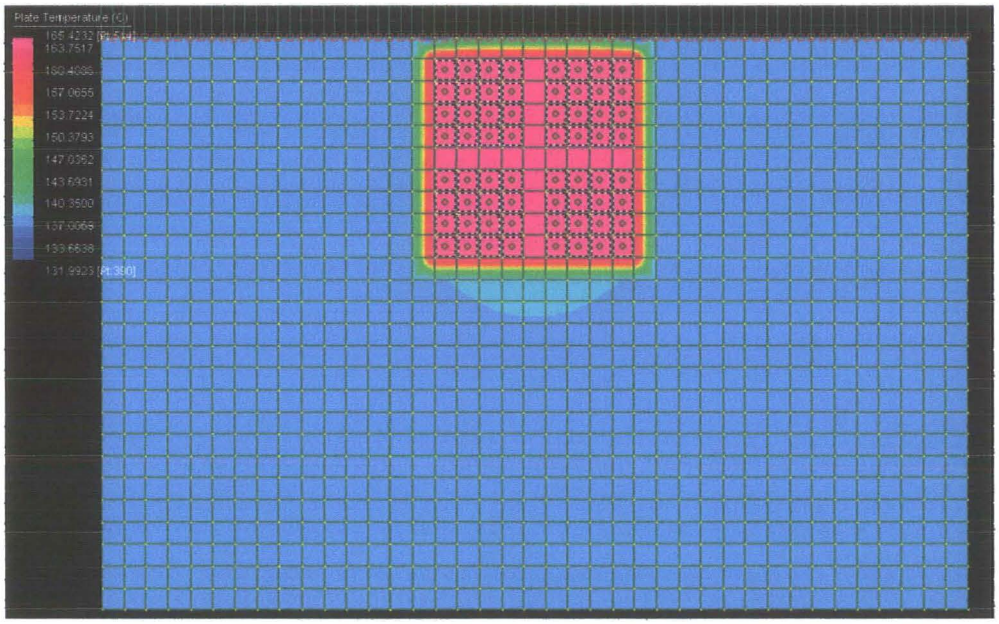

a)

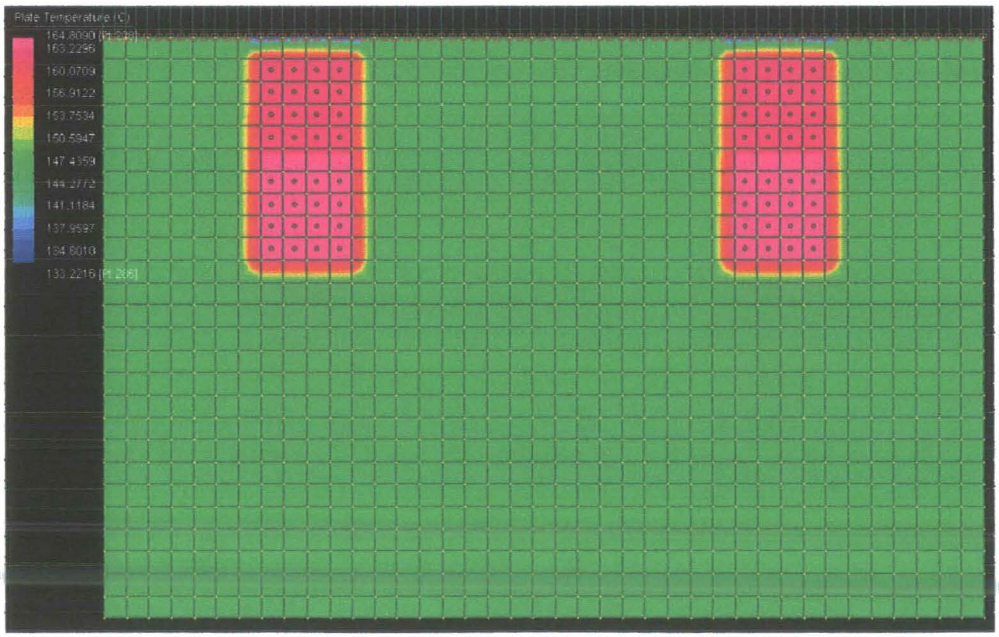

b)

Figure 5.35: Temperature contours from thermal FEA: a) 1 slot/pole/phase, b) 2 slots

The information yielded by this analysis is now used to estimate the allowable current in the slotted machines based on that allowed in the TORUS. Firstly, the ratio between the magnitudes of the power loss densities allowable in the windings of the TORUS and slotted variants for a given temperature rise is defined:

$$k_{loss} = \frac{P(/m^3)_{slotted}}{P(/m^3)_{TORUS}} \qquad \text{Eq. 5.62}$$

Since it is assumed that the majority of the heat is generated by I^2R loss in the winding, the power loss density is assumed to be proportional to the square of the current. Hence the allowable current in the slotted machines is related to that in the TORUS by:

$$I_{slotted} = \sqrt{k_{loss}} I_{TORUS} \qquad \text{Eq. 5.63}$$

Given that the current rating of 62.11A in the TORUS was equivalent to an allowable specific loss of 27.4MW/m^3 in the stator, the current ratings of the slotted variants can be approximated by the above method, and the results are given below:

	Allowable specific loss (MW/m^3)	**k_{loss}**	**I_{rated} (A)**
TORUS	27.4	1	62.11
1 slot/pole/phase	21.5	0.88	58.26
2 slots/pole/phase	22.5	0.91	59.25

Table 5.9: Calculation of approximate rated current

5.10. Performance prediction

In summary, this chapter has so far considered two slotted variants of the original 40kW TORUS machine. The analytical techniques described for the TORUS have been modified to be applicable to slotted machines; the predictions have been verified using a range of electromagnetic FEA techniques which had previously been benchmarked alongside analytical methods and experimental results for two

prototype TORUS machines. FEA has also been used to investigate the effects of rotor skew on cogging torque and the open-circuit EMF waveforms of the slotted variants, and some thermal FEA has yielded an approximation to their current rating. The parameters required for equivalent circuit analysis of all three machines are now available and are show in Table 5.10 for operation at 4500RPM.

	TORUS	**1 slot**	**2 slots**
E (V)	229	390	378
R (Ω)	0.17	0.17	0.17
X_{syn} (μH)	0.317	0.590	0.536
I_{rated} (A)	62	58	59

Table 5.10: Equivalent circuit parameter for the TORUS and slotted variants

Efficiency calculations are inappropriate at this stage given that sources of loss other than the I^2R effect have not yet been considered in the case of the slotted variants. However, simple equivalent circuit analysis allows computation of a load line assuming unity power factor, and the per-phase terminal voltage at the TORUS rated of 4500RPM, shown in Figure 5.36 and Figure 5.37.

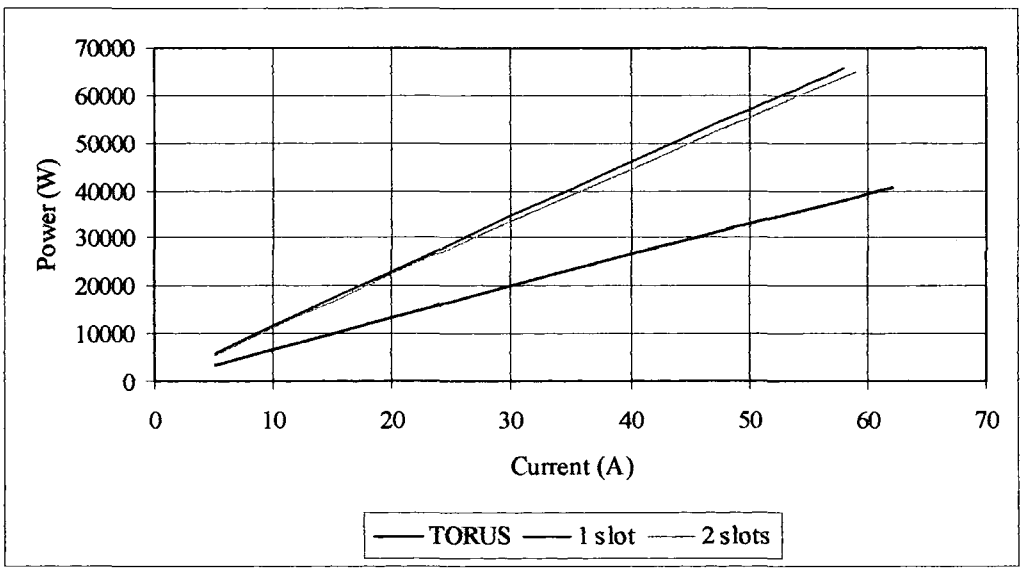

Figure 5.36: Predicted power against current comparison at 4500RPM

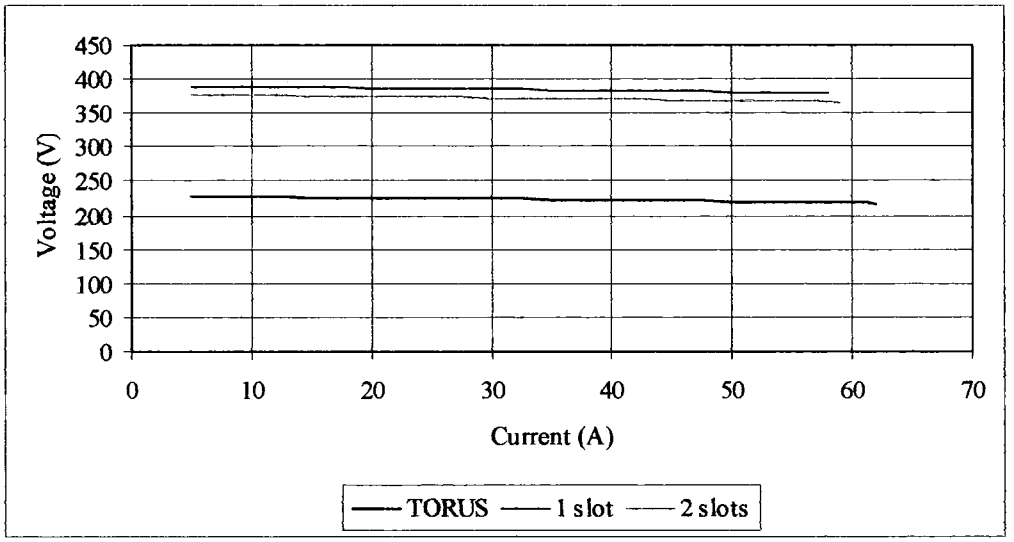

Figure 5.37: Predicted terminal voltage against current comparison at 4500RPM

Clearly, the slotted variants are predicted to produce significantly more power output, owing principally to the increased open circuit EMF afforded with a relatively small drop in the current rating. The power ratings for both slotted machines are in the region of 65kW compared with 40kW in the case of the TORUS, indicating an increase of over 60%. This is slightly different to the 70% increase in EMF itself; the difference being attributable to the slight reduction in current rating, as well as the increased synchronous reactance causing slightly more voltage regulation in percentage terms. However, the magnitudes of the synchronous reactance of the slotted variants are still small when compared with conventional machines and the resulting voltage regulation is low, indicating that the slotted variants are still electrically stiff.

One final comparison takes the added back iron required by the slotted variants into account. The power density is defined as the power per unit volume of the respective machine, where the critical parameters are the outer diameter of the rotors and the axial distance between the outer faces of the rotors.

The rotor diameter in all three cases is 0.410m but the axial lengths differ, with the TORUS having a length of 0.075m and the 1 and 2 slots/pole/phase variants having lengths equal to 0.084m and 0.085m respectively. Hence the power densities are as shown in Table 5.11.

	Power density (kW/m^3)
TORUS	4040
1 slot	5951
2 slots	5793

Table 5.11: Power density comparison

The slotted variants exhibit an increase in power density of less than 50%, and this comparison is somewhat harsh on the TORUS machine given that the stator core thickness is somewhat higher than the calculated requirement for the reasons set out in section 5.4.4.

The results of this investigation so far suggest that slotted machines are capable of generating up to 50% more power per unit volume than the air-gap wound TORUS. The trade-off against this increase is that slotted machines are more complicated and thus more difficult and potentially more expensive to make. Also, some cogging torque is likely in slotted machines, as is the existence of harmonics in the output.

This is based on a like for like comparison involving slight modification of a TORUS machine, which is clearly not the most advantageous design procedure. Also, calculation of loss and thermal modelling of the slotted variants was very limited. Chapter 6 concludes this investigation of slotted machines by developing an independent design approach for slotted machines and producing a 40kW design for comparison with the TORUS.

5.11. Discussion

In this chapter, the analytical methods and FEA techniques developed and benchmarked alongside the results of experimental tests were extended to the design of an axial flux generator with a slotted winding.

In order to facilitate as close a comparison with the air-gap wound TORUS as possible, this study commenced by devising two slotted variants of the 40kW prototype TORUS described in Chapter 4. These variants had the same specification and geometry as the TORUS as far as possible, with the exceptions that the winding was placed in slots and the back-iron specification was increased to cater for the increased flux levels. This approach enabled the analytical approaches to be extended to slotted machines in a straightforward manner, and detailed FEA was used to check the analytical methods and quantify the assumptions made.

Although the two slotted variants resulted in three designs that could be closely compared and were helpful stages in extending the analysis to slotted machines, this design approach was far from optimal. The results indicated that slotted machines were capable of achieving much higher power densities than the TORUS by way of an increased magnetic loading. However, the TORUS winding specification severely constrained the design of the slotted machines; whilst the electric loading was predicted to be only slightly diminished in the slotted machines owing to the poorer cooling characteristics, it was thought that the benefits of slotting were not nearly realised by this approach, particularly with regard to the electric loading. Chapter 6 thus contains an original design approach to a slotted machine which gives significantly more freedom in the specification.

Chapter 6. Design of a 40kW generator with a slotted stator winding

In this final part of the investigation of slotted axial flux machines a new design for a 40kW, 4500RPM prototype machine is drawn up for comparison with the 40kW TORUS prototype of Chapter 4. The previous work concerning slotted variants of the basic TORUS machine is utilised, but a more independent design procedure is used. Furthermore, analytical expressions for the loss mechanisms in the new slotted design are derived along with a more sophisticated thermal model so that the entire design process can be carried out using analytical methods which may be implemented in a spreadsheet.

The major departure from the previous work in the case of this new design is that the winding is a *"mush"* winding, i.e. narrow-gauge wire is specified and the number of turns depends upon the cross-sectional area of the slot and a specified fill-factor. This approach gives a much more favourable fill-factor than the TORUS winding with its thick conductors comprising twisted strands and layers of insulation. The number of turns increases, resulting in a reduced current rating and increased voltage and reactance parameters.

In Chapter 4 the analytical methods derived for the TORUS were shown to agree well with FEA and the results of experimental tests, and in Chapter 4 the extension of these methods to the slotted variants of the TORUS was shown to give results comparable with FEA predictions, hence this design procedure is carried out solely from an analytical perspective. A general design procedure for slotted machines is developed and a new design for a slotted 40kW machine is drawn up. Rather more

freedom is taken in the process so that the result is a new design as opposed to a rough modification to an existing machine. In this way, slotted machines can be more fairly assessed, and the chapter concludes with a comparison between the 40kW TORUS design and the new 40kW slotted design, utilising the analytical methods verified in Chapter 4 to arrive at performance predictions.

6.1. General design of axial flux machines: approximate sizing

Since this new design is not based on an existing machine or set of parameters, an approximate sizing procedure is first outlined which uses a derivation of the electromagnetic torque developed by a generalised axial flux machine. The basic torque production mechanism is considered by analysis of the Lorentz force in terms of the magnetic and electric loadings present in a generalised axial flux toroidal generator. Considering the arrangement shown in Figure 6.1, current carrying conductors in a region of magnetic flux experience a Lorentz force given by:

$$F = Bil \qquad \text{Eq. 6.1}$$

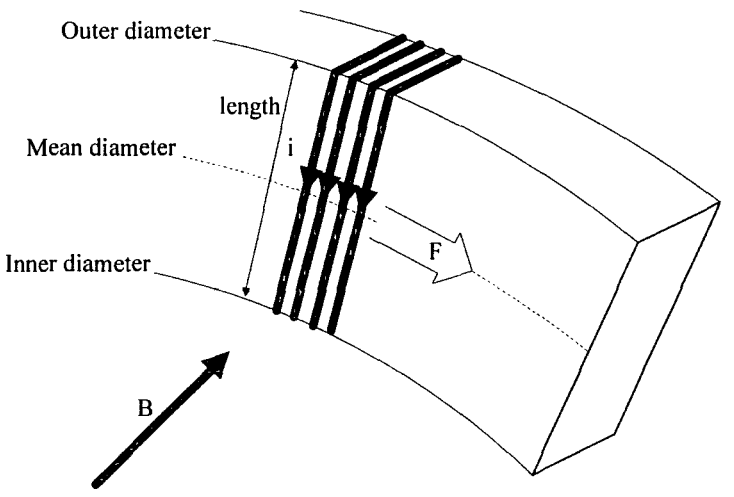

Figure 6.1: Lorentz force arrangement

Here, i represents the total current, such that an array of conductors has a linear current density (electric loading) at the mean diameter:

$$A = \frac{i}{\pi D_m} \qquad \text{Eq. 6.2}$$

Rearranging for current and substituting into Eq. 1.1 gives:

$$F = BA\pi D_m l \qquad \text{Eq. 6.3}$$

Noting that $(\pi D_m l)$ is the active area of one side of the stator, the conductors experience a force per unit area, or a shear stress:

$$\sigma = BA \qquad \text{Eq. 6.4}$$

If B and A are assumed to be sinusoidal distributions in space, both in phase and having the same frequency:

$$\sigma = \hat{B}\hat{A}\sin^2\theta \qquad \text{Eq. 6.5}$$

The mean shear stress is then:

$$\overline{\sigma} = \frac{1}{\pi}\int_0^{\pi}\hat{B}\hat{A}\sin^2(\theta)d\theta = \frac{\hat{B}\hat{A}}{2} = \frac{\hat{B}A_{RMS}}{\sqrt{2}} \qquad \text{Eq. 6.6}$$

This shear stress acts over the active area of the machine, which is defined here as the two main faces of the stator cores, given:

$$a = \pi D_m(D_o - D_i) \qquad \text{Eq. 6.7}$$

Hence the resultant force:

$$F = \overline{\sigma}a = \frac{\hat{B}A_{RMS}}{\sqrt{2}}\pi D_m(D_o - D_i) \qquad \text{Eq. 6.8}$$

And the torque:

$$T = \frac{\hat{B}A_{RMS}}{\sqrt{2}}\frac{\pi D_m^2(D_o - D_i)}{2} \qquad \text{Eq. 6.9}$$

Consideration of the rotational speed finally yields the power output:

$$P = \frac{\hat{B}A_{RMS}}{\sqrt{2}}\pi^2 D_m^2(D_o - D_i)\frac{n}{60} \qquad \text{Eq. 6.10}$$

Campbell, [13] described a similar machine and optimised the ratio between the inner and outer core diameters. A ratio of $\sqrt{3}$ gives the maximum power from the winding where the conductors are essentially radial. If this ratio is assumed constant in the design process, the active area can be expressed:

$$a = \frac{\pi D_o^2}{3} \qquad \text{Eq. 6.11}$$

Hence also the power can be given in terms of the outer diameter:

$$P = \frac{\hat{B}A_{RMS}}{\sqrt{2}} \frac{\pi^2 D_o^3 (1+\sqrt{3})}{6\sqrt{3}} \frac{n}{60} \qquad \text{Eq. 6.12}$$

Eq. 6.12 is important since the power is expressed in terms of the magnetic and electric loadings, the speed of rotation, and the diameter of the machine. It is interesting to note that the power output of an axial flux machine increases with the cube of diameter. This is the fundamental difference between axial and radial flux machines. The active area of a radial flux machine depends on the diameter and the axial length of the machine; hence the power output is proportional to the axial length and the square of the diameter. In the case of an axial flux machine, the power output has a reduced dependency on axial length and a heavier dependency on machine diameter. Two important corollaries of this are that a small increase in the diameter of an axial flux machine yields a large change in the power output, and that a short axial length is a natural feature of this machine which steers its design and application. Eq. 6.12 is used here as a rough sizing tool, since values of magnetic and electric loading obtained from experience can be combined with a required power and speed rating to yield an outer diameter, given:

$$D_o = \sqrt[3]{\left(\frac{60\sqrt{216}P}{\hat{B}A_{RMS}\pi^2(1+\sqrt{3})n} \right)} \qquad \text{Eq. 6.13}$$

The magnetic loading tends to be quoted as the peak value of the first harmonic, and the electric loading as an RMS value. In air-gap wound machines, the work in

Chapter 4 indicates that the magnetic loading is typically of the order of 0.5T and electric loadings as high as 14kA/m can be achieved. The conductors are only approximately radial in real machines, hence their spacing is restricted by the inner radius and the shape of the resultant arrangement of conductors in the main winding region is rectangular; this is true for slotted and air-gap windings. Therefore, the electric loading varies with radius and the value at the mean radius is used for these calculations unless stated. For the 40kW, 4500RPM specification, application of Eq. 6.13 with the assumed values of magnetic and electric loadings described above indicates a machine outer diameter of 0.373m. Hence the inner diameter:

$$D_i = \frac{D_o}{\sqrt{3}} \qquad \text{Eq. 6.14}$$

Also the mean diameter:

$$D_m = \frac{(D_o + D_i)}{2} \qquad \text{Eq. 6.15}$$

This could be used as the rough basis for a design and makes a good comparison with the actual design of the 40kW prototype analysed and tested in Chapter 4: that machine has a stator core outer diameter of 378mm, although the ratio of $\sqrt{3}$ between the core diameters was not strictly adhered to in the design. This is because the actual power output of a real machine may have a pronounced non-linear dependency on the inner and outer core diameters, depending on the nature of the winding. In the case of the 40kW prototype air-gap wound machine, the conductors are formed from twisted strands and are hence quite thick. This gives a low number of turns, and a small increase in the inner diameter may facilitate the inclusion of an extra turn and would therefore result in a step change in the power output. Similarly, reducing the inner diameter slightly may not reduce the turn number but would increase the active area. In short, the ratio of $\sqrt{3}$ is a good starting point but does not necessarily yield the optimum design.

6.2. The design procedure

6.2.1. Outline design

In this and the following sections, aspects of the design are discussed and demonstrated so as to complement the analytical methods described in Chapter 4. During the course of this research, these methods were incorporated into a MS Excel spreadsheet-based design program which allowed variation of the parameters and thus facilitated the genesis of a number of designs. Hence the tools for design and analysis take the form of generalised equations which are linked together by certain key parameters now described. The spreadsheet calculations are presented in Appendix 2.

The design process thus begins with the power and speed rating and some assumed values of magnetic and electric loadings. This is converted to a rough diameter, as described in the previous section, which forms the basis of the design. Following a number of initial design decisions, a more detailed geometry emerges. The stator winding is then specified and this sets the geometry sufficiently for the flux density calculations to be carried out. Analysis of the field arising from the permanent magnets allows for the rotor and stator sizing and the calculation of induced EMF. Analysis of the field arising from current in the winding facilitates calculation of the synchronous reactance. Since the stator size has now been fully specified, the length of the conductors and thus the phase resistance can be determined. Finally, the losses are calculated and some thermal modelling is carried out. Thermal analysis yields a total allowable power loss for a specified temperature rise based on ambient conditions and material properties. The iron losses and the conductor eddy losses are first calculated, since these do not depend on current, and subtracted from the total to leave a remaining loss allowance; this is allocated to I^2R loss. Since the resistance is

known, the rated current can be determined. The previously defined calculations are thus performed in order to calculate the equivalent circuit parameters. The actual magnetic and electric loadings emerge from this analysis and may be iterated as required. This occurs alongside some further design optimisations to result in a finalised design which may be modelled for the prediction of the performance of the design. Figure 6.2 illustrates this outline design process.

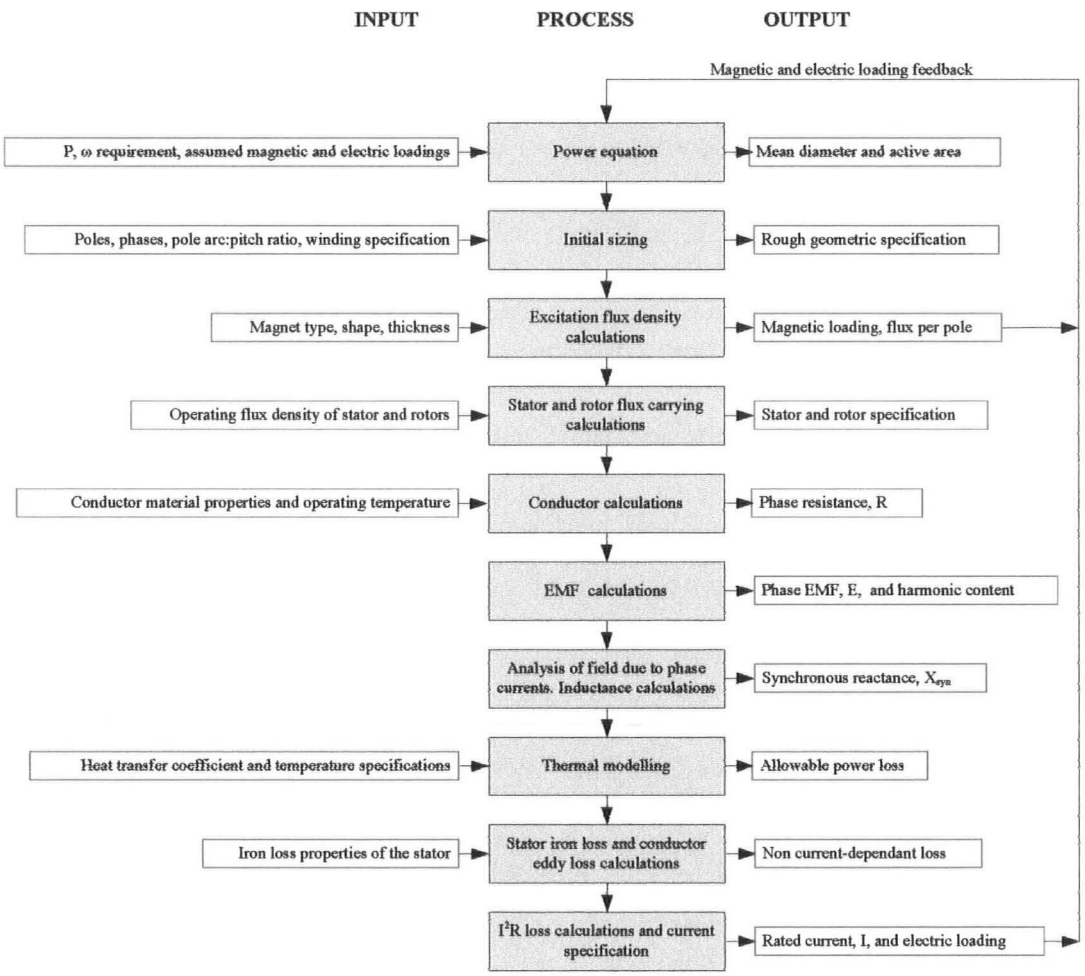

Figure 6.2: Outline design procedure

6.2.2. Initial design decisions

A number of further design decisions which must be made before the design can be specified in more detail are discussed here. Since a spreadsheet design approach was specified, these parameters can all be modified within the spreadsheet at a later stage,

as can the speed/power ratings and the ratio between the inner and outer core diameters.

The number of phases is a fundamental concern. As a generator, the permanent magnet axial flux machine operates like a synchronous machine and hence requires a polyphase winding. The winding is distributed and a large phase number coupled with many poles may result in an unrealisable winding design. Otherwise, the decision concerning phase number is unrestricted, but the standard 3 phases are used here.

The choice of pole number is similarly important and there are two main concerns. Firstly, the shape of the magnets is an important consideration since high performance permanent magnet material can be costly, particularly where unusual shapes or aspect ratios are required. Small pole numbers result in large, unwieldy, and expensive magnets, whereas large pole numbers could require odd aspect ratios that are expensive and perhaps impossible to manufacture. Magnets purchased in small quantities are often cut from square or rectangular section, and therefore magnets with aspect ratios close to 1:1 would make good use of the material and be simple to make. One design approach is to aim for a pole pitch equal to the active length, i.e. half the difference between the inner and outer diameters. A further consideration is that the rotor and stator iron must be sized according to the flux carrying requirement. The flux per pole could be large where small pole numbers are used, resulting in a large axial length. This goes against the advantages and very nature of these machines and so is avoided. In some cases, an axially short machine can result in a bearingless design where the rotors of the generator are simply cantilevered from the existing prime-mover bearing.

For medium to high speed applications, high pole numbers result in high output frequencies which may impact upon the power electronics interface where used. At the very high end, the frequency could be prohibitive, but up to a certain point this is not a concern and the devices required for smoothing at higher frequencies will be smaller hence advantageous. Choice of pole number is a balance between the issues described and is best chosen from experience and iteration of the design procedure. 16 poles are chosen as an appropriate starting point here.

The pole arc to pole pitch ratio is also specified at this stage. The main impacts of this choice are the air-gap flux density waveform and the level of inter magnet leakage flux. Since the permanent magnets have permeability similar to that of free space, the effective air-gap of the machine is large. Larger pole arcs will increase the harmonic presence and the inter magnet leakage; smaller pole arcs will increase the harmonic presence and make poor use of space. These effects will depend on the type and dimensions of the magnet, the amount of running clearance required and the dimensions of the air-gap winding. In this slotted design the flux density profile is likely to be square owing to the reduced air-gap and so a ratio of 0.66 is specified since a pole arc of $120^{o}_{electrical}$ yields no 3^{rd} harmonics.

One final point on the construction of a slotted stator concerns the nature of the end-windings. Since the core is strip-wound, it would be impossible to slot the end-windings as well as the main winding regions since this would break the continuity of the strip. Therefore, the resulting core structure assumed for this design study has slotted main winding regions and air-gap wound end-winding regions. The effective length of a flux path linking the end-winding will now be significantly longer than one linking the main winding owing to the slotted nature of the machine. Hence

designing the magnets to overhang the core ends is likely to be ineffectual and so exploitation of the end-winding regions by this method is not attempted in the design of slotted machines.

6.2.3. Winding design

The air-gap winding of the 40kW TORUS achieved a magnetic loading of 0.5T with an effective air-gap composed of roughly 6mm magnets, 6mm winding thickness and 2mm running clearance. The slotted structure effectively removes the conductors from this gap, hence reducing it by 43%. As a rough guide, it is assumed here that the magnetic loading increases accordingly in a slotted machine to approximately 0.7T. If the electric loading of the air-gap wound machine was to be maintained in the slotted machine, the increased magnetic loading alone would yield a new rough outer diameter of 323mm; a reduction of 13% on that of the air-gap wound machine. This may be at the expense of an increased axial length owing to the slot depth and the increased flux-carrying requirements of the rotor and stator, however. This result is not particularly encouraging given the increased complexity of a slotted machine.

As this study proceeded it became apparent that the winding used in the air-gap wound machine was an unfavourable choice in the case of a slotted machine. This is attributed to the poor fill-factor encountered with the thick conductors formed from twisted strands and the fact that the overall size of the conductor puts unwieldy limits on the number of turns that could be accommodated in a given slot, or the slot geometry required for a given number of turns. Also, slotted conductors are less susceptible to eddy loss since they are rather more shielded from the main field than those residing in the air-gap, and so the precautions taken in the design of the winding for the air-gap machine are somewhat excessive where slots are used. This

would be particularly true if semi-closed slots were specified, as may be the case at a later stage. Given the high pole number and correspondingly high electrical frequency, it would be prudent again to use narrow gauge conductors, but it is not as critical for the whole winding to be formed from twisted strands. Since the slots provide good location, a winding consisting of tightly-packed narrow gauge wire with as many turns as possible is a strong alternative; this arrangement is sometime called a *"mush"* winding. The principal advantage is the better use made of the available space enabling more copper to be packed into the machine. This is likely to result in a larger number of turns, but parallel-connected strands could still be used to control the voltage and current output as necessary.

There are a number of variables in the design of a suitable winding for this type of machine. The winding is assumed to take the form of toroidal coils, each of which is individually placed into a slot. Parallel slots in a toroidal stator make for trapezoidal teeth, and a tooth-to-slot ratio of 1:1 is often used in conventional machine design. In this case, the ratio is specified at the mean diameter and this means that the teeth will be wide at the outer diameter and narrow at the inner, making the inner section of the tooth a limiting factor in the design. Narrow teeth would be mechanically weak, difficult to manufacture and highly susceptible to saturation and so the teeth dimensions must be considered carefully. The 1:1 ratio is an obvious starting point and the core diameters are restricted somewhat by the application of Campbell's $\sqrt{3}$ coefficient, [13]; hence this strategy should result in sensible designs. The design of a *"mush"* winding is now described. The space available per slot is calculated and an assumed fill factor then specifies the number of turns.

Firstly, the tooth-to-slot ratio, k_{tooth}, is defined:

$$k_{tooth} = \frac{w_{tooth}}{w_{slot}} \qquad \text{Eq. 6.16}$$

The slot space available for conductors per pole per phase is:

$$w_{slots\_total} = \frac{\pi D_m}{mp(1 + k_{tooth})} \qquad \text{Eq. 6.17}$$

The width of an individual slot is thus:

$$w_{slot} = \frac{w_{slots\_total}}{n_{slots/pole/phase}} \qquad \text{Eq. 6.18}$$

The mechanical strength of the teeth at the inner diameter (their narrowest point) must be considered with particular reference to the manufacturing method. Milled cores will be less forgiving of narrow teeth than pre-punched cores. The individual tooth width at its narrowest is given by:

$$w_{tooth\_inner} = k_{tooth} w_{slot} \frac{D_i}{D_m} \qquad \text{Eq. 6.19}$$

The width of slot available for the conductors depends upon the thickness of the slot liner used:

$$w_{conductor} = w_{slot} - 2t_{liner} \qquad \text{Eq. 6.20}$$

Once the width of the slot is fixed, the slot depth can be altered by changing the aspect ratio of the slot, defined:

$$k_{slot} = \frac{d_{slot}}{w_{slot}} \qquad \text{Eq. 6.21}$$

The slot depth available for the conductors is:

$$d_{conductor} = k_{slot} w_{slot} - t_{insulation} \qquad \text{Eq. 6.22}$$

Unlike those of a radial flux machine these slots have a perfectly rectangular cross section and where open slots are used the fill factor is likely to be high.

A value of 0.7 is used here and the total area of conductor cross section is given:

$$a_{slot} = k_{fill} w_{conductor} d_{conductor} \qquad \text{Eq. 6.23}$$

The cross sectional area of the wire is:

$$a_{wire} = \frac{\pi D_{wire}^2}{4} \qquad \text{Eq. 6.24}$$

Hence the number of turns per slot with $n_{parallel}$ strands in parallel is given:

$$N_{slot} = \text{int}\left(\frac{a_{slot}}{a_{wire} n_{parallel}} \right) \qquad \text{Eq. 6.25}$$

The number of turns per pole per phase is then:

$$N = N_{slot} n_{slots/pole/phase} \qquad \text{Eq. 6.26}$$

Thus the full winding is specified by the tooth/slot ratio, the diameter of the machine, the number of slots per pole per phase, the slot depth/width ratio, the slot liner thickness, the wire diameter, and the number of parallel strands. The equations described above can easily be implemented in a spreadsheet or computer program and the parameters varied in search of an appropriate, optimal design.

As can be seen from the outline design procedure illustrated in Figure 6.2, once the power and speed have been specified, and the initial design decisions concerning poles, phases, pole arc to pole pitch ratio have been made, only the magnets are yet to be specified before the design equations developed in Chapter 4 can be implemented to flesh out the design and yield the equivalent circuit parameters. It has so far been assumed that this new slotted machine design will utilise a similar topology to the previous designs, with the main differences being a new winding specification and freedom of certain choices concerning the sizing and geometrical parameters. It is envisaged that the strip-wound core would remain the same with slots milled appropriately as described previously, at the prototyping stage at least.

Hence the rotor design is also similar, based on a solid steel disc with peripherally mounted trapezoidal permanent magnets, but the number of poles and the magnet geometry is now subject to design variation.

6.2.4. Losses and thermal modelling

With the analytical techniques described earlier in the chapter, and the initial design decisions described in sections 6.2.1 to 6.2.3, the stator and rotor geometries can be specified and the equivalent circuit parameters duly calculated. The next stage in the design procedure is the thermal modelling of the machine which, along with consideration of the loss mechanisms, facilitates calculation of the rated current. In keeping with the overall design approach, generalised equations which were used in a spreadsheet context are here derived for this aspect of the design.

So far in this thesis, quantitative consideration of loss in slotted machines has been confined to I^2R loss in the main winding conductors. A more detailed consideration of sources of loss in the TORUS was provided in Chapter 3 and is now extended to the slotted design under consideration. Once again, the total allowable loss is calculated from a thermal model and the non-current dependant losses are subtracted from this to leave a loss that is allocated to I^2R loss in the conductors. From knowledge of this and the phase resistance, the allowable (rated) current can be calculated.

The slotted machine has slightly more complicated heat transfer characteristics than the TORUS, and so an equivalent thermal circuit is derived here in place of the simplified assumptions concerning heat loss in the TORUS, which were described in Chapter 3. Since the conductors are in slots and only the top layer is directly exposed

to the external air-flow, the approach is revised to take the heat transfer paths through the teeth and stator core into account. This is more sophisticated than that used in the analysis of the air-gap wound machine, but a simple check can be performed by using the air-gap wound thermal model and assuming all the loss is transferred to the air via the slots. This is a worst-case scenario since it ignores the extra, parallel paths via the teeth but it is a useful check.

The loss mechanisms modelled in the slotted machine are described here. Firstly, I^2R loss originating within the conductors is again assumed to be the main source of loss. Eddy loss in the conductors is also likely to be present, owing to the potentially high frequency of the excitation field where large pole numbers are specified. Unlike the TORUS, not all the conductors will be exposed to the full field; those at the bottom of the slot will be much less susceptible to this and so the rough approximation that only half of the conductors in the main winding region experience this loss is used here. Finally, iron loss comprising eddy and hysteretic components originating in the stator core and teeth are considered. Since the teeth experience higher flux density levels than the back iron of the core, this of loss is separated into two components originating in the teeth and core according to the respective flux density levels.

The thermal model is obtained by considering a single pole on one side of the stator core. The analysis is carried out per metre of core length, assuming all the heat transfer to occur in the main winding region. Thus heat dissipation via the end windings is ignored, making this a conservative approach with some allowance for the approximate nature of this type of thermal analysis. The resultant model is shown in Figure 6.3 with the thermal equivalent circuit.

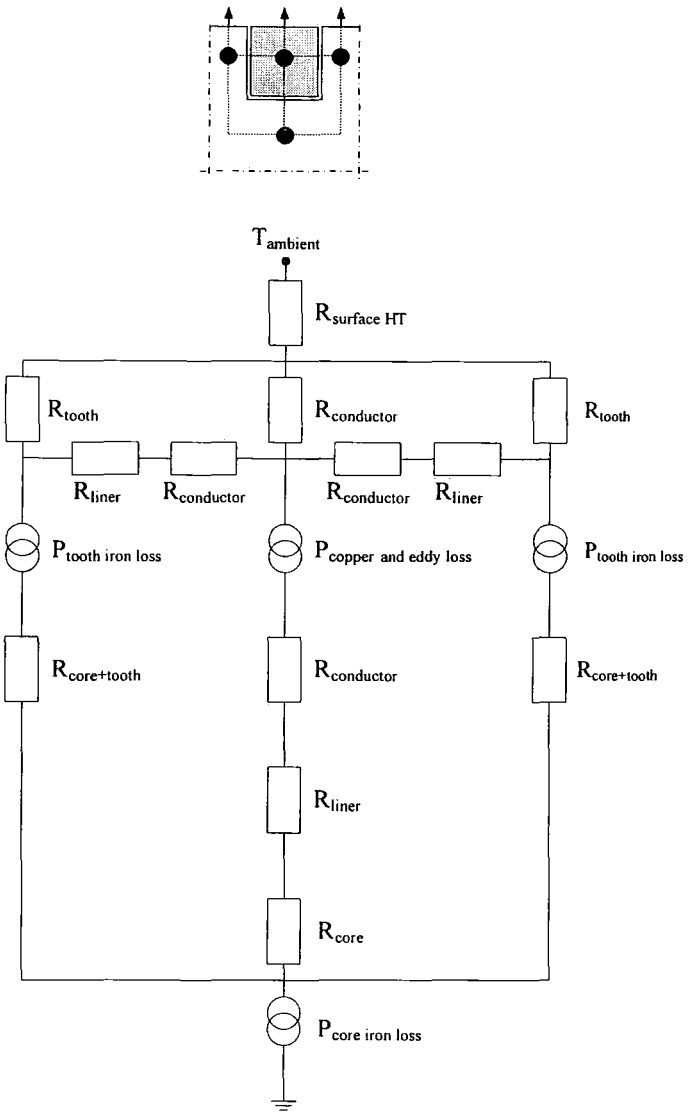

Figure 6.3: Thermal model of 1 slot and the equivalent circuit

Clearly there are four sources of power loss and a number of heat transfer routes. Each half tooth has an associated tooth iron loss and the core back has an associated core iron loss. The individual conductors are modelled by a copper mass in the slot having a lumped loss for I^2R and conductor eddy losses. Although the case of 1 slot/pole/phase is the simplest slotted arrangement, this circuit is quite complicated and can be simplified further. Firstly, the TORUS report indicated that I^2R and conductor eddy losses combined were an order of magnitude larger than the iron losses. Thus it is reasonable to place the source of all the loss in the slot region. In

the case of the slotted geometry, this underestimates the heat transfer path arising from the core back iron losses, but these are expected to be minimal compared with the tooth iron losses, owing to the larger flux density encountered there. Conversely, the heat transfer path of the tooth losses would be more resistive in the simplified model, which should more than compensate.

Also, the model can be reduced further by considering only half a slot and half a tooth. Symmetry in the structure indicates that tangential heat flux boundaries are present at the axial centre of the machine and at the centre of the slots and teeth. The reduced model and its circuit diagram are shown, Figure 6.4.

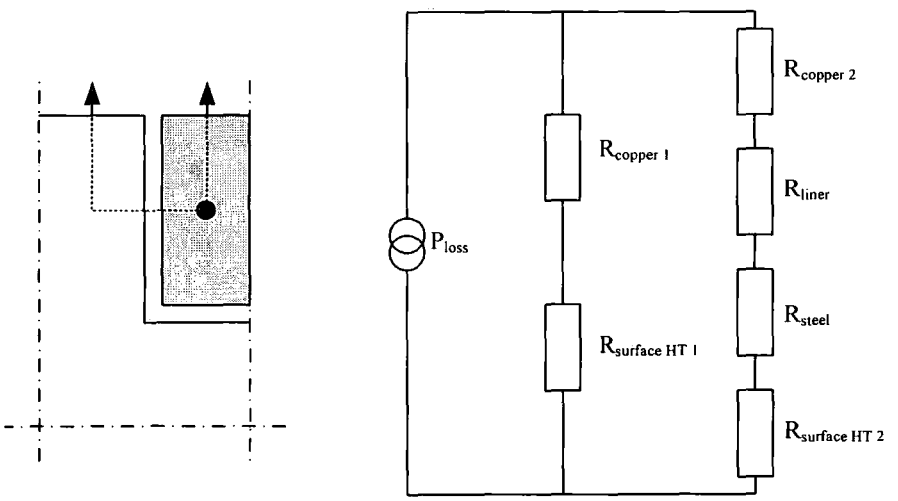

Figure 6.4: Simplified thermal circuit

The components of the thermal equivalent circuit are defined as: power loss, P_{loss} *(W)*, equivalent to a DC current source; temperature rise, ΔT *(°C)*, equivalent to a potential difference; and thermal resistance, R *(W/°C)*, equivalent to a resistance.

The standard equation for 1D heat transfer is given by Say, [96]:

$$\frac{\partial T}{\partial t} = \frac{k}{c_p \delta} \frac{\partial^2 T}{\partial x^2} \qquad \text{Eq. 6.27}$$

In the steady state, this can be expressed:

$$P = \Delta T k \frac{a}{x} \qquad \text{Eq. 6.28}$$

Comparing this with Ohm's law for an electrical circuit indicates that the thermal equivalent resistance is:

$$R = \frac{x}{ka} \qquad \text{Eq. 6.29}$$

The parameters that constitute this resistance are: the path length, x *(m)*; the surface area, a *(m^2)*; and the heat transfer coefficient, k *(W/m^oC)*. The calculations are performed in 2D, per unit core length into the page.

An effective thermal conductivity is approximated for the copper winding region. Considering a 1D path through the region, the length, x, is initially assumed to consist of copper and insulation in the ratio defined by the fill factor, k_{fill}:

$$x = x_{copper} + x_{insulation} = k_{fill} x + (1 - k_{fill}) x \qquad \text{Eq. 6.30}$$

Hence the 1D thermal resistances:

$$\frac{x}{k_{winding}} = \frac{k_{fill} x}{k_{copper}} + \frac{(1 - k_{fill}) x}{k_{insulation}} \qquad \text{Eq. 6.31}$$

Finally, the effective thermal conductivity of the winding:

$$k_{winding} = \frac{k_{insulation} k_{copper}}{k_{fill} k_{insulation} + (1 - k_{fill}) k_{copper}} \qquad \text{Eq. 6.32}$$

In practice, the space surrounding the copper is composed of insulation and air. Whilst the copper is fully defined, having a thermal conductivity of 390W/m.°C, the space will have a conductivity somewhere between that of air (0.03W/m.°C) and insulation (0.5W/m.°C) depending on their relative proportions. This allows the effective thermal conductivity of the winding to be specified between two limits, namely 1.66 (all insulation) and 0.10 (all air). In fact, empirical data from related

work carried out in the School of Engineering at Durham on the thermal properties of axial flux machines suggests a value of 0.5W/m.°C, [98]. This value falls between the limits calculated here and is therefore used for the remainder of the analysis.

A surface heat transfer coefficient of $h = 150W/m^2.^oC$ as obtained by Spooner and Chalmers for a similar machine [5] is applied to the main winding region, where the rotors effect good cooling by pumping air radially across the tooth and slot surfaces. Table 6.1 summarises the thermal constants used.

Material	Thermal constant
Winding (thermal conductivity)	0.5W/m.°C
Insulation (thermal conductivity)	0.5W/m.°C
Steel core (thermal conductivity)	150W/m.°C
Surface (heat transfer coefficient)	150W/m^2.°C

Table 6.1: Thermal constants

The individual resistances are approximated as follows.

$R_{copper\ 1}$: This represents the path through the conductors towards the air-gap. The length is roughly half the slot depth and the cross-section has an area that is roughly half the slot width per unit core length:

$$R_{copper\_1} = \frac{d_{slot}}{k_{winding} w_{slot}} \qquad \text{Eq. 6.33}$$

$R_{surface\ HT\ 1}$: This represents surface transfer from the slot to the air, having a cross-sectional area roughly equal to half the slot width per unit core length:

$$R_{surface\_HT\_1} = \frac{2}{h w_{slot}} \qquad \text{Eq. 6.34}$$

$R_{copper\ 2}$: This represents the path through the conductors towards the tooth; the length is roughly a quarter of the slot width and the cross-section has an area that is roughly the slot depth per unit core length:

$$R_{copper\_1} = \frac{w_{slot}}{4k_{winding}d_{slot}} \qquad \text{Eq. 6.35}$$

R_{liner}: This represents the slot liner thickness between the copper and the tooth. The length is set to t_{liner} and the cross-section has an area that is roughly the slot depth per unit core length:

$$R_{liner} = \frac{t_{insulation}}{k_{insulation}d_{slot}} \qquad \text{Eq. 6.36}$$

R_{steel}: This represents the path through the tooth steel. The length of a simplified path is equal to half the slot depth and a quarter of the tooth width, and the cross-section has an area of at least the tooth width per unit core length.:

$$R_{steel} = \frac{2d_{slot} + w_{tooth}}{2w_{tooth}k_{steel}} \qquad \text{Eq. 6.37}$$

$R_{surface\ HT\ 2}$: This represents surface transfer from the tooth to the air; the cross-section has an area that is roughly half the tooth width per unit core length:

$$R_{surface\_HT\_2} = \frac{2}{hw_{slot}} \qquad \text{Eq. 6.38}$$

The individual paths are series combinations of the above components:

$$R_{slot} = R_{copper\_1} + R_{surface\_HT\_1} \qquad \text{Eq. 6.39}$$

And:

$$R_{tooth} = R_{copper\_2} + R_{liner} + R_{steel} + R_{surface\_HT\_2} \qquad \text{Eq. 6.40}$$

The total resistance is a parallel combination of two paths: one via the slot, the other via the tooth. Hence:

$$R_{tot} = \frac{R_{slot} R_{tooth}}{R_{slot} + R_{tooth}} \qquad \text{Eq. 6.41}$$

The allowable power loss can then be deduced from the temperature difference between ambient and the allowable operating temperature of the materials, and this thermal resistance:

$$P_{half\_slot/tooth} = \frac{T_{\max} - T_{amb}}{R_{tot}} \qquad \text{Eq. 6.42}$$

Taking a whole slot/tooth unit into account and factoring in the number of slots/pole/phase, the number of poles and phases, and multiplying by the core length which is $(D_o - D_i)$ since there are 2 sides, gives:

$$P_{loss} = 2P_{half\_slot/tooth} n_{slots/pole/phase} pm(D_o - D_i) \qquad \text{Eq. 6.43}$$

Having obtained the total allowable loss, the non current dependant losses are calculated so that, when subtracted from the total, the I^2R loss remains from which the rated current may be deduced.

Firstly, the eddy loss of a single wire conductor is considered and then multiplied up by the number of parallel strands, half of the number of turns per slot, the number of slots per pole per phase, and the number of phases. The resistivity used is that defined earlier in this chapter at an appropriate operating temperature for the machine based on the material properties involved. A modified version of the equation derived from Carter, ([93], pp254-256), for the TORUS in Chapter 3 can thus be used:

$$P_{eddy} = \frac{N_{slot}}{2} n_{slots/pole/phase} mpn_{parallel} \frac{\pi}{4} \frac{d_{wire}^4}{16} \frac{\hat{B}_1^2 \omega^2}{\rho} (D_o - D_i) \qquad \text{Eq. 6.44}$$

Assuming use of the same strip wound stator core material as that specified for the TORUS, the expression for iron loss obtained by Bumby and Spooner [9], is used again. The core of the slotted machine is divided into the core back, where a working flux density of 1.4T was assumed in order to specify the stator thickness, and the teeth, where the flux density is calculated as follows.

The profile of the flux density arising from the magnets is approximately square, with a peak value given by according to the analysis described earlier in this chapter. The flux density in the tooth will vary with the width of the tooth over the core length, since the teeth are trapezoidal to allow for parallel slot edges. The mean tooth width is considered here, and the worst case flux level is applied. A tooth lying opposite the centre of a magnet pole will experience the highest level of axial flux density, represented by the peak of the square wave profile. It is assumed that this flux density is constant across a slot pitch, and that the resultant flux is carried by a single tooth. This situation is illustrated, Figure 6.5.

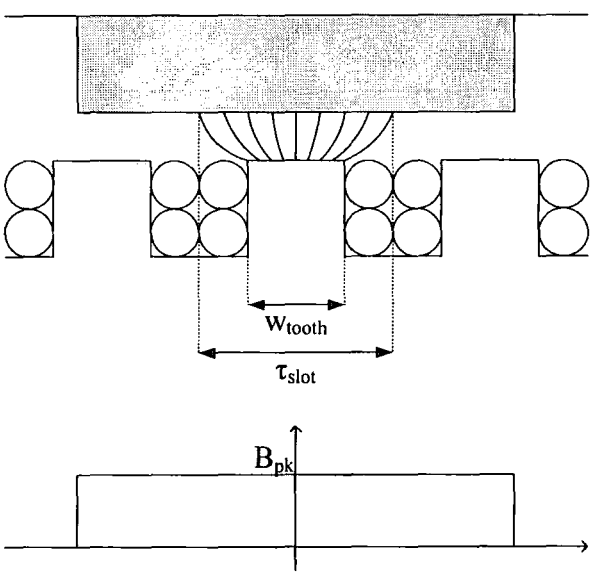

Figure 6.5: Tooth flux density

It is clear that the flux density in the tooth will be related to the axial flux density and the ratio between the tooth width and the slot pitch:

$$\hat{B}_{tooth} = \hat{B}\frac{\tau_{slot}}{w_{tooth}} \qquad \text{Eq. 6.45}$$

Observation of this parameter at the winding specification stage can aid the design process. Assuming saturation at around the 2T mark and ensuring the flux density in the teeth remains below this level, the slot width can be increased to incorporate more copper or reduced to diminish the iron losses in the teeth.

The total mass of the teeth and core components is given:

$$m_{stator} = m_{teeth} + m_{core} \qquad \text{Eq. 6.46}$$

Where:

$$m_{teeth} = \pi D_m \frac{k_{tooth}}{k_{tooth}+1}\frac{\left(D_o - D_i\right)}{2} 2 d_{slot} \rho_{core} \qquad \text{Eq. 6.47}$$

And:

$$m_{core} = \pi \frac{\left(D_o^2 - D_i^2\right)}{4} t_{core} \rho_{core} \qquad \text{Eq. 6.48}$$

Hence the total iron losses can be obtained as a sum of two components:

$$P_{iron} = \left[\frac{f_{elec}}{50}\right]^{1.32}\left(\left[\frac{\hat{B}_{tooth}}{1.5}\right]^{1.97} m_{tooth} + \left[\frac{\hat{B}_{core}}{1.5}\right]^{1.97} m_{core}\right) \qquad \text{Eq. 6.49}$$

Once the non current dependent losses have been calculated they can be subtracted from the total allowable loss returned by the thermal model to leave the I^2R loss from which the rated current can be deduced as described in Chapter 3. The current density facilitates a check of the thermal rating; a limit of $20A/mm^2$ is a good rough guide.

6.3. Design of a 40kW slotted machine

6.3.1. Initial design iteration

The above calculation of rated current completes the design procedure. The equations and the analysis techniques described earlier in this chapter have been automated using a MS Excel spreadsheet, shown in Appendix 2. The first iteration through the design process is illustrated in this appendix, and the predicted performance is summarised, Table 6.2.

Equivalent circuit	
Phase open circuit EMF (V)	10046
Phase resistance (Ω)	55.112
Synchronous reactance (Ω)	354.337
Rated current (A)	1.715
V phase (V)	9934
Power output (W)	51103
Efficiency (%)	97.4
Power density	
Volume of machine (m^3)	6.77E-03
Power density (kW/m^3)	7545.91

Table 6.2: Performance summary for the initial design

Although the design presented in Appendix 2 is only the first iteration of the design process, a number of observations can be made. Firstly, the magnetic loading is significantly greater than the TORUS being in excess of 0.9T. This also represents a slight increase over that of the slotted variants previously described, owing to a slightly reduced running clearance. Also, the electric loading is maintained at a level comparable with that achieved in the TORUS. Although the allowable I^2R loss is less than half that of the TORUS, owing to the poorer cooling and the extra non-current dependant loss, the improved use of space has resulted in an overall increase in performance. Furthermore, in section 6.2.4 it was pointed out that a current density of $20A/mm^2$ represents a rule-of-thumb upper limit. The value of $8.73A/mm^2$

returned by the design spreadsheet in gives some indication that the thermal model is in order.

6.3.2. Final design

The design process was iterated with alteration of various parameters, starting with the feedback of the actual magnetic and electric loadings obtained here. Parameters such as the outer diameter, the wire and slot dimensions, the number of poles, and the pole arc to pole pitch ratio were varied until some degree of optimisation had been achieved and a practicable 40kW design for comparison with the 40kW TORUS was complete. This final design is summarised, Table 6.3.

Design summary	
Speed (RPM)	4500
Phases	3
Poles	12
Electrical frequency (Hz)	450
Core OD (m)	0.275
Core ID (m)	0.143
Core length (m)	0.066
Mean magnet width (m)	0.036
Parallel strands	12
Turns/pole/phase	14
Running clearance (m)	0.002
Magnet thickness (m)	0.006
Rotor thickness (m)	0.012
Stator thickness (m)	0.039
Axial length (m)	0.079
Rotor OD (m)	0.285

Table 6.3: Final 40kW slotted design summary

The predicted performance is given, Table 6.4.

Performance prediction	
Magnetic loading (T)	0.876
E_{phase} (V)	646
R_{phase} (Ω)	0.41
$X_{syn\ phase}$ (Ω)	2.662
I_{rated} (A)	21
V_{phase} (V)	635
Current density (A/mm^2)	9
Electric loading at D_{mean} (A/m)	16256
Efficiency (%)	97.5
Power density (kW/m^3)	7964

Table 6.4: Performance prediction for the final 40kW slotted design

This final design fulfils the power and speed rating within a small geometrical frame. A high efficiency is predicted and the dimensions and performance parameters are practical and realisable. In particular, the use of parallel strands has reduced the phase induced EMF to a more sensible level.

6.3.3. Comparison between the 40kW TORUS and the final slotted design

This final slotted design is compared with the 40kW TORUS, Table 6.5 and Figure 6.6.

	TORUS	Slotted
Magnetic loading (T)	0.509	0.876
Flux per pole (mWb)	1.341	1.938
E_{phase} (V)	229	646
R_{phase} (Ω)	0.168	0.41
$X_{syn\ phase}$ (Ω)	0.317	2.662
I_{rated} (A)	62	21
V_{phase} (V)	217	635
Current density (A/mm^2)	27	9
Electric loading at D_{mean} (A/m)	12176	16256
Efficiency (%)	94.0	97.5
Rotor outer diameter (m)	0.415	0.285
Axial length (m)	0.075	0.079
Power density (kW/m^3)	4022	7964
Mass of steel/magnets (kg)	36.5	24.4
Power density (kW/kg)	1.12	1.65

Table 6.5: Performance comparison between the TORUS and final slotted design

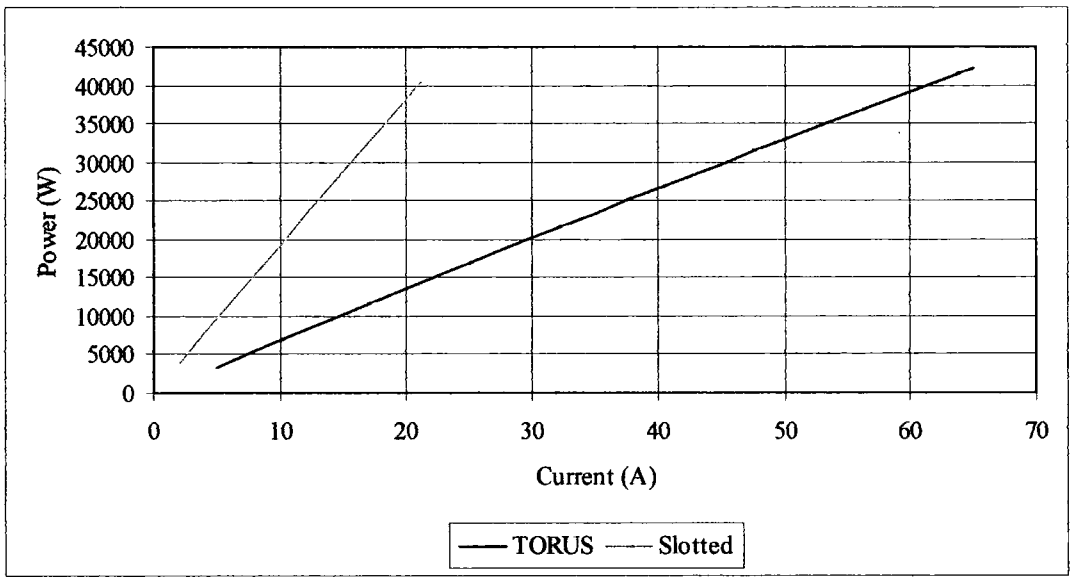

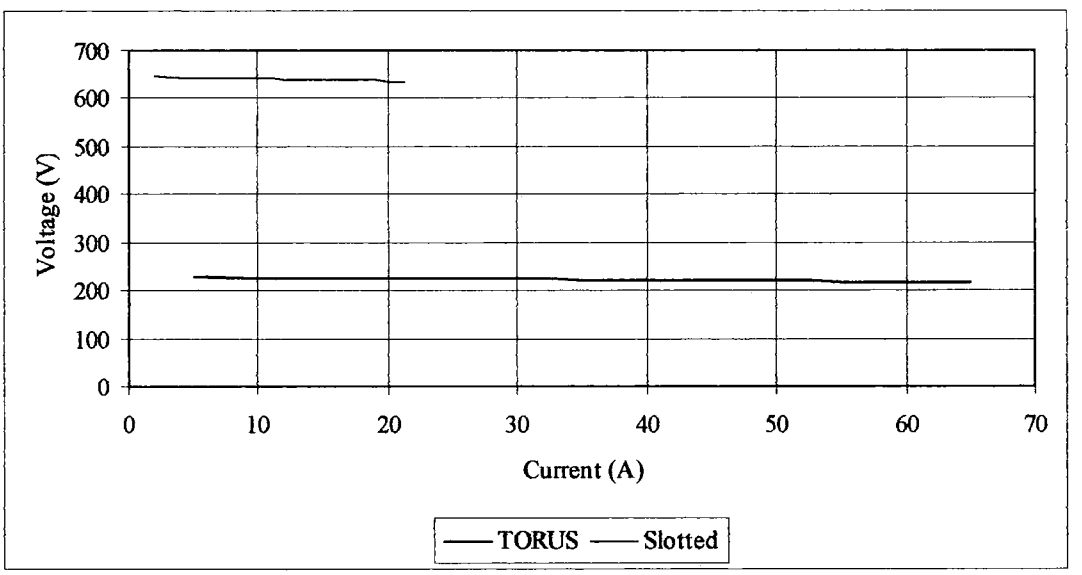

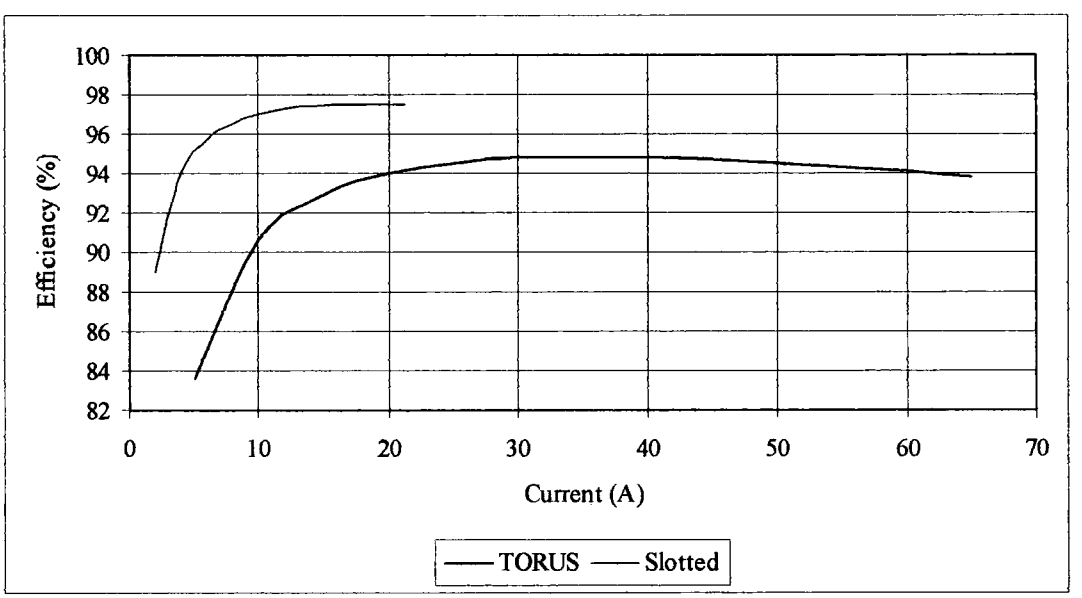

Figure 6.6: TORUS and final slotted machine performance predictions

Whilst both machines are predicted to achieve the same rating of 40kW at 4500RPM, there are marked differences in the designs as well as the performances. Firstly, the slotted machine has significantly bigger magnetic and electric loadings, thus resulting in a more compact machine with a power density almost twice that of the TORUS. This is a result of the decreased air-gap and the extra space for winding material facilitated by the slots.

Although the allowable loss is reduced in the slotted machine, owing to the poorer heat transfer characteristics, this is not prohibitive and the reduced current rating is compensated for by the increased space for the winding. In fact, the reduced capacity for loss means that the efficiency of the slotted machine is predicted to be better than that of the TORUS.

By design, the voltage and current output of the slotted machine is different, having an increased voltage resulting from the many turns of narrow gauge wire the *"mush"* winding design can accommodate. Without the use of parallel strands, this may result in too high a voltage and too low a current, but the specification of 12 parallel strands per conductor brings the output to appropriate levels. The voltage regulation of both machines is still quite low since the synchronous reactance in each is still low by comparison with more conventional machines.

The axial length of the slotted design is 79mm, compared with the 75mm of the 40kW TORUS. It should also be noted that calculations showed the thickness of the stator of the TORUS to be in excess of the flux-carrying requirement, hence although the TORUS has a larger diameter, it could still be the axially shorter machine. This is

minimal when compared with the reduced diameter and the increased power density of the slotted machine is considered.

6.4. Discussion

In this chapter, a generalised design procedure for axial flux machines was described, starting from the Lorentz Force principle and using the optimal ratio between the inner and outer stator core diameters derived by Campbell, [13]. This approach takes a power and speed requirement and uses approximate electric and magnetic loadings based on experience to yield a machine diameter which formed the basis of a design. A new winding design process was described, as was an enhanced approach to the thermal modelling of slotted machines. Along with the analytical methods described in Chapter 4, this completed the design process for a slotted machine and a spreadsheet approach to the new design was described.

Since the conductors in the slotted machines are out of the air-gap, the winding could theoretically be much less restricted, and a *"mush"*-type winding of narrow gauge conductors was specified to this end. The result was considerably more freedom in the winding design, resulting in a predicted increase in the electric loading possible in the slotted machine by comparison with the TORUS.

The final comparison between the 40kW TORUS and the predicted performance of the new slotted design showed that, whilst both designs achieve the specified power and speed ratings, there are some significant differences. Firstly, the slotted machine is much smaller, having a rotor outer diameter of 285mm compared with 415mm in the case of the TORUS. Although the axial length of the TORUS is very slightly less, the slotted machine still exhibits a power density almost twice that of the TORUS.

Also, the permanent magnet material used in the slotted machine is much less owing to its smaller size and the fact that the same magnet thickness (6mm) was specified in both cases; although the price of these rare-earth magnets has decreased over recent years, magnets can still be the overwhelming cost in such a machine and so this is a significant advantage.

Much of this investigation into was carried out at the request of Newage-AVK-SEG who provided CASE sponsorship of this research. It is particularly relevant to the ongoing research and development in the field of diesel engine-generator sets that are made by Newage-AVK-SEG for portable power generation applications. From that perspective, the results of this investigation are encouraging since Newage-AVK-SEG has a generator set with an air-gap wound TORUS-type machine which has recently been made available on the market and is constantly looking to improve this product in cost and performance terms.

There are some differences in the slotted machine that could potentially be disadvantageous, however. Primarily, it is a more complicated machine and this would affect the manufacture in a number of ways. The methods of producing a slotted stator have been mentioned, and the *"mush"* winding specification is likely to require more input than the simpler air-gap winding. Also the aspect ratio of the machine is subtly altered. Although the diameter is significantly decreased, the slotted machine naturally moves to an increased axial length on account of the extra flux. This may render the slotted machine less attractive in applications where the pancake geometry of the TORUS was an advantage, for example in the case of diesel engine generator sets, where the short axial length of the TORUS enabled a bearing-less design. The axial length in crease is comparatively very slight, however.

Furthermore, an investigation into cogging torque in Chapter 4 highlighted the naturally smooth and relatively harmonic-free operation of the TORUS, and gave some indication of the potential problems of slotted machines in this respect. It was shown that various methods exist for suppression and limitation of these effects, which may be sufficient in the case of diesel engine-generator sets. However, other possible applications of axial flux machines may be less forgiving. It has been pointed out that a number of manufacturers of small-scale wind turbines have expressed an interest in axial flux machines and some already use this technology to some extent. The starting torque and the potential noise and vibration resulting from these harmonics are a serious disadvantage, particularly in the case of vertical axis wind turbines which tend to have zero or minimal starting torque.

Nevertheless, this investigation has enabled the extension of the previously developed methods of analysis to a new design, facilitating significant improvements on the TORUS concept which are likely to be of use in the diesel engine-generator application. In the next chapter, analytical methods and FEA techniques are further extended to a novel axial flux machine with an ironless stator, primarily for the small scale wind turbine application, which is now the subject of an international patent, [7].

Chapter 7. FEA and experimental test of a novel air-cored machine

In previous chapters, axial flux machines have been investigated primarily for use in conjunction with a diesel engine as a portable power supply. The results include the development and benchmarking of a range of techniques for the design and analysis of these machines. Latterly, a modification to the TORUS design with a slotted-type winding was described and predicted to have an improved performance and a higher power density, at the expense of increased complexity of design and manufacture and the introduction of slot harmonics.

Prior to the investigation of slotted-type machines, a rewound version of the 20kW prototype TORUS machine described in Chapter 3 had been supplied to a local firm with an interest in developing a Savonius vertical axis wind turbine (VAWT) for use in urban environments. Some tests were performed with the generator actually mounted on a turbine and, whilst the firm were very interested in pursuing the direct-drive axial flux theme owing to the advantages offered by this topology, some significant problems emerged. Chiefly, the TORUS winding proved impractical since the small running clearance gave little allowance for any imbalance in the setup or for the difficulty faced by the firm in assembling the turbine in the field. This inevitably resulted in contact between the rotor magnets and the exposed winding, causing immediate destruction. This was exacerbated to a great extent by the large forces of attraction present between the rotors and the iron stator. Also, although the mechanical aspects of the TORUS design are simple, the winding design and interconnection proved rather complicated for a small mechanical workshop to deal with.

Consequently, an axial flux design was conceived elsewhere within the school which addressed the problems highlighted by the transfer of the TORUS to this wind turbine and capitalised on the natural suitability of axial flux machines to this application. Although this is rather different to the diesel engine-generator set application, and the respective generator requirements lead to a very different design, the techniques which have so far been developed are readily extended in this new direction. The new design is different from previous ones principally because an air-cored arrangement is specified, and also because it was conceived with simplicity and ease of manufacture in mind. In this way it complements the designs so far considered, expanding the family of axial flux machines and thereby fulfilling one of the original aims of this research project.

The design specification for the new generator is described, drawing particularly upon the experience gained from the testing of the TORUS in this application. The air-cored topology is introduced as a solution to the design problem and the main differences between this and the iron-cored machines so far considered are highlighted. A machine fulfilling the design criteria was designed at Durham University by Bumby, [6] and is now the subject of an international patent [7]. The work described here focuses on the FEA and experimental test of a prototype designed and built by Wong as a final year MEng project, [99]. An outline of the analytical approaches used in the design is given, along with a summary of the predicted performance of the prototype. FEA techniques are used to verify aspects of the analytical strategy as well to facilitate quantitative comparison with the predictions. Finally, experimental tests are described from which the equivalent circuit parameters are obtained for comparison with the predictions and from which a range of performance characteristics are measured and presented.

7.1. Axial flux machines for small wind turbines

7.1.1. The wind turbine application

There is currently significant interest in the development of small, low power wind turbines for the urban environment, [6], although suitable generators are not readily available. Companies with neither electrical machines manufacturing expertise nor appropriate facilities are frequently forced down the route of using a standard induction machine and gearbox arrangement, but this has a number of disadvantages. The necessary inclusion of a gearbox results in extra cost, increased noise, lower efficiency, regular maintenance needs, and increased space requirement for the drive-train. Also, wind turbine manufacturers have cited gearbox breakdown as a failure mode; elimination of this particular component is desirable for a variety of reasons. The induction machine runs at essentially constant speed, with some slip variation allowing for a slightly softer coupling than exactly constant speed and thus facilitating some protection from extreme mechanical loads in high wind conditions. Truly variable speed operation would facilitate greater protection and also increase energy capture, since the rotational speed of the turbine could vary with the incoming wind speed in order to maximise the coefficient of performance. Large variable speed turbines tend to utilise either a fully rated AC-DC-AC converter between a synchronous machine and the grid, or a doubly-fed induction generator employing a converter, rated at approximately 30% of the generator output, to provide variable excitation via a wound field, resulting in a greater speed variation capability than a directly connected machine, [37]. Low power wind turbines are generally used for off-grid applications; the benefits of grid connection are limited, but the appropriate power electronics and control equipment for either case is readily available anyway. It is clear that a purpose built direct-drive synchronous machine operating at variable speed is a strong candidate for low powered wind turbines.

7.1.2. The suitability of axial flux machines

The high electric and magnetic loadings achievable in permanent magnet axial flux machines such as those described so far in this thesis, as well as the correspondingly high reaction torque and the compact geometry, make this genre of machine a suitable candidate for low speed direct-drive wind turbines, particularly at the low power end of the spectrum. This is especially true in the case of VAWTs where axial length is at a premium, ruling out an in-line gearbox arrangement and not being naturally suited to the incorporation of a conventional radial flux machine. Conversely, the radial dimension is much less restrained in VAWTs and a disc-shaped generator may quite naturally be mounted between the base support and the turbine blades. In fact, the large radial dimensions of the generator may provide a welcome addition to the inertia of the turbine and may even be designed so as to make a separate flywheel arrangement redundant.

However, all of the axial flux varieties considered so far in this thesis have been iron cored, resulting in heavy machines with large forces of attraction between the rotors and the central stator. These forces require care during assembly and introduce a certain amount of sensitivity towards axial disturbances which are likely to be encountered in this application. The exposed air-gap winding is also vulnerable to such disturbances, with field tests resulting in numerous cases of the winding being stripped from the core on contact with the edges of the permanent magnets as described in the case of the prototype TORUS tested in the field.

Also, air-gap toroidal windings are not straightforward to manufacture, ideally requiring a dedicated winding machine and a suitable non-magnetic, non-conducting former for any level of production beyond the prototype stage. The interconnection

of poles and phases is complex and results in either long end-windings or multiple connection points. Axial flux machines with slotted windings of the sort described in Chapter 4 are even less suitable for this application. The geometry of slotted machines has been shown to tend towards a reduced diameter at the expense of an increased axial length, which is contrary to the requirements of a VAWT as outlined above. Manufacture of such machines is more complicated and costly, and the reduced effective air-gap would result in a dramatic increase in the forces of attraction between the rotors and stator making assembly difficult.

7.1.3. Design specification for a VAWT generator

The aim of the design was to address the shortcomings of the machines so far described, whilst capitalising on the natural suitability of axial flux machines in the direct-drive VAWT application. Specifically, the design specification may be divided into three sections: performance, geometry, and manufacture and assembly.

In performance terms the design must preserve the high electric and magnetic loadings so far demonstrated to be a feature of axial flux machines, in order to develop the torque required to enable a suitably sized machine to operate at the low speeds determined by the wind turbine without the need for a gearbox. Nominal ratings, based on "C_p-λ" data obtained for a Savonius VAWT, were set at 1kW at 300RPM, or 2kW at 500RPM as outlined in the internal report, [98]. Since the turbine would operate at variable speed, it is envisaged that the resultant variable frequency electrical output of the generator would require significant conditioning via a power electronic interface. Given that the energy harnessed by the turbine is already a mere fraction of the total available in the wind, it is doubly important for the generator to also have a high efficiency rating.

The geometrical requirement is for a machine having as small an axial length as possible and being easily incorporated onto the driveshaft of a VAWT at a location between the turbine blades and the supporting base. Prototype turbine measurements indicate that blades having an outer diameter of 0.78m are required to generate power in the range specified above, namely 0 – 2kW, and so the generator measurement should ideally fall within this dimension. However, the blades are mounted on a supporting disc with a diameter exceeding that of the blades and, furthermore, a flywheel is specified for mechanical smoothing of the turbine. A generator with rotating parts having a large radial dimension could provide inertia significant enough to offset or even eliminate the flywheel requirement. The overall implication is that the axial dimension of the generator is critical and must be minimised in order to maximise the space available for energy capture, but that there is a significant radial allowance which may be used to gain an overall advantage.

Finally, the focus of the machine design is on simplicity of manufacture and assembly such that these tasks could be achieved by a mechanical engineering workshop with little or no experience in the field of electrical machinery. In this way, the specification is tailored to the requirements of a number of engineering firms investigating small-scale wind power and the overall design is far simpler than the conventional induction motor and gearbox drive. It must be acknowledged that this is achievable primarily because of the availability of rare-earth permanent magnets with energy densities high enough to make axial flux topologies viable, and also because of the availability of a power electronic interface sufficient to match the output of a direct-drive synchronous generator to the requirements of a typical stand-alone load such as a battery charging unit.

7.1.4. Air-cored axial flux machines

Flux paths in the TORUS consist of an axial crossing of the air-gap, with circumferential paths in the core linking the stator coils and in the rotor to facilitate flux return. As has been described in previous chapters, this is an evolution of earlier axial flux designs, notably those of Campbell [13]. In Campbell's machines the working field is entirely axial with circumferential paths only for flux return; this is sometimes referred to as the shine-through principle. The difference is shown in Figure 7.1 relative to the TORUS topology so far considered.

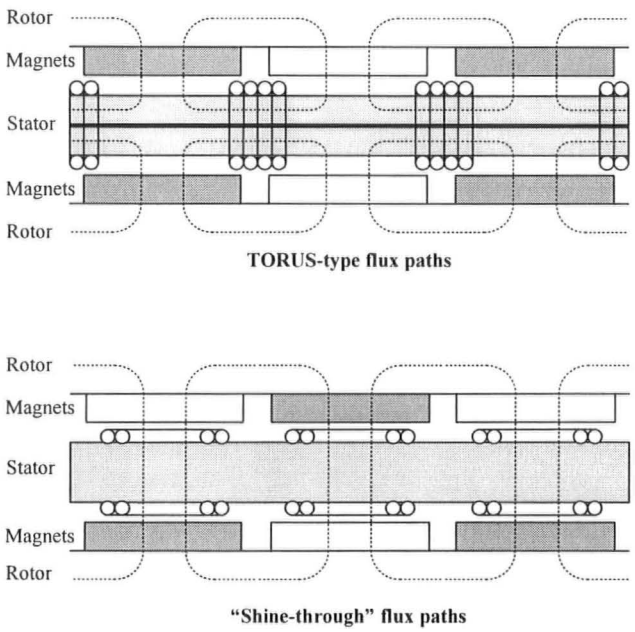

Figure 7.1: Flux paths in different axial flux machines

It can be seen that the shine-through topology could be realised without the inclusion of iron in the stator core as was demonstrated in the single rotor design of Campbell [13]. This is very attractive in this application since the troublesome forces of attraction between the rotors and the stator are eliminated and the weight of the machine significantly reduced. Other advantages include the elimination of iron losses in the stator and the potential for a preformed, encapsulated winding which

could greatly ease manufacture and assembly as well as provide some protection for the conductors. The primary disadvantage is that an ironless stator adds to the already large effective air-gap characteristic of axial flux machines with rare-earth permanent magnets. However, the air-gap winding of the TORUS takes up significant axial space either side of the stator iron. If the winding of an air-cored machine were of comparable axial length it would be possible to achieve a similar magnetic loading to the TORUS with an ironless stator. This would also serve to limit the axial length of the machine which is such an important consideration in this application.

For these reasons, the air-cored axial flux topology utilising shine-through flux paths was used as the basis for the novel design of a generator for a small scale VAWT and the prototype machine is described in the next section. The electromagnetic principle of the machine is very similar to that of the TORUS in that it may be considered as a polyphase synchronous generator with permanent magnet excitation; this characteristic permits the extension of the analytical techniques and finite-element modelling approaches previously developed to this new application. The customarily large air-gap coupled with the adoption of shine-through flux paths causes the validity of a purely 2D approach to come into doubt; FEA is thus an important tool in verification not only of the analytical predictions but of the underlying assumptions. Indeed, FEA gives an insight into the fundamental electromagnetic phenomena involved which could not be obtained through traditional laboratory tests, and is the basis of this chapter.

7.2. A novel air-cored axial flux machine

7.2.1. The new topology

The new topology consists of two steel rotors discs with axially-polarised permanent magnets and a single, non-magnetic stator disc with a winding composed of an array of concentrated coils. The particular novelty in this machine comes from the use of plastic bobbins for winding concentrated, circular coils and a plastic stator structure in which the coils are located.

An alternative method, which would allow the use of different shaped coils, is to pre-wind open coils on a former using epoxy coated wire, bond them and then drop the coils into a stator structure and impregnate them into place, [100]. It can be shown that trapezoidal-type coils give a power output advantage since they maximise the use of space, but for a machine of this rating the simplicity of winding a circular coil on a bobbin is a serious advantage.

Circular magnets can be used with circular coils in order to maximise the flux linkage for a given volume of magnet, but square magnets could also be used and may be less expensive. For a polyphase output, the number of coils and magnets cannot be the same, but the coils and magnets should be similarly sized in order to maximise the flux linkage. Conventionally, a 3-phase, 16-pole machine may have 1 coil per pole per phase, resulting in a winding made up of 48 distributed coils, but this is clearly not possible with a concentrated winding. The choice of pole and coil numbers is critical in ensuring correct, optimal operation with the desired number of phases, and this is an important design consideration. Appropriate equations for this are derived in section 7.2.3, and the impact of this on the mode of operation is explored in section 7.4.4.

Figure 7.2 shows the rough concept of the generator design with circular coils wound on bobbins.

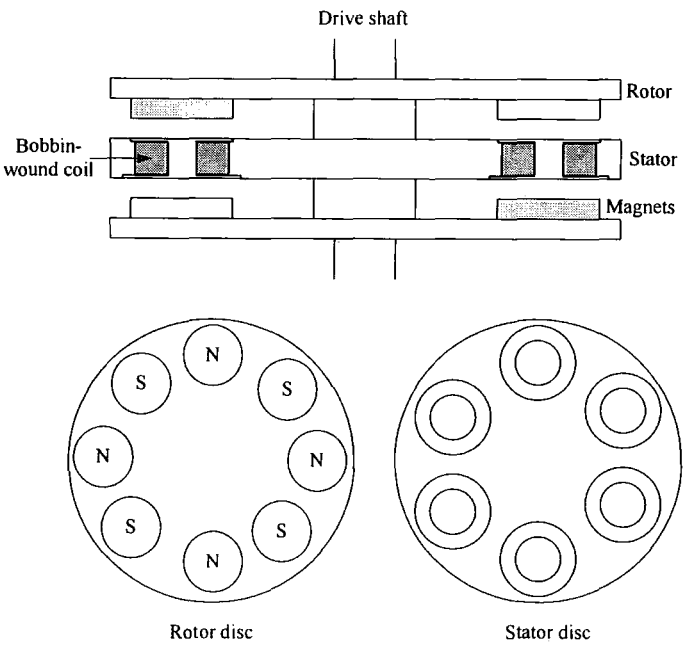

Figure 7.2: The new air-cored topology

Since the coils are concentrated, the stator and rotor sections can be modular in construction, which may simplify manufacture and assembly of the machine and is particularly relevant to VAWTs, where breaking the drive-train for generator installation/removal is non-trivial. The details of this machine concept and its variants are covered by a British Patent, [7].

7.2.2. Construction of a prototype

A rotor of the prototype machine is shown in Figure 7.3, consisting of a steel disc upon which circular, NdFeB permanent magnets are mounted. A plastic retainer ring facilitates assembly and retention of the magnets, particularly against outward radial motion upon rotation; gluing could also make the positioning more permanent beyond the prototype stage. Such discs were readily sourced flame-cut to the

required dimensions. The magnets were purchased already cut to size and magnetised, and a wedge of plastic was used in conjunction with the specially designed retainer ring for ease of positioning the magnets onto the discs in the required arrangement. In this way, the sourcing of the component parts of the rotors and their eventual assembly can be achieved relatively simply by any small engineering outfit, without recourse to specialist experience or machinery.

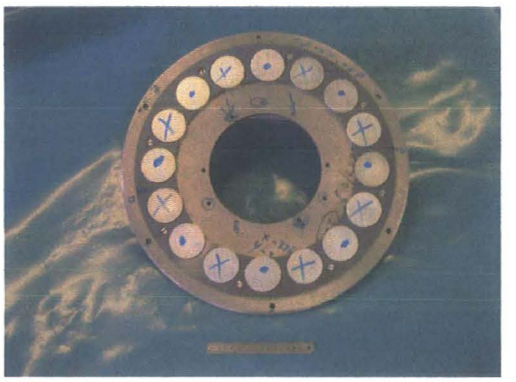

Figure 7.3: A rotor of the prototype, [99]

The stator is shown in Figure 7.4, consisting of a non-magnetic supporting structure made from PVC (grey), into which the pre-wound plastic bobbins (white) are inserted.

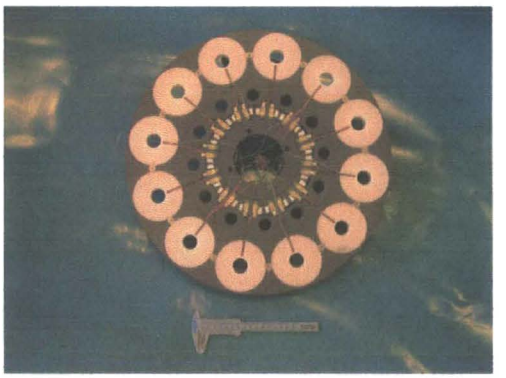

Figure 7.4: Stator and coil connection detail, [99]

The coils were individually pre-wound and slotted into the stator where a series of end terminations allow for electrical connection at the inner radius of the stator support, as shown in Figure 7.5.

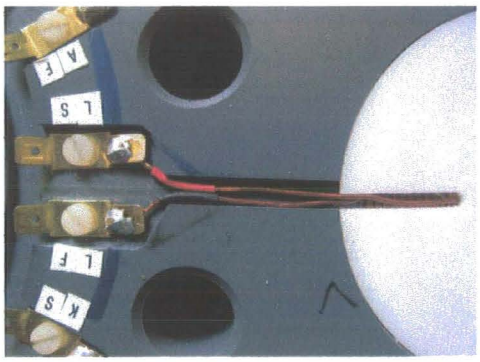

Figure 7.5: Coil end connections, [99]

The stator support and the plastic bobbins were made by a local firm so as to have appropriate mechanical and thermal properties for the application. The winding of the bobbins was carried out in a mechanical engineering workshop using a lathe and standard insulated copper wire. It is clear that one of the defining characteristics of this machine is that it consists of a small number of simply assembled components that can easily and inexpensively be sourced. Table 7.1 shows a summary of the main design parameters. The following analysis is based upon this data.

Rated speed (RPM)	300
Number of poles per disc	16
Number of armature coils	12
Magnet material	NdFeB
$\mathbf{B_{rem}}$	1.2
μ_{rec}	1.07
Magnet thickness (mm)	8
Magnet diameter (mm)	60
Magnet mean pole pitch (mm)	70
Coil height (mm)	14
Coil inner diameter (mm)	30
Coil outer diameter (mm)	75
Coil mean pole pitch (mm)	93.3
Turns per coil	276
Rotor outer diameter (mm)	446.5
Rotor thickness (mm)	7
Mean diameter (mm)	356.5
Stator inner diameter (mm)	281.5
Stator outer diameter (mm)	431.5
Stator thickness (mm)	20
Running clearance (mm)	3
Total axial length (mm)	56

Table 7.1: Prototype generator design parameters

7.2.3. Principle of operation

The coils of the machine are arranged and connected so as to give a three phase output. Working as an AC generator, the machine operates exactly as a permanent magnet synchronous machine and can therefore be analysed as such. The permanent magnets on the rotor provide the excitation and induce EMF in the stator coils, which can be estimated from analysis of the excitation field. If connected to a load, the resulting currents interact with the excitation field resulting in the development of torque. The resistance of the coils can be estimated and the synchronous reactance can again be estimated from analysis of the field resulting from phase currents. This way, the standard per phase synchronous machine model of an induced EMF, E, in series with a resistance and a synchronous reactance, (R, X_{syn}), and resulting in a

terminal voltage, V, may be used. Figure 7.6 shows the equivalent circuit and phasor diagram for the synchronous generator.

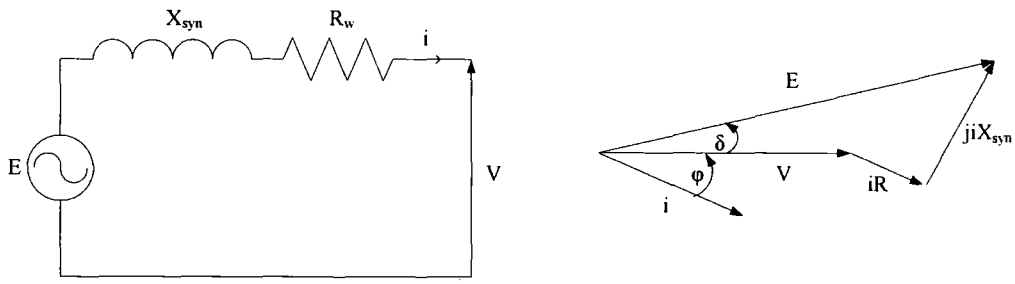

Figure 7.6: Equivalent circuit and phasor diagram

There are important factors to consider when choosing the number of poles and coils. Firstly, the pole number combines with the speed of the generator to dictate the frequency of the electrical output. The number of coils must then be chosen to ensure a polyphase output with the correct number of phases. A similar numbers of coils and poles make the best use of the excitation field available given the geometrical constraints of circular magnets and coils. However, the number of coils must not equal the number of poles, or a multiple of the pole number, since this would result in single phase operation. In fact, it is shown here that the number of coils can be chosen such each coil belongs to and is exactly in phase with a phase grouping, and the phase difference between the groupings results in the correct number of balanced phases.

Firstly, the angle between magnet poles is defined:

$$\theta_p = \frac{2\pi}{p} = \pi_{elec} \qquad \text{Eq. 7.1}$$

Hence:

$$\theta_p p = 2\pi \qquad \text{Eq. 7.2}$$

Similarly, the angle between coils is given:

$$\theta_c = \frac{2\pi}{c} \qquad \text{Eq. 7.3}$$

Eq. 7.2 and Eq. 7.3 are combined to give the electrical angle between coils in terms of the number of poles and coils, in electrical radians:

$$\theta_c = \pi \frac{p}{c} \qquad \text{Eq. 7.4}$$

So, for an *m*-phase machine:

$$\frac{p}{c} = \frac{n}{m} \qquad \text{Eq. 7.5}$$

For this to hold, *n/m* must be a non-integer value as described above. For example, a generator design could proceed as follows. Knowledge of the prime mover speed and the required electrical frequency gives the required pole number:

$$p = 2 \times \text{int}\left(\frac{f_{elec}}{f_{mech}}\right) \qquad \text{Eq. 7.6}$$

If the required number of phases is known, then the number of coils is:

$$c = \text{int}\left(\frac{pm}{n}\right) \qquad \text{Eq. 7.7}$$

It should be noted that c must also be greater than or equal to *m*. For example, a wind turbine rotating at 300RPM and requiring a 50Hz output would need 20 poles. For a 3 phase machine, possible values of n would be 1, 2, 4, 5, 10, 20. Hence there could be coil numbers 60, 30, 15, 12, 6, 3. To ensure that the coils and magnets are similarly sized, 15 coils would be a sensible choice, resulting in an electrical angle of:

$$\theta_c = \pi \frac{p}{c} = \frac{4\pi}{3} \qquad \text{Eq. 7.8}$$

This is equivalent to 240° electrical, which implies that the coils can be connected to give a 3 phase output as required. In this configuration, the resultant currents set up a

field composed of even harmonics and it is anticipated that torque is transferred on the 4th harmonic, since this would set up a rotating field with the same angular frequency as the excitation field. The integer value, n, gives the current harmonic of torque transfer. A conventional machine with a distributed winding would have only odd harmonics and transfer torque on the fundamental; thus $n = 1$ and there would be 60 coils (1/pole/phase). A similar analysis was presented by Mitcham et al, [101], when considering fault-tolerant machines.

Generally, a larger number of magnets than coils make better use of the field since the magnets are smaller than the coils and so surplus field beyond the outer diameter of the coils is avoided. Owing to various sizing considerations and the availability of materials, the prototype generator considered here has 16 magnet poles and 12 coils. Hence the electrical angle between adjacent coils is similarly $4\pi/3$, again resulting in a 3 phase output. The value of n is given by rearranging Eq. 7.5:

$$n = \frac{pm}{c} = 4 \qquad \text{Eq. 7.9}$$

Similarly, the prototype machine is expected to transfer torque on the 4th harmonic, and analysis of the field arising from currents in the coils during synchronous operation should indicate the presence of a strong 4th harmonic in the flux density waveform.

Finally, the thermal characteristics of the prototype machine are considered. No forced cooling is specified, and the natural pumping action of the rotors is once more relied upon for cooling the conductors in the stator. These are now much less exposed resulting in less favourable heat transfer characteristics. However, in the absence of stator iron, only eddy loss and I^2R loss occurring in the conductors are assumed relevant.

7.3. Analytical methods

7.3.1. Introduction to the analytical approach

The analytical approach described here consists of simple magnetic circuit-type approximations to the analysis of the excitation field and the field arising from coil currents. The aim of the analysis is to provide some guidance in the development of the various FEA techniques later described and to roughly corroborate the predictions of the more sophisticated analytical methods described in a recent publication on the design of this prototype machine, [6]. The simple analytical approach is a transfer of the so-called magnetic circuit analysis described in Chapter 3 and Chapter 4 for the TORUS machine. The more sophisticated method is briefly described and the results of the two methods are compared. In particular, attention is drawn to the assumptions made in the two analytical methods since one of the purposes of the FEA described later was to verify these.

7.3.2. Analysis of the excitation field

The field arising from the presence of the permanent magnets only is shown in a simplified radial view into a 2D linear development of the machine, Figure 7.7.

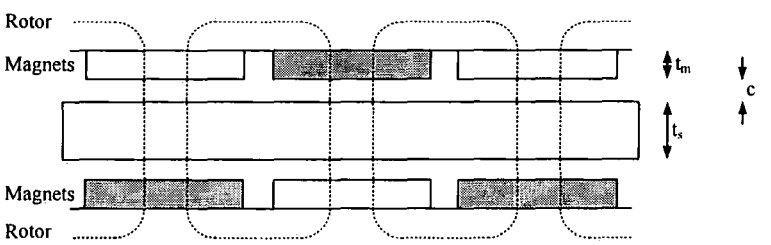

Figure 7.7: Symmetry conditions for the excitation field

Ampère's Law is applied to one of the flux loops, neglecting leakage flux and assuming the steel rotors to be infinitely permeable, to give:

$$\oint H.dl = 2H_m t_m + 2H_a c + H_a t_s = 0 \qquad \text{Eq. 7.10}$$

Flux density is continuous in magnets and air, so:

$$B = \mu_0 H_a = B_r + \mu_0 \mu_r H_m \qquad \text{Eq. 7.11}$$

Substituting Eq. 7.10 into Eq. 7.11 gives:

$$B = \frac{B_r \frac{t_m}{\mu_r}}{\frac{t_m}{\mu_r} + c + \frac{t_s}{2}} \qquad \text{Eq. 7.12}$$

The calculations above assume a square flux density profile such that all the flux crosses the gap perpendicularly between the magnets, and that the characteristic is constant into the page. One approach would be to consider the first harmonic of the square flux density profile which would have a peak of:

$$B_{fund} = \frac{4B}{\pi} \sin\left(\frac{\tau_m}{2}\right) \qquad \text{Eq. 7.13}$$

In reality, given the iron-less nature of the stator, the correspondingly large effective air-gap, and the circular magnets specified, it is unlikely that the flux density is constant in either the radial or axial directions with respect to the rotor discs and it is likely that the value of flux density yielded by Eq. 1.12 is an over-estimate. To make some allowance for this it is assumed that the flux density varies sinusoidally in the circumferential direction having a peak value given by Eq. 1.12 (i.e. smaller than that of the first harmonic given by Eq. 1.13). The simple analytical approach rather crudely assumes the RMS value of such a sinusoid to remain constant across the coil and considers all the turns to be concentrated at the mean radius of the coil, r_m. Hence the area:

$$a_{turn} = \pi r_m^{\,2} \qquad \text{Eq. 7.14}$$

The flux linking this turn is taken to be the peak of a sinusoidally-varying flux, and so the flux linkage is given:

$$\hat{\lambda} = N_{coil} \hat{\phi} = N_{coil} \frac{B}{\sqrt{2}} a_{turn} \qquad \text{Eq. 7.15}$$

Assuming this flux to vary sinusoidally, the resultant EMF per coil is:

$$E_{RMS} = 4.44 f_{elec} \hat{\lambda} \qquad \text{Eq. 7.16}$$

This equation gives a value of 10.95V per coil per 100RPM using the parameters from Table 7.1. The more sophisticated analytical method, alluded to in section 7.3.1, makes two significant improvements to this approach. Firstly, the flux density at the axial centre of the machine is calculated more precisely through application of the field solution first outlined in Chapter 3. In the case of this machine, the iron-less stator allows consideration of a reduced model since symmetry means that the field behaves as if an iron boundary were present at this axial centre, Figure 7.8.

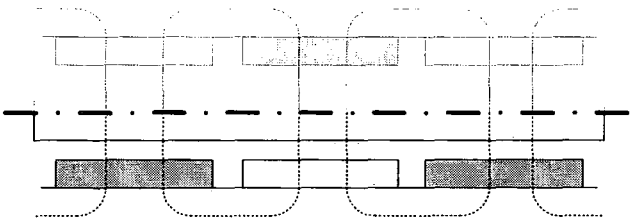

Figure 7.8: Iron boundary condition in the field solution

Given this reduction, the problem is exactly the same as that in the TORUS machine, namely the solution of the field at an iron boundary resulting from the presence of permanent magnets mounted on another iron boundary across an effective air-gap. The full summation of harmonic components can be used to obtain an accurate circumferential flux density variation for comparison with the results of later FEA.

Secondly, the actual flux density distribution and the radial spread of the turns with respect to the coils are taken into consideration when calculating the flux linkage and induced EMF. Three methods for this were described in the original paper [6], each taking a different approach to the radial spread of the turns. The axial spread of the turns in the coil is taken to be of negligible importance, assuming the field at the

axial centre of the machine to be constant across this dimension. To further simplify the analysis only the first harmonic of flux density is used for these calculations but, since the poles are circular and the effective air-gap large, the flux density is assumed to reduce radially from the centre of each pole in all directions such that it takes the form of a sinusoidal *"hill"*. In reality, the magnets are isolated poles in the radial dimension, and so a change of polarity in the analysis may cause an underestimate of flux; allowance can be made for this in the form of a flux enhancement factor, k_1, described below. The three methods use the flux density distribution of Figure 7.9 and consider the flux through a ring of elemental thickness also shown.

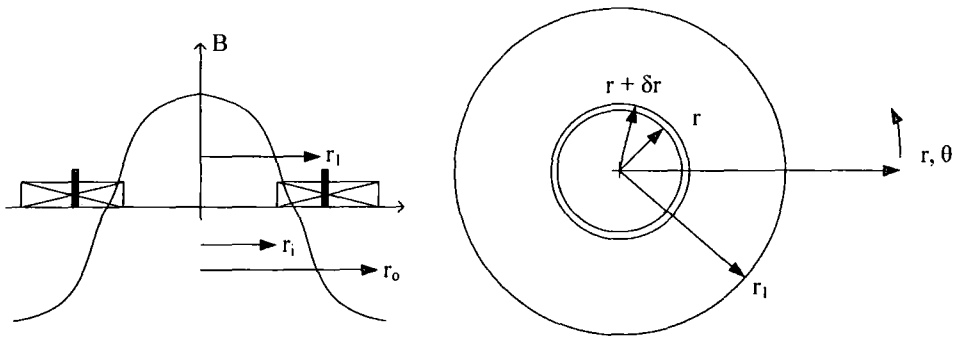

Figure 7.9: The flux linkage model

Integration of an expression for the elemental flux between *0* and r_1, for example, yields:

$$\phi = 2\pi\hat{B}\left[\left(\frac{\tau}{\pi}\right)^2\left(\cos\frac{\pi}{\tau}r_1 - 1\right) + \frac{\tau}{\pi}\left(r_1 \sin\frac{\pi}{\tau}r_1\right)\right] \qquad \text{Eq. 7.17}$$

The first method assumes all the turns, N_{coil}, are concentrated at the mean radius, r_m, and so the flux linkage is:

$$\hat{\lambda} = 2\pi N\hat{B}\left[\left(\frac{\tau}{\pi}\right)^2\left(\cos\frac{\pi}{\tau}r_m - 1\right) + \frac{\tau}{\pi}\left(r_m \sin\frac{\pi}{\tau}r_m\right)\right] \qquad \text{Eq. 7.18}$$

This may be substituted into Eq. 7.16 to give the RMS induced EMF per coil.

The second method performs a manual summation considering the turns divided between three locations and applying Eq. 7.17 to each. The flux linkage is then:

$$\hat{\lambda} = \frac{N}{3}(\phi_1 + \phi_2 + k_1\phi_3) \qquad \text{Eq. 7.19}$$

The flux enhancement factor, k_1 (≥ 1), makes allowance for the fact that the flux linking the outer turns is generally underestimated by this method since the sinusoidal flux distribution should only really change polarity in the circumferential direction and not in the radial direction.

The third method is analytically correct for a sinusoidal flux density distribution, considering the flux linkage in two components: one resulting from flux within the inner radius of the coil, which links all N_{coil} turns, and the other resulting from the flux passing between the inner and outer coil radii where the turns are assumed to be linearly distributed according to a turns function, Figure 7.10.

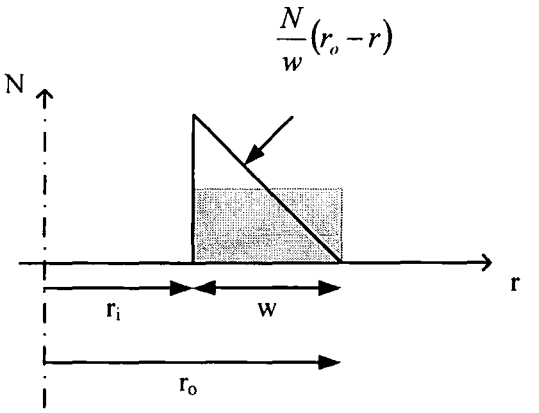

Figure 7.10: Turns function

Where $u = \pi/\tau$, the flux linkage arising from flux through the centre of the coil is:

$$\lambda_0 = 2N\pi\hat{B}\left[\left(\frac{1}{u}\right)^2(\cos ur_i - 1) + \frac{1}{u}(r_i \sin ur_i)\right] \qquad \text{Eq. 7.20}$$

The flux passing between r_i and r_o causes flux linkage:

$$\hat{\lambda}_1 = 2\pi \frac{N\hat{B}}{w}\left[-\frac{r_o}{u^2}\cos ur_o + \frac{(2r_i - r_o)}{u^2}\cos ur_i + \frac{2}{u^3}\sin ur_o + \left(\frac{r_i^2}{u} - \frac{r_o r_i}{u} - \frac{2}{u^3}\right)\sin ur_i\right] \qquad \text{Eq. 7.21}$$

Hence the total flux linkage:

$$\hat{\lambda} = \hat{\lambda}_1 + \hat{\lambda}_o \qquad \text{Eq. 7.22}$$

Eq. 7.16 may then be used to obtain the EMF per coil. The concentrated coil approach predicts 11.63V/100RPM, the manual summation predicts 11.21V with a flux enhancement factor of k_f equal to 1.05, and the correct analytical method predicts 10.89V. The manual summation is the preferred approach since it is more sophisticated than assuming the coil to be concentrated, and more readily adjusted by the flux enhancement factor than the analytically correct approach.

One further point of interest in relation to the excitation field concerns the forces of attraction between the rotors. In section 7.1.2, the large forces of attraction experienced with TORUS machines and the even larger forces expected to occur in slotted machines given the increased magnetic loading were cited as disadvantages of iron-cored machines. Some calculation of these forces is required for a more informed comparison and an approach is described here for later corroboration with the results of FEA. Firstly, assuming constant permeance in the air-gap, the tensile Maxwell Stress (acting in the same direction as the field orientation) is given by Carter, [93], p. 201:

$$t_m = \frac{B^2}{2\mu_o} \qquad \text{Eq. 7.23}$$

Following the approximations of the rough method described first in this section, it is assumed that the average flux density across a pole face is given:

$$\overline{B} = \frac{B}{\sqrt{2}} \qquad \text{Eq. 7.24}$$

The flux density, B, is given by Eq. 7.12, and the result of Eq. 7.24 is then assumed to act over the entire pole-face between a pair of magnets. This gives a force of 153N per magnet pair, or 2441N between the two discs.

The more sophisticated approach to the calculation of the excitation field may is also extended to the calculation of these forces, [6]. Assuming the flux density again to take the form of a sinusoidal magnetic *"hill"* in the *(r, θ)* plane, and integrating the elemental force on the ring shown in Figure 7.9 over a pole-pitch *(0 to r = τ/2)*, the total closing force is given:

$$F_{total} = 2p\frac{\hat{B}^2\pi}{\mu_0}\left[\frac{r^2}{4} + \frac{r\sin 2ur}{4u} + \frac{1}{8u^2}(\cos 2ur - 1)\right] \qquad \text{Eq. 7.25}$$

This gives a force of 1710N for the whole machine.

7.3.3. Analysis of the field arising from phase currents

In order to calculate the coil inductance and ultimately to quantify the synchronous reactance equivalent circuit parameter, the field arising from unit current in a single phase is considered. As explained in section 7.2.3, this field is even, such that all the coils in a given phase are connected in the same direction such that the excitation of a single phase sets up a field that can be modelled using tangential symmetry conditions, as shown in Figure 7.11.

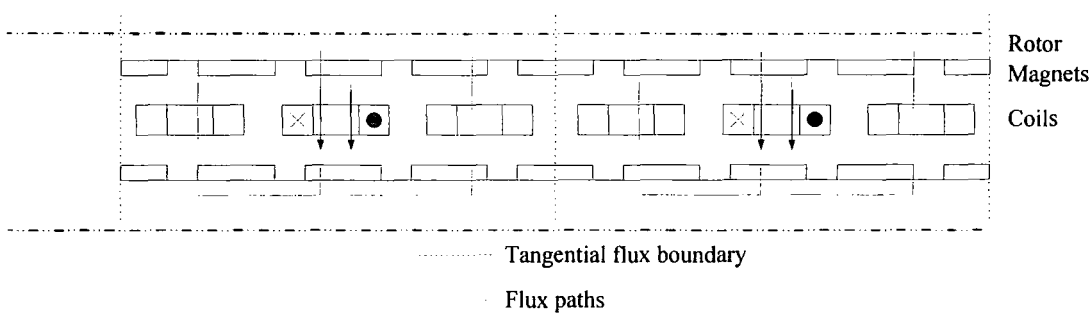

Figure 7.11: Symmetry in the field arising from single phase excitation

The turns are assumed to be concentrated at the axial centre of the machine and at the mean radius of the coil. The resulting flux density is assumed to have a square profile, such that the field to be calculated is as shown in Figure 7.12.

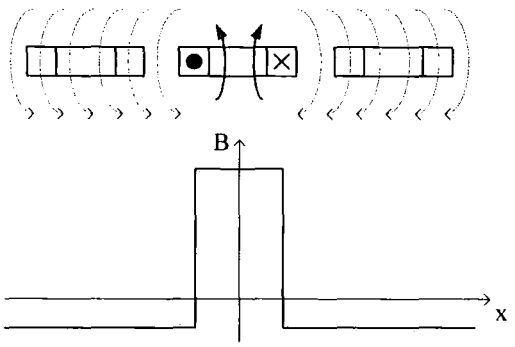

Figure 7.12: Approximation to the field arising from single phase excitation

The effective gap, g_{eff}, is given:

$$g_{eff} = 2\frac{t_m}{\mu_r} + 2c + t_s \qquad \text{Eq. 7.26}$$

Since the area of the flux return path is significantly larger (resulting in a reduced flux density as illustrated in Figure 7.12), the associated reluctance is much smaller than that of the path through the energised coil and so this approximate approach considers only the latter. Thus for unit current in the coil, the flux density at the coil is approximated by:

$$B = \frac{\mu_0 N_{coil}}{g_{eff}} \qquad \text{Eq. 7.27}$$

This flux density is assumed constant across the area bounded by the mean circumference of the coil where the turns are assumed to be concentrated; hence the coil self-inductance is given:

$$L = \frac{N_{coil}\phi}{I} = N_{coil} B \pi r_m^2 \qquad \text{Eq. 7.28}$$

This yields a value of 6.12mH per coil.

Again, the more sophisticated approach to the analysis is extended to the calculation of inductance, [6]. Once more, the axial spread of the turns is ignored and allowance is made for the radial distribution by either a manual summation or a full integration. It is assumed that the flux density at the axial centre of the machine arising from single phase excitation follows the characteristic of the turns function between r_i and r_o, remaining at a maximum value over the centre of the coil. The development of this assumption in the *(r, θ)* plane centre on the coil leads to a conical flux density distribution. In reality, leakage effects increase the magnitude of the flux density around the coil at the expense of the magnitude of flux forming a circuit with the rotors; this is accounted for by a leakage factor $(k_l \geq 1)$. The magnitude of the flux density used by the more sophisticated method is that given by Eq. 7.27 used previously. The assumed flux density profile is illustrated in 2D, Figure 7.13.

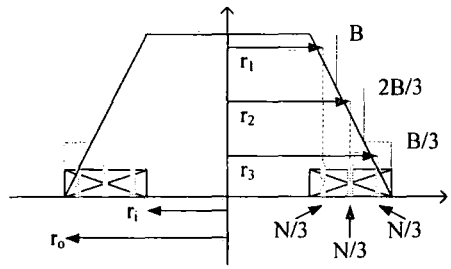

Figure 7.13: Flux density profile arising from single phase excitation

Where a manual summation of the inductance across three sections of the coil is used, the respective fluxes are given:

$$\phi_1 = \pi r_1^2 B$$
$$\phi_2 = \phi_1 + \frac{2}{3} B\pi(r_2^2 - r_1^2) \qquad \text{Eq. 7.29}$$
$$\phi_3 = \phi_2 + \frac{1}{3} B\pi(r_3^2 - r_2^2)$$

The coil self-inductance is then:

$$L = k_l \frac{N}{3}(\phi_1 + \phi_2 + \phi_3) \qquad \text{Eq. 7.30}$$

Where a uniformly turns distribution is assumed, the full integration method gives:

$$L = k_l\left[B_m N\pi r_i^2 + 2\frac{B_m N\pi}{w^2}\left(\frac{1}{12}r_o^4 - \frac{1}{2}r_o^2 r_i^2 + \frac{2}{3}r_i^3 r_o - \frac{1}{4}r_i^4\right)\right] \qquad \text{Eq. 7.31}$$

The results of the manual summation and the full integration are 4.90mH and 4.74mH respectively. In all cases, mutual effects are ignored since this effect is expected to be far smaller and less predictable. Hence the synchronous reactance is composed entirely of self-inductances.

7.3.4. Summary of analytical electromagnetic predictions

The analytical predictions made using the various methods are summarised here, Table 7.2.

		Sophisticated Analytical		
	Simple Analytical	**Concentrated Coil**	**Manual Summation**	**Analytical Summation**
E_{RMS} per coil per 100RPM (V)	10.95	11.63	11.21	10.89
L_{syn} per coil (mH)	6.12	6.12	4.90	4.74
Attractive force between rotors (N)	2441	----------1710----------		

Table 7.2: Summary of electromagnetic predictions

7.3.5. Analysis of loss and thermal behaviour in the machine

Since the stator is iron-less, the principle loss mechanisms in the machine are I^2R loss and eddy loss in the coils. An approximation to the thermal behaviour of the machine is described in the recent publication, [6], similar to the approach used for the TORUS and slotted machines and described in Chapter 3 and Chapter 6. However, the techniques described require values of certain heat-transfer coefficients to be

determined experimentally. This is the subject of further research beyond the scope of this thesis and so the method is only briefly outlined here.

It is assumed that all the loss is generated within the coil and that it is dissipated from the axially-oriented bobbin surface to the moving air being naturally pumped in a radial direction by the magnets. Thus no heat is transferred in the radial direction within the stator. Symmetry is exploited and the heat generated in the copper is split equally between three sections in the axial direction. Thus the heat transfer within the copper is modelled, as is the heat transfer across the plastic of the bobbin structure and from the bobbin surface to the moving air, illustrated in Figure 7.14.

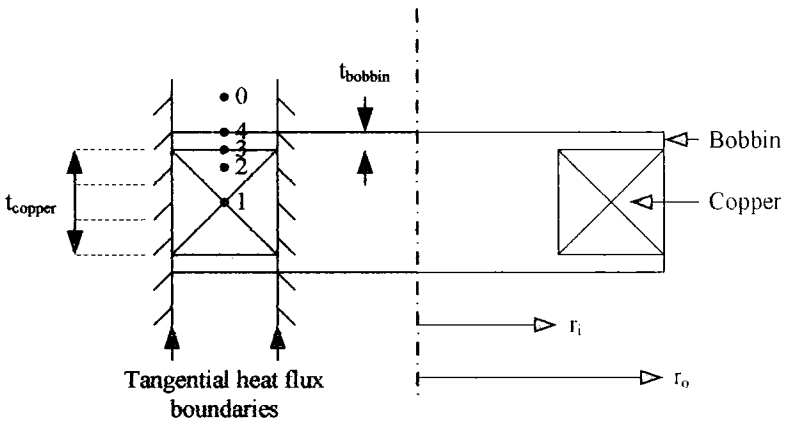

Figure 7.14: Axial heat transfer model of a coil

The thermal equivalent circuit for this model is shown, Figure 7.15.

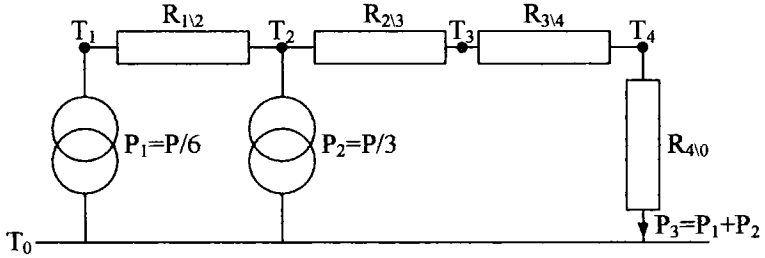

Figure 7.15: Thermal equivalent circuit

The equivalent thermal resistances depend on the appropriate geometry and the material properties:

$$R_{1\backslash 2} = \frac{t_{coil}}{3k_{copper}a}; \qquad R_{2\backslash 3} = \frac{1}{2}R_{12}; \qquad R_{3\backslash 4} = \frac{d_{bobbin}}{k_{bobbin}a}; \qquad R_{4\backslash 0} = \frac{1}{ha} \qquad \text{Eq. 7.32}$$

Where:

$$a = \pi\left(r_o^2 - r_i^2\right) \qquad \text{Eq. 7.33}$$

The surface heat transfer coefficient, h, requires experimental determination; the value used in the TORUS model is not extended to this analysis since the geometry, materials, and rated speed are all markedly different.

Once the total allowable power loss is obtained a deduction is made for eddy loss, calculated using the method outlined by Carter, [93], pp. 254-256., similar to that used in the analysis of the TORUS described in Chapter 3. The remaining allowable power loss is attributed to I^2R loss; a simple calculation of resistance based on the length of a turn at the mean radius, the number of turns per coil, and an assumed operating temperature of 80°C in line with the material properties concerned finally enables calculation of a current rating of 1.53A.

7.4. 3D FEA of the prototype machine

7.4.1. Modelling strategy

In this section a range of 3D models are used to verify the analytical methods previously described. The intention is to quantitatively compare the results of the analytical methods with FEA results and also to substantiate some of the approximations made in the development of the analytical methods. In particular, the FEA is used to visualise the fields arising in the prototype machine in a way that

conventional analysis and experimental test cannot, thus enhancing the understanding of the machine, its mode of operation, and its equivalent circuit parameters.

In this topology, the working flux acts in the axial direction, but it can be appreciated that there will be significant flux density variations across the pole-face in the circumferential and radial dimensions with respect to the rotors, owing to the geometry of the machine; the circular magnets impart this characteristic in particular. This variation will clearly be of a similar scale in both of these dimensions, so the assumption that the model can be represented as being infinitely long in either of these would result in significant inaccuracy. In short: this is a three dimensional problem that requires three dimensional analysis. The analytical method circumnavigates this by assuming the flux density at the axial centre of the machine to represent that over the full axial thickness of the coil, thereby collapsing the model to 2D.

Following the precedent set by previous analyses in this thesis, the field arising from the permanent magnets and that arising from phase currents is each considered separately. In both cases the fields are illustrated and the respective parameters are calculated such that equivalent circuit analysis may be carried out so as to predict the electromagnetic performance of the machine.

With 16 magnets and 12 coils, a quarter model of the machine in the circumferential direction is sufficient for the magnetostatic analysis, since this allows for the presence of a full three phases, and boundary conditions can be imposed to account for symmetry. It is also possible to model only half the axial length and impose a

normal flux condition across the resulting z-plane; this is effectively an iron boundary as used by the analytical method described in section 7.3.2. However, the coils would straddle this symmetry condition if their axial length was modelled in full. Since coils in 3D are accounted for by an automatic cut in the mesh which is replaced by a reduced scalar region this symmetry condition has been found to cause problems for the solver, so the full axial length is modelled. Figure 7.16 shows the entire model and a detailed view of the mesh.

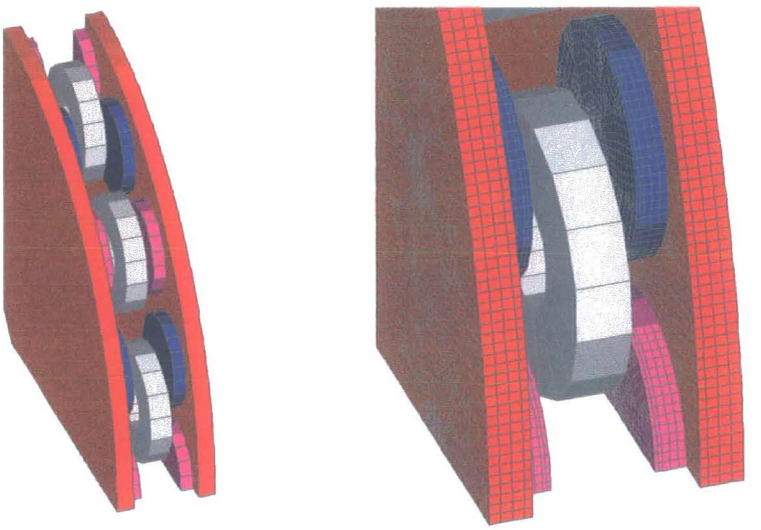

Figure 7.16: 3D magnetostatic FEA mesh of the machine

The correct boundary conditions can be implemented in a few different ways, and were set up here by defining various symmetry planes in the model. The outer, axially-oriented planes of the rotors have a tangential flux symmetry condition; this means that no flux crosses this boundary, which is the desired situation. Similarly, the planes at the radial edges of the model also have a tangential flux condition imposed.

The flux conditions in the model arising from the presence of the permanent magnets is shown in a 2D linear development of the model taking a radial view into the machine, Figure 7.17, illustrating the validity of this approach.

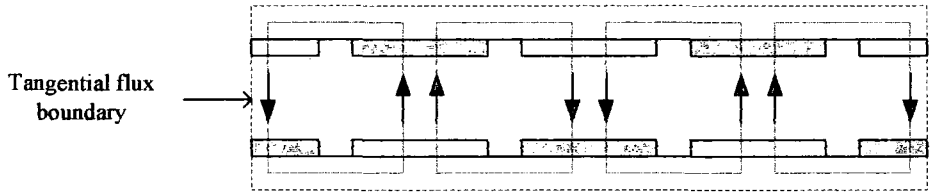

Figure 7.17: Symmetry conditions for the excitation field

The field arising from phase current is an even waveform in the circumferential direction, as has been described in section 7.2.3. The implication is that all the coils in a given phase are connected in the same direction, such that excitation of a single phase sets up flux patterns that can be modelled using tangential flux symmetry conditions in the fractional model described. This is illustrated in Figure 7.18.

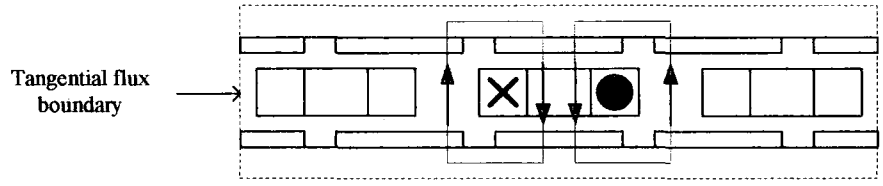

Figure 7.18: Symmetry conditions with single phase excitation

Were the machine operating under synchronous conditions, *i (A)* would flow in the central phase of the model, accompanied by *-0.5i (A)* in the two adjacent phases. Again, the tangential flux boundary conditions hold and this is shown in Figure 7.19.

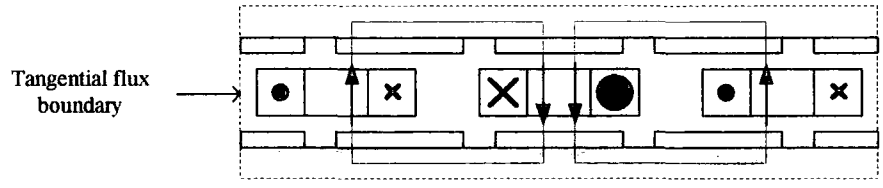

Figure 7.19: Symmetry conditions with three phase excitation

The outer circumferential edge is not bounded by iron, and so boundary conditions are more difficult to apply. With this in mind a region of air is modelled beyond the outer circumference of the machine, and the boundary conditions at the outer circumference of the air region are unspecified. The tangential flux symmetry conditions specified elsewhere are enough to make the problem unique, and the unbounded air region allows accurate analysis of end leakage effects.

The machine was designed for a flux density of less than 1T in the rotor discs, so saturation should not be a problem. Thus a linear solver can be used, which saves considerable processing time. The flux density in the rotors is later examined, to check that the machine operates in the linear region of the BH characteristic of the material.

7.4.2. Magnetostatic FEA of the excitation field

In this section, analysis of the field arising from the presence of the permanent magnets is described. The intention is to verify the quantitative predictions of the axial flux density at the axial centre of the machine. Also, the analysis is intended to substantiate the assumptions made in the analytical approach: that the field at the axial centre of the machine is equivalent to a sinusoidal *"hill"* of axial flux density in the (r, θ) plane with respect to the pole face, and furthermore, that the axial spread of the coil is of negligible importance in the evaluation of this flux density such that the field at the axial centre of the machine accurately represents that experienced by the whole coil.

The axial component of flux density arising from the presence of the permanent magnets is computed; this allows visualisation of the field for validation of the

analytical approach, and accurate evaluation of the field for verification of the analytical results. The coils are open-circuited with a zero current condition specified, and the problem is solved in the static state.

Since the machine is air-cored, the entire region between the rotor plates constitutes the effective air-gap and the axial field over the plane at the axial centre of the machine (exactly halfway across the effective gap) is illustrated and used for comparisons here. Values of axial flux density are obtained from the FEA, taken at the centroid of each element over this plane. The information can be illustrated directly within the FEA program as contours of B_z, with different colours representing the presence and respective flux density distributions of the north and south poles, Figure 7.20.

The field clearly exhibits significant spatial variation in the radial and circumferential dimensions, and it is the temporal variation of the axial field which induces EMF in the coils, thus affirming the 3D nature of the problem and confirming the need for a 3D approach.

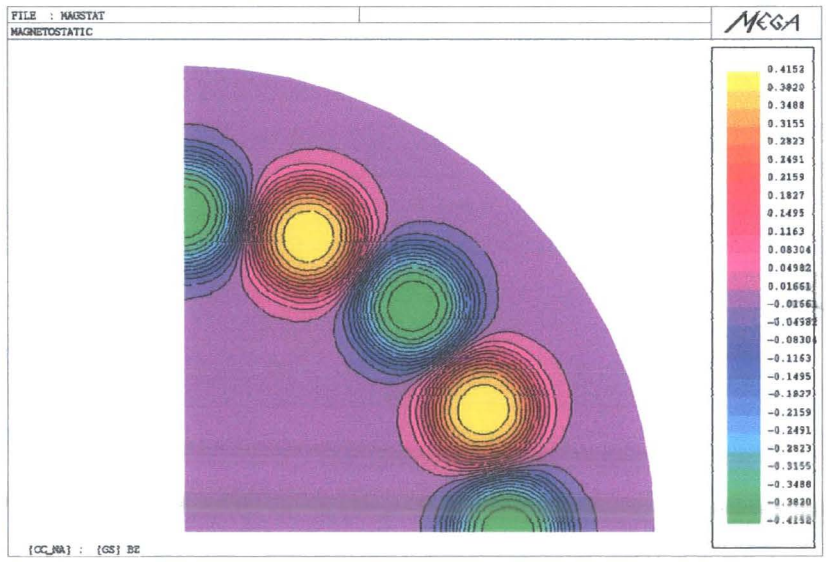

Figure 7.20: Contours of axial flux density arising from the permanent magnets

The Matlab routine described in Appendix 1 was used to transform this information into a regularly spaced *x-y* grid of B_z values that can then be displayed as a 3D mesh or surface, Figure 7.21. The results indicate a peak value of axial flux density arising from the permanent magnets of 0.42T at the axial centre of the machine.

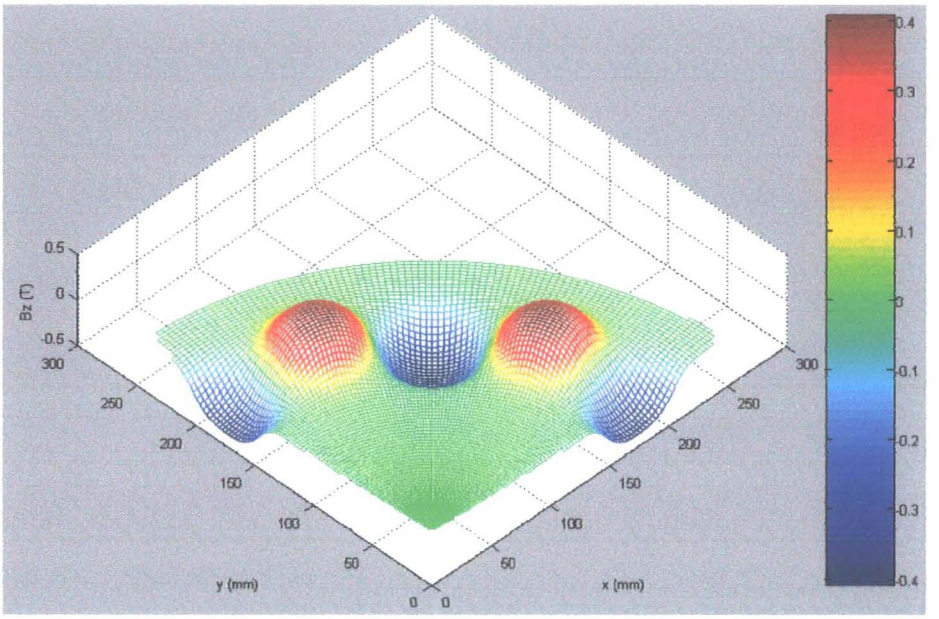

Figure 7.21: 3D FEA excitation field results: axial flux density in the stator region

As the 3D mesh of Figure 7.21 shows, the flux density surface at the axial centre of the machine is approximately a sinusoidal *"hill"*, verifying the analytical approach to some extent. Furthermore, Figure 7.22 shows a comparison between these FEA results and the predictions yielded by the analytical methods described in section 7.3.2.

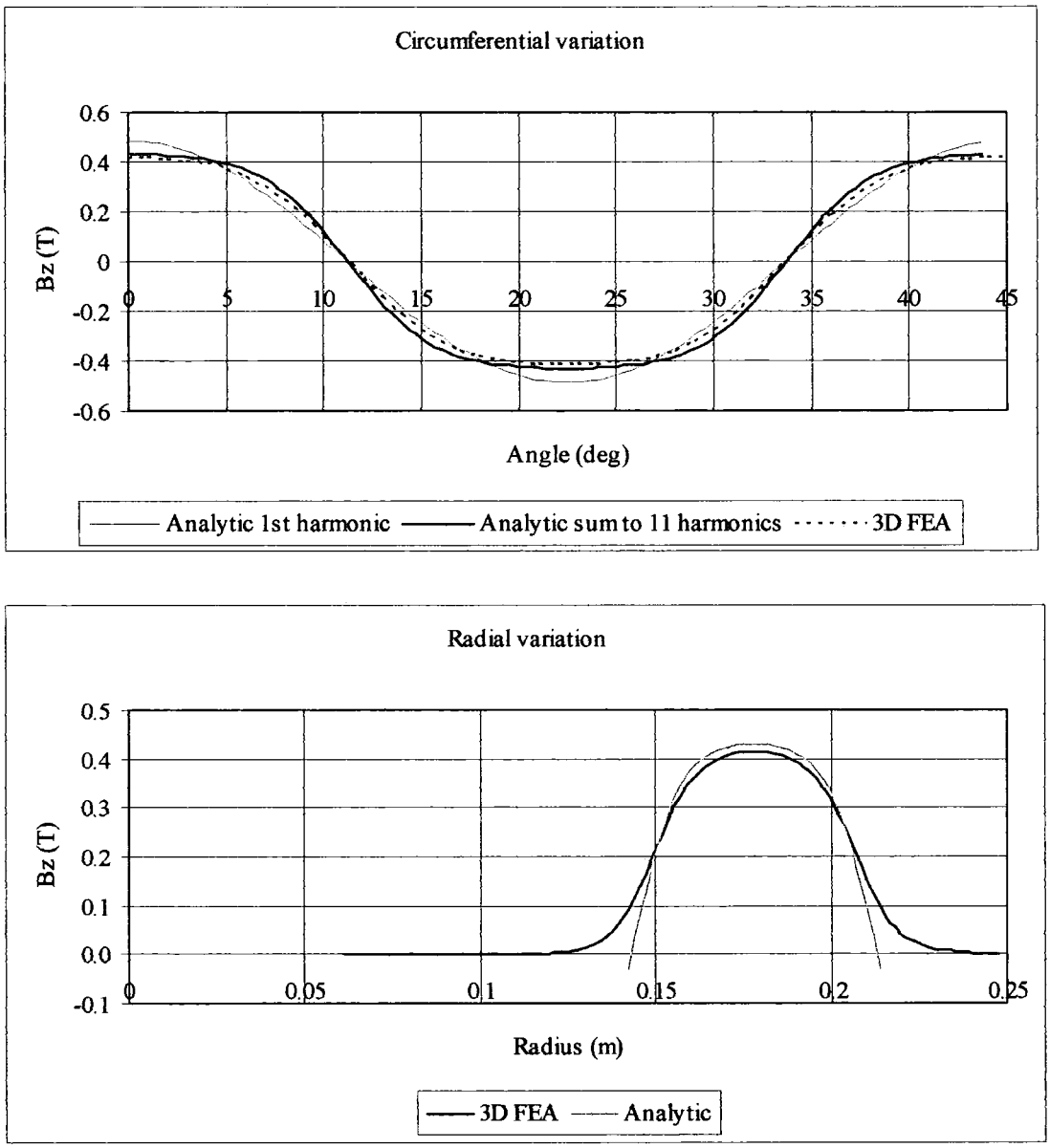

Figure 7.22: Comparison of FEA results with the analytical predictions

This shows good comparison between the two, although the radial variation obtained from FEA shows a tapering to zero at the edges, whereas the sine approximation is periodic and exhibits a changing polarity. The fact that the circumferential variation goes negative but the radial one only goes to zero in the real situation was accounted for in the analytical method by use of a flux enhancement factor.

Relative motion between the rotors and the stator coils would cause the coils to experience a varying flux in this field. If we assume that the coil experiences a flux that varies sinusoidally with time, the RMS value of EMF can be approximated by:

$$E_{coil} = 4.44 f N \hat{\phi} \qquad \text{Eq. 7.34}$$

Figure 7.16 illustrated the FEA model, which consists of three coils and four magnets per rotor disc. The central coil in the model is in the position for maximum flux linkage, since it sits directly between two magnet poles in the axial direction. Hence the voltage induced per coil may be approximated by obtaining the peak flux experienced by this coil from the FEA model and applying Eq. 7.34. The fundamental problem with this approach is that the peak value of flux linking this coil is difficult to define since the individual turns of the coil experience different amounts of flux.

Firstly, there is a range of turns with different radii. Turns close to the inner radius of the coil present a smaller area, and is logical that these will link a smaller amount of flux. Turns at larger radii present a larger area, but this does not automatically mean that they will always link more flux. The sinusoidal variation of flux density could cause turns at the outer extreme to experience flux linkage of the opposite polarity. This will be possible where the pitch of the turn exceeds the magnet pole pitch, which is a likely occurrence where more magnet pairs than coils are used.

Secondly, the field arising from the magnets varies axially in the machine. Close to the magnet faces there will be a certain quantity of flux that travels between adjacent magnets on the same rotor without crossing the gap. This inter-magnet leakage varies with axial position and at the axial centre of the machine it should equal zero, owing to symmetry. In the position for maximum flux linkage discussed here, this leakage

flux could still make a positive contribution to the EMF. The term leakage is used loosely, since the whole field could reasonably be described as a leakage field, so separating the leakage flux from the flux which makes a useful contribution is non-trivial.

In order to illustrate the effects described, a slice into the FEA model is made, directly across a pole face, such that a radial view into the machine at the mean diameter is provided, Figure 7.23. This also shows flux density vectors arising from the magnet excitation when the coil shown is in the position for maximum flux linkage, and clearly indicates these variations of flux linkage.

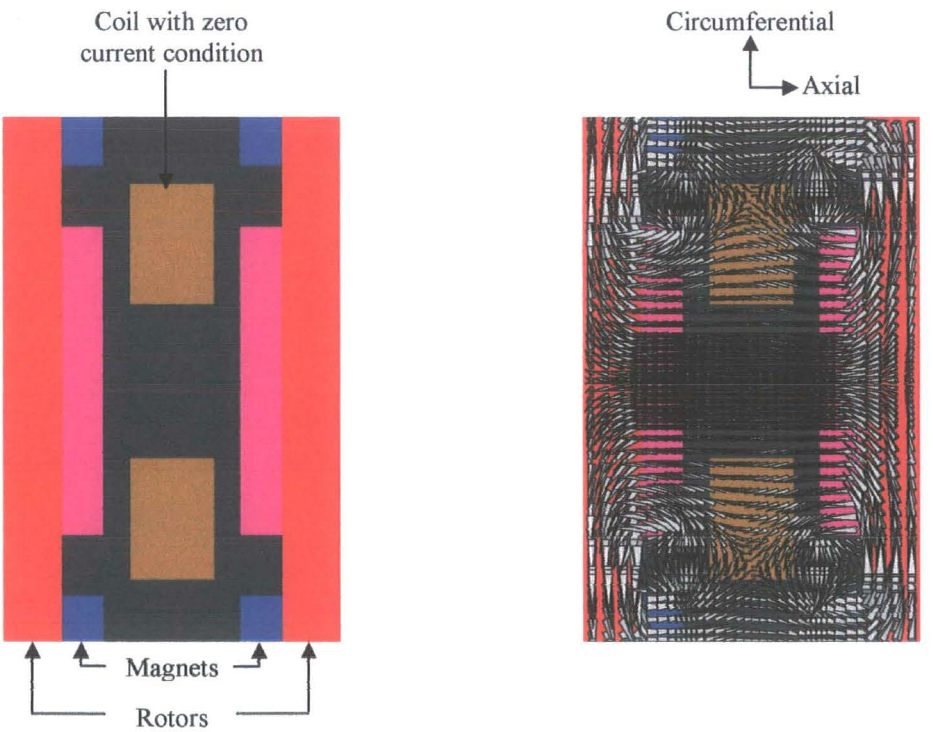

Figure 7.23: Axial variation of flux linkage

In order to quantify this variation, the EMF induced in the coil was calculated using Eq. 7.34, assuming the turns all to be located in a fixed position. A number of positions were analysed and so a range of values of induced EMF was calculated. The relevant planar surfaces were defined in the FEA model, and the previously

computed flux density integrated across the respective surfaces to give the flux which was assumed to link all concentrated turns equally in that position. A selection of surfaces covering the radial and axial dimension of the coil was defined like this and the induced EMF calculated from the resulting flux. Table 7.3 shows the results.

		Radial position		
	(EMF/coil/100RPM)	**Inner**	**Mean**	**Outer**
Axial Position	**Axial centre of machine**	4.28	12.7	16.7
	¼ axial distance across coil	4.25	12.9	16.7
	Centre of running clearance	4.28	12.7	16.7

Table 7.3: EMF approximations for various positions of average turn

It can be seen that the axial position of the turns has a very slight effect on the flux linkage but that the effect of the radius is much more pronounced. Taking the mean of the nine positions evaluated in Table 7.3 gives a value of 11.25V per coil per 100RPM. This compares well with the result of 11.21V obtained analytically by the manual summation method, and also verifies the assumption that the axial spread of the coil is of negligible importance and can be ignored in the analysis, but that the radial spread has a pronounced impact on the flux linkage and therefore must be accounted for.

The method of extending the FEA of the excitation field to calculation of the EMF described above is still only approximate, however. Firstly, the area for integration of the flux density vector may only be defined by discrete selection of constituent elements, thus the refinement of the mesh places a limit upon the accuracy of the result. Secondly, the manual averaging of the EMF arising from perfectly concentrated coils at various locations provides good comparison with the analytical approach, but is another layer of approximation. Finally, the supposition that the

approximately sinusoidal *"hills"* of flux density moving with respect to the stationary coils expose the same coils to a sinusoidally varying flux is not necessarily correct. In order to address these limitations, the next section describes dynamic analysis of the problem using 3D FEA.

7.4.3. Dynamic FEA of the excitation field

As described in section 3.4.3, periodic boundary conditions enabling fractional models of axial flux machines may not be implemented with disc-shaped sliding interfaces. Hence Figure 7.24 shows the FEA model spanning the full 360° and a close-up of the mesh detail for this air-cored machine.

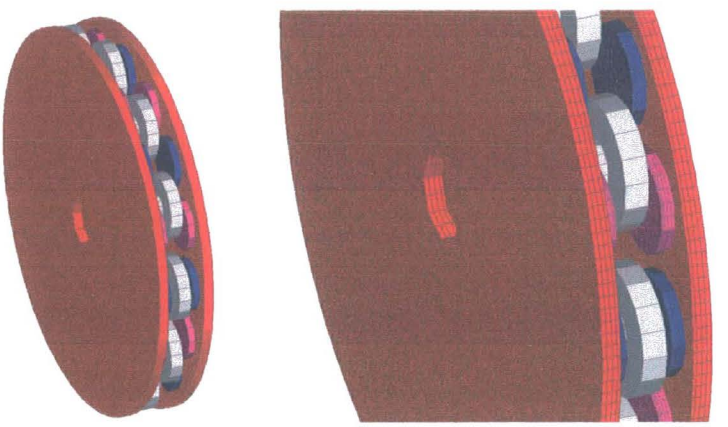

Figure 7.24: 3D dynamic FEA model and mesh detail

The solver returned the induced EMF in one coil of each phase for a rotational speed of 297RPM; this was for direct comparison with an experimental test result, run as close as possible to the rated 300RPM. Assuming the EMF waveforms to be sinusoidal, the mean RMS voltage induced per coil per 100RPM is given as 11.4V. Comparison with the more approximate result obtained by averaging the nine values given in Table 7.3 indicates that the approximation was in agreement to within 2%. The very basic analytical approach gave 10.95V, indicating an error of 4%, and the more sophisticated approach utilising a manual summation with a flux enhancement

factor gave 11.21V, indicating an error of less than 2%. Figure 7.25 shows the FEA-computed voltage waveforms per coil across the 3 phases at 297 RPM.

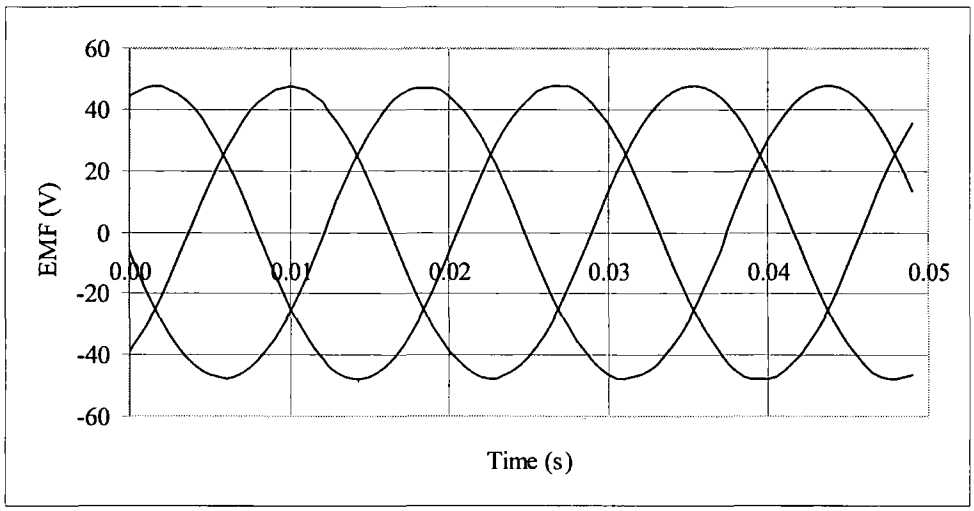

Figure 7.25: EMF induced in three adjacent coils at 297RPM from 3D dynamic FEA

The mesh is relatively coarse, as shown in Figure 7.24, owing to the restriction on periodic boundary conditions where the sliding interface is disc-shaped. However the analytical predictions and the FEA results are reassuringly close and the experimental results may yet provide further verification.

One potential approach which could allow for a more refined mesh would be to reduce the FEA model to a linear format by unwrapping the machine such that r, θ become y, x respectively. This was investigated in Chapter 4 for a slotted TORUS and is considered in Chapter 8 for a larger air-cored generator than the one considered here. With a larger diameter and many poles, the topology becomes more akin to a ring than a disc, and curvature becomes less important. With a linear mesh, the Lagrange surfaces are rectangular and symmetry conditions are accepted, resulting in the possibility of a fractional model and a suitably refined mesh.

7.4.4. Magnetostatic FEA of the field arising from phase currents

In the magnetostatic analysis of the field resulting from phase currents, the FEA model described in section 7.4.2 is used with some modification. The remanent flux density of the magnets is set to zero so that the excitation field is not present, but the permeability of the magnet regions remains, and the coils are energised with a range of current values. The aim is to visualise the field arising in order to verify the analytical approach described in section 7.3.3, and to analyse the harmonics in order to verify the principle of operation described in section 7.2.3. This analysis also permits the calculation of coil inductances and allows the equivalent circuit parameter X_{syn} (per-phase synchronous reactance) to be obtained.

Firstly, the 3 coils in the model are energised to synthesize an instant in synchronous operation. The central coil is energised with the current rating of 1.53A specified in the design spreadsheet, and the 2 adjacent coils are energised with half that current in the opposing polarity. The field is evaluated at the axial centre again, and is illustrated in Figure 7.26.

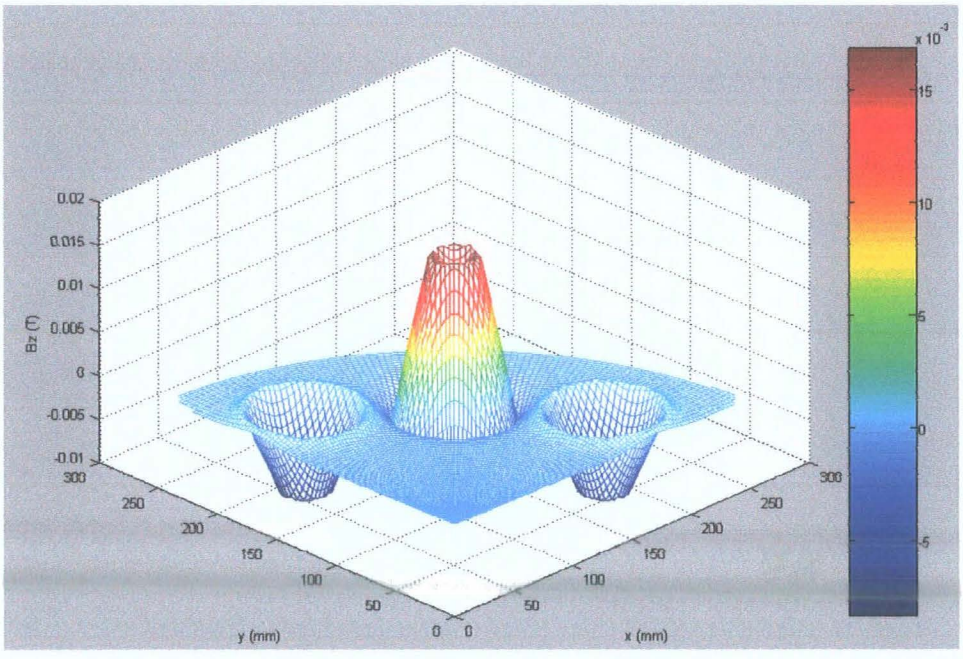

Figure 7.26: Surface of axial flux density arising from three-phase coil excitation

The profile of this flux density distribution is basically conical, with slight ripples around the base and peak of each cone owing to leakage effects. Each cone maps to the respective energised coil; the rising sides indicate the radial spread of each coil since the MMF driving the flux is a function of the number of turns, and the number of turns varies linearly between the inner and outer radii. Again, circumferential and radial variations of axial flux density taken at the mean diameter and across the centre of a coil respectively are shown in Figure 7.27.

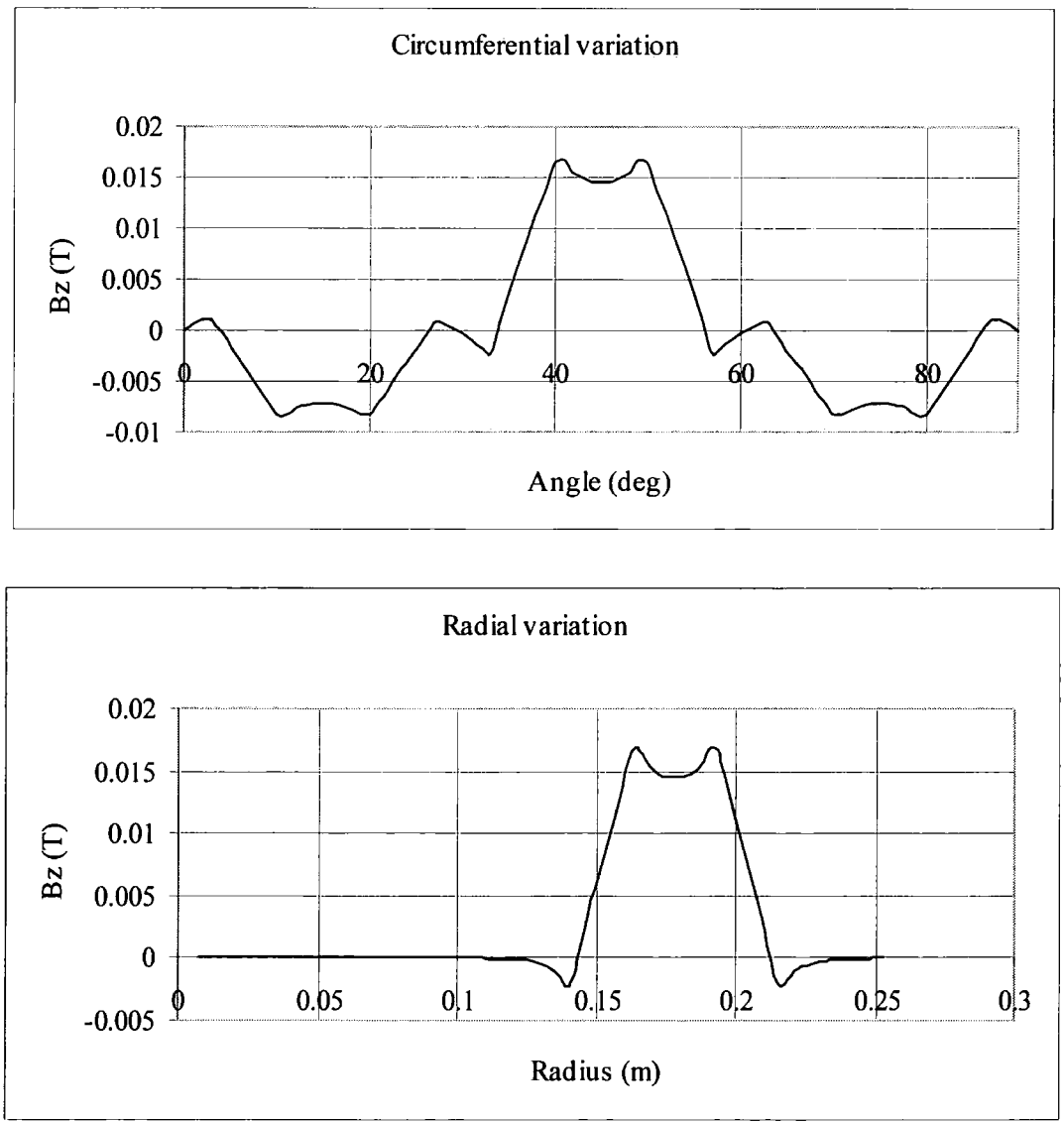

Figure 7.27: Flux density variations arising from three-phase coil excitation

Some axial variation of the flux density is expected in this field since leakage effects described and illustrated above affect the flux density profile, acting to increase the flux density at the coil. Figure 7.28 shows this variation, comparing the circumferential flux density profile taken at the axial centre of the machine with that taken at the rotor surface.

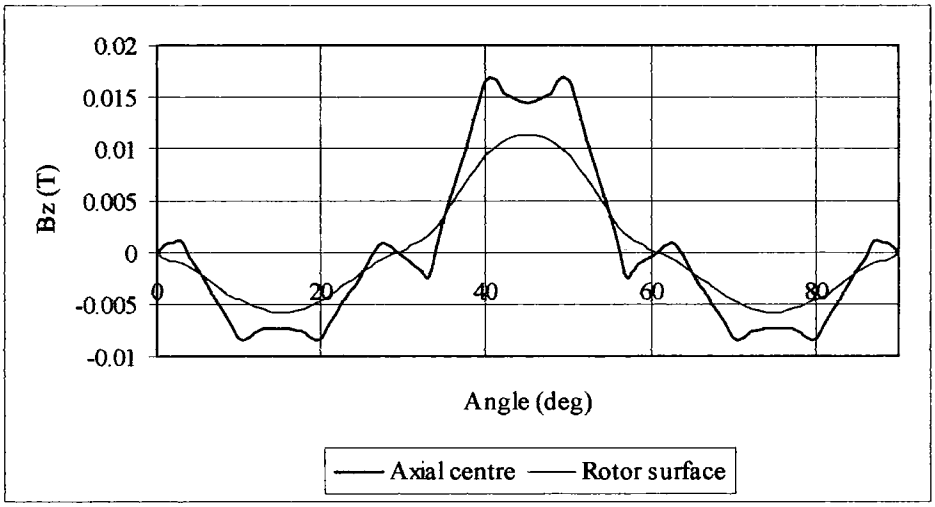

Figure 7.28: Circumferential flux density profile in different axial locations

A slice into the FEA model is made directly across the central coil such that a radial view into the machine at the mean diameter is provided, Figure 7.29. This displays flux density vectors arising from phase current and gives another illustration of the leakage effects described above.

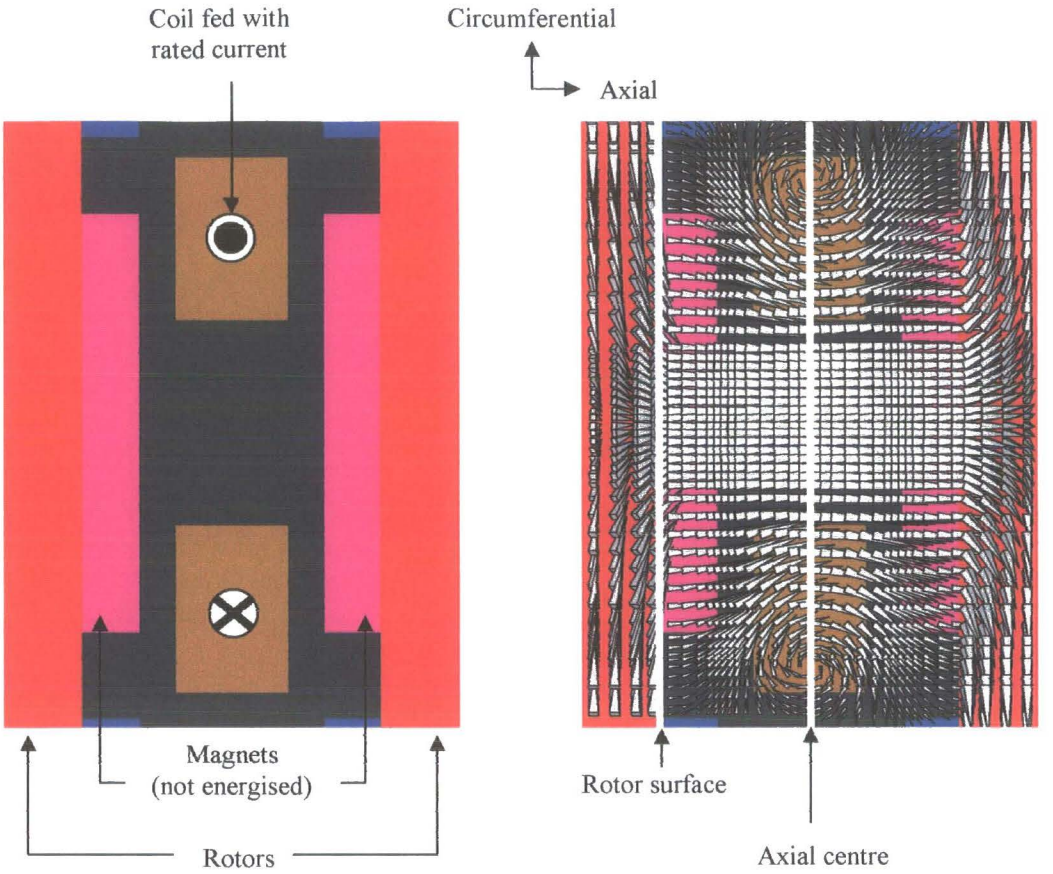

Figure 7.29: Flux density vectors arising from coil excitation

The circumferential variation of axial flux density, shown in Figure 7.27, is now used to determine the harmonic content of the static field arising from three-phase currents. As described in section 7.2.3, this field is should contain even harmonics. All the coils of a phase are connected up with the same polarity, such that the instantaneous pattern of Figure 7.27 simply repeats itself around the circumference without inversion. In order to undertake Fourier analysis of this waveform, a full period must be present and Matlab was used to assimilate this without recourse to extending the FEA mesh to 180° mechanical. The Fast Fourier Transform (FFT) command was then used within Matlab to calculate the different harmonic components in this waveform, and the magnitudes of the first few harmonics are

tabulated, Table 7.4. For clarity, the range 0 – 90° is reverted to, and Figure 7.30 shows how these harmonics combine to give the full waveform.

Harmonic number	Magnitude (T)
2	0.0078
4	0.0068
6	0.0000
8	0.0025

Table 7.4: Harmonic content of the field arising from three-phase currents

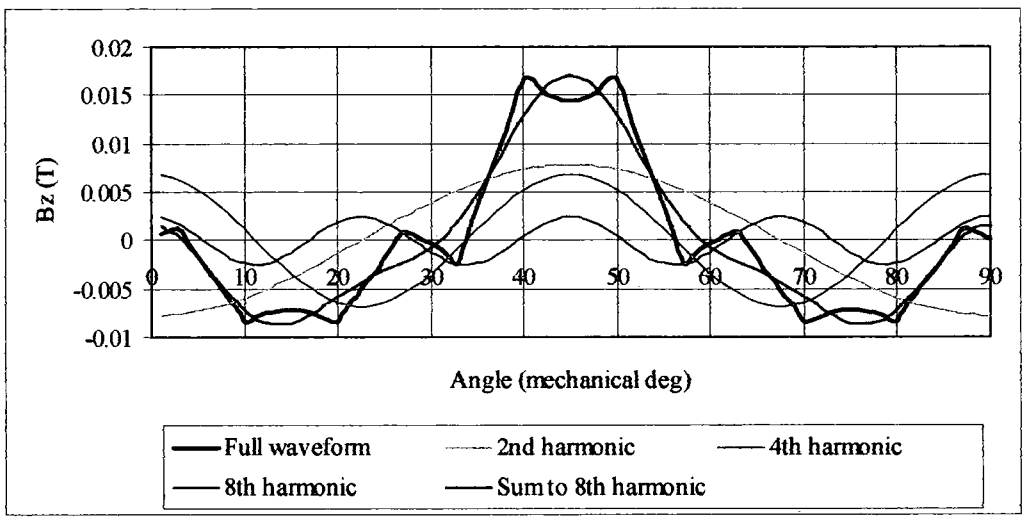

Figure 7.30: Fourier analysis of the field arising from three-phase excitation

So far, some assumptions inherent in the analytical approach have been substantiated, namely an essentially conical flux density profile with leakage flux paths around the coil causing the actual flux linkage to vary with the axial spread. Also, the principle of operation described in section 7.2.3 is corroborated to some extent, through demonstration of the harmonic makeup of the field arising from three-phase currents and the evaluation of a significant 4^{th} harmonic.

Now attention is turned to the synchronous reactance. The magnetostatic and the dynamic FEA models are both used to calculate this equivalent circuit parameter

using two different approaches, and the results are compared with the predictions of the analytical methods. Using the magnetostatic model, the back-EMF induced in a coil as a result of rated AC current passing in the same coil or in an adjacent coil is used to calculate the per-coil self and mutual inductances respectively, in the same manner as previous analyses. During 3-phase operation, a current of i in the central coil of the reduced model used here would be accompanied by $-i/2$ in each of the adjacent coils. The currents in the adjacent coils, although of negative polarity, set up fluxes that reinforce the flux of the central coil, and so the phase synchronous inductance is again composed of the self inductance of a phase and a component of mutual inductance arising from current in each of the other 2 phases. The resulting values per coil are: $L_{self}=4.311mH$; $M=0.278mH$; $L_{syn}=4.589mH$. This can be verified by simulating an instance of normal operation, passing i_{rated} through phase B and $-0.5i_{rated}$ through phases A and C, as per the field visualisation described above. The resulting EMF measured in phase B for a given current in phase B corresponds directly to the synchronous reactance, and the result is $L_{syn}=4.589mH$, as before.

Although the low winding impedance prohibits an experimental short-circuit test, this can be simulated by FEA using the dynamic model described in section 7.4.3. The individual coils are shorted and the simulation is run once again. The resulting short-circuit currents and the open circuit EMF per coil obtained in section 7.4.3 can then be used to calculate the coil impedance. Since the resistance is not accounted for in the FEA, this impedance is simply the per-coil synchronous reactance:

$$Z_{coil} = \frac{E_{coil\_open-circuit}}{I_{coil\_short-circuit}} = X_{syn\_coil} = \omega L_{syn\_coil} \qquad \text{Eq. 7.35}$$

Assuming the current waveforms to be sinusoidal, the mean RMS current is 43.8A, which yields a coil impedance of 1.09Ω and a synchronous inductance of 4.39mH. This compares well with the value of 4.59mH obtained from the more refined static model, indicating an agreement to within 5%. The values of open-circuit EMF and short-circuit current are averages between phases; slight variability was encountered between phases and is indicative of a mesh that is verging on the coarse side. This is thought to account for the discrepancy between the static and dynamic results overall, and the value from the more refined static mesh is assumed to be more accurate in the case of the inductance. Figure 7.31 shows the resulting short-circuit currents in three adjacent coils.

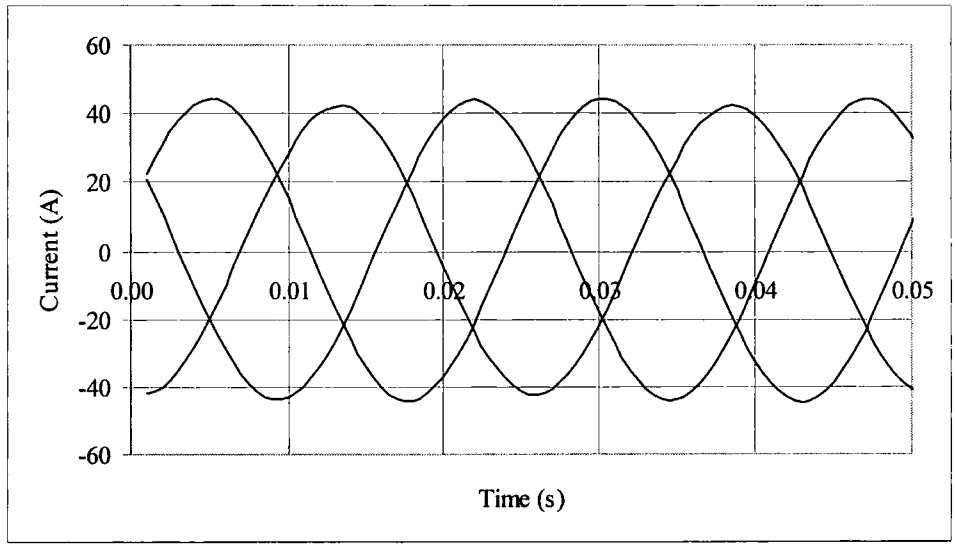

Figure 7.31: Short-circuit current per coil of each phase at 297RPM

7.4.5. Summary of the analyses

Table 7.5 shows the predicted equivalent circuit parameters of E and X_{syn} obtained from the FEA described in this section, and compares them with those obtained from the analytical approaches outlined earlier in this chapter; all values are per coil at 297RPM for comparison with the experimental test result described later.

	FEA	Rough analytical	Sophisticated analytical
E_{RMS} (V)	33.89	32.52	33.29
X_{syn} (Ω)	1.14	1.52	1.22

Table 7.5: Summary of the FEA and analytical predictions

These predictions show good agreement, particularly in the calculation of the open circuit EMF. The radial distribution of turns in particular has a pronounced effect on the calculation of reactance owing to the dependence of this parameter upon the number of turns squared; hence the assumptions made in the rough analytical approach concerning the field arising from phase currents give rise to the most pronounced disagreement in the predictions. Nevertheless, the predictions of the FEA and the sophisticated analytical approach were expected to show good agreement since the FEA verified some of the assumptions inherent in this analytical procedure, and the final values are reassuringly similar.

The thermal model outlined in 7.3.5 was based on the assumption that the operating temperature of the machine would be 80°C. Considering the coil geometry, the resistance can be calculated:

$$R = \frac{\rho l_{coil}}{a} = \frac{\rho\pi\left(D_{coil\_outer} + D_{coil\_inner}\right)N}{2a} \qquad \text{Eq. 7.36}$$

This gives a resistance of 1.21Ω per coil at operating temperature. The thermal analysis described in section 7.3.5 also yielded a rated current prediction of 1.53A for continuous, steady-state operation at this temperature.

These values complete the set of parameters required for the prediction of the performance of this prototype using the synchronous machine equivalent circuit described in section 7.2.3. The calculations were performed and the resulting

predictions are compared with the results of experimental tests described in the next section.

7.5. Experimental test of the prototype

7.5.1. Outline of the testing procedure

Two identical prototypes were built: one for testing in the laboratory, and one to be fitted to an existing wind turbine for field tests. Since the prototype was designed for vertical axis operation, the laboratory machine was also mounted in this configuration. In order to verify the FEA and analytical methods described in the preceding sections, static tests, open-circuit tests, and AC load tests were conducted by the author.

Static tests were performed on the stator prior to full assembly, and dynamic tests were performed using a specially designed test rig which utilised an induction motor with a variable speed drive, coupled to the generator on test by a belt drive. A Voltec power analyser measured the generator output, a Techtronix oscilloscope was used to capture the various waveforms, and a 3 phase resistor bank was used to load the generator to test loaded AC operation. Figure 7.32 shows the laboratory generator mounted on the test rig.

Figure 7.32: Prototype generator and laboratory test rig, [99]

7.5.2. Static tests

Static tests were carried out on the stator prior to the assembly of the machine. An inductance analyser was used to determine the resistance and inductance of each of the 12 coils at room temperature. Table 7.6 shows the results.

Coil	Resistance (Ω)	Inductance (H)
A	1.0655	0.005010
B	0.9990	0.004537
C	1.0115	0.004722
D	1.0245	0.004766
E	1.0510	0.005034
F	1.0050	0.004624
G	1.0000	0.004708
H	1.0035	0.004062
I	1.0045	0.004704
J	1.0145	0.004687
K	1.0515	0.005068
L	1.0095	0.004724
MEAN:	**1.0200**	**0.004721**

Table 7.6: Inductance analyser test results

Applying the temperature coefficient of resistivity, and the assumed operating temperature of 80°C yields an average resistance of 1.26Ω. Also, a laboratory test was carried out elsewhere in the department, [98], where a single coil was removed from the machine and indicated a hot resistance of 1.2Ω under artificial forced cooling conditions. Although it is difficult to make a close comparison without testing during actual machine operation at a precise temperature, these results compare well with the analytical prediction of 1.21Ω.

The inductance tests were carried out with the stator core sandwiched between two strip-wound cores from another project, with spacers to account for the permanent magnet thickness and the running clearance. Strip-wound cores were used instead of the rotors of the machine in order to limit eddy currents arising from stationary components subjected to an AC field since, in normal operation, the rotors and the stator field should be stationary with respect to one another. This is the same approach used in the TORUS testing described in Chapter 4, and was used for the same reason: namely that the low inductance of this genre of machine prohibits performance of the conventional short-circuit test

It should be noted that the flux conditions created by energising a single coil are not the same as those encountered when a whole phase is energised. With a single coil the return path the flux takes across the air-gap is bounded only by the dimensions of the entire machine; the energisation of a full phase results in the tangential flux boundaries shown in Figure 7.18, thereby restricting the return path rather more. As illustrated in Figure 7.12, the return path is expected to have a much lower reluctance than the primary path and so this test is likely to give a good indication of the inductance.

7.5.3. Open-circuit tests

In order to obtain the open circuit characteristic, the phase EMF was measured with the 4 coils of each phase connected in series. This was carried out across a range of speeds and the resulting characteristic is shown in Figure 7.33. The gradient of the graph indicates an open-circuit EMF of 11.03V per coil per 100RPM.

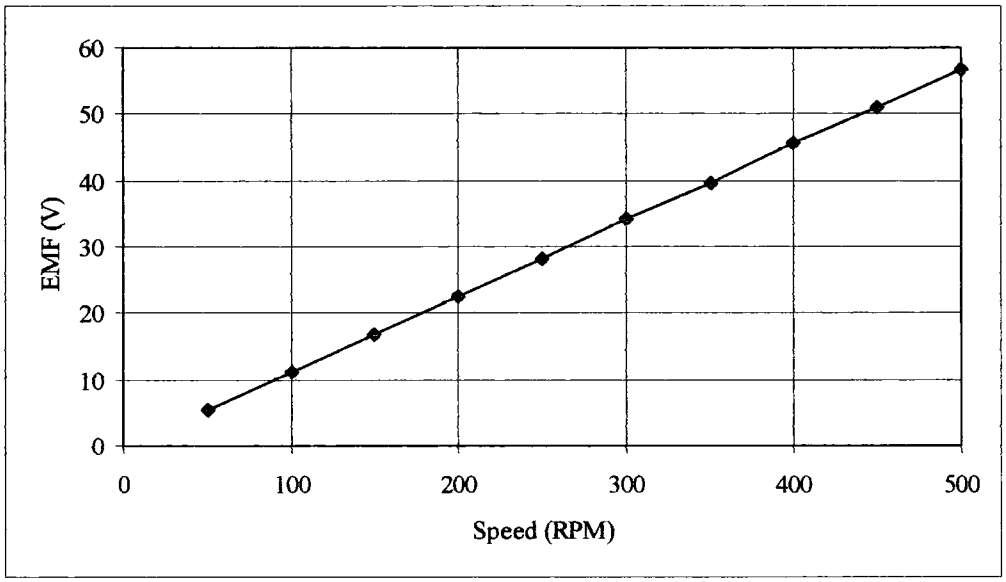

Figure 7.33: Induced EMF per-coil from open circuit tests (RMS values)

The actual 3-phase voltage waveforms of the open-circuit EMF measured across 3 adjacent coils at 297RPM were also captured using a Techtronix oscilloscope, and these are compared directly with the results of the 3D dynamic FEA simulation in Figure 7.34.

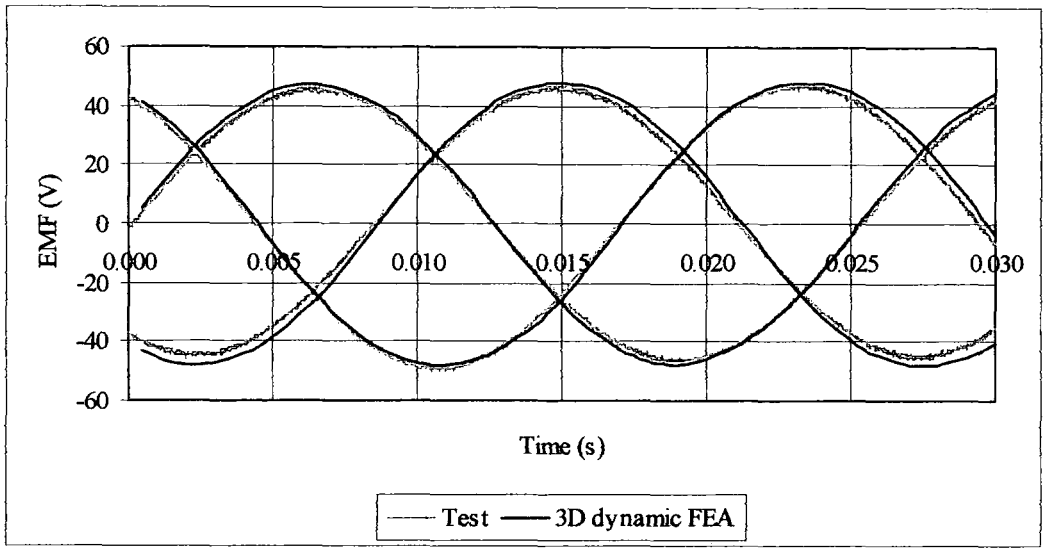

Figure 7.34: Test result and FEA prediction of open-circuit EMF at 297RPM

7.5.4. Equivalent circuit parameters: results compared with predicted values

Table 7.7 compares the results of the static and open-circuit dynamic test results with the predictions of the FEA, the simple analytical, and the manual summation version of the more sophisticated analytical methods.

	E_{RMS} per coil per 100RPM (V)	X_{syn} (Ω)
Test result	11.03	1.17
FEA	11.4	1.14
Error	3%	3%
Rough analytical	10.95	1.52
Error	1%	30%
Sophisticated analytical	11.21	1.22
Error	2%	4%

Table 7.7: Equivalent circuit parameters

7.5.5. Load tests

Finally, load tests were performed the four coils of each phase connected in series. A 3-phase resistor bank was used to run zero power factor load tests directly from the generator's AC output at speeds between 100 and 500RPM, taking voltage and current readings across a load range in keeping with the predicted thermal limits. An infra-red temperature gun and an array of thermocouples at various locations in the stator were used to monitor the temperature. Figure 7.35 compares the experimental results with the predictions using the equivalent circuit parameters obtained from FEA and the resistance approximation.

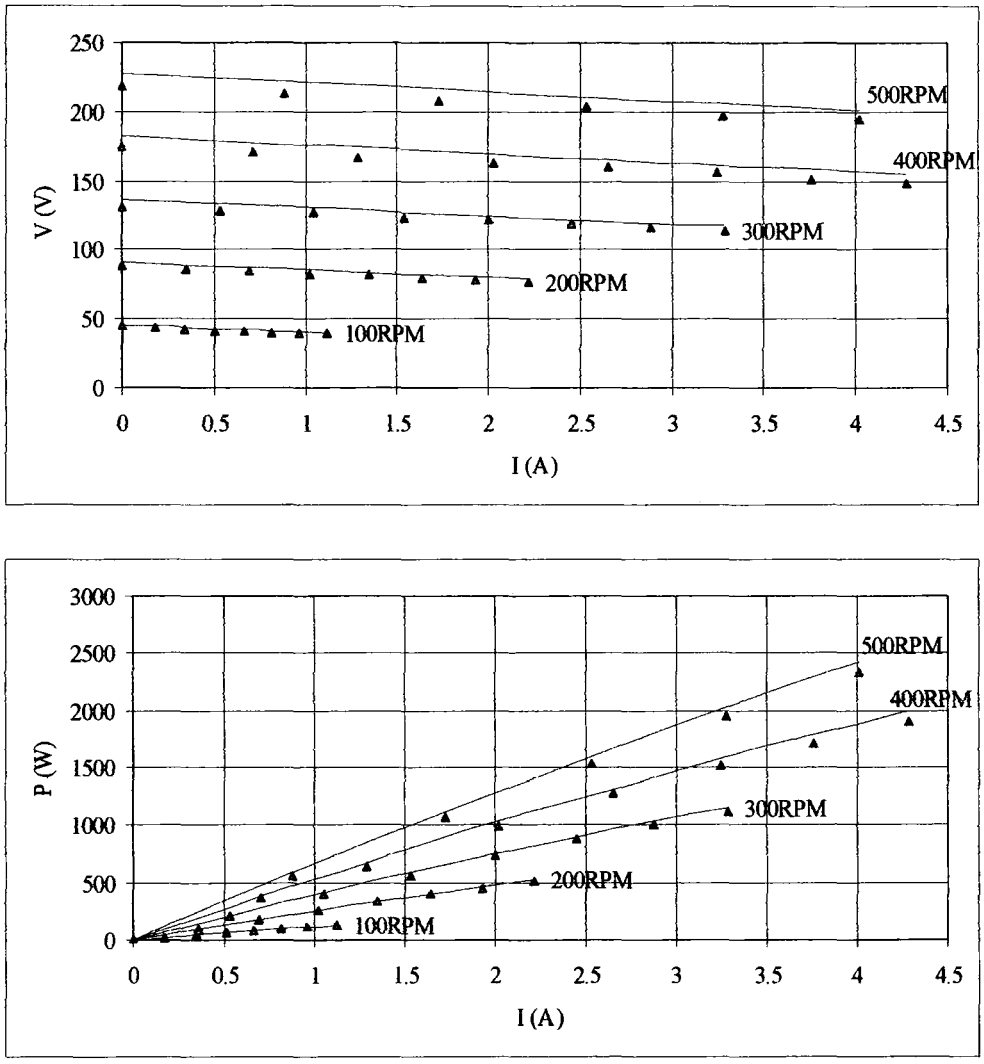

Figure 7.35: Terminal voltage against current and power against current (— predicted, ▲ test values)

The main loss in the machine is I^2R loss arising from the winding resistance. The absence of a stator core means that iron losses are non-existent, and eddy losses in the conductors are expected to be minimal owing to the narrow gauge wire used. Efficiency characteristics are thus obtained from the on-load tests and the static resistance measurements, using:

$$\eta = \frac{P_{out}}{P_{in}} = \frac{P_{out}}{P_{out} + P_{loss}} = \frac{P_{out}}{P_{out} + 3I^2 R_{phase}} \qquad \text{Eq. 7.37}$$

These are shown in Figure 7.36.

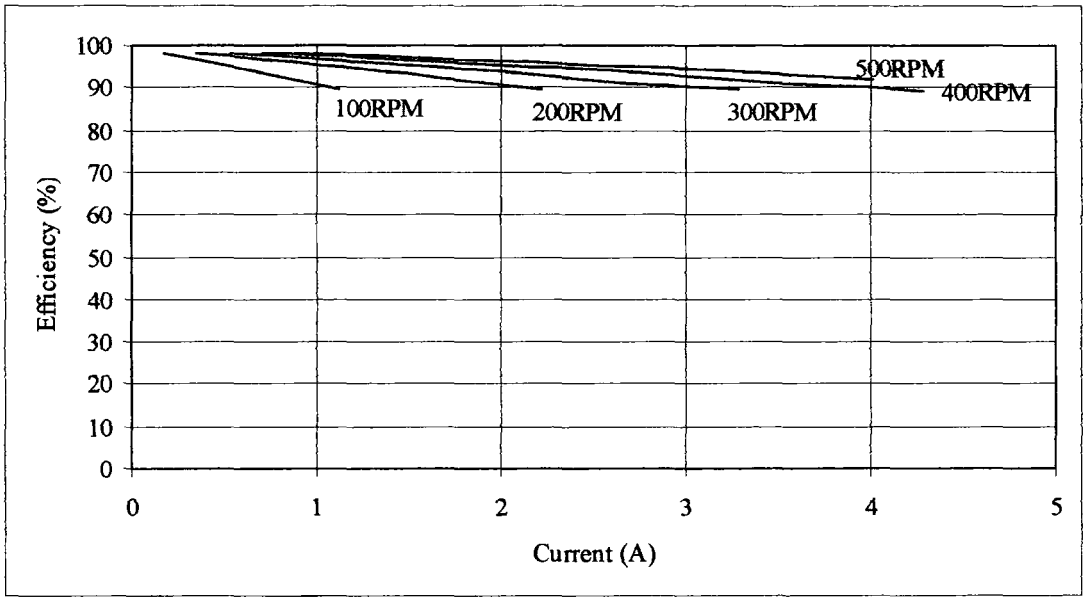

Figure 7.36: Electrical efficiency characteristics obtained from load tests

7.6. Discussion

In this chapter, a novel axial flux machine was introduced, [6], [7]. The machine was specifically designed for small VAWTs, and produced in collaboration with two local engineering firms. The design has a topology similar to machines described in previous chapters, but there are two principle differences. Firstly, the paths of the working flux in the new machine are purely axial, as opposed to the circumferential

paths through the stator exhibited by the TORUS and its slotted relations. Secondly, to make best use of the resultant field whilst making the winding as simple as possible, the stator was conceived as a plastic disc in which bobbin-wound concentrated coils are mounted, resulting in an air-cored design. The requirements of the small VAWT application were described and an appropriate specification for a suitable generator was described. The novel topology was then detailed in terms of its principle of operation, its geometry, and the design and construction of a prototype machine.

The overarching aim was to extend the FEA modelling techniques developed in previous chapters to this new design in order to validate the assumptions inherent in the analytical techniques used for the design and analysis, to provide quantitative verification of the analytical predictions, to investigate the mode of operation of the machine, and to enhance the understanding of its electromagnetic behaviour. The analytical methods for verification are described in a recent publication on the original design of this machine, [6]. These were outlined here and a simpler, robust analytical approach was derived in order to provide rough corroboration of the FEA as the models were developed. Finally, experimental testing of a prototype machine was described and the outcomes compared with the predictions of the FEA in order to complete the investigation. FEA of the excitation field supported the predictions of the analytical method, showing agreement to within 2%. Also, this facilitated visualisation of the field and corroboration of certain assumptions, namely that the excitation field experienced by the coil is a sinusoidal *"hill"* of axially-directed flux density, that the radial spread of the turns of each coil has a marked effect on the flux linkage and the resultant induced EMF, and that the axial spread of the coil is comparatively unimportant. Furthermore, the force of attraction between the rotors

was calculated. It was shown that this depended upon the magnitude of the flux density and the area over which this flux density was present. Since the TORUS exhibited a flux density of a similar magnitude and was a similarly-sized machine, it is unlikely that this new design presents a significant reduction in these forces of attraction. However, the protection afforded to the winding, the fact that the rotors are physically separated from one another by the plastic stator, and the increased separation of the two parts still offers significant improvements over the TORUS in this application. Certainly, the slotted relations of the TORUS are at an overwhelming disadvantage in terms of attractive forces owing to the higher flux densities present in that topology. Similarly, FEA of the field arising from phase currents facilitated visualisation of the field, and Fourier analysis of this gave an insight into the mode of operation of the machine, in particular the transfer of torque on higher-order harmonics. The visualisation of the field also corroborated the assumption that the radial distribution of the turns gives rise to a conical variation of axial flux density in the air-gap. This verified the analytical approach to some extent, whilst the quantification of the synchronous reactance of the machine showed agreement between the analytical and FEA predictions to within 10%.

Finally, the conclusions of the experimental tests were twofold. Firstly, the results showed agreement with the analytical and FEA predictions to within 5%, giving confidence in the extension of these approaches to further designs. Secondly, the prototype machine was demonstrated to perform as required by the application, producing in excess of 2kW at 500RPM and in excess of the rated 1kW at 300RPM. Both of these results were demonstrated with efficiencies in excess of 90%. In the following chapter, a case-study of this generator in the VAWT application is given and some further applications of the novel topology are described.

Chapter 8. Further applications of the novel air-cored machine

In the previous chapter, a novel axial flux topology, [6], [7], was described. A prototype machine designed and built by Wong as a final year MEng project in the School, [99], was detailed and used by the author to develop and benchmark a range of analytical and FEA approaches alongside the results of experimental tests on the prototype. The results showed that the novel topology performed as expected with high efficiency and that the analytical and FEA methods agreed with the results of experimental tests to within 5%.

This is the final topology considered in this thesis, which has seen the development of analytical, experimental, and finite element approaches for the analysis and design of a range of axial flux machines for direct-drive applications. The well-established TORUS machine with its air-gap winding was the starting point; slotted versions of the TORUS were then considered prior to the development of a design procedure for more original slotted machines, and the final concept was an air-cored machine with concentrated coils. From an applications perspective, the approach started with developmental work on the TORUS for use in diesel-engine generator sets followed by an investigation of slotted axial flux machines to evaluate the potential for improved performance and increased power density in the same application. Finally, consideration of the transfer of these machines to the VAWT application led to the examination of the air-cored machine with concentrated coils, which improved upon many of the shortcomings identified in the machines previously considered.

The air-cored machine proved successful in that it performed well and the experimental, analytical, and finite element results agreed to a good level of accuracy. Therefore this topology is the subject of ongoing research both in the VAWT application and in alternative applications, and three further incarnations of it are considered in this chapter prior to the conclusion of the thesis. Each of the three offers something new in terms of either a particular design nuance, extension to a new application, or the finite-element approach required as a result of these advances.

Firstly, since the development of the generator for the Savonius wind turbine, a number of other wind turbine manufacturers and researchers in this field have shown an interest in this machine in the wind turbine application and in a variety of VAWTs in particular. This has inevitably led to the consideration and specification of larger designs with different pole and coil numbers. Whilst the diameter of the designs increased considerably, the effective air-gap reduced in proportion. This arose from some initial design optimisation and resulted in a specification that was much more difficult to model in finite elements. The large overall size of the machine coupled with the small dimensions of the active area, particularly in the axial dimension, made gradation of the mesh very awkward and thus placed considerable demands on the computational capacity available. This was compounded by the requirement for a model of the full machine where disc-shaped sliding interfaces were used. The original design for the Savonius was only just capable of being analysed using disc-shaped sliding interfaces, but the computational requirements of the larger design prohibited comparable dynamic solutions.

Therefore, linear finite element models of a fraction of the machine were devised to overcome this problem and magnetostatic results compared with those from disc-shaped models, prior to dynamic modelling. Section 8.1 describes the new design, benchmarks the linear model along side a disc-shaped model in the magnetostatic case, and uses the more refined linear model to predict the performance of the design from both magnetostatic and dynamic solutions. These predictions are once more supported by the results of analytical calculations.

Secondly, axial flux machines have achieved prominence in an application quite different to those considered so far in this thesis, namely as a motor for solar-powered cars. The geometry, high efficiency, and large starting torque available through the naturally large radius of permanent magnet axial flux machines, renders them ideal as in-wheel motors in this application. When the School of Engineering at Durham University mooted the idea of a solar-powered car for secondary school demonstrations and as a prototype racing car, the novel topology of Bumby, [6], [7], was deemed to offer many of the benefits of the design of Lovatt et al, [65], but in a format that could feasibly be realised in the School's mechanical engineering workshop at minimum cost. The increased importance of a lightweight machine with the maximum power density achievable in this application led to a modification to the original prototype in the form of trapezoidal magnets and coils. This represents a move back to the principles of the TORUS, which makes the design slightly more complex but is advantageous in that it decouples the radial length of the active area from the number of poles to some extent, resulting in a more optimised design in line with the work of Campbell, [13]. The move back to trapezoidal poles also improves the resultant flux density profile, moving away from the sinusoidal *"hill"* exhibited in the case of the Savonius generator to a profile that may more accurately be

approximated as infinitely long in the radial direction, thereby simplifying the analysis. It also requires a slight modification to the FEA approach and section 8.2 describes the models devised and used in this analysis.

The disadvantage rests primarily with the coils, since concentrated coils are more difficult to form in this shape and are perhaps less optimal in terms of the ratio between the length of a turn and the magnitude of flux it links. However, the difficulties in making such a machine were overcome and a prototype built in the School. Some open-circuit tests were performed with the machine operating in its generating mode and the results compared with analytical and FEA predictions, also in section 8.2.

Finally, section 8.3 presents a combination of the principles outlined in the previously in the chapter, namely a move to a significantly larger machine for the VAWT application which utilises trapezoidal poles and coils much like the motor designed for the solar-powered car. As the size of the Savonius generator is stretched, and the rotational speed of direct-drive turbines reduces owing to the increased power rating, the number of poles required increases and this inevitably yields a design which consists of a narrow strip of active area situated at a large diameter. Such a design is visibly wasteful of the volume and material it requires, owing to the considerably large amount unused within the inner radius. Two methods of addressing this were considered: firstly, rotor and stator designs which were more ring-shaped as opposed to disc-shaped, thereby limiting the unused material; secondly, employment of trapezoidal poles and coils so as to extend the radial length of the active area.

The resulting design and analytical predictions are summarised, and an approach to the FEA modelling is described. Since the radius is still large, as is the pole number, curvature is less pronounced and this design is especially suited to a linear approach. This makes the modelling of the coils rather simpler by comparison with the motor design and the results are presented and compared.

8.1. Analysis of a 7.5kW air-cored machine

8.1.1. Introduction

This section considers a design specification similar to that described in Chapter 7 for the Savonius wind turbine. In this case, the design was drawn up at the request of a consultancy firm specialising in mechanical engineering that has developed a novel VAWT with significant advantages over traditional turbines of this type. Once again, the light, simple, efficient, and easily manufactured design of Bumby, [6], [7], is highly suited to the application and the firm involved was keen for a study to commence that would yield a generator design suitable for their turbine, with some FEA verification of the design predictions. The turbine is rated at 7.5kW based on an operating speed of 132RPM (dictated by optimal aerodynamic operation of the turbine) and the resulting generator design parameters are summarised in Table 8.1.

Number of magnets per rotor disc	32
Number of coils	24
Rotor ring inner diameter (mm)	1000
Rotor ring outer diameter (mm)	1140
Rotor thickness (mm)	9
Magnet diameter (mm)	70
Magnet thickness (mm)	10
Pole pitch at mean radius (mm)	105
Pole arc to pole pitch ratio	0.67
Stator outer diameter (mm)	1200
Stator thickness (mm)	25
Coil outer diameter (mm)	130
Coil inner diameter (mm)	40
Coil height (mm)	21
Number of turns/coil	499
Running clearance (mm)	2
Magnet-to-magnet gap (mm)	29

Table 8.1: Design summary for a 7.5kW 132RPM machine

8.1.2. Analytical performance predictions

The analytical methods outlined in Chapter 7 are used to predict various electromagnetic parameters such as the flux density arising in the air-gap from the permanent magnets mounted on the rotors, the peak excitation flux linkage, and the EMF induced in each coil at rated speed. Again, three approaches to the calculation of EMF are used: firstly, assuming all the turns of a coil to be concentrated at the mean radius; secondly, splitting the turns into three portions each concentrated at different radii within the coil and performing a manual summation; finally, representing the radial spread of the turns analytically through the application of a linear turns function, and performing an integration. Of the three methods, the manual summation involving three portions is preferred since it takes some account of the radial spread of the coil, which was shown in Chapter 7 to have a pronounced effect on the flux linkage, and also because it can be modified by means of a flux

enhancement factor to compensate for inaccuracy arising from the sinusoidal representation of the field. The predictions concerning the excitation field are summarised, Table 8.2.

Flux density:	
Peak [magnetic circuit calculation] (T)	0.470
Peak [at axial centre, full analytical solution] (T)	0.484
Mean [assuming a sinusoidal distribution] (T)	0.31
Concentrated coil:	
Induced EMF per coil (V)	136.0
Coil in three portions:	
Flux through inner segment (mWb)	0.972
Flux through middle segment (mWb)	1.74
Flux through outer segment (mWb)	1.87
Flux enhancement factor	1.05
Induced EMF per coil (V)	121.6
Full analytical:	
Bore flux linkage (Wb-turns)	0.282
Flux linkage within the coil (Wb-turns)	0.468
Induced EMF per coil (V)	117.2

Table 8.2: Analytical predictions of the excitation field

The flux density predictions of the various methods are compared, Figure 8.1.

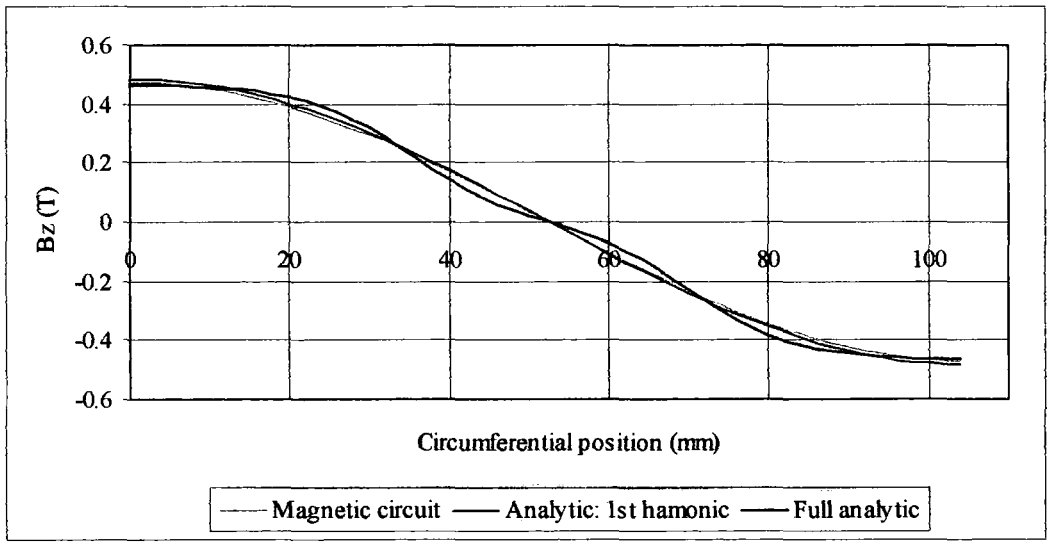

Figure 8.1: Predicted flux density variation experienced by the coils

Similarly, using the three methods for calculating the inductance per coil as outlined in Chapter 7, the coil self inductance is calculated. The mutual effects are ignored and the operating electrical frequency factored in so as to give the contribution of a single coil to the synchronous reactance of the machine. The predictions are summarised, Table 8.3.

Flux leakage factor	1.1
Concentrated coil:	
L coil (mH)	40.95
X_{syn} per coil (Ω)	9.05
Coil in three portions:	
Inner inductance (H)	5.72
Middle inductance (H)	11.01
Outer inductance (H)	14.78
L coil total (H)	31.51
X_{syn} per coil (Ω)	6.96
Full analytical:	
Bore inductance (H)	9.07
Inductance within the coil (H)	21.26
L_{coil} total (H)	30.33
X_{syn} per coil (Ω)	6.70

Table 8.3: Analytical inductance predictions

Lastly, a thermal model along the lines of that described in Chapter 7 is used to model the heat transfer characteristics of steady-state operation so as to obtain an allowable loss per coil. Some approximate calculations of eddy loss in the conductors along with data concerning the material properties involved and a specified operating temperature enables the calculation of a maximum operating current, and thus the equivalent circuit characteristics of a single coil are calculated. The relevant results are summarised, Table 8.4.

Ambient temperature (°C)	18
Operating temperature (°C)	85
Surface heat transfer coefficient (W/m²/°C)	40
Eddy current loss/coil (W)	4.35
Allowable I²R loss per coil (W)	25
Resistivity at operating temperature (Ωm)	2.11E-08
Coil resistance (Ω)	2.30
Rated coil current (A)	3.31
EMF per coil (V)	121.6
Terminal voltage per coil [AC resistive load] (V)	111.0
Power output per coil (W)	368

Table 8.4: Heat transfer and equivalent circuit characteristics per coil

The equivalent circuit parameters are calculated on a per coil basis since the coil connections can be altered according to the requirements of the load. This was described in Chapter 7 in the case of the Savonius, where the coil terminations were made away from the machine such that different series and parallel configurations could be investigated. In this case, four parallel branches of two series-connected coils give an appropriate per phase voltage and current output, and the equivalent circuit parameters are shown in Table 8.5 along with the predicted peak performance of the design. Figure 8.2 shows some graphical predictions of the performance across the operating range.

EMF per phase (V)	243.2
Phase resistance (Ω)	1.14
Phase reactance (Ω)	3.48
Phase current (A)	13.25
Terminal volts per phase (V)	209.2
Total power output (W)	8177
Total I²R loss (W)	600
Total eddy loss (W)	104
Efficiency (%)	92.2

Table 8.5: Machine equivalent circuit parameters and peak performance prediction

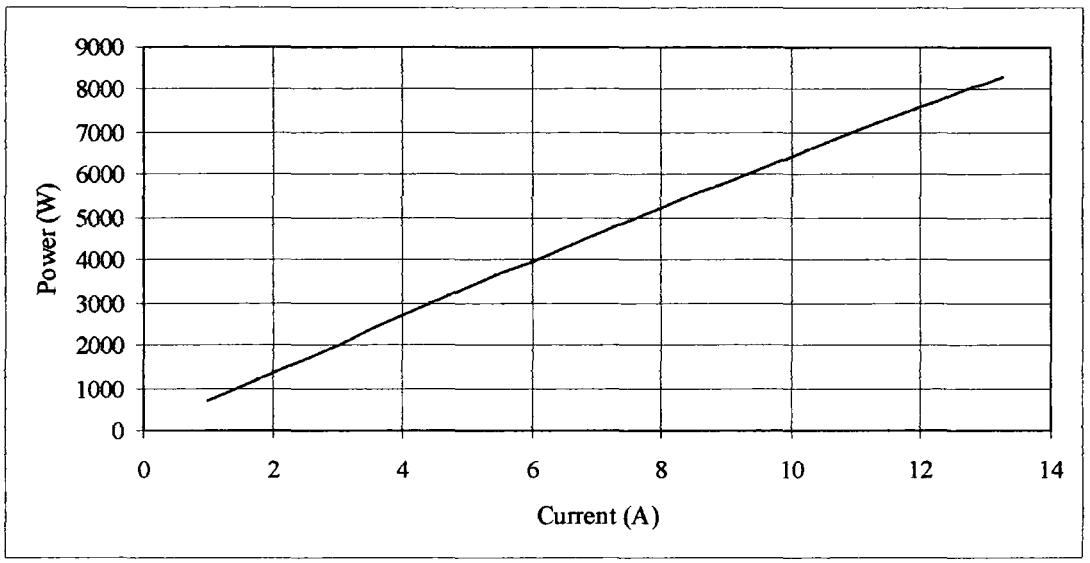

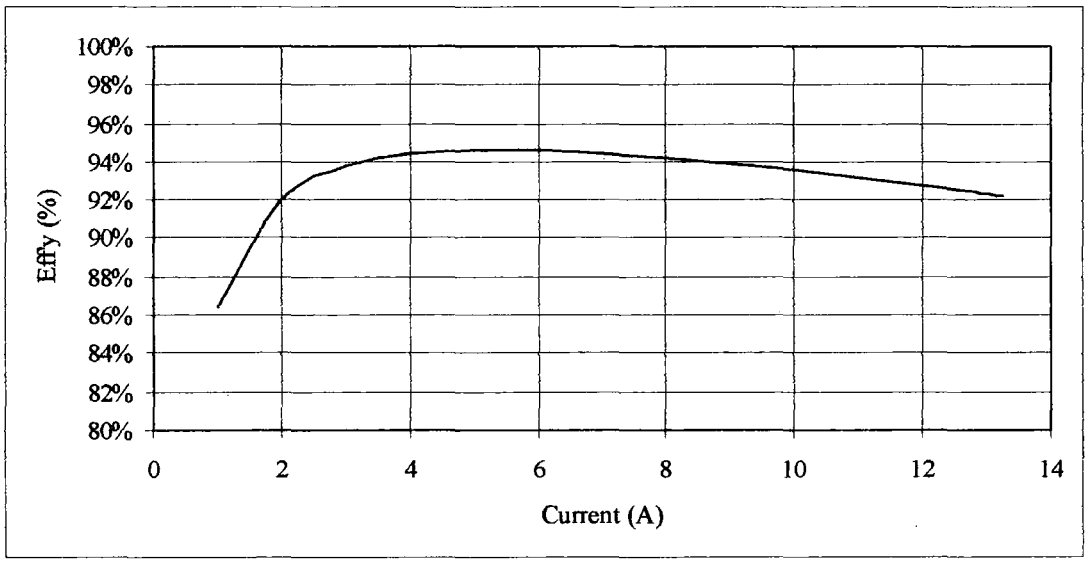

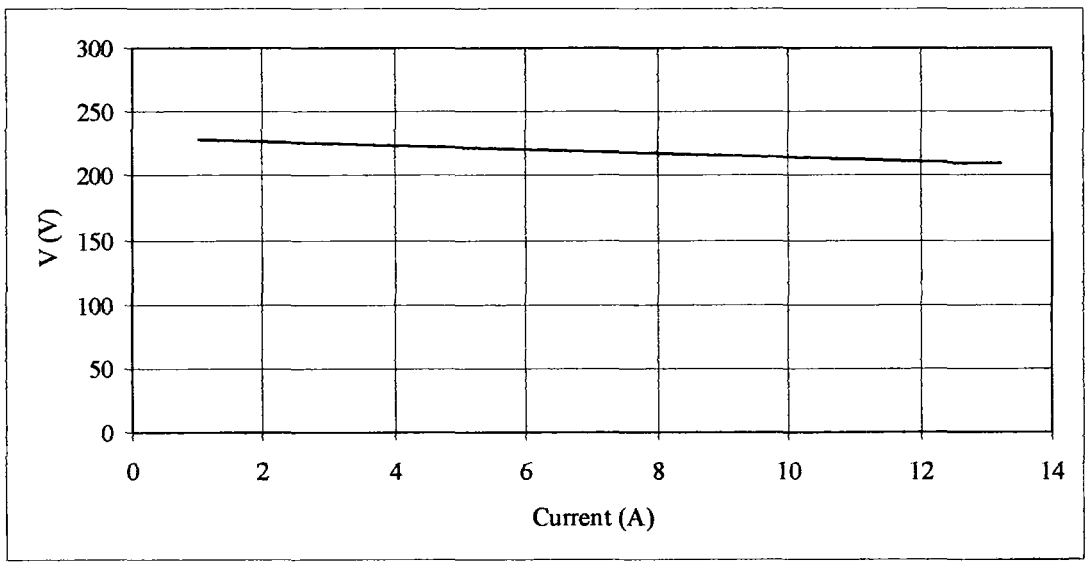

Figure 8.2: Generator performance at the rated speed of 132RPM

8.1.3. 3D magnetostatic FEA

In this section, FEA of the design outlined earlier in section 8.1 is described. In the magnetostatic case, the process is exactly the same as that described in Chapter 7 for the Savonius generator. The intention is to check the analytical predictions for this new design by modelling the electromagnetic behaviour. As well as providing a numerical check, the FEA is used to visualise the fields so as to substantiate some of the approximations implicit in the analytical methods.

Once more the analysis proceeds in 3D considering the full axial length of the machine but using boundary conditions such that a only a fraction of the machine need be modelled in the rotational dimension. This saves processing time and conserves the limited number of elements so as to facilitate an appropriately refined mesh. In this case, an eighth of the machine encompasses four magnetic poles per rotor and a full three coils and this fraction can be meshed with appropriate boundary conditions so as to accurately represent the entire machine in the static case. Two views of the model are shown in Figure 8.3 and it can be appreciated from this illustration that, as the size and the number of poles increase, the machine tends towards a ring shape.

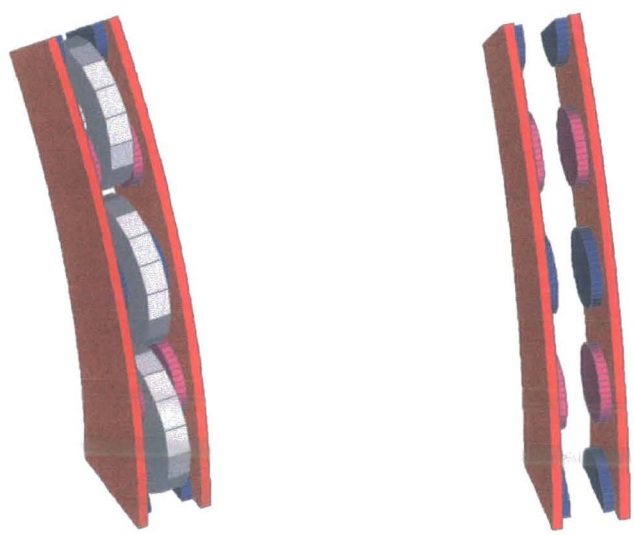

Figure 8.3: Two views of the FEA model (with and without coils)

With zero current passing through the coils, the field at the axial centre of the machine arising from the magnets only is illustrated, Figure 8.4.

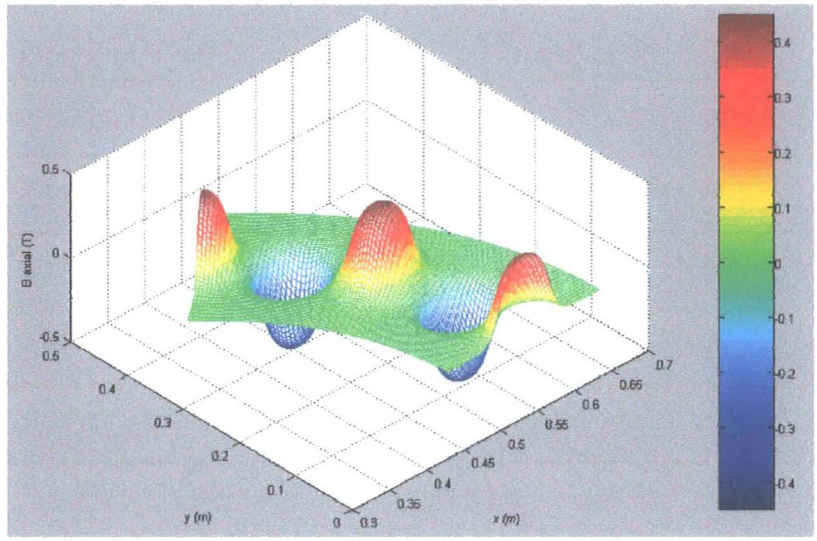

Figure 8.4: Visualisation of the excitation field from 3D FEA

Again, it is apparent that the flux density variation takes the form of a sinusoidal *"hill"* coinciding with the position of the circular magnets. The circumferential variation of this axial flux density at the mean radius of the machine and the axial centre is compared with the analytically-derived prediction, Figure 8.5.

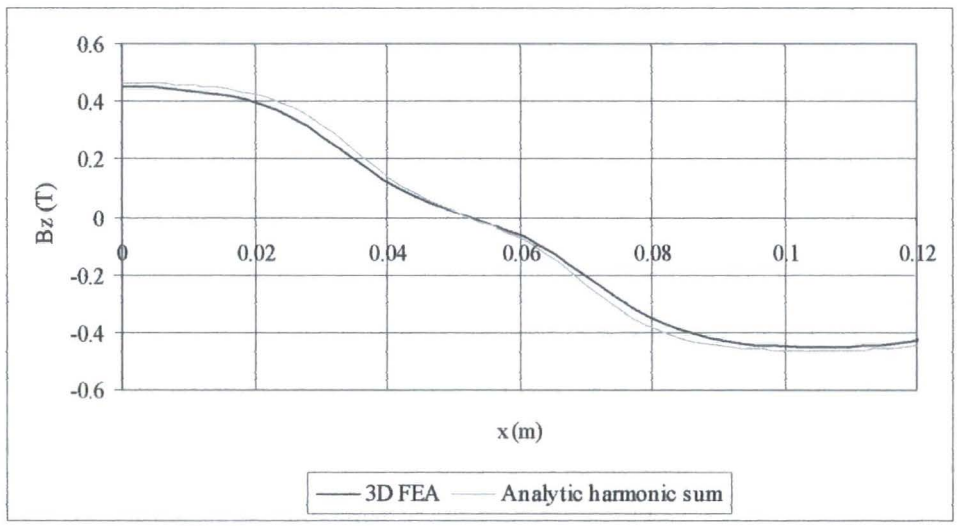

Figure 8.5: Predictions of the circumferential variation of axial flux density

The waveforms show good agreement with a peak value of 0.449T (FEA) comparing with the analytical prediction of 0.463T. This indicates an error of 3% in the analytical prediction.

With the remanent flux density of the magnets now set to zero and the three coils energised so as to simulate an instant in three-phase operation, namely with the central coil being fed rated current (i_{rated}) and the two coils adjacent to the central coil being fed with $(-i_{rated}/2)$, the resultant field is once again illustrated as shown in Figure 8.6. This shows the axial flux density over the plane at the axial centre of the machine, that is to say the flux density present at the centre of the coil regions arising from current passing through the coils.

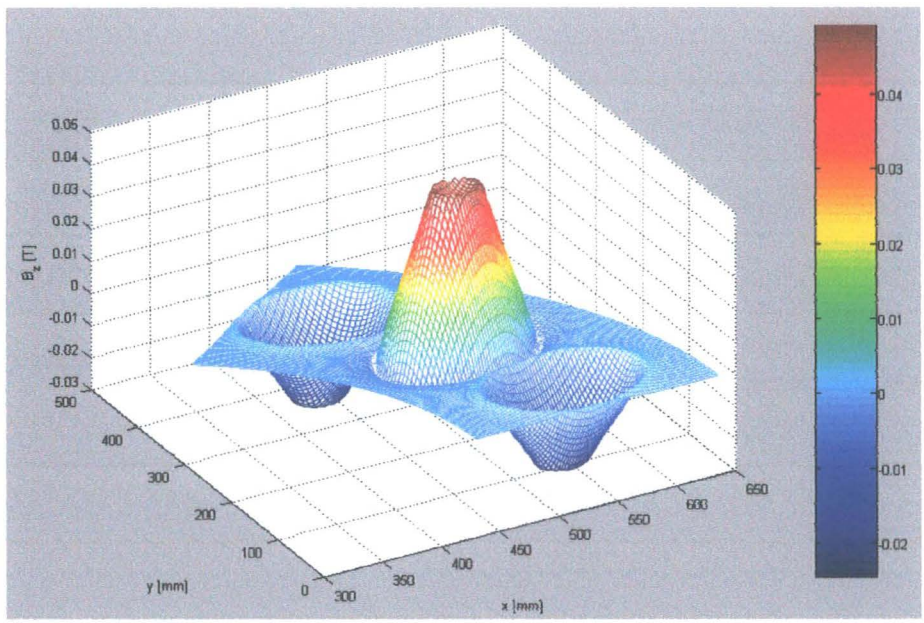

Figure 8.6: Surface of axial flux density arising from three-phase coil excitation

The back-EMF induced in the coils as a result of rated AC current passing through them at a frequency corresponding to the electrical frequency of the machine at the rated speed of 132RPM is used to calculate the self and mutual inductances per coil.

These are combined according to give the synchronous reactance and the results are tabulated, Table 8.6.

(per coil)	Analytical	FEA	Error (%)
X_{self} (Ω)	6.96	6.36	9%
X_{mutual} (Ω)	(-)	0.02	(-)
X_{syn} (Ω)	6.96	6.38	9%

Table 8.6: Comparison of the reactance predictions

The conical flux density surface verifies the assumptions inherent in the analytical approach as described in Chapter 7. Furthermore, the reactance predictions show good comparison. The FEA result shows clearly that the synchronous reactance is heavily dominated by the self inductance to such an extent that the mutual inductance effects may be ignored as per the analytical approach.

8.1.4. 3D dynamic FEA

The magnetostatic FEA results of section 8.1.3 show good agreement with the analytical prediction of synchronous reactance and verify the approach used in the modelling of the electromagnetic fields arising from the presence of the permanent magnets and of three-phase coil currents considered as separate cases. This section considers FEA of the machine for the determination of the induced EMF on open circuit at rated speed.

Like the disc-shaped sliding interfaces encountered previously in the determination of induced EMF from FEA of such machines, the annular sliding interface required in this case does not permit the use of periodic boundary conditions and so the full 360° are modelled. The machine is large and has many poles so the resulting mesh

has to be quite coarse in order not to exceed the maximum number of elements, but this is disadvantageous since the accuracy of the results may be directly compromised by the coarseness of the mesh. Also, the level of mesh refinement in the axial dimension required to accurately model the air-gap geometry may require coarseness in the r, θ directions that results in elements with extreme aspect ratios, again resulting in inaccuracy. Finally, the element limits only feasibly allow modelling of half the axial length of the machine, resulting in the uncertainty regarding the coil position described in Chapter 7.

Nevertheless, a mesh is defined for the full 360° circumferential but only half the axial length, having a normal flux boundary condition at the axial centre of the machine to compensate. The coil position then replicates that of the analytical solution which takes the coil inner to outer diameter spread into account but ignores the axial depth of the coil, thereby assuming it is axially thin and located at the axial centre of the machine, Figure 8.7.

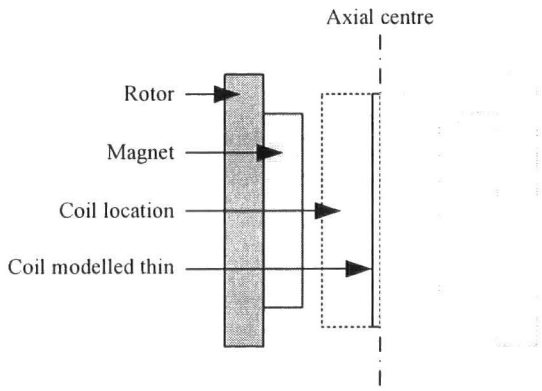

Figure 8.7: Illustration of the coil model

Figure 8.8 shows the resulting FEA model of the rotor ring, with and without element outlines, and a close-up of the mesh.

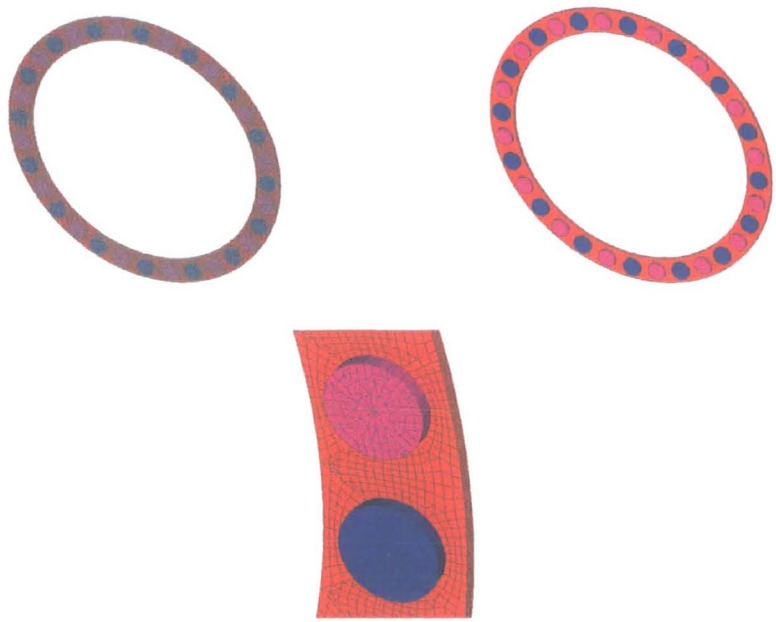

Figure 8.8: FEA model of the rotor ring

Since the mesh is near the limits of computational power, the program does not allow all the coils to be modelled. This is not a problem when the coils are open-circuited, since they carry no current and thus have no impact on the field. Only one coil need be modelled and the EMF for the whole machine can be assimilated from that of one coil, factoring in knowledge of the machine geometry and winding connections. Three adjacent coils were modelled, and Figure 8.9 shows the EMF measured at each coil from the FEA solution.

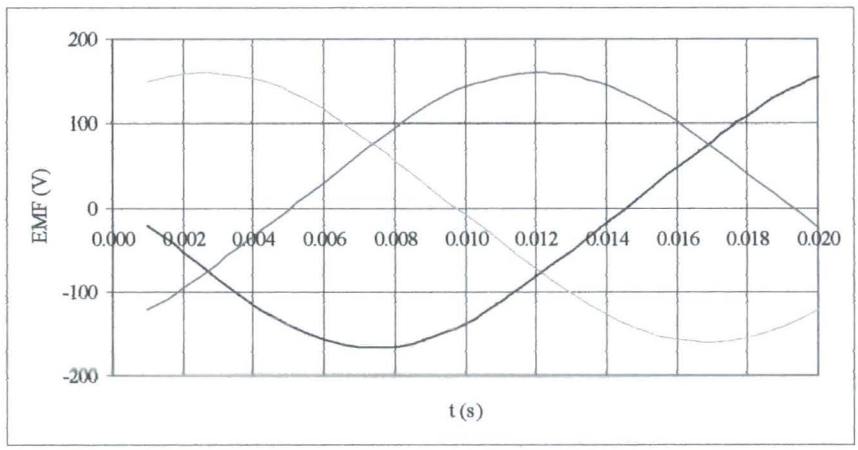

Figure 8.9: Open-circuit EMF induced in three adjacent coils at 132RPM

Variability was encountered in the results obtained from this model, indicating that the coarseness of the mesh is beginning to limit the accuracy somewhat. Nevertheless, an average across the three coils gives a peak EMF of 162V per coil and assuming this to be sinusoidal the resulting RMS value is 115V. This compares well with the spreadsheet design value of 121.6V. The waves are not exact sinusoids, and the true RMS value is likely to be larger than the FEA result quoted. It is also expected that both methods under-predict since the turns of the real coil that are situated away from the axial centre experience more flux linkage owing to the contribution of leakage flux, i.e. flux which does not fully traverse the gap. The 120° difference between phases is apparent, and can also be deduced from the relative positions of coils and magnets, illustrated in Figure 8.10.

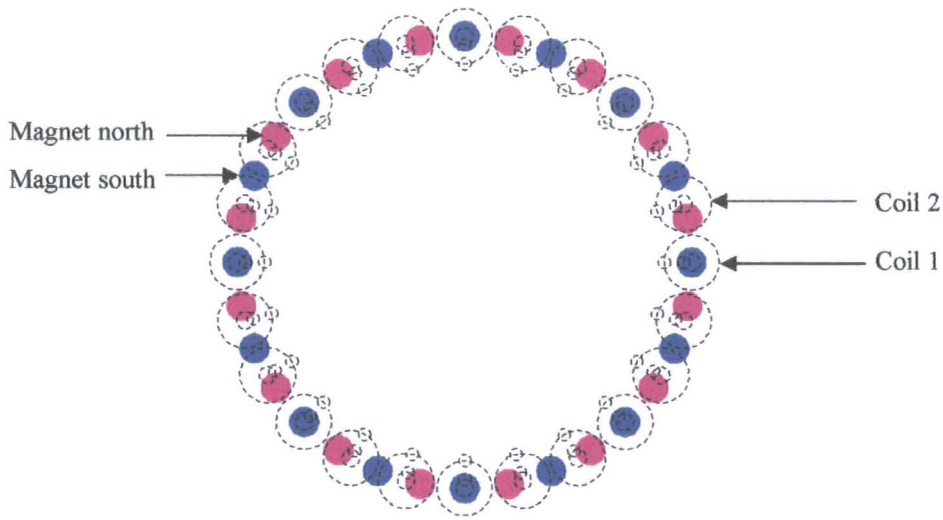

Figure 8.10: Positioning of coils and magnets in the FEA model

Although the results are reasonable, the mesh is of limited refinement and the variability encountered in the results gives little confidence. Furthermore, the axially thin approach to the modelling of the coil is an approximation used in both the analytical and the FEA approaches and hence no verification of the validity of this assumption is given in the case of this machine. Therefore, a different approach to

this FEA was taken utilising a linearised model of the machine. Since the ring-shaped active area is radially short and is situated at a comparatively large radius, curvature is slight in this machine. This property may allow accurate representation of the machine by a linear model, and this alternative offers significant advantages. Most importantly, periodic boundaries can be used with translating Lagrange interfaces, meaning that only a fraction of the machine need be modelled again. The mesh can therefore be refined, enhancing accuracy, and both sides of the machine can be modelled, allowing the real coil to be accurately represented and the axial spread of the turns to be accounted for.

To this end, two magnet poles were modelled along with one coil starting in a central position, and the excitation field was analysed first in the static case for comparison with previous results by way of verifying the linear approach. The FEA mesh is shown in Figure 8.11, and the excitation flux surface obtained from this model is shown in Figure 8.12.

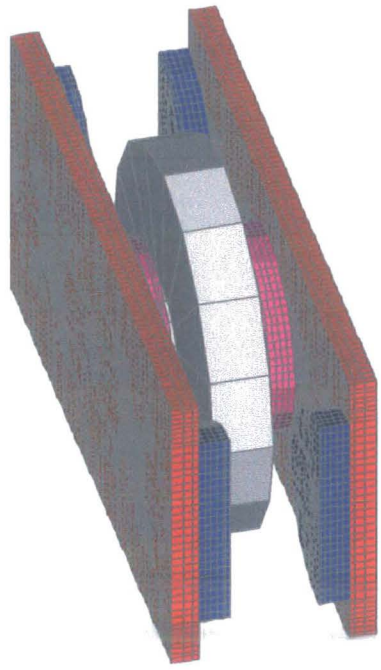

Figure 8.11: Translating, linear 3D FEA model

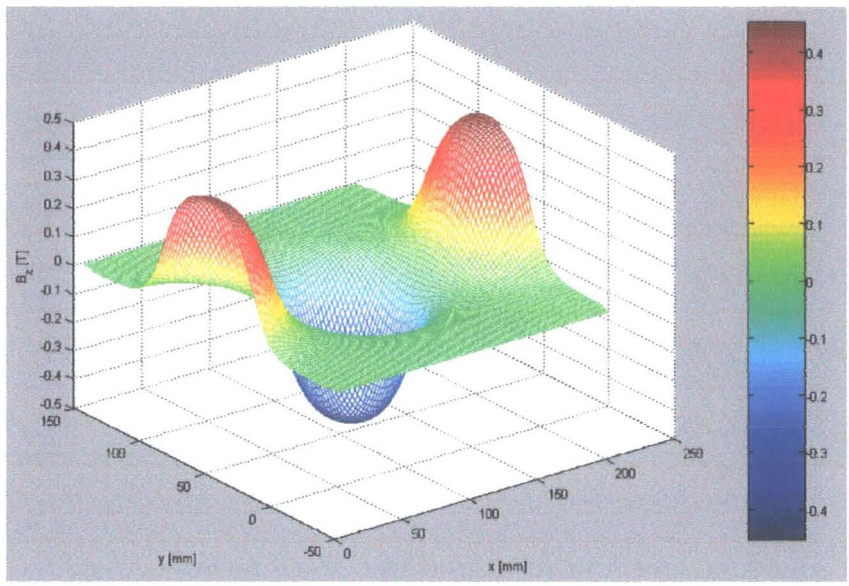

Figure 8.12: Surface of axial flux density arising from permanent magnet excitation

Figure 8.13 shows the circumferential variation of axial flux density arising from the presence of the permanent magnets only, taken at the axial centre of the machine and at the mean radius, comparing results obtained from the circular model of section 8.1.3 and the new linear model; the waveforms are almost indistinguishable.

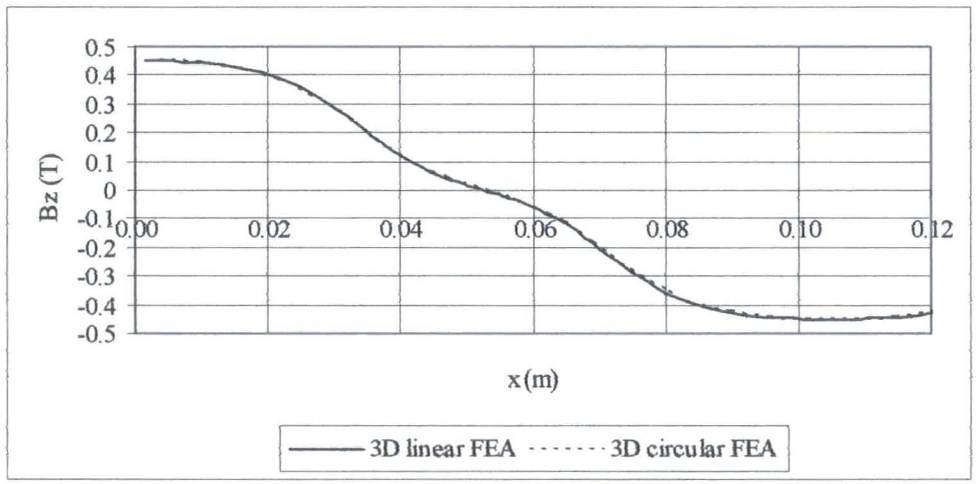

Figure 8.13: Circumferential variation of axial flux density from magnet excitation

The linear model also facilitates a clear radial equivalent view into the machine, where flux density vectors provide an alternative illustration of the excitation field. Figure 8.14 shows the model with and without vectors.

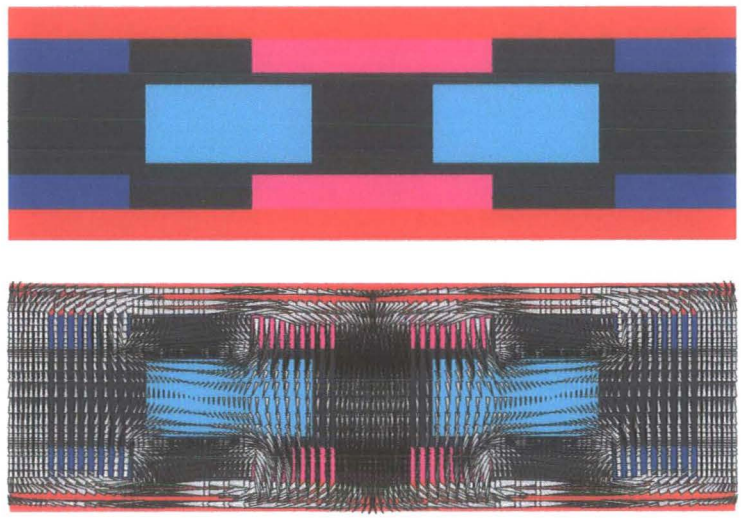

Figure 8.14: Flux density vectors from magnet excitation

Once verified in the static case, this linear model was set up as a time-stepping model. The resulting EMF waveform measured at the coil directly within the FEA program is shown, Figure 8.15.

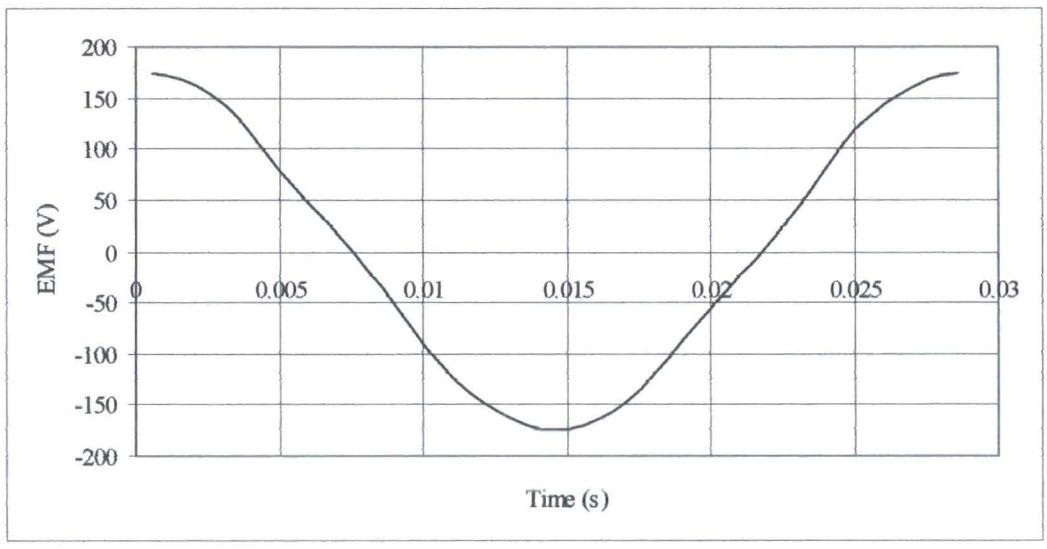

Figure 8.15: Open circuit induced EMF per coil from 3D linear FEA

The coil EMF peaks at 174V, indicating an RMS value of 123V assuming a sinusoidal waveform. This compares with the analytical prediction of 121.6V indicating an error in the analytical prediction of just over 1%.

8.1.5. Discussion

In summary, section 8.1 described a generator design for a VAWT rated at 7.5kW at 132RPM. The design is simply a larger version of the Savonius machine described in Chapter 7. The parameters of the design were outlined and the analytical predictions for the performance of the design were summarised, with particular focus on the electromagnetic performance.

Secondly, FEA verification of the analytical approach to the calculation of the electromagnetic parameters of the machine was described. The magnetostatic analysis yielded illustrations of the fields present in the machine as well as some numerical results for direct comparison with the analytical predictions. This showed the underlying assumptions of the analytical approach described in Chapter 7 to be consistent with the fields present in this particular design. Also, the FEA-computed flux density arising from permanent magnet excitation and the synchronous reactance calculated from three-phase coil excitation showed good agreement with the analytical predictions.

Finally, 3D dynamic FEA of the machine was attempted, firstly with a circular model and latterly with a linear, translating model. Confidence in the results obtained from the circular model was limited by the close proximity to the limits of computational power and the resulting variability in the figures obtained, and the approximate replication of the coils. A linear model was devised as an alternative and shown to

give results in agreement with the accurate, magnetostatic circular model; hence the linear model was extended to the calculation of open circuit EMF directly from a dynamic solution. This gave a result that was in good agreement with the analytical prediction.

8.2. An air-cored motor for a solar car

8.2.1. Generalised power output considerations

The power output of a permanent magnet axial flux machine was derived in Chapter 6 from consideration of the Lorentz force. The general result of this derivation is the assertion that the mean shear stress arising between in-phase, sinusoidal distributions of magnetic and electric loadings in space can be expressed:

$$\overline{\sigma} = \frac{\hat{B}A_{RMS}}{\sqrt{2}} \qquad \text{Eq. 8.1}$$

Extension of this to an axial flux machine with trapezoidal permanent magnet poles and approximately radial conductors yielded an expression for the power output in terms of the core diameters:

$$P = \frac{\hat{B}A_{RMS}}{\sqrt{2}} \pi^2 D_m^2 (D_o - D_i) \frac{n}{60} \qquad \text{Eq. 8.2}$$

Campbell, [13], described an approach to the optimisation of the ratio between the inner and outer core diameters, showing that ratio of $\sqrt{3}$ gives the maximum power from the winding in this type of machine. If this ratio is fixed in the design process, the active area can be expressed:

$$a = \frac{\pi D_o^2}{3} \qquad \text{Eq. 8.3}$$

Hence also the power can be given in terms of the outer diameter:

$$P = \frac{\hat{B}A_{RMS}}{\sqrt{2}} \frac{\pi^2 D_o^3 (1+\sqrt{3})}{6\sqrt{3}} \frac{n}{60} \qquad \text{Eq. 8.4}$$

In the case of the novel air-cored machine designed for the Savonius turbine, the active area, and hence the shear stress and power output, is limited to some extent by the radius of the coils. This is a result of the decision to use circular poles and coils; the primary reason for this approach was to making manufacture and assembly significantly simpler than previous axial flux topologies and thus concentrated, pre-wound, circular coils are the salient feature of this patented design, [7]. However, as shown in section 8.1.3, this can result in rotors which have a small active length situated at a large diameter such that the area within the inner diameter is under-used and the power density suffers.

Where bigger machines are specified, or where the power density is critical, there are two modifications to the topology which can be used together in order to improve the situation. The first involves a move back to the trapezoidal-type machines previously considered; it is thought that the air-cored, pre-wound, concentrated nature of the coils could be retained but that trapezoidal formers could be used so as to extend the active area in the radial direction. It was perceived that this would make the manufacture of coils slightly more complex than was the case with circular coils, but that techniques such as embedding bobbin-less, pre-formed coils in epoxy would possibly facilitate refinement of the design as well as improved power density.

A second modification to the original design for the Savonius turbine is to embrace the move to a ring-shaped machine by specifying annular rotors as opposed to solid discs and designing an efficient, lightweight mechanical structure to yield an active area at a large diameter. This approach has been investigated by Spooner et al, [102], [103], for an air-cored radial flux machine which utilises a spoked structure similar to that of a bicycle wheel.

8.2.2. The solar car application

Recent years have seen increased interest in the use of renewable energy for transportation. In particular, various races for solar powered vehicles have attracted a great deal of attention and sponsorship such that the solar car has been moved from relative obscurity to the focal point of significant expenditure and engineering expertise. One of the main areas of progress in this application has been in the design of lightweight, high-performance, highly efficient motor and drive systems. Many of the current competitors use permanent magnet axial flux machines operating in the brushless-DC motor mode since this genre of machine offers high efficiency, good controllability, and a torque-speed characteristic appropriate for the application. In addition, the axial flux geometry may be incorporated into a wheel, resulting in a lightweight direct-drive system of great simplicity and with a high efficiency, not least through the elimination of a mechanical drive train. Much work has gone into the use of materials and the mechanical design specifics of these in-wheel motors, and the design of Lovatt et al, [65], demonstrates the extent to which the concept may be taken, utilising a distributed winding and a Halbach array of permanent magnets so as to specify a truly iron-less machine. The resulting design is lightweight and highly efficient but is also exceptionally costly in terms of materials and manufacturing methods. Whilst facilitating the inclusion of a lot of copper, and enabling a truly iron-less design, the distributed winding and Halbach magnet array proved highly unwieldy and, coupled with the high costs involved, this rules the design out for all but the most serious teams with high levels of sponsorship and commercial backing.

The School of Engineering at Durham University launched a project to design and build a solar car which coincided with some of the work described in this thesis. The

ultimate aim was to compete in one of the races but the short term idea was to demonstrate engineering principles to high school students in the region. The design specification called for an in-wheel motor with maximum efficiency, producing 1kW at 1000RPM, to fit a 17" wheel, i.e. within an outer diameter of 400mm and a short axial length. This project had significant restraints on resources and expenditure and so the novel topology of Bumby, [6], [7], was deemed to offer many of the benefits of the design of Lovatt et al, [65], but in a format that could feasibly be realised in the School's mechanical engineering workshop at minimum cost. The increased importance of a lightweight machine with the maximum power density achievable in this application led to a modification to the original prototype in the form of trapezoidal-type magnets and coils, for the reasons explained in section 8.2.1.

8.2.3. The prototype motor

A prototype machine was designed by Bumby, and built in the School of Engineering at Durham University. It has 16 arc-shaped (approximately trapezoidal) magnets mounted on a steel rotor disc with a stainless steel outer ring for retention, Figure 8.16. A pole arc to pole pitch ratio of 0.81 was specified; this is larger than values previously described in this thesis and gives two advantages: firstly, an increased magnetic loading and therefore power density, and secondly a more flat-topped EMF waveform to improve performance in the brushless DC motor mode. The stator coils were pre-wound onto a trapezoidal former using wire with an epoxy coating that facilitated bonding of the coils prior to insertion into the stator. Each coil has a Tufnol centrepiece as shown, Figure 8.17. The stator consists of a pair of Tufnol discs which sandwich and protect the coils, and are attached to a central support shaft so as to provide the necessary reaction torque. Figure 8.18 shows the full array of coils mounted on one of the Tufnol discs, and the final wheel assembly.

Figure 8.16: Rotor of the solar car machine prior to assembly

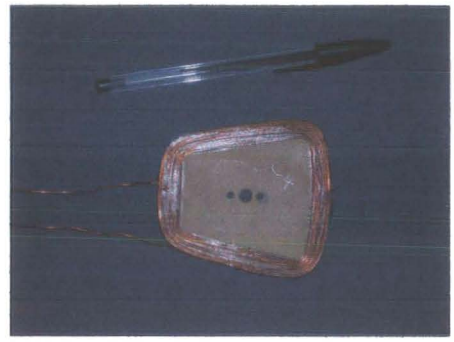

Figure 8.17: Pre-formed stator coil

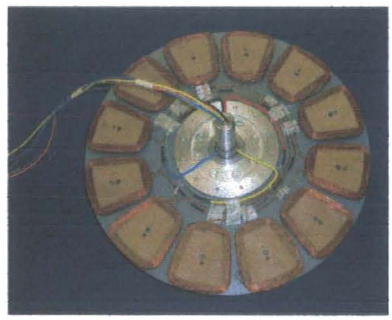

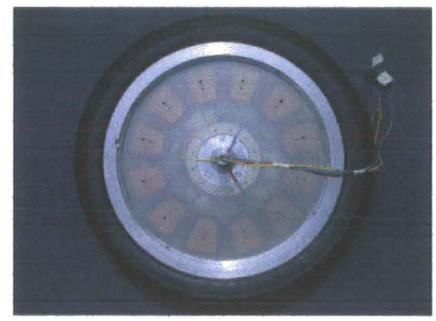

Figure 8.18: Coil array and fully assembled in-wheel motor

The main parameters of the prototype are given in Table 8.7. The analytical and FEA approaches are outlined in the following sections, proceeding in a similar way to the previous analyses.

Number of phases	3
Number of magnets	16
Number of coils	12
Magnet length (mm)	69
Magnet width at OD (mm)	60
Magnet width at ID (mm)	36
Magnet thickness (mm)	6
Magnet arc to pole pitch ratio	0.81
Rotor thickness (mm)	10
Outer diameter of rotor (mm)	384
Stator thickness (mm)	8
Coil pitch (mechanical deg)	30
Coil outer diameter (mm)	386
Coil inner diameter (mm)	226
Coil radial length (mm)	80
Coil winding width (mm)	10
Coil winding depth (mm)	6
Wire diameter (mm)	1.0
Number of turns/coil	46
Running clearance (mm)	2
Total gap [rotor to rotor] (mm)	26

Table 8.7: Summary of the solar car motor design

Furthermore, some preliminary tests were performed on the prototype in the generating mode for the verification of the design and subsequent analysis.

8.2.4. The analytical approach

With the extension of the active length in the radial direction, the sinusoidal *"hill"* approximation is no longer used in the analysis of the excitation field. Instead, the model was assumed infinitely long in the radial dimension and a 2D solution in the axial/circumferential plane was used. Thus the field was calculated much like that in the TORUS, comparing the result of a simple magnetic circuit solution with a more refined field solution based on the solution to Laplace's equation as outlined in Chapter 3. Again, an iron boundary exists at the axial centre and the circumferential variation of axial flux density was calculated at the mean radius in that axial position.

In calculating the flux linkage and hence the EMF a simpler version of the method used in the analysis of the Savonius generator was applied. The model is assumed infinitely long in the radial direction, and an effective length used to modulate the flux linkage appropriately. Since there will be some reduction in the flux density at the radial limits of the magnet, the magnet length was used as a conservative estimate of the effective length, regardless of the coil dimensions. The simplest approach considers all the turns concentrated at the mean coil radius and places some reliance on the offset between a reduced EMF induced in the inner turns and an increased EMF induced in the outer turns. A more sophisticated approach involves a manual summation of the EMF induced in three segments each having a third of the total number of turns and situated at different radii within the coil. As was the case in the analysis of the Savonius machine, the manual summation is preferred to a full integration since it enables the use of approximate flux reduction factors to account for the radial variation of the field by attenuating the flux accordingly.

Similar methods were used for the inductance calculations, assuming infinite length in the radial direction and modulating the flux by an effective length representing the radial dimension of the coil. The flux density arising from coil excitation was approximated using a magnetic circuit solution with all the turns assumed concentrated at the mean coil radius.

Heat dissipation in the machine was modelled in exactly the same way as outlined for the Savonius machine in Chapter 7, and eddy loss in the conductors was calculated similarly. The predictions of the design spreadsheet are summarised for operation in the generating mode at 1000RPM, Table 8.8.

Excitation flux density [magnetic circuit] (T)	0.58
Excitation flux density [field solution, fundamental] (T)	0.65
EMF induced per coil [concentrated coil] (V)	42.6
EMF induced per coil [manual summation] (V)	39.6
Coil inductance (mH)	0.45
Coil synchronous reactance (Ω)	0.38
Ambient temperature (°C)	20
Maximum winding temperature (°C)	100
Total allowable loss per coil (W)	3.73
Eddy loss per coil (W)	2.1
Allowable I^2R loss per coil (W)	1.6
Resistivity at operating temperature (Ωm)	2.21E-08
Coil resistance (Ω)	0.33
Rated coil current (A)	2.2
Terminal voltage per coil (V)	38.9
Power output per coil (W)	87

Table 8.8: Analytical performance predictions of the solar car motor

The overall predicted performance is a power output of just over 1kW with efficiency in excess of 96%. Predicted load lines are shown in comparison with measured values in section 8.2.6.

8.2.5. FEA of the prototype design

FEA of the field arising from the permanent magnets in the static case followed a similar approach to previous analyses, using a 3D fractional model of two poles over half the axial length, as shown in Figure 8.19. The winding was not modelled in the static case since this analysis was carried out in a very limited timeframe and the inductances were expected to be of relatively little importance. However, the circumferential variation of the excitation field was obtained at the axial centre of the machine for direct comparison with the characteristic obtained analytically. Also, the radial variation of the excitation field at the axial centre of the machine was obtained for comparison with the analytical assumption that the flux density remains at a

maximum across the length of the magnet in this direction. The two comparisons are shown, Figure 8.20 and Figure 8.21.

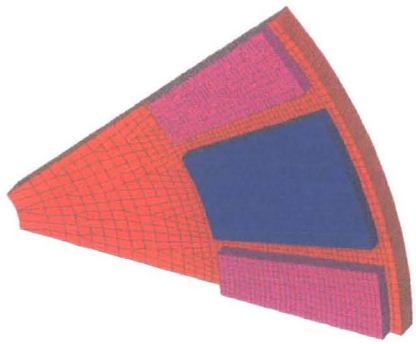

Figure 8.19: Static FEA mesh

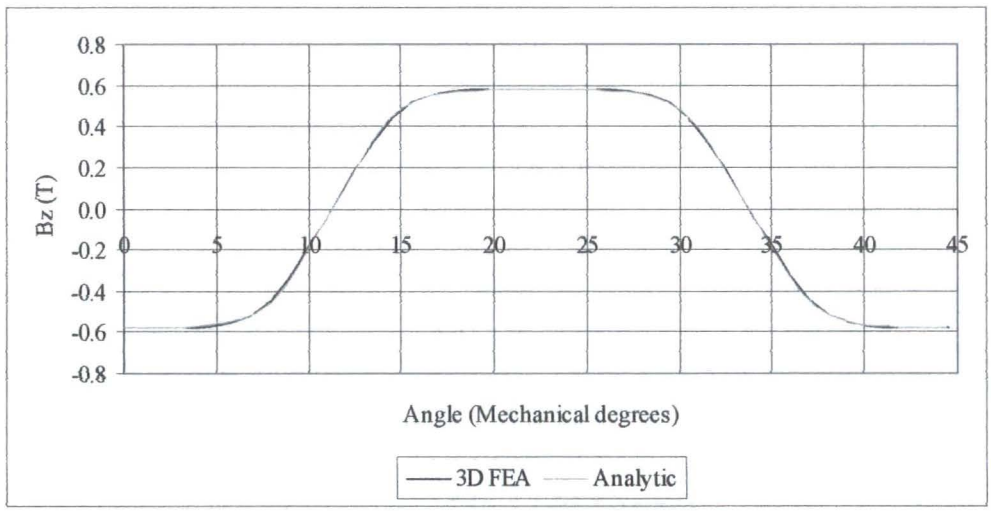

Figure 8.20: Circumferential variation of axial flux density

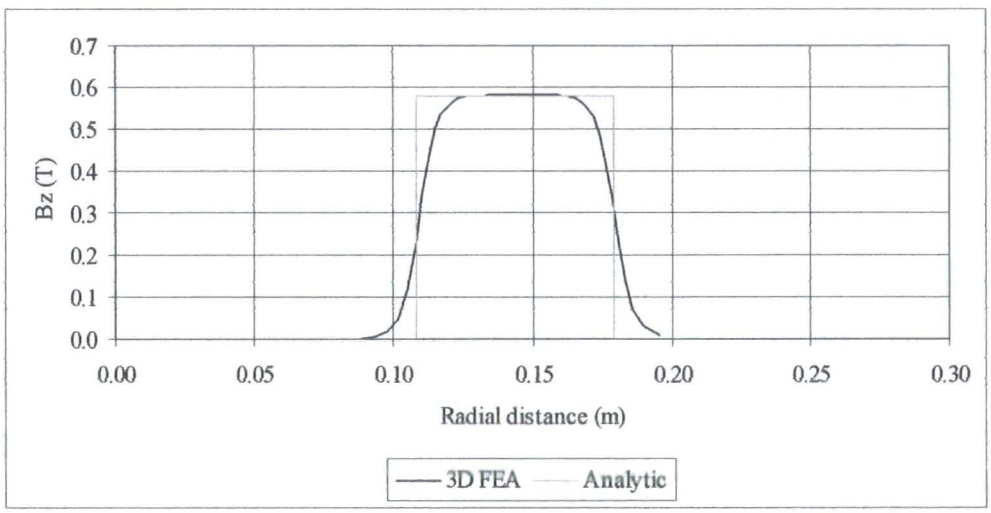

Figure 8.21: Radial variation of axial flux density

These characteristics are also apparent in the flux density surface representing the excitation field across the *(r, θ)* plane at the axial centre of the machine, which was obtained from the model for illustration and is shown below, Figure 8.22.

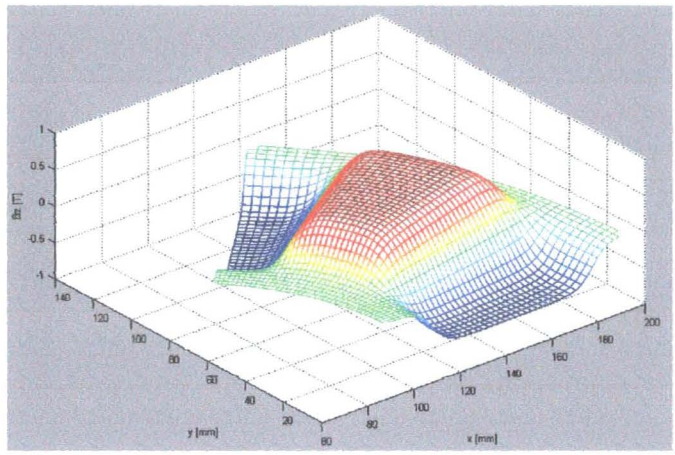

Figure 8.22: Excitation flux density distribution at the axial centre of the machine

A 3D dynamic FEA model was devised to obtain the open-circuit EMF induced in the coils at rated speed. With hindsight, given the work described in section 8.1, a linear model would have been much easier to implement and would probably have given accurate results. However, a disc-shaped model of the full 360° was created at the time, covering only half the axial length so as to conserve computational power for as detailed a mesh as could be achieved given the limitations imposed by the necessity of a full 360° for the sliding interface between the rotor and stator components. The coils were modelled axially thin and located at the axial centre of the machine in accordance with the analytical solution, and only the radial spread of the coils was taken into account.

The coils were rather more difficult to model than previous types, since the simple *"racetrack"* coils used in the case of the TORUS and slotted machines are no longer applicable where the trapezoidal shaper is required. Instead, the coils were assembled

as arc-shaped arrangements of the component segments available in the MEGA program, [4]. One such coil is illustrated, Figure 8.23.

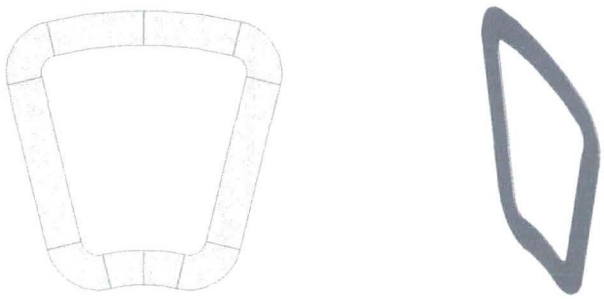

Figure 8.23: FEA model of an axially thin stator coil

Finally, the dynamic FEA model of half the axial length of the machine with a full array of thin coils situated at the axial centre of the machine is shown, Figure 8.24.

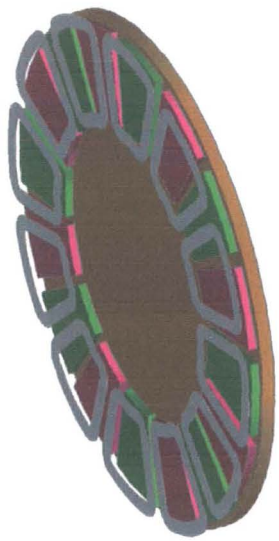

Figure 8.24: Full 3D dynamic FEA model

The three-phase open-circuit EMF waveform returned directly from the FEA solver for rotation at rated speed of 1000RPM is shown, Figure 8.25.

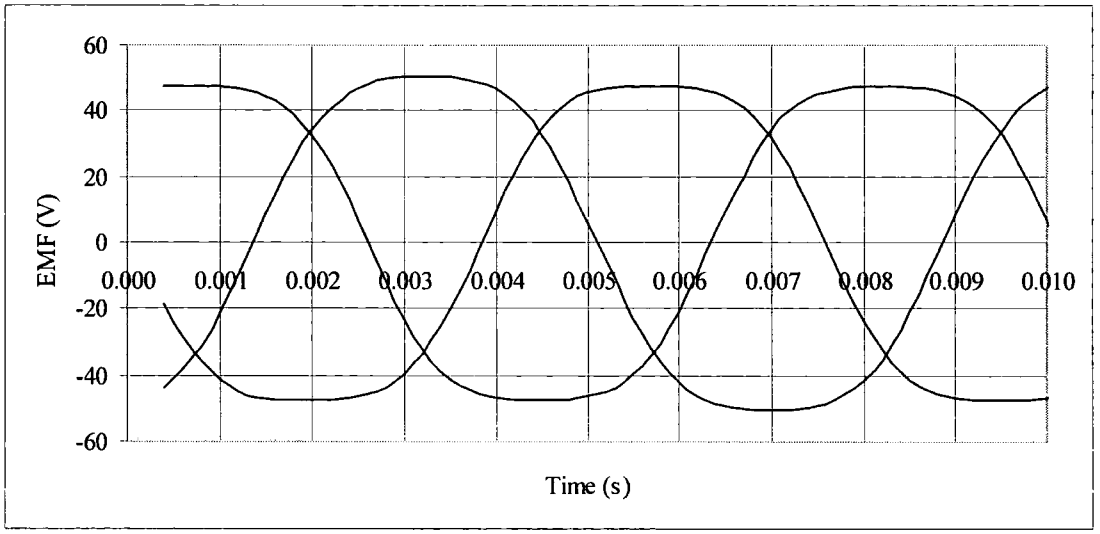

Figure 8.25: EMF waveforms returned from 3D dynamic FEA

Some variability between phases is noticeable; this is attributed to the coarseness of the mesh resulting from the constraint of modelling the full 360°. As a rough approximation, the average RMS voltage per phase across the three phases is 38.6V, comparing well with the analytical prediction of 36.9V and indicating an error of less than 5% in the analytical prediction. The mean peak voltage is 48.5V.

8.2.6. Experimental test of the prototype

Some initial tests were performed on the machine in the generating mode of operation prior to incorporation into the solar car itself. The time for this was limited by the solar car project, but an open circuit test was performed as well as a resistive load test at two speeds. Open circuit EMF waveforms captured by digital oscilloscope are shown in Figure 8.26 for operation at 144RPM.

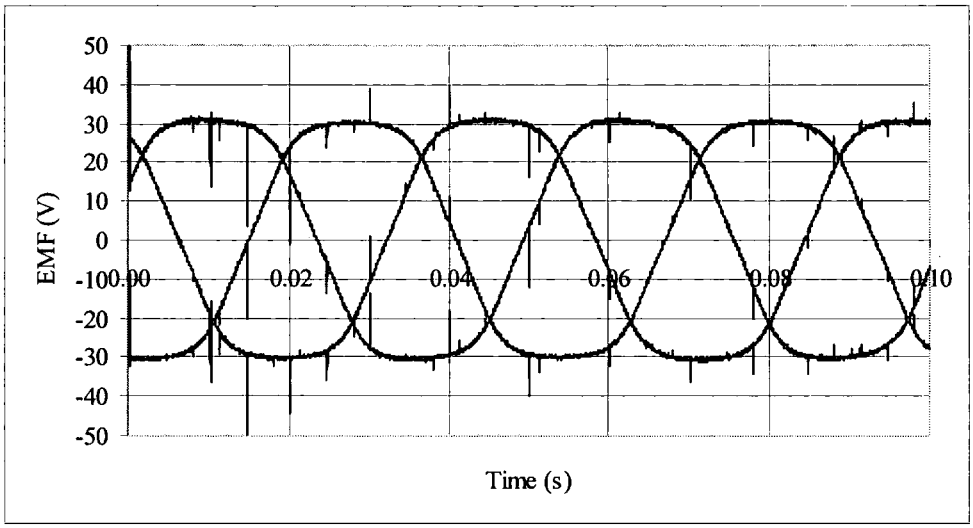

Figure 8.26: Oscilloscope plot of open-circuit EMF measured from the prototype

This waveform is of a similar shape to those obtained from the dynamic FEA. Table 8.9 summarises the measured and predicted parameters.

	Analytical	**FEA**	**Measured**
Excitation flux density (T)	0.585	0.585	N/A
EMF per phase per 1000RPM (V_{RMS})	39.6	38.6	42.2

Table 8.9: Measured and predicted parameters for the solar car motor

Finally, the results of AC resistive load tests are compared with load lines predicted from the equivalent circuit parameters derived analytically and presented in Table 8.8. The four coils of each phase were connected in series, and the tests were conducted at speeds of 331RPM and 860RPM according to the capability of the prime-mover. No allowance was made for the resistance of the leads between the machine output and the load. The predicted values were adjusted for an operating temperature of 60°C, approximated according to the discrepancy between the test speeds and the 1000RPM rating of the machine. Power, terminal voltage, and electrical efficiency are compared in Figure 8.27, Figure 8.28, and Figure 8.29.

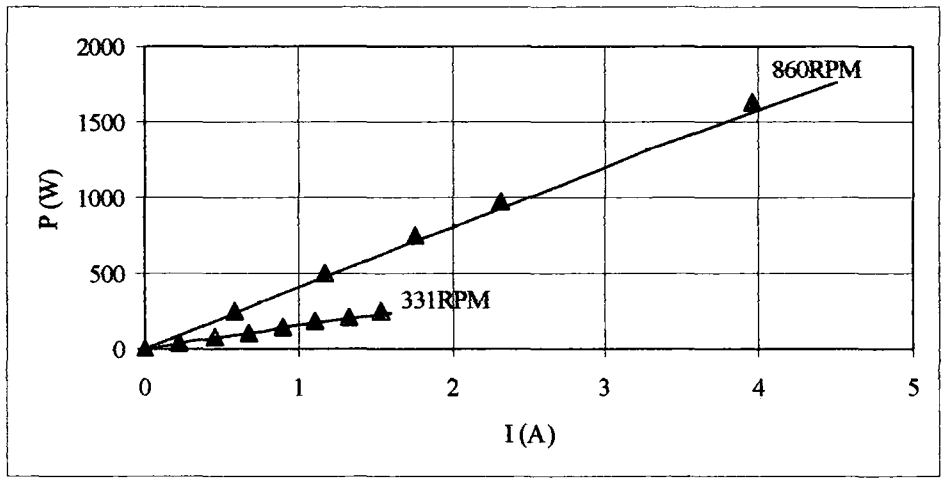

Figure 8.27: Load line comparison: total power output against phase current
▲ = measured; ▬ = predicted

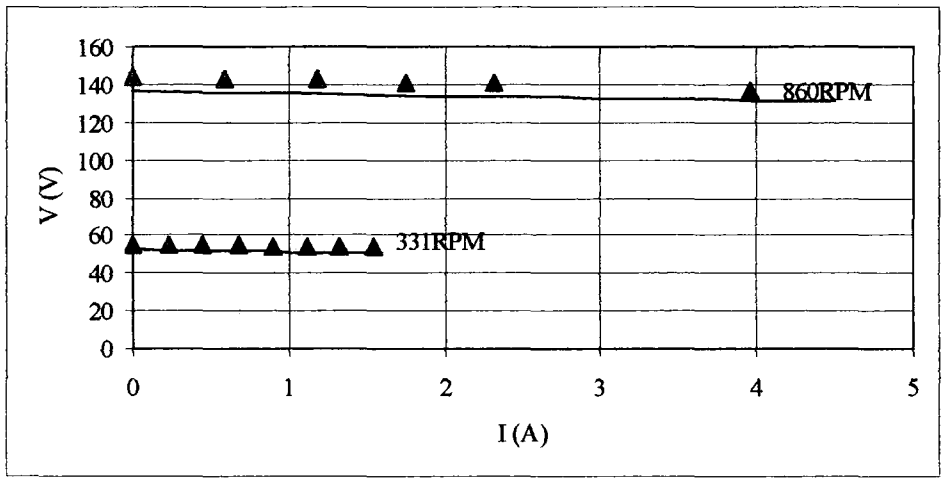

Figure 8.28: Load line comparison: phase terminal voltage against current
▲ = measured; ▬ = predicted

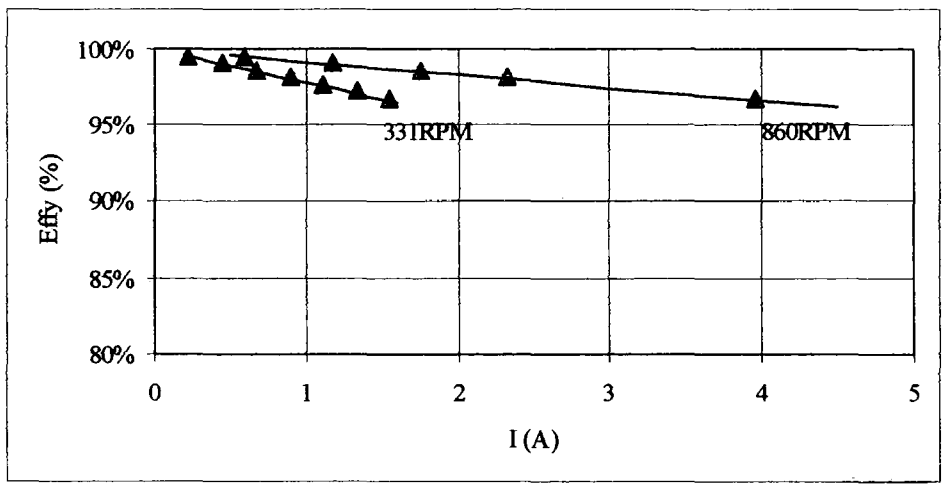

Figure 8.29: Load line comparison: Efficiency against phase current
▲ = measured; ▬ = predicted

8.2.7. Discussion

In summary, this section on the motor designed for a solar car has described a slight variation on the original Savonius design of Bumby through the use of trapezoidal (or arc-shaped) magnets and coils. The reason for this design alteration was to increase the use of the volume occupied by the machine through the extension of the active radial length of the machine and the prototype gave an output of over 1600W at 860RPM with an efficiency in excess of 95% across the operating range tested, so it is expected that the rating of 2kW at 1000RPM is attainable also with a suitably high efficiency.

The application of FEA to verify the analytical approaches, both quantitatively and in terms of the simplifying approximations made to the excitation field in the analytical solution, was described. This once more highlighted the limitations of modelling disc-shaped machines and, given more time, a linear (translating) approach to the FEA would have been used. The approach actually used required the definition of trapezoidal coils within the FEA programme which represents a complication to the coils considered previously in this thesis. Such coils were defined and used within a dynamic 3D model to predict the open-circuit EMF to within 9% of that measured during experimental test. The inaccuracy is thought to be attributable to variation between the actual prototype machine and the design specification, perhaps affecting the effective air-gap, and also to some unpredictability encountered in the FEA programme where large models having disc-shaped sliding interfaces are modelled. In general, the analytical and FEA predictions agreed well with the results of experimental tests; the performance of the machine, as far as could be ascertained from the tests described in this section, is likely to meet the design specification.

8.3. A 10kW air-cored generator design for a VAWT

8.3.1. Introduction

This section describes the final machine considered in this thesis, using the approaches to FEA of axial flux machines described and developed through the thesis to predict the performance of a new design for a 10kW, 140RPM air-cored generator for a VAWT.

The machine has yet to be built, but represents the continuing direction of research in this area, namely the design of larger, improved versions of the novel, air-cored, concentrated coil design of Bumby, [6], [7], as direct-drive permanent magnet generators for small-scale wind turbines. The modifications described in the previous two sections of this chapter also come together in this section through the specification of a design having a high number of poles at a big diameter such that the machine is ring-shaped, and utilising trapezoidal magnets and coils for improved use of space by comparison with the simpler design conceived for the Savonius turbine.

The design is first outlined and the analytical methods used for the Savonius generator and the solar car motor are used to arrive at predictions of the electromagnetic fields arising and the accompanying equivalent circuit parameters. The results of thermal modelling are then used to approximate a rated current value from which the performance of the generator can then be predicted. Finally, 3D static and dynamic FEA models are used to illustrate the fields and verify the electromagnetic aspects of the analytical approaches so as to give assurance to the design and analysis procedure and the resultant performance predictions.

8.3.2. Design specification and performance predictions

Table 8.10 gives an outline summary of the machine geometry. The analytical methods are the same as those used for the analysis of the solar car motor, that is to say a combination of the techniques used for the TORUS and slotted-type machines with trapezoidal coils and poles, and those used for the air-cored generator for the Savonius turbine with concentrated coils. Values of flux density obtained from the analysis of permanent magnet excitation are shown, Table 8.11.

Number of magnets per rotor	32
Magnet mean diameter (mm)	840
Magnet radial length (mm)	120
Magnet thickness (mm)	10
Magnet arc/pole pitch	0.725
Radial length of rotor ring (mm)	150
Rotor ring thickness (mm)	10
Rotor outer active diameter (mm)	990
Number of phases	3
Number of stator coils	24
Number of phase coils in series	1
Number of phase coils in parallel	8
Number of turns per coil	58
Stator mean diameter (mm)	840
Coil outer radial length (mm)	180
Coil outer width at stator mean diameter (mm)	100
Coil inner width at stator mean diameter (mm)	40
Coil axial depth (mm)	16
Stator thickness (mm)	20
Running clearance (mm)	3
Total gap [magnet to magnet] (mm)	26
Total axial length (mm)	66

Table 8.10: 10kW 140RPM design parameters

Flux density at the axial centre [magnetic circuit solution] (T)	0.506
Flux density at the axial centre [field solution, n=1] (T)	0.533
Average value of flux density assuming sinusoidal distribution (T)	0.340

Table 8.11: Excitation field predictions

Table 8.12 shows the EMF predictions:

Concentrated coil	
EMF/coil (V)	29.8
Manual summation over three coil sections	
EMF induced in inner segment	8.3
EMF induced in inner segment	9.9
EMF induced in inner segment	11.9
EMF/coil (V)	30.1

Table 8.12: EMF predictions

Table 8.13 shows the synchronous reactance predictions:

Leakage factor	1.2
Effective air-gap (m)	0.046
Coil inductance (mH)	1.16
Coil synchronous reactance (Ω)	0.27

Table 8.13: Synchronous reactance predictions

Table 8.14 details the predicted loss and thermal behaviour:

Ambient temperature (^{o}C)	20
Operating temperature within the winding (^{o}C)	80
Allowable power loss/coil (W)	43.46
Eddy current loss per coil (W)	1.3
Allowable I^2R loss per coil (W)	42.2
Resistivity at operating temperature	2.08E-08
Coil resistance (Ω)	0.14
Rated current (A)	141

Table 8.14: Predicted losses and thermal behaviour

Finally, since the equivalent circuit parameters are now fully defined, load lines can be estimated so as to give a clear performance prediction for an AC resistive load, Figure 8.30, Figure 8.31, and Figure 8.32.

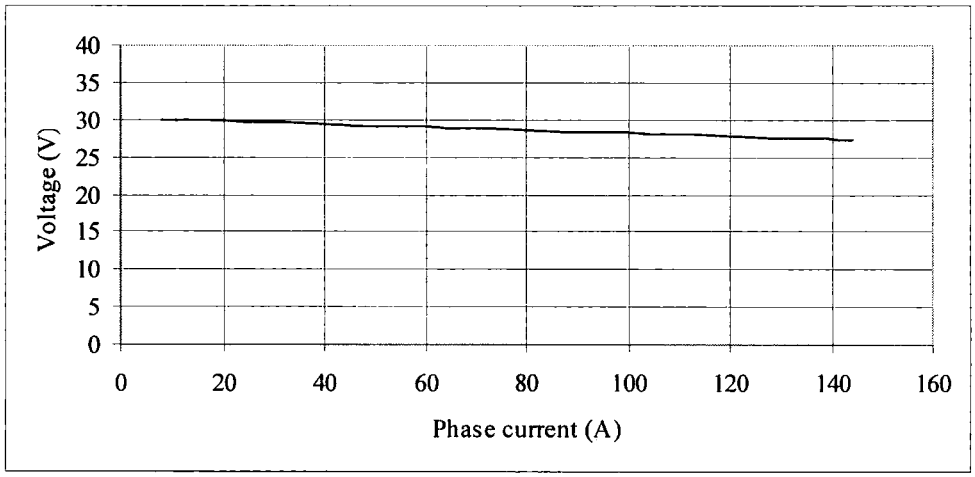

Figure 8.30: Predicted phase terminal voltage versus current at 140RPM

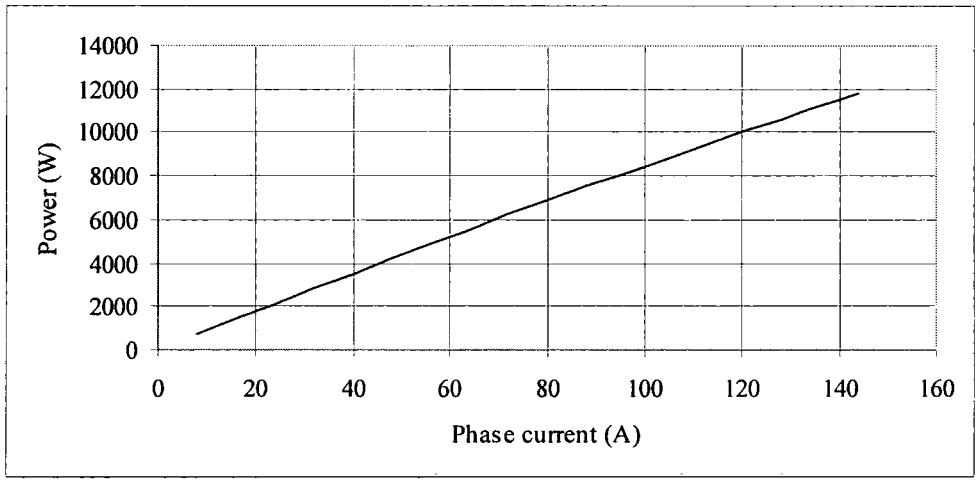

Figure 8.31: Predicted total power output versus phase current at 140RPM

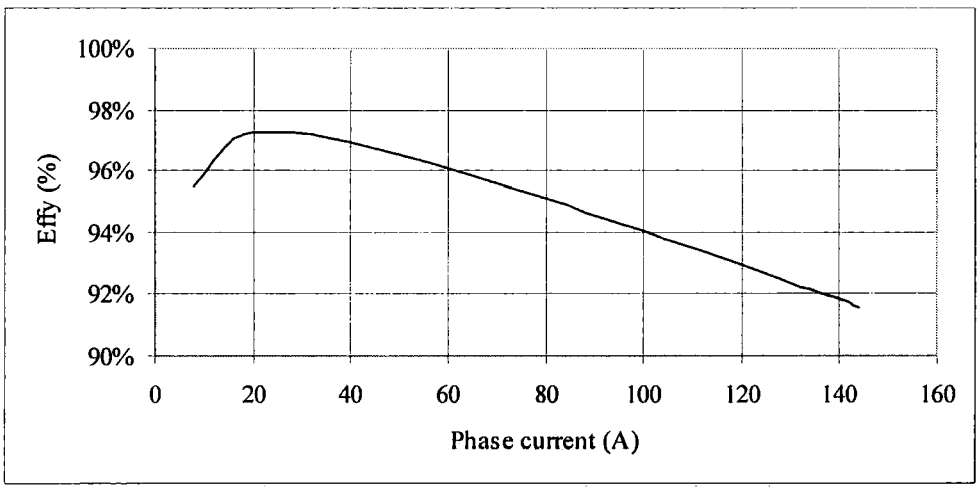

Figure 8.32: Predicted efficiency versus phase current at 140RPM

8.3.3. FEA of the design

A magnetostatic solution of the field arising from the magnets was performed using a 45° model with the standard symmetry conditions. The model represents the magnets by use of arcs and radii in accordance with the design approach. Figure 8.33 illustrates the model.

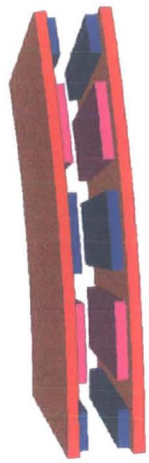

Figure 8.33: 3D FEA magnetostatic model

The solution gives the axial flux density the axial centre of the machine, as illustrated by the surface in Figure 8.34.

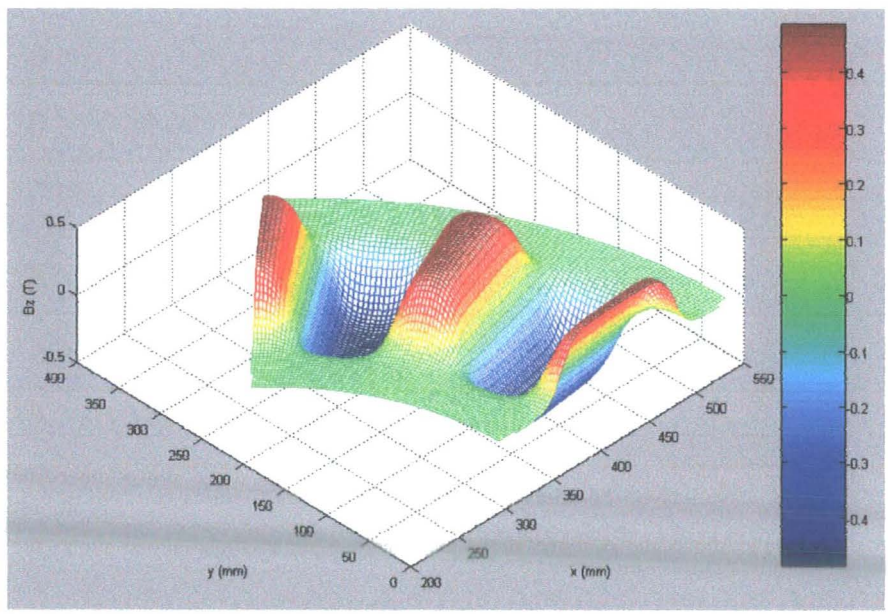

Figure 8.34: Axial flux density in the coil regions from the FEA model

Interpolation of this data at the mean radius of the machine and across the face of a magnet at a fixed radius give the circumferential and radial variations of axial flux density across a pole-face respectively, which are shown in comparison with the analytical predictions, Figure 8.35 and Figure 8.36.

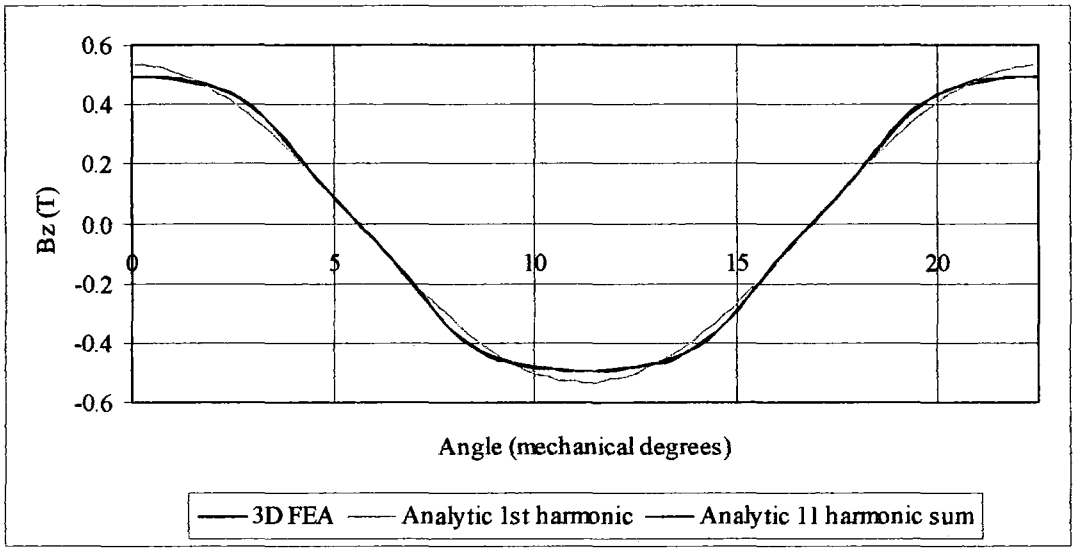

Figure 8.35: Circumferential variation of axial flux density in the winding region

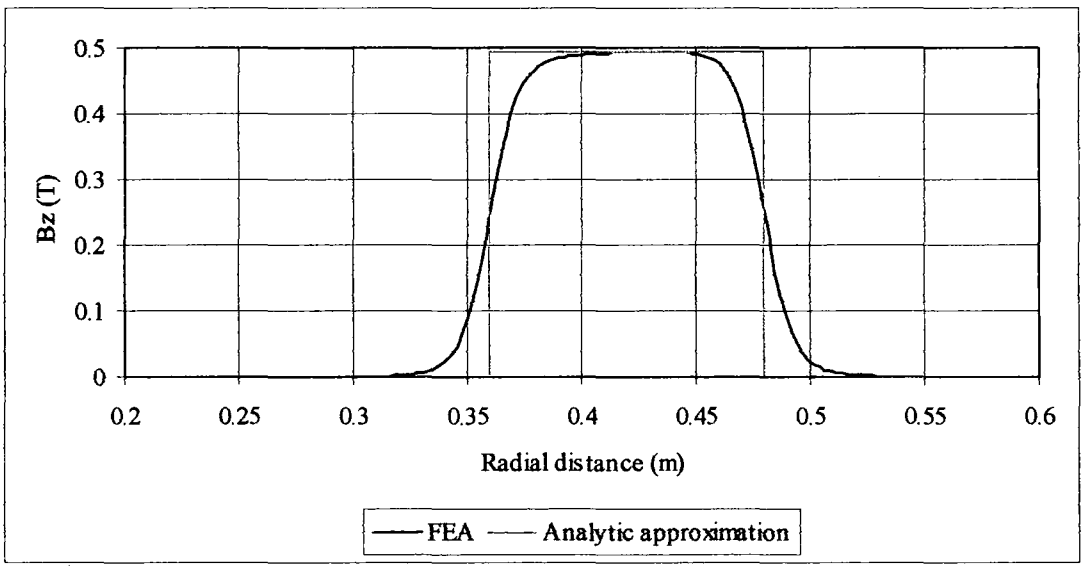

Figure 8.36: Radial variation of axial flux density in the winding region

Owing to the difficulty experienced in modelling trapezoidal coils in the FEA of the solar car motor, the problems previously described when performing dynamic FEA with disc-shaped models, and the good agreement shown between a linear (translating) model and a disc-shaped (rotating) model in section 8.1.4, a linear approach was adopted at this stage. The intention was to check the linear model against the disc-shaped model in the magnetostatic analysis of the field arising from the permanent magnets, prior to analysing the field arising from coil excitation for the determination of the synchronous reactance, and ultimately setting up a dynamic linear model. Figure 8.37 shows the resulting linear FEA mesh, spanning three coils and four magnets per rotor, and having the usual tangential flux boundary conditions at the edges of the model and the outer-facing rotor surfaces.

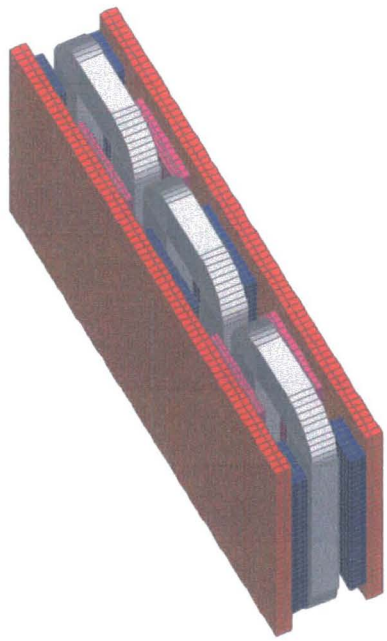

Figure 8.37: Linear 3D FEA mesh

The effect of the linearization is to reduce the coil and magnet spans at the outer radius and increasing them at the inner radius such that the full magnet/coil exhibits the circumferential span previously only encountered at the mean radius. Thus arc

shaped magnets become simple rectangles and the complicated arc-shaped coils encountered in the solar car FEA are replaced by the standard race-track coil. Where curvature is small as a result of a high pole number at a large radius, the difference between the coil and magnet widths at the inner and outer radii is minimal and the accuracy of such an approximation is good, as is expected to be the case here. Figure 8.38 illustrates the field arising from the magnets as obtained from the linear model, and Figure 8.39 compares the circumferential and radial characteristics obtained from the disc-shaped and linear models. As can be seen, the field plots obtained from the two FEA models are indistinguishable, giving confidence in the linear model for the analysis of the field arising from coil excitation.

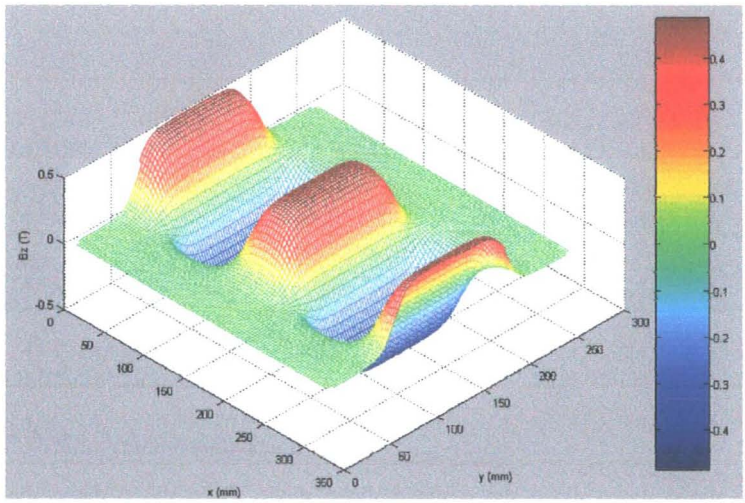

Figure 8.38: Flux density from the linear model for comparison with Figure 8.34

Figure 8.40 shows the axial flux density variation in the region of the winding, i.e. at the axial centre of the machine, where the central coil in the linear model has been energised with rated current.

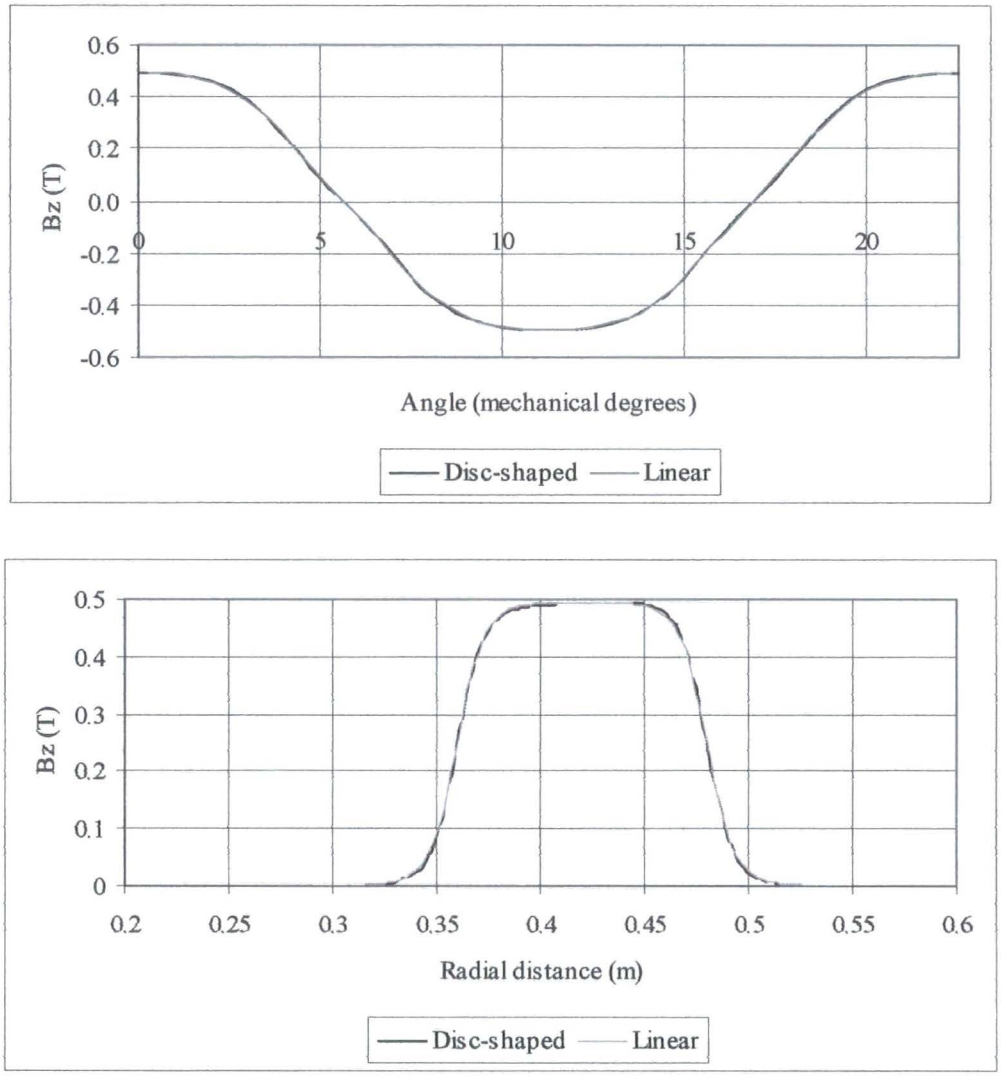

Figure 8.39: Circumferential and radial field comparisons

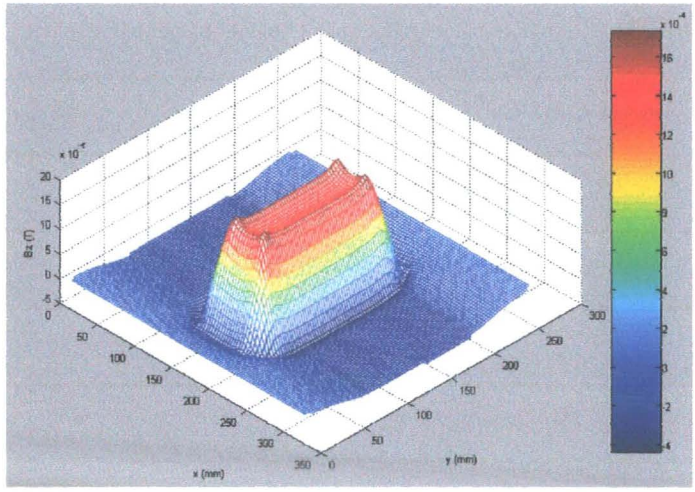

Figure 8.40: Axial flux density arising from coil excitation

The peak of the graph in Figure 8.40 is clearly longer in the radial direction in accordance with the coil dimensions, giving some endorsement of the analytical method where the radial direction is assumed infinitely long and modulated by an effective length equal to the radial length of a mean turn. Additionally, the steep sides encountered in the circumferential direction arise from the relatively small spread of the coil turns in this plane. Hence the assumption made in the analytical predictions that all the turns are concentrated at the mean position seems appropriate. Again, interpolation of the data shown in Figure 8.40 facilitates illustration of the circumferential and radial characteristics at the mean diameter and across the centre of a pole face respectively, for comparison with the value used in the analytical inductance calculation, Figure 8.41 and Figure 8.42.

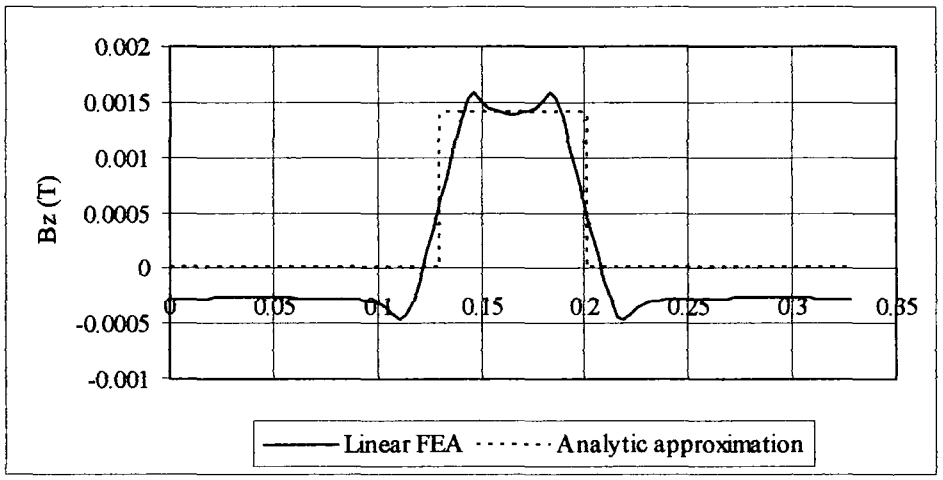

Figure 8.41: Circumferential variation of flux density from coil excitation

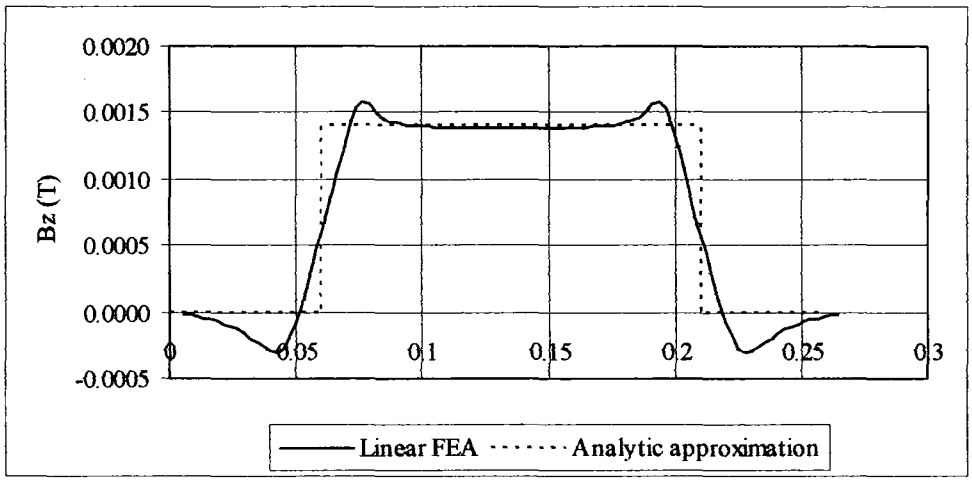

Figure 8.42: Radial variation of flux density from coil excitation

Additionally, an AC current of 1A was forced in the central coil and the resulting back-EMF at each of the three coils was returned by the FEA solver. Since there is zero resistance present, these back-EMF values are simply the inductive reactance contributed by each of the coils. Factoring in the frequency of the AC enables calculation of the self- and mutual-inductances. As has been described previously, the sum of the magnitudes of the self- and mutual-inductance gives the synchronous inductance from which the synchronous reactance may be obtained for comparison with the analytical value as used in the equivalent circuit predictions. Table 8.15 summarises the inductance values per coil.

L_{self} (mH)	0.713
M (mH)	0.165
L_{sync} (mH)	0.878
X_{sync} (Ω)	0.206

Table 8.15: Per-coil inductance parameters from 3D FEA

This contrasts somewhat with the value of 0.27Ω obtained analytically. There are a number of reasons for the difference. Notably, the analytical method neglected the mutual inductance effect and its contribution to the synchronous reactance. As Figure

8.41 shows, there is a considerable flux density in the regions flanking the energised coil such that a significant mutual inductance may be expected; this is further supported by the values shown in Table 8.15. Also, the analytical method uses a simple magnetic circuit approach which assumes an idealised case where all the flux crosses the gap perpendicularly to the rotor surfaces, and then applies a leakage factor to allow for the fact that a sizeable proportion of the flux linkage in the energised coil will be attributable to leakage in the large effective air-gap in the real case. It may be the case that the leakage factor applied is responsible for the introduction of significant inaccuracy. However, the synchronous reactance is small and the analytical approach can be improved along similar lines to the field solution approach taken with the TORUS and slotted machines.

Finally, the linear model was modified such that the rotors move with respect to the stator coils, and the FEA program returned the waveforms of the resultant EMF induced in the coils. Firstly, the tangential flux conditions at the rotor edges are removed and replaced with periodic boundary conditions. These effectively wrap one edge of the rotor fraction to the other; hence the stator coils see a continuous array of poles. Sliding interface surfaces are defined as close to the centre of the running clearance as the mesh allows; Lagrange polynomials are used at these surfaces to give the solution continuity across a break in the mesh. Dynamic movement is defined for the rated speed of 140RPM. This is equivalent to a linear velocity of 6.16m/s at the mean diameter of the machine. A distance of 2 pole-pitches is modelled in order to capture a full EMF cycle; this takes approximately 0.028s, which is divided into 50 time-steps of 0.00056s. Figure 8.43 shows the EMF induced in the 3 coils.

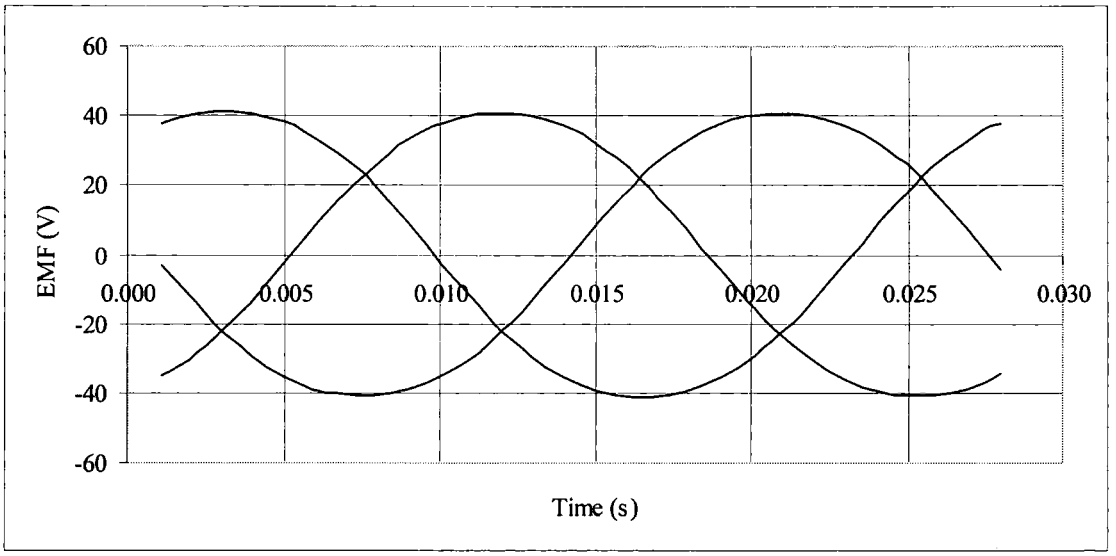

Figure 8.43: Coil induced EMF at 140RPM from 3D dynamic FEA

The 3 coils have 120° separation and the RMS value of the open-circuit EMF is 29.5V which compares well with the analytical prediction of 30.0V.

8.3.4. Conclusion

This final section of the thesis described the as yet unrealised design of a 10kW, 140RPM air-cored generator for a VAWT. The modifications described in the previous two sections of this chapter came together through the specification of a design having a high number of poles at a big diameter such that the machine is ring-shaped, and utilising trapezoidal magnets and coils for improved use of space by comparison with the simpler design conceived for the Savonius turbine.

The established analytical methods yielded predictions for the performance of such a machine, and static and dynamic FEA in 3D was used to illustrate the fields and verify the electromagnetic aspects of the analytical approaches so as to give assurance to the design and analysis procedure and the resultant performance predictions.

The field plots obtained from FEA generally showed excellent agreement with the analytical predictions. The synchronous reactance values were comparatively inaccurate, but possible reasons for this are apparent and evidenced in the field predictions; also, the magnitudes in question are of little relevance. Finally, the dynamic FEA generated open-circuit EMF waveforms that again showed good agreement with the analytical predictions.

In summary, the outcome is promising for the performance of this particular design, and for the application of the analytical and FEA methods described and developed in this thesis to continuing research in the field of axial flux permanent magnet machines.

Chapter 9. Conclusions and further work

9.1. Summary

This thesis has described the verification and benchmarking of a range of methods and techniques for the design and analysis of permanent magnet axial flux machines for direct-drive applications including compact engine-generator sets, VAWTs, and in-wheel motors. There has been a particular focus on the use of electromagnetic FEA to evaluate the assumptions and verify the predictions of analytical methods, predict the electromagnetic performance of the machines considered, corroborate the results of experimental tests, and illustrate the electromagnetic fields present in such machines.

The thesis commenced with the derivation, verification and benchmarking of a range of methods and techniques specifically for the design and analysis of the air-gap wound TORUS machine of Spooner and Chalmers, [5].

The methods and techniques developed were then extended to the investigation of permanent magnet axial flux machines having a slotted stator winding. A design procedure utilising a unified 2D analytical solution for machines with a slotted stator winding was developed and the design of a 40kW, 4500RPM generator for a compact diesel engine generator set was specified using this approach.

The methods and techniques were then developed and further extended to Bumby's novel permanent magnet axial flux machine, having an ironless stator with concentrated coils, and being the subject of an international patent, [7]. The full

range of analytical, FEA, and experimental approaches were performed and benchmarked for this new topology.

Finally, further investigation of VAWT generators was carried out, covering different pole shapes and larger specifications, as well as the FEA and experimental test of Bumby's novel permanent magnet axial flux machine as an in-wheel motor for a solar-powered car.

The permanent magnet axial flux machines considered in this thesis were conceived with simplicity, economy, and ease of assembly and manufacture in mind; these are overarching principles of the research here described. In summary, the thesis contains proven methods and techniques of design and analysis which were used in the development of a range of novel machines for direct-drive applications, and will be of use in the course of further research in this field.

9.2. Conclusions

9.2.1. General analysis of air-gap wound toroidal generators

Equations and methods of analysing the basic TORUS design were presented. In particular, two approaches to the electromagnetic analysis were described: one based on a general, unified, 2D field solution and the other utilising simple magnetic circuit analysis. The losses in the machine were analysed and evaluation techniques described; an approximate thermal model was described which facilitates an estimation of the total allowable loss and therefore allows the rated current to be calculated. Using these methods, the performance of air-gap wound toroidal generators can be predicted.

9.2.2. FEA and experimental test of air-gap wound toroidal generators

The analytical methods previously derived for air-gap wound toroidal generators were applied to two prototype machines. Further to this, a range of electromagnetic FEA techniques were described and the results of the FEA were compared directly with the analytical predictions for the benchmarking of the two approaches.

The analytical methods use a 2D approximation, and the FEA was carried out in both 2D and 3D in order to verify the analytical predictions and check the applicability of the 2D approach to a 3D problem. The field solution showed excellent agreement with the FEA, particularly in 2D where the results were almost identical. Although comparison with the 3D FEA results highlighted some slight inaccuracy in the 2D approach, the overall conclusion is that the 2D approximation is sufficiently accurate for analytical design and analysis purposes.

The predictions concerning the field arising from the permanent magnet excitation were closely corroborated by the FEA. Some slight differences were encountered in the analysis of the field arising from phase currents, but the inductance values were so slight that highly accurate prediction is accepted to be difficult and also not of great importance. Principally, the electromagnetic FEA was carried out in order to predict the electromagnetic equivalent circuit parameters E and X_{syn} for comparison with the analytical predictions, and the results obtained from the two methods agreed to within 3%, giving confidence in further application of both approaches to this type of machine.

Finally, a series of laboratory tests confirmed the accuracy of the analytical and FEA approaches with both predictions of E agreeing to within 1% of the test result for

both machines, the 20kW predictions of X_{syn} agreeing to within 3% of the test result and the 40kW to within 11% owing to the very small overall value of inductance. In the case of the 40kW machine the measured value of X_{syn} exceeded the predictions, indicating that the source of error is likely to be stray inductance owing to the leads and connections which were not considered in the analyses but are expected to have a significant effect given the small values involved.

This work provided a foundation for the investigation of modifications to the TORUS design and of more novel machines in Chapter 4 to Chapter 8; the good results obtained in Chapter 4 gave confidence in the further application of these methods.

9.2.3. A slotted stator winding modification to the TORUS

The analytical and FEA methods and techniques were extended to the design of an axial flux generator with a slotted winding. In order to facilitate as close a comparison with the air-gap wound TORUS as possible, this study commenced by devising two slotted variants of the 40kW prototype TORUS. The analytical and FEA predictions of the open circuit EMF agreed to within 5% and those for the synchronous reactance agreed to within 6%, giving confidence in the accuracy of the design study.

In addition, FEA was used to investigate the effects of slot harmonics and evaluate the accompanying cogging torque. Slot harmonics were shown to have a detrimental effect on the EMF waveform and the cogging torque predicted for one of the slotted variants was of a similar magnitude to the overall electromagnetic torque developed. A number of ways to remedy these undesirable effects were discussed and rotor skew

was shown to reduce cogging torque by 75% and significantly improve the EMF waveform at the expense of a very slight (<1%) attenuation of the EMF.

Although the two slotted variants formed useful stages in the extension of the analysis to slotted machines, this design approach was far from optimal. The TORUS winding specification severely constrained the design of the slotted machines such that the benefits of slotting were not fully realised by this approach. However, the results indicated that slotted machines were capable of generating up to 50% more power per unit volume than the TORUS by way of an increased magnetic loading at the expense of slot harmonics and increased complexity of design and construction.

9.2.4. Design of a 40kW generator with a slotted stator winding

In Chapter 6 the formulation of a new design for a 40kW axial flux permanent magnet generator with a slotted stator winding was detailed. The process commenced with the description of a generalised design procedure for axial flux machines based on the Lorentz Force principle and using the optimal ratio between the inner and outer stator core diameters derived by Campbell, [13]. A new winding design process was described, as was an enhanced approach to the thermal modelling of slotted machines. Along with the analytical methods described in Chapter 4, this concluded the development of a design process for an original slotted machine and a spreadsheet approach to this task was described. An initial run through the spreadsheet was illustrated, and some iteration of this process yielded a final design, the parameters of which were summarised.

By comparison with the modifications to the TORUS design described in Chapter 4, this approach gave considerably more freedom in the winding design, resulting in a

predicted increase in the electric loading possible in the slotted machine over that previously encountered in the air-gap wound TORUS. A final comparison between the original TORUS and the predicted performance of the new slotted design showed that, whilst both designs would potentially achieve the specified power and speed ratings, there are some significant differences. Firstly, the slotted machine is much smaller, having a rotor outer diameter of 285mm compared with 415mm in the case of the TORUS, and exhibits a power density almost twice that of the TORUS. Also, the mass of permanent magnet material required by the slotted machine is less than 60% of that used in the TORUS.

This study of slotted machines is particularly relevant to the ongoing research and development in the field of diesel engine-generator sets for portable power generation applications. From that perspective, the results of this investigation are encouraging since Newage-AVK-SEG is currently trialling such a generator set with an air-gap wound TORUS-type machine, and is constantly looking to improve this product in cost and performance terms.

Disadvantages of slotted machines were highlighted in Chapter 4 and Chapter 6. Firstly, it was indicated that slotted machines are more complicated and this would affect the complexity and therefore cost of manufacture. A more subtle but potentially important effect is the alteration of the aspect ratio of permanent magnet axial flux machines where slotted stator windings are specified. Such machines naturally tend towards an increased axial length and this may render the slotted machine less attractive in applications where the pancake geometry of the original TORUS was an advantage, for example, where the short axial length of the TORUS enabled a bearing-less design. Furthermore, the investigation into slot harmonics

highlighted the naturally smooth and relatively harmonic-free operation of the original TORUS, and gave some indication of the potential problems of slotted machines in this respect. It was shown that various methods exist for suppression and limitation of these effects, which may be sufficient in the case of diesel engine-generator sets. However, other possible applications of axial flux machines may be less forgiving. VAWTs in particular tend to have zero or minimal starting torque, and so the cogging torque and the potential noise and vibration resulting from these harmonics are a serious disadvantage.

9.2.5. FEA and experimental test of a novel air-cored machine

In Chapter 7, the requirements of the small VAWT application were described and an appropriate specification for a suitable generator was described. Bumby's novel axial flux generator for this application, having an iron-less stator with bobbin-wound concentrated coils, and being the subject of an international patent, [7], was then detailed in terms of its principle of operation, its geometry, and the design and construction of a prototype machine carried out by Wong, [99]. The intention of the author was to extend the FEA modelling techniques developed in previous chapters to this new design in order to validate the assumptions inherent in the analytical techniques used for the design and analysis, to provide quantitative verification of the analytical predictions, to investigate the mode of operation of the machine, and to enhance the understanding of its electromagnetic behaviour. In addition, experimental testing of a prototype machine carried out by the author was described and the outcomes compared with the predictions of the FEA and analytical methods in order to complete the investigation.

FEA of the excitation field supported the predictions of the analytical method, showing agreement to within 2% of predicted values of flux density and induced EMF. Also, this process facilitated visualisation of the field and corroboration of certain assumptions, namely that the excitation field experienced by the coil is a sinusoidal *"hill"* of axially-directed flux density, that the radial spread of the turns of each coil has a marked effect on the flux linkage and the resultant induced EMF, and that the axial spread of the coil is comparatively unimportant.

Similarly, FEA of the field arising from phase currents facilitated visualisation of the field, and Fourier analysis of this gave an insight into the mode of operation of the machine, in particular the transfer of torque on higher-order harmonics. The visualisation of the field also corroborated the assumption that the radial distribution of the turns gives rise to a conical variation of axial flux density in the air-gap. This verified the analytical approach to some extent, whilst the quantification of the synchronous reactance of the machine showed agreement between the analytical and FEA predictions to within 10%.

Finally, the conclusions of the experimental tests were twofold. Firstly, the results showed agreement with the analytical and FEA predictions to within 5%, giving confidence in the extension of these approaches to further designs. Secondly, the prototype machine was demonstrated to perform as required by the application, producing in excess of 2kW at 500RPM and in excess of the rated 1kW at 300RPM, with efficiencies in excess of 90% in both cases. These are very positive results in the development of novel, application-specific machine topologies and merit development and further investigation, some ideas for which are presented in section 9.3.

9.2.6. Further applications of the novel air-cored axial flux machine

Bumby's novel axial flux generator, [7], described in Chapter 7, proved successful in that it performed well and the experimental, analytical, and finite element results agreed to a good level of accuracy. Therefore this topology is the subject of ongoing research in the VAWT application as well as other alternative applications. Three further incarnations of the topology were considered in Chapter 8 prior to the conclusion of the thesis. Each of the three offered something new in terms of either a particular design nuance, extension to a new application, or the finite-element approach required as a result of these advances.

The first section described the analysis of a generator design for a VAWT rated at 7.5kW at 132RPM, being simply a larger version of that described in Chapter 7. FEA verification of the analytical approaches showed the underlying assumptions of the analytical methods to be consistent with the fields present in this particular design. Specifically, 3D dynamic FEA of the machine using a linear (translating) model was shown to give results in good agreement with the analytical predictions.

The second section concerned the motor designed for a solar car by Bumby, being a slight variation on the original novel axial flux generator, [7]. Trapezoidal (or arc-shaped) magnets and coils are specified in this design so as to increase the use of the volume occupied by the machine through the extension of the active radial length of the machine. The revised analytical methods for this variation were verified by FEA both quantitatively and in terms of the simplifying approximations made to the excitation field in the analytical solution. The FEA approach required the definition of trapezoidal coils within the FEA programme which represents a complication to the coils considered previously in this thesis. Such coils were defined and used

within a dynamic 3D model to predict the open-circuit EMF to within 9% of that measured during experimental test. The inaccuracy is thought to be attributable to variation between the actual prototype machine and the design specification, perhaps affecting the effective air-gap, and also to some unpredictability encountered in the FEA programme where large models having disc-shaped sliding interfaces are used. In general, the analytical and FEA predictions agreed well with the results of experimental tests.

This final section of the thesis described the as yet unrealised design of a 10kW, 140RPM air-cored generator for a VAWT. The modifications described in the previous two sections of this chapter came together through the specification of a design having a high number of poles at a big diameter such that the machine is ring-shaped, and utilising trapezoidal magnets and coils for improved use of space by comparison with the original design.

The established analytical methods yielded predictions for the performance of such a machine, and static and dynamic FEA in 3D was used to illustrate the fields and verify the electromagnetic aspects of the analytical approaches so as to give assurance to the design and analysis procedure and the resultant performance predictions.

The field plots obtained from FEA generally showed excellent agreement with the analytical predictions. The synchronous reactance values were comparatively inaccurate, but possible reasons for this were apparent and evidenced in the field predictions. Finally, the dynamic FEA generated open-circuit EMF waveforms that again showed good agreement with the analytical predictions.

In summary, the outcome is promising for the performance of this particular design, and for the application of the analytical and FEA methods described and developed in this thesis to continuing research in the field of axial flux permanent magnet machines.

9.3. Further work

This thesis described the author's work in the continued development of novel permanent magnet machines at the University of Durham. The machines investigated are the subjects of continual research in this field and in this section a number of potential avenues for further work are briefly discussed under two headings. Firstly, further work concerning iron cored machines with slotted stator coils is mentioned with particular reference to the engine generator set application. Finally, further work concerning the novel, air-cored design of Bumby, [7], is discussed.

9.3.1. Iron-cored machines with slotted stator coils

The obvious extension of the work in this direction would be to build an iron-cored machine with slotted stator coils using the design methodology developed in Chapter 4 and Chapter 6. Laboratory testing of a prototype would hopefully verify the analytical and FEA work here described. In addition to the electromagnetic analysis which this work is primarily concerned with, the verification and further improvement of the loss and heat transfer calculations would be of significant interest. The thermal performance of electrical machines is critical and yet the methods and techniques available for design and analysis are often inferior by comparison with those used for the electromagnetic issues. A thorough consideration

of heat transfer in axial flux machines would complement the work described in this thesis and the testing of a prototype having slotted stator coils would be an ideal vehicle for this. In particular, it would be very useful to establish heat transfer coefficients for a number of machines, and the extra mechanical losses from pumping and windage would help complete the efficiency evaluation.

Newage-AVK-SEG has expressed continued interest in developments concerning the understanding of iron-cored axial flux machines with slotted stator coils. In the latter stages of this work the author designed a 5.2kW 2900RPM machine of this type, using the methods outlined in Chapter 4 and Chapter 6, specifically for a diesel engine generator set being developed by Newage-AVK-SEG as part of a cost improvement programme; an opportunity for further development of this would be ideal for prototyping an iron-cored axial flux machine with slotted stator coils

9.3.2. Air-cored machines with concentrated coils

The air-cored machine of Bumby, [7], is a new development and, as such, opens up a range of potential directions for further work. As described in section 9.3.1, further development of the modelling of loss and heat transfer would complement the work described in this thesis. This area is of particular interest in the context of the air-cored machine since much reliance is placed upon plastic materials that are not conventionally used in electrical machines. Detailed analytical and experimental work concerning heat transfer in the stator is potentially crucial to the performance of this machine, particularly in the direct-drive wind turbine application where low rotational speeds limit the cooling effects.

Additionally, the original prototype devised by Wong, [99], specified the inclusion of holes in the rotor as well as at the centre of the stator coils for enhanced heat dissipation. The general optimisation of the mechanical design for heat dissipation would further advance this research. A related matter concerns the potential development of the machine for the market. Prototypes built to date have been of rudimentary construction giving easy access for modification and experimentation, but in the eventuality of a final product going to the market, the machine would be fully enclosed and therefore perhaps less well cooled. Inclusion of dedicated fan components may be worthy of investigation, and forced cooling may likewise be of interest where large machines are concerned. Again, it would be very useful to establish heat transfer coefficients and mechanical losses for this topology.

The greater understanding of the electromagnetic behaviour of air cored machines with concentrated coils afforded by this thesis opens up numerous possibilities for the extension and further exploration of this topology in general. First and foremost, little in the way of optimisation has been achieved for these machines and so there is a great deal of work to be done concerning the choice of phase number, pole number, pole shape, coil shape, and other parameters within the confines of the topology investigated in Chapter 7 and Chapter 8. Pole and coil shapes are of particular interest since factors such as the cost of certain magnets shapes and the ease of manufacture of coils are entwined in the fundamentals of performance. Furthermore, these considerations have deep seated effects on the analytical methods used. The motor described in Chapter 8 for a solar powered car was an initial investigation of varying pole and coil shapes and demonstrated these concerns. For example, it is likely that rectangular magnets are less costly than circular, trapezoidal, or arc shapes. With magnets forming a significant proportion of the cost of such machines,

the relative effects on costliness of improved performance through the specification more expensive magnets and of diminished performance through specification of sub-optimal magnets would make for an interesting study. Consideration of related parameters such as magnet and effective air-gap thicknesses is also fundamental to further work on design optimisation.

From a materials perspective, the use of alternatives to traditional laminated electromagnetic steel is a huge area for potential investigation. In particular, the requirements of VAWT manufactures led to the specification of a plastic stator and coil fixtures, but materials improvements to the existing design could give rise to better heat transfer and improved electromagnetic characteristics. Materials considerations could be considered alongside intelligent mechanical design, and would also impact upon the optimisation of the design described above.

The physically large machines considered in Chapter 8 highlight the metamorphosis of the disc-type TORUS machine into an annular profile as both pole number and diameter increase in order to meet the requirements of wind turbines, where speed of rotation decreases as power increases. The unused volume within the inner diameter of the active material yields two options, namely the inclusion of more electromagnetic material so as to make better use of the space, or an ingenious structural design to give lightweight, inexpensive support to an active area at a large radius. Such structural considerations are an interesting area for potential investigation and may give rise to alternative topologies which use some of the characteristics of the novel design of Bumby, [7]. One possibility is a move back to radial flux designs, extrapolating the concepts of twin rotors, concentrated coils, and an ironless stator as shown in Figure 9.1. This approach does not solve the structural

problem of supporting the active material at a large radius, but may facilitate the extension of the active length in a manner uninhibited by the constriction effects of the inner radius encountered in axial flux machines. By inspection of Figure 9.1 it is clear that the analytical and FEA approaches developed in this thesis are readily extended to this arrangement.

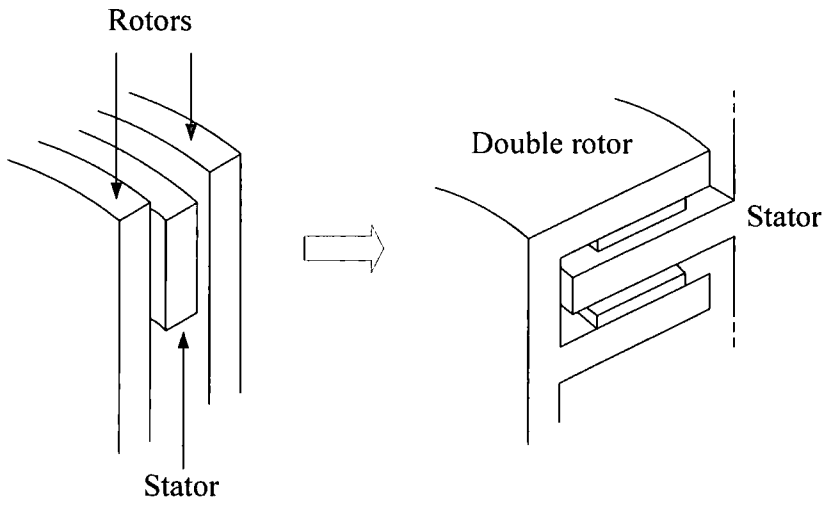

Figure 9.1: Axial to radial flux conversion

The author is of the opinion that the good characteristics exhibited by the air-cored, concentrated coil principle when used between twin rotors having surface mounted permanent magnets, and the accurate methods and techniques for the design and analysis of such an arrangement as described in this thesis merit further work in this area.

Appendix 1

Matlab program for organising an FEA dataset

Elements of the FEA meshes used in this thesis were not regularly spaced across an x-y grid. In order to remedy this, a Matlab program was written where a regularly spaced grid was defined, and interpolation commands were used to fit the FEA data to a regular grid. The resulting dataset could then be displayed as a 3D surface. Sample code for this is given below, and similar programs were devised to interpolate the FEA data in order to plot 2D graphs.

```
% Read in the data and define the columns
dat=xlsread('C:\Richard Martin\PhD\thesis writeup\Chapter 4\40kW 3D FEA
excitation field.xls');
x=dat(:,1);
y=dat(:,2);
r=dat(:,3);
b=dat(:,4);

% Define a regularly spaced grid in polar coordinates to cover the model
phi=(0:0.375:22.5)*pi/180;
rad=min(r:((max(r)-min(r))/60):max(r);

% Convert the grid to rectangular coordinates
k=0;
for i=1:length(phi)
        for j=1:length(rad)
                k=k+1;
                xx(k)=rad(j)*cos(phi(i));
                yy(k)=rad(j)*sin(phi(i));
        end
end

% Interpolate the data to fit the regular grid
[xi,yi,zi] =griddata(x,y,b,xx,yy,'linear');
xr=reshape(xi,61,61);
yr=reshape(yi,61,61);
zr=reshape(zi,61,61);

% Plot the axial flux density over the grid as a 3D mesh
mesh(xr,yr,zr);
```

Appendix 2

Spreadsheet design of slotted machines using MS Excel

This appendix briefly describes the first iteration through the design spreadsheet for a slotted axial flux machine developed in Chapter 6.

Firstly, a number of material constants are defined. The speed and power requirements are input along with fundamental choices such as pole number, phase number, and pole arc to pole pitch ratio. Assuming the magnetic loading to be 0.7T and the electric loading to be 12kA/m, and using the rough sizing equation derived in section 6.1, an initial outer diameter is obtained.

Assuming Campbell's ratio between the core diameters to hold, specifying an initial magnet thickness, and specifying no magnet overhang relative to the inner and outer core diameters, gives the initial sizing.

Wire specification, choice of number of slots per pole per phase, and choice of number of parallel strands per turn facilitates the winding design.

Specification of the running clearance then allows the excitation field to be analysed resulting in the calculation of the magnetic loading and the induced EMF. The analytical results are those obtained from application of the field solution and appear alongside those results obtained by the more simple magnetic circuit solution, both described in Chapter 4.

Once the flux carrying requirements have been ascertained, the dimensions of the stator and rotors can be defined accordingly with specification of the rotor inner diameter and the rotor disc extension. The rotors built for the TORUS have tended to be flame-cut from electrical steel and the inner diameter can be specified accoutring to the input from the prime mover. The outer diameter must exceed that of the magnets so that some form of magnet retainer can be implemented to fix the radial position of the magnets. The mass of the various components and the rotor inertia can also now be calculated. Since the winding is fully defined now that the stator dimensions are set, specification of the operating temperature allows calculation of the phase resistance.

Following this, the synchronous reactance is calculated and no further design decisions are required to this end. Finally, thermal analysis and loss calculation must be carried out to obtain a current rating. Specification of the ambient temperature facilitates this. Now this initial design is fully specified, its performance can be modelled using an equivalent circuit approach.

On the following pages the design spreadsheet is replicated, firstly with the actual values and then with spreadsheet formulae. This shows only the first iteration. The spreadsheet was then altered to yield the final design described in Chapter 6.

Richard Martin	
Design Spreadsheet for Slotted Axial Flux Machine - 1st iteration	
SUMMARY	
Power (W)	51872
Speed (RPM)	4500
Phases	3
Poles	16
Elec Freq (Hz)	600
Core OD (m)	0.326
Core ID (m)	0.188
Core length (m)	0.069
Mean magnet width (m)	0.033
Wire dia (m)	0.00054
Parallel strands	1
Turns/pole/phase	122
Clearance (m)	0.002
Magnet thickness (m)	0.006
Rotor thickness (m)	0.011
Stator thickness (m)	0.036
Axial length (m)	0.076
Rotor OD (m)	0.336
Magnet mass (kg)	3.261
Magnet cost at £20/kg	65.226
Mass of steel and magnet (kg)	31.344
Inertia of magnets and rotors (kg.m^2)	0.282
Magnetic loading (T)	0.888
E phase (V)	9776
R phase (ohms)	54.85
X syn phase (ohms)	347.058
I rated (A)	2
Current density (A/mm^2)	9
Elec loading at Dmean (A/m)	12979
Efficiency (%)	97.4
Power density (kW/m^3)	7731.02

Richard Martin	
Design Spreadsheet for Slotted Axial Flux Machine - 1st iteration	
DESIGN	
	Constant
	Input
	Calculate
CONSTANTS	
μ 0 (H/m)	1.257E-06
Br (T)	1.200
μ r	1.070
B core (T)	1.400
B disc (T)	1.200
Density of steel (kg/m^3)	7.85E+03
Density of magnet (kg/m^3)	7.40E+03
Resisivity of copper at 0 deg-C (Ohm-m)	1.55E-08
Temperature coefficient of resistance	4.26E-03
Heat transfer coefficient (W/m^2.deg-C)	150
k winding (W/m.deg-C)	0.50
k insulation (W/m.deg-C)	0.50
k steel (W/m.deg-C)	150
INPUT PARAMETERS	
Power (W)	40000
Speed (RPM)	4500
Number of phases	3
Number of poles	16
Electrical frequency (Hz)	600
Electrical frequency (rad/s)	3770
Pole arc/pitch ratio	0.66
APPROXIMATE SIZING	
Magnetic loading (T)	0.70
Electric loading (A/m)	12000
k campbell	0.58
Approximate outer diameter (m)	0.326
INITIAL SIZING	
Outer core diameter (m)	0.326
ID/OD	0.58
Inner diameter (m)	0.188
Mean diameter (m)	0.257
Core length (m)	0.069
Magnet overhang at ID and OD (m)	0.000
Magnet length (m)	0.06889
Magnet OD (m)	0.326
Magnet ID (m)	0.188
Pole pitch (rad)	0.393
Pole pitch (m)	0.0505
Pole arc (rad)	0.259
Pole arc (m)	0.0333
Pole area (m^2)	0.003
Magnet mass (kg)	3.261
Magnet inertia (kg.m^2)	0.058
Magnet cost at £20/kg (£)	65.23

WINDING DESIGN - MUSH WINDING	
Wire diameter (m)	0.00054
Slots/pole/phase	2
Liner insulation thickness (m)	0.0008
k tooth	1.000
k slot	2.000
k fill	0.700
Parallel strands	1
Total slot width available per pole per phase (m)	0.00841
Slot width (m)	0.00421
Tooth width (m)	0.00421
Tooth width at ID (m)	0.00308
Slot pitch (m)	0.00841
Peak flux density in tooth at D mean (T)	1.654
Slot depth (m)	0.00841
Slot width available for conductors (m)	0.00261
Slot depth available for conductors (m)	0.008
Slot area available for conductors (m)	1.985E-05
Wire cross sectional area (m^2)	2.278E-07
Conductors per slot	61
N per pole per phase	122
Fundamental distribution factor >1 slot/pole/ph	0.9549
Fund distribution factor - 1/pole/ph only	0.9971
EXCITATION FLUX	
Running clearance (m)	0.002
Magnet thickness (m)	0.0060
Slot opening/Running clearance	1.912
k carter	0.265
kc	1.153
Effective gap (m)	0.0081
Flux density (T)	0.826
Peak flux density - fundamental of square wave (T)	0.905
1st harmonic peak flux per pole (Wb)	2.005E-03
Peak flux per pole from square wave (Wb)	1.897E-03
FULL 1st harmonic B pk (T)	0.888
FULL sum to 21 harmonics B pk (T)	0.827
FULL 1st harmonic peak flux per pole (Wb)	1.966E-03
FULL sum to 21 harmonics phi pp pk (T)	1.889E-03
OPEN CIRCUIT EMF	
E/pole/ph 1st harmonic from magnetic circuit (V)	622
E phase 1st harmonic from magnetic circuit (V)	9956
FULL E coil sum to n = 21 (V)	611
FULL E phase sum to n = 21 (V)	9776
Full E phase /100RPM (V)	217
ROTOR SIZING	
Rotor disc extension (m)	0.005
Rotor ID (m)	0.020
Rotor OD (m)	0.336
Peak disc flux (Wb)	9.45E-04
Disc minimum thickness (m)	0.01143
Mass of 2 rotors (kg)	15.9
Inertia of rotors (kg.m^2)	0.224
Inertia of rotors and magnets (kg.m^2)	0.282

STATOR DESIGN	
Peak core flux (Wb)	1.89E-03
Core thickness (m)	0.020
Teeth mass - both sides (kg)	3.68
Core mass (kg)	8.56
Combined mass of stator iron (kg)	12.23
Core and teeth thickness (m)	0.036
Total axial length	0.076
Total mass (kg)	31.344
PHASE RESISTANCE	
Operating temperature (deg-C)	160
Resisivity at operating temperature (Ohm-m)	2.606E-08
Strand copper diameter (m)	5.000E-04
Conductor cross sectional area (m^2)	1.963E-07
Length of mean turn (m)	0.21
Length of phase conductor (m)	413.17
Phase resistance (Ohms)	54.85
INDUCTANCE	
L main fund per pole (H)	2.952E-03
M main fund per pole (H)	1.476E-03
L slot leakage per pole (H)	2.309E-07
L gap leakage per pole (H)	1.137E-06
End geff (m)	1.607E-02
L end fund per pole (H)	6.081E-04
M end fund per pole (H)	3.041E-04
L syn phase (H)	8.546E-02
X syn (Ohms)	322.184
FULL L main fund per pole (H)	3.200E-03
FULL M main fund per pole (H)	1.600E-03
FULL L end fund per pole (H)	6.081E-04
FULL M end fund per pole (H)	3.041E-04
FULL L syn phase fund (H)	9.143E-02
FULL X syn fund (Ohms)	344.669
FULL L main per pole (H)	3.474E-03
FULL M main per pole (H)	1.355E-03
FULL L end per pole (H)	7.101E-04
FULL M end per pole (H)	2.134E-04
FULL L syn phase (H)	9.206E-02
FULL X syn (Ohms)	347.058
THERMAL MODEL	
Ambient temperature (deg C)	20
Temperature difference (deg C)	140
R copper 1 (W/degC)	5.841E+00
R surface HT 1 (W/degC)	5.115
R copper 2 (W/degC)	1.712E-01
R liner (W/degC)	0.210
R steel (W/degC)	1.540E-02
R surface HT 2 (W/degC)	3.169
R slot (W/degC)	10.956
R tooth (W/degC)	3.566
R total (W/degC)	2.690
Allowable loss per half slot/tooth (W)	52
Total allowable loss (W)	1377

LOSSES	
Eddy loss (W)	532
Core back iron loss (W)	199
Teeth iron loss (W)	118
Total iron loss (W)	317
Allowable I2R loss (W)	527
I rated (A)	1.790
Current density (A/mm^2)	9.117
Electric loading at Dm (A/m)	12979
EQUIVALENT CIRCUIT	
Phase open cct EMF (V)	9776
Phase resistance (Ohms)	54.847
Synchronous reactance (Ohms)	347.058
Rated current (A)	1.790
V phase (V)	9658
Power output (W)	51872
Efficiency (%)	97.4
POWER DENSITY	
Volume of machine (m^3)	6.71E-03
Power density (kW/m^3)	7731.02

Richard Martin													
Design Spreadsheet for Slotted Axial Flux Machine - 1st iteration													
FIELD SOLUTION													
n	1	3	5	7	9	11	13	15	17	19	21	SUM	
un (rad)	6.22E+01	1.87E+02	3.11E+02	4.36E+02	5.60E+02	6.85E+02	8.09E+02	9.33E+02	1.06E+03	1.18E+03	1.31E+03		
Jn (A/m^2)	60866028.57	2221162.787	-63008135.24	58485711.5	6654722.446	-64897585.48	55874578.04	11062018.96	-66532914.59	53042933.15	15425658.73		
x	Bn											B	B sine
0.000	0.888	0.009	-0.128	0.066	0.004	-0.027	0.015	0.002	-0.008	0.004	0.001	0.827	0.905
0.001	0.886	0.009	-0.122	0.060	0.004	-0.021	0.011	0.001	-0.004	0.002	0.000	0.826	0.904
0.002	0.881	0.009	-0.104	0.042	0.002	-0.005	-0.001	-0.001	0.004	-0.003	-0.001	0.824	0.898
0.003	0.873	0.008	-0.076	0.017	0.000	0.013	-0.012	-0.002	0.008	-0.004	-0.001	0.824	0.890
0.004	0.861	0.007	-0.041	-0.011	-0.003	0.025	-0.015	-0.002	0.004	0.000	0.000	0.825	0.878
0.005	0.846	0.006	-0.002	-0.038	-0.004	0.028	-0.009	0.000	-0.004	0.004	0.001	0.825	0.862
0.006	0.827	0.004	0.037	-0.057	-0.004	0.016	0.002	0.002	-0.008	0.003	0.000	0.821	0.843
0.007	0.805	0.002	0.073	-0.066	-0.003	-0.002	0.012	0.002	-0.004	-0.002	-0.001	0.818	0.821
0.008	0.780	0.001	0.102	-0.062	-0.001	-0.019	0.015	0.001	0.005	-0.004	0.000	0.816	0.796
0.009	0.752	-0.001	0.121	-0.047	0.001	-0.027	0.008	-0.001	0.008	-0.002	0.001	0.814	0.767
0.010	0.722	-0.003	0.128	-0.023	0.003	-0.023	-0.004	-0.002	0.003	0.003	0.001	0.806	0.736
0.135	-0.462	0.009	0.051	-0.042	0.004	0.007	-0.011	0.002	0.001	-0.004	0.001	-0.444	-0.471
phi pp n	1.966E-03	-6.939E-06	-5.680E-05	-2.088E-05	1.104E-06	5.525E-06	2.608E-06	-2.970E-07	-1.065E-06	-5.206E-07	9.490E-08	1.889E-03	
kd n 1 slot/pole/phase	0.997146657	0.974495358	0.93011895	0.865824725	0.784213304	0.688552802	0.582621602	0.470527982	0.356516063	0.244768145	0.139213623		
kd n > 1	0.954929659	0.638619772	0.190985932	-0.136418523	-0.212206591	-0.086811787	0.073456128	0.127323954	0.056172333	-0.050259456	-0.090945682		
E coil n	610.71	-4.31	-17.64	6.48	-0.69	-1.72	0.81	-0.18	-0.33	0.16	-0.06	611.0192706	
L coil main n	3.20E-03	2.44E-04	1.21E-05	4.37E-06	8.21E-06	1.12E-06	6.81E-07	1.77E-06	3.05E-07	2.18E-07	6.46E-07	3.47E-03	
M coil main n	1.60E-03	-2.44E-04	6.06E-06	2.18E-06	-8.21E-06	5.62E-07	3.40E-07	-1.77E-06	1.52E-07	1.09E-07	-6.46E-07	1.36E-03	
L coil end n	6.081E-04	9.009E-05	4.865E-06	1.773E-06	3.337E-06	4.569E-07	2.768E-07	7.207E-07	1.238E-07	8.866E-08	2.627E-07	7.10E-04	
M coil end n	3.041E-04	-9.009E-05	2.432E-06	8.865E-07	-3.337E-06	2.284E-07	1.384E-07	-7.207E-07	6.189E-08	4.433E-08	-2.627E-07	2.13E-04	

Richard Martin							
Design Spreadsheet for Slotted Axial Flux Machine - 1st iteration							
EQUIVALENT CIRCUIT							
E (V)	9776						
R (Ohms)	54.847						
Xsyn (Ohms)	347.058						
I rated (A)	1.790						
Eddy loss (W)	532						
Iron loss (W)	317						
I (A)	I2R loss (W)	Total loss (W)	R load (Ohms)	Power out (W)	V phase (V)	Efficiency (%)	Voltage regulation (%)
2	658	1507	4820.97	57852	9641.9	97.46	1.37
4	2633	3482	2364.46	113494	9457.9	97.02	3.26
6	5924	6773	1537.15	166012	9222.9	96.08	5.66
8	10531	11380	1116.87	214440	8935.0	94.96	8.61
10	16454	17303	859.11	257732	8591.1	93.71	12.12
12	23694	24543	682.22	294721	8186.7	92.31	16.26
14	32250	33100	551.11	324053	7715.5	90.73	21.08
16	42123	42972	448.04	344095	7168.6	88.90	26.67
18	53312	54161	362.93	352769	6532.8	86.69	33.18
20	65817	66666	289.38	347254	5787.6	83.89	40.80
21.177	73791	74641	249.57	335769	5285.1	81.81	45.94

Richard Martin	
Design Spreadsheet for Slotted Axial Flux Machine - 1st iteration	
SUMMARY	
Power (W)	=Design!B202
Speed (RPM)	=Design!B28
Phases	=Design!B29
Poles	=Design!B30
Elec Freq (Hz)	=Design!B31
Core OD (m)	=Design!B44
Core ID (m)	=Design!B46
Core length (m)	=Design!B48
Mean magnet width (m)	=Design!B56
Wire dia (m)	=Design!B64
Parallel strands	=Design!B70
Turns/pole/phase	=Design!B83
Clearance (m)	=Design!B89
Magnet thickness (m)	=Design!B90
Rotor thickness (m)	=Design!B118
Stator thickness (m)	=Design!B130
Axial length (m)	=Design!B131
Rotor OD (m)	=Design!B116
Magnet mass (kg)	=Design!B58
Magnet cost at £20/kg	=Design!B60
Mass of steel and magnet (kg)	=Design!B132
Inertia of magnets and rotors (kg.m^2)	=Design!B121
Magnetic loading (T)	=Design!B99
E phase (V)	=Design!B109
R phase (ohms)	=Design!B142
X syn phase (ohms)	=Design!B166
I rated (A)	=Design!B191
Current density (A/mm^2)	=Design!B192
Elec loading at Dmean (A/m)	=Design!B193
Efficiency (%)	=Design!B203
Power density (kW/m^3)	=Design!B208

Richard Martin	
Design Spreadsheet for Slotted Axial Flux Machine - 1st iteration	
DESIGN	
	Constant
	Input
	Calculate
CONSTANTS	
μ 0 (H/m)	=4*PI()*10^-7
Br (T)	1.2
μ r	1.07
B core (T)	1.4
B disc (T)	1.2
Density of steel (kg/m^3)	7850
Density of magnet (kg/m^3)	7400
Resisivity of copper at 0 deg-C (Ohm-m)	0.0000000155
Temperature coefficient of resistance	0.00426
Heat transfer coefficient (W/m^2.deg-C)	150
k winding (W/m.deg-C)	0.5
k insulation (W/m.deg-C)	0.5
k steel (W/m.deg-C)	150
INPUT PARAMETERS	
Power (W)	40000
Speed (RPM)	4500
Number of phases	3
Number of poles	16
Electrical frequency (Hz)	=(B28/60)*(B30/2)
Electrical frequency (rad/s)	=2*PI()*B31
Pole arc/pitch ratio	0.66
APPROXIMATE SIZING	
Magnetic loading (T)	0.7
Electric loading (A/m)	12000
k campbell	=1/SQRT(3)
Approximate outer diameter (m)	=POWER(240*SQRT(2)*B27/(B37*B38*PI()^2*(1+B39)*(1-B39^2)*B28), (1/3))
INITIAL SIZING	
Outer core diameter (m)	0.326
ID/OD	=B39
Inner diameter (m)	=B44*B45
Mean diameter (m)	=0.5*(B44+B46)
Core length (m)	=(B44-B46)/2
Magnet overhang at ID and OD (m)	0
Magnet length (m)	=B48+2*B49
Magnet OD (m)	=B44+2*B49
Magnet ID (m)	=B46-2*B49
Pole pitch (rad)	=(2*PI())/B30
Pole pitch (m)	=(PI()*B47)/B30
Pole arc (rad)	=B33*B53
Pole arc (m)	=B33*B54
Pole area (m^2)	=(PI()*(B44^2-B46^2))/(4*B30)
Magnet mass (kg)	=2*B30*B56*B50*B90*B17
Magnet inertia (kg.m^2)	=B58*(B51^2+B52^2)/8
Magnet cost at £20/kg (£)	=20*B58

WINDING DESIGN - MUSH WINDING	
Wire diameter (m)	0.0005385
Slots/pole/phase	2
Liner insulation thickness (m)	0.0008
k tooth	1
k slot	2
k fill	0.7
Parallel strands	1
Total slot width available per pole per phase (m)	=PI()*B47/(B29*B30*(B67+1))
Slot width (m)	=B71/B65
Tooth width (m)	=B67*B72
Tooth width at ID (m)	=B73*B46/B47
Slot pitch (m)	=B54/(B29*B65)
Peak flux density in tooth at D mean (T)	=B100*B75/B73
Slot depth (m)	=B68*B72
Slot width available for conductors (m)	=B72-2*B66
Slot depth available for conductors (m)	=B77-B66
Slot area available for conductors (m)	=B78*B79
Wire cross sectional area (m^2)	=PI()*B64^2/4
Conductors per slot	=INT(B69*B80/(B81*B70))
N per pole per phase	=B82*B65
Fundamental distribution factor >1 slot/pole/ph	=SIN(PI()/(2*B29))/(PI()/(2*B29))
Fund distribution factor - 1/pole/ph only	=SIN(PI()*B72/(2*B54))/(PI()*B72/(2*B54))
EXCITATION FLUX	
Running clearance (m)	0.0022
Magnet thickness (m)	0.006
Slot opening/Running clearance	=B72/B89
k carter	=0.00053*B91^3 - 0.0153*B91^2 + 0.16522*B91 + 0.00175
kc	=B75/(B75-B92*B72)
Effective gap (m)	=(B90/B13)+B89*B93
Flux density (T)	=(B12*B90/B13)/B94
Peak flux density - fundamental of square wave (T)	=(4*B95/PI())*SIN(B33*PI()/2)
1st harmonic peak flux per pole (Wb)	=2*B96*B50*B47/B30
Peak flux per pole from square wave (Wb)	=B95*(B50*B56)
FULL 1st harmonic B pk (T)	='Field solution'!B12
FULL sum to 21 harmonics B pk (T)	='Field soln sum'!B12
FULL 1st harmonic peak flux per pole (Wb)	='Field solution'!B27
FULL sum to 21 harmonics phi pp pk (T)	='Field soln sum'!B27
OPEN CIRCUIT EMF	
E/pole/ph 1st harmonic from magnetic circuit (V)	=4.44*B84*B83*B31*B97
E phase 1st harmonic from magnetic circuit (V)	=B106*B30
FULL E coil sum to n = 21 (V)	='Field soln sum'!B30
FULL E phase sum to n = 21 (V)	=B108*B30
Full E phase /100RPM (V)	=100*B109/B28
ROTOR SIZING	
Rotor disc extension (m)	0.005
Rotor ID (m)	0.02
Rotor OD (m)	=B44+(2*B114)
Peak disc flux (Wb)	=B102/2
Disc minimum thickness (m)	=(2*B117)/(B15*(B44-B46))
Mass of 2 rotors (kg)	=PI()*(B116^2-B115^2)*B118*B16/2
Inertia of rotors (kg.m^2)	=B119*(B116^2+B115^2)/8
Inertia of rotors and magnets (kg.m^2)	=B120+B59
STATOR DESIGN	
Peak core flux (Wb)	=B102
Core thickness (m)	=(2*B125)/(B14*(B44-B46))
Teeth mass - both sides (kg)	=PI()*B47*B67*(B44-B46)*2*B77*B16/(2*(B67+1))
Core mass (kg)	=PI()*(B44^2-B46^2)*B126*B16/4
Combined mass of stator iron (kg)	=B127+B128
Core and teeth thickness (m)	=B126+2*B77
Total axial length	=2*(B118+B89+B90)+B130
Total mass (kg)	=B58+B119+B129
PHASE RESISTANCE	
Operating temperature (deg-C)	160
Resisivity at operating temperature (Ohm-m)	=B18*(1+(B19*B136))
Strand copper diameter (m)	0.0005
Conductor cross sectional area (m^2)	=B70*PI()*B138^2/4
Length of mean turn (m)	=2*(B48+B126+2*B77)

Length of phase conductor (m)	=B140*B83*B30+2*PI()*B44
Phase resistance (Ohms)	=B137*B141/B139
INDUCTANCE	
L main fund per pole (H)	=4*B54*B11*B83^2*B84^2*B48/(B94*PI()^2)
M main fund per pole (H)	=B146/2
L slot leakage per pole (H)	=B65*B11*B77*(B44-B46)/(3*B72)
L gap leakage per pole (H)	=B65*B11*LN((PI()*B73+B72)/B72)/PI()
End geff (m)	=B54/PI()
L end fund per pole (H)	=4*B54*B11*B83^2*B84^2*(B126+B77)/(B150*PI()^2)
M end fund per pole (H)	=B151/2
L syn phase (H)	=B30*(B146+B147+B148+B149+B151+B152)
X syn (Ohms)	=PI()*B28*B30*B153/60
FULL L main fund per pole (H)	='Field solution'!B32
FULL M main fund per pole (H)	='Field solution'!B33
FULL L end fund per pole (H)	='Field solution'!B34
FULL M end fund per pole (H)	='Field solution'!B35
FULL L syn phase fund (H)	=B30*(SUM(B155:B158)+B148+B149)
FULL X syn fund (Ohms)	=PI()*B28*B30*B159/60
FULL L main per pole (H)	='Field soln sum'!B32
FULL M main per pole (H)	='Field soln sum'!B33
FULL L end per pole (H)	='Field soln sum'!B34
FULL M end per pole (H)	='Field soln sum'!B35
FULL L syn phase (H)	=B30*(SUM(B161:B164)+B148+B149)
FULL X syn (Ohms)	=PI()*B28*B30*B165/60
THERMAL MODEL	
Ambient temperature (deg C)	20
Temperature difference (deg C)	=B136-B170
R copper 1 (W/degC)	=B79/(B21*B78)
R surface HT 1 (W/degC)	=2/(B20*B78)
R copper 2 (W/degC)	=B78/(4*B21*B79)
R liner (W/degC)	=B66/(B22*B79)
R steel (W/degC)	=(2*B79+B73)/(2*B73*B23)
R surface HT 2 (W/degC)	=2/(B20*B73)
R slot (W/degC)	=B172+B173
R tooth (W/degC)	=B174+B175+B176+B177
R total (W/degC)	=B178*B179/(B178+B179)
Allowable loss per half slot/tooth (W)	=B171/B180
Total allowable loss (W)	=2*B181*B65*B30*B29*(B44-B46)
LOSSES	
Eddy loss (W)	=B70*B83*B29*B30*(B44-B46)*PI()*B138^4*B99^2*B32^2/(2*4*16*B137)
Core back iron loss (W)	=(B31/50)^1.32*(B14/1.5)^1.97*B128
Teeth iron loss (W)	=(B31/50)^1.32*(B76/1.5)^1.97*B127
Total iron loss (W)	=B187+B188
Allowable I2R loss (W)	=B182-B189-B186
I rated (A)	=SQRT(B190/(B29*B142))
Current density (A/mm^2)	=B191/(1000^2*B139)
Electric loading at Dm (A/m)	=B191*B83*B29*B30/(PI()*B47)
EQUIVALENT CIRCUIT	
Phase open cct EMF (V)	=B109
Phase resistance (Ohms)	=B142
Synchronous reactance (Ohms)	=B166
Rated current (A)	=B191
V phase (V)	=SQRT(B197^2-(B200*B199)^2)-B191*B198
Power output (W)	=3*B201*B191
Efficiency (%)	=100*B202/(B202+B182)
POWER DENSITY	
Volume of machine (m^3)	=PI()*B116^2*B131/4
Power density (kW/m^3)	=B202/(1000*B207)

Richard Martin	
Design Spreadsheet for Slotted Axial Flux Machine - 1st iteration	
FIELD SOLUTION e.g. n=1	
n	**1**
un (rad)	=(2*PI()*B6)/(2*Design!$B$54)
Jn (A/m^2)	=4*Design!$B$12*SIN('Field solution'!B$6*PI()*Design!$B$33/2)/(Design!$B$11*Design!$B$13*Design!$B$54)
x	**Bn**
0	=(B$8*Design!$B$11*SINH(B$7*Design!$B$90)*COS(B$7*$A12))/(B$7*SINH(B$7*Design!$B$94))
0.001	=(B$8*Design!$B$11*SINH(B$7*Design!$B$90)*COS(B$7*$A13))/(B$7*SINH(B$7*Design!$B$94))
0.002	=(B$8*Design!$B$11*SINH(B$7*Design!$B$90)*COS(B$7*$A14))/(B$7*SINH(B$7*Design!$B$94))
0.003	=(B$8*Design!$B$11*SINH(B$7*Design!$B$90)*COS(B$7*$A15))/(B$7*SINH(B$7*Design!$B$94))
0.004	=(B$8*Design!$B$11*SINH(B$7*Design!$B$90)*COS(B$7*$A16))/(B$7*SINH(B$7*Design!$B$94))
0.005	=(B$8*Design!$B$11*SINH(B$7*Design!$B$90)*COS(B$7*$A17))/(B$7*SINH(B$7*Design!$B$94))
0.006	=(B$8*Design!$B$11*SINH(B$7*Design!$B$90)*COS(B$7*$A18))/(B$7*SINH(B$7*Design!$B$94))
0.007	=(B$8*Design!$B$11*SINH(B$7*Design!$B$90)*COS(B$7*$A19))/(B$7*SINH(B$7*Design!$B$94))
0.008	=(B$8*Design!$B$11*SINH(B$7*Design!$B$90)*COS(B$7*$A20))/(B$7*SINH(B$7*Design!$B$94))
0.009	=(B$8*Design!$B$11*SINH(B$7*Design!$B$90)*COS(B$7*$A21))/(B$7*SINH(B$7*Design!$B$94))
0.01	=(B$8*Design!$B$11*SINH(B$7*Design!$B$90)*COS(B$7*$A22))/(B$7*SINH(B$7*Design!$B$94))
0.135	=(B$8*Design!$B$11*SINH(B$7*Design!$B$90)*COS(B$7*$A24))/(B$7*SINH(B$7*Design!$B$94))
phi pp n	=B$12*Design!$B$47*Design!$B$50*SIN('Field solution'!B$6*PI()/2)/('Field solution'!B$6*Design!$B$30/2)
kd n 1 slot/pole/phase	=SIN(B$6*PI()*Design!$B$72/(2*Design!$B$54))/(B$6*PI()*Design!$B$72/(2*Design!$B$54))
kd n > 1	=SIN(B$6*PI()/(2*Design!$B$29))/(B$6*PI()/(2*Design!$B$29))
E coil n	=SQRT(2)*PI()*B$6*B$29*Design!$B$83*Design!$B$31*'Field solution'!B$27
L coil main n	=4*Design!$B$11*Design!$B$83^2*B$29^2*Design!$B$48*COSH(Design!$B$94*'Field solution'!B$7)/(PI()*'Field solution'!B$6*SINH(Design!$B$94*'Field solution'!B$7))
M coil main n	=B32*COS(B$7*(Design!$B$54/Design!$B$29))
L coil end n	=4*Design!$B$11*Design!$B$83^2*B$29^2*(Design!$B$126+Design!$B$77)/(PI()*'Field solution'!B$6)
M coil end n	=B$34*COS(B$7*(Design!$B$54/Design!$B$29))

Richard Martin	
Design Spreadsheet for Slotted Axial Flux Machine - 1st iteration	
FIELD SOLUTION SUM	
n	**SUM**
un (rad)	
Jn (A/m^2)	
x	**B**
0	=SUM('Field solution'!B12:L12)
0.001	=SUM('Field solution'!B13:L13)
0.002	=SUM('Field solution'!B14:L14)
0.003	=SUM('Field solution'!B15:L15)
0.004	=SUM('Field solution'!B16:L16)
0.005	=SUM('Field solution'!B17:L17)
0.006	=SUM('Field solution'!B18:L18)
0.007	=SUM('Field solution'!B19:L19)
0.008	=SUM('Field solution'!B20:L20)
0.009	=SUM('Field solution'!B21:L21)
0.01	=SUM('Field solution'!B22:L22)
0.135	=SUM('Field solution'!B24:L24)
phi pp n	=SUM('Field solution'!B27:L27)
kd n 1 slot/pole/phase	
kd n > 1	
E coil n	=SQRT('Field solution'!B30^2+'Field solution'!C30^2+'Field solution'!D30^2+'Field solution'!E30^2+'Field solution'!F30^2+'Field solution'!G30^2+'Field solution'!H30^2+'Field solution'!I30^2+'Field solution'!J30^2+'Field solution'!K30^2+'Field solution'!L30^2)
L coil main n	=SUM('Field solution'!B32:L32)
M coil main n	=SUM('Field solution'!B33:L33)
L coil end n	=SUM('Field solution'!B34:L34)
M coil end n	=SUM('Field solution'!B35:L35)

Richard Martin	
Design Spreadsheet for Slotted Axial Flux Machine - 1st iteration	
FIELD SOLUTION SINE	
n	
un (rad)	
Jn (A/m^2)	
x	**B sine**
0	=Design!$B$96*COS(2*PI()*'Field solution'!A12/(2*Design!$B$54))
0.001	=Design!$B$96*COS(2*PI()*'Field solution'!A13/(2*Design!$B$54))
0.002	=Design!$B$96*COS(2*PI()*'Field solution'!A14/(2*Design!$B$54))
0.003	=Design!$B$96*COS(2*PI()*'Field solution'!A15/(2*Design!$B$54))
0.004	=Design!$B$96*COS(2*PI()*'Field solution'!A16/(2*Design!$B$54))
0.005	=Design!$B$96*COS(2*PI()*'Field solution'!A17/(2*Design!$B$54))
0.006	=Design!$B$96*COS(2*PI()*'Field solution'!A18/(2*Design!$B$54))
0.007	=Design!$B$96*COS(2*PI()*'Field solution'!A19/(2*Design!$B$54))
0.008	=Design!$B$96*COS(2*PI()*'Field solution'!A20/(2*Design!$B$54))
0.009	=Design!$B$96*COS(2*PI()*'Field solution'!A21/(2*Design!$B$54))
0.01	=Design!$B$96*COS(2*PI()*'Field solution'!A22/(2*Design!$B$54))
0.135	=Design!$B$96*COS(2*PI()*'Field solution'!A24/(2*Design!$B$54))

Richard Martin							
Design Spreadsheet for Slotted Axial Flux Machine - 1st iteration							
EQUIVALENT CIRCUIT							
E (V)	=Design!B109						
R (Ohms)	=Design!B142						
Xsyn (Ohms)	=Design!B199						
I rated (A)	=Design!B191						
Eddy loss (W)	=Design!B186						
Iron loss (W)	=Design!B187+Design!B188						
I (A)	**I2R loss (W)**	**Total loss (W)**	**R load (Ohms)**	**Power out (W)**	**V phase (V)**	**Efficiency (%)**	**Voltage regulation (%)**
2	=3*A13^2*$B$6	=B13+$B$9+$B$10	=SQRT(($B$5^2/A13^2)-$B$7^2)-$B$6	=3*A13^2*D13	=A13*D13	=100*E13/(E13+C13)	=100*($B$5-F13)/$B$5
4	=3*A14^2*$B$6	=B14+$B$9+$B$10	=SQRT(($B$5^2/A14^2)-$B$7^2)-$B$6	=3*A14^2*D14	=A14*D14	=100*E14/(E14+C14)	=100*($B$5-F14)/$B$5
6	=3*A15^2*$B$6	=B15+$B$9+$B$10	=SQRT(($B$5^2/A15^2)-$B$7^2)-$B$6	=3*A15^2*D15	=A15*D15	=100*E15/(E15+C15)	=100*($B$5-F15)/$B$5
8	=3*A16^2*$B$6	=B16+$B$9+$B$10	=SQRT(($B$5^2/A16^2)-$B$7^2)-$B$6	=3*A16^2*D16	=A16*D16	=100*E16/(E16+C16)	=100*($B$5-F16)/$B$5
10	=3*A17^2*$B$6	=B17+$B$9+$B$10	=SQRT(($B$5^2/A17^2)-$B$7^2)-$B$6	=3*A17^2*D17	=A17*D17	=100*E17/(E17+C17)	=100*($B$5-F17)/$B$5
12	=3*A18^2*$B$6	=B18+$B$9+$B$10	=SQRT(($B$5^2/A18^2)-$B$7^2)-$B$6	=3*A18^2*D18	=A18*D18	=100*E18/(E18+C18)	=100*($B$5-F18)/$B$5
14	=3*A19^2*$B$6	=B19+$B$9+$B$10	=SQRT(($B$5^2/A19^2)-$B$7^2)-$B$6	=3*A19^2*D19	=A19*D19	=100*E19/(E19+C19)	=100*($B$5-F19)/$B$5
16	=3*A20^2*$B$6	=B20+$B$9+$B$10	=SQRT(($B$5^2/A20^2)-$B$7^2)-$B$6	=3*A20^2*D20	=A20*D20	=100*E20/(E20+C20)	=100*($B$5-F20)/$B$5
18	=3*A21^2*$B$6	=B21+$B$9+$B$10	=SQRT(($B$5^2/A21^2)-$B$7^2)-$B$6	=3*A21^2*D21	=A21*D21	=100*E21/(E21+C21)	=100*($B$5-F21)/$B$5
20	=3*A22^2*$B$6	=B22+$B$9+$B$10	=SQRT(($B$5^2/A22^2)-$B$7^2)-$B$6	=3*A22^2*D22	=A22*D22	=100*E22/(E22+C22)	=100*($B$5-F22)/$B$5
21.177	=3*A23^2*$B$6	=B23+$B$9+$B$10	=SQRT(($B$5^2/A23^2)-$B$7^2)-$B$6	=3*A23^2*D23	=A23*D23	=100*E23/(E23+C23)	=100*($B$5-F23)/$B$5

References

[1] Brown, NL: "Compact electrical generators for diesel drive generating sets", PHD THESIS, THE UNIVERSITY OF DURHAM, 2002

[2] Chalmers, BJ, Wu, W, and Spooner, E: "An axial flux permanent magnet generator for a gearless wind energy system", IEEE TRANSACTIONS ON ENERGY CONVERSION, Vol. 14, No. 2, 1999, pp. 251-257

[3] Patterson, DJ and Spee, R: "The design and development of an axial flux permanent magnet brushless DC motor for wheel drive in a solar powered vehicle", PROC. IEEE INDUSTRIAL APPLICATIONS SOCIETY CONFERENCE, DENVER, USA, 1994, pp. 188-195

[4] User Manual, MEGA version 6.29m © 1986 - 2003, UNIVERSITY OF BATH, 1986

[5] Spooner, E and Chalmers, BJ: "Torus - a slotless, toroidal-stator, permanent magnet generator", IEE PROCEEDINGS-B ELECTRIC POWER APPLICATIONS, Vol. 139, No. 6, 1992, pp. 497-506

[6] Bumby, JR and Martin, R: "Axial flux permanent magnet air-cored generator for small-scale wind turbines", IEE PROC.-ELECTR. POWER APPL., Vol. 152, No.5, 2005, pp. 1065-1075

[7] Bumby, JR: "Axial flux, permanent magnet electrical machine", BRITISH PATENT APPLICATION, 2004, No. 0412085.3

[8] Bumby, JR, Martin, R, Mueller, MA, Spooner, E, Brown, NL, and Chalmers, BJ: "Electromagnetic design of axial flux permanent magnet machines", IEE PROC.-ELECTR. POWER APPL., Vol. 151, No.2, 2004, pp. 151-160

[9] Bumby, JR and Spooner, E: "Torus generator: Design, build and test of two prototypes", UNIVERSITY OF DURHAM, SCHOOL OF ENGINEERING, INTERNAL REPORT, 2000

[10] Faraday, M: "Experimental researches in electricity", ABSTRACTS OF THE PAPERS PRINTED IN THE PHILOSOPHICAL TRANSACTIONS OF THE ROYAL SOCIETY OF LONDON, VOL. 3, 1830 – 1837

[11] Bumby, JR: "Superconducting rotating electrical machines", CLARENDON PRESS, OXFORD, 1983

[12] Davenport, T: "Improvement in propelling machinery by magnetism and electromagnetism", US PATENT OFFICE NO. 132, FEB 25TH 1837

[13] Campbell, P: "Principles of a permanent magnet axial field DC machine", PROC. IEE, Vol. 121, No. 12, 1974, pp. 1489-1494

[14] Evans, PD and Eastham, JF: "Double-disc alternator with AC-side excitation", IEE PROCEEDINGS-B ELECTRIC POWER APPLICATIONS, Vol. 130, No. 2, 1983, pp. 95-102

[15] Campbell, P: "Performance of a permanent magnet axial-field DC machine", IEE PROC.-ELECTR. POWER APPL., Vol. 151, No.2, 1979, pp. 139-144

[16] Campbell, P, Rosenberg, DJ, and Stanton, DP: "The computer design and optimization of axial-field permanent magnet motors", IEEE TRANSACTIONS ON POWER APPARATUS AND SYSTEMS, Vol. PAS-100, No. 4, 1981, pp. 1490-1497

[17] Chan, CC: "Axial-field electrical machines - design and applications", IEEE TRANSACTIONS ON ENERGY CONVERSION, Vol. 2, No. 2, 1987, pp. 294-300

[18] Brown, NL, Haydock, L, and Spooner, E: "Three Dimensional analysis of a toroidally wound axial flux permanent magnet generator", UNIVERSITIES POWER ENGINEERING CONFERENCE, 1999, VOL. 2.

[19] Brooking, P and Bumby, JR: "An integrated engine-generator set with power electronic interface for hybrid electric vehicle applications", IEE INTERNATIONAL CONFERENCE ON ELECTRICAL MACHINES AND DRIVES, BATH, 2002

[20] Brown, NL, Haydock, L, and Bumby, JR: "An idealised approach to electromagnetically comparing axial and radial flux permanent magnet machines", PROC. INTERNATIONAL CONFERENCE ON ELECTRICAL MACHINES, BRUGGE, BELGIUM, 2002

[21] Brown, NL, Haydock, L, and Bumby, JR: "Foresight vehicle: a toroidal, axial flux generator for hybrid IC engine/battery electric vehicle applications", PROC. SAE CONFERENCE, DETROIT, USA, 2002, Paper no. 2002-01-0829

[22] Bumby, JR, Haydock, L, and Brown, NL: "Axial flux machines and their use in hybrid electric vehicles", UK MAGNETICS SOCIETY SEMINAR ON "MOTORS AND ACTUATORS FOR AUTOMOTIVE APPLICATIONS", TRW, BIRMINGHAM, 2002

[23] Bumby, JR and Martin, R: "An axial flux, permanent magnet, generator for engine integration", INTERNATIONAL CONFERENCE ON STIRLING ENGINES, UNIVERISTY OF DURHAM, 2005

[24] Coles, PC, Rodger, D, Hill-Cottingham, RJ, and Lai, HC: "Design and analysis of an axial flux permanent magnet machine", 2ND IEE PEMD CONFERENCE, 2004, pp. 840-843

[25] Hill-Cottingham, RJ, Coles, PC, Rodger, D, and Lai, HC: "Finite element modelling of an axial flux PM machine", 2ND IEE PEMD CONFERENCE, 2004, pp. 552-555

[26] Walker, A, Anpalahan, P, Coles, PC, Lampérth, M, and Rodger, D: "Automotive integrated starter generator", 2ND IEE PEMD CONFERENCE, 2004, pp. 46-48

[27] Nakata, T, Takahashi, N, and Uehara, K: "Analysis of magnetic characteristics of a brushless DC motor taking into account the distribution of magnetization", IEEE TRANSACTIONS ON MAGNETICS, Vol. MAG-22, No. 5, 1986, pp.1084-1086

[28] Furlani, EP: "A method for predicting the field in permanent magnet axial field motors", IEEE TRANSACTIONS ON MAGNETICS, Vol. 28, No. 5, 1992, pp. 2061-2066

[29] Proca, AB, Keyhani, A, and El-Antalby, A: "Analytical model for permanent magnet motors with surface mounted magnets", IEEE TRANSACTIONS ON ENERGY CONVERSION, Vol. 18, No. 3, 2003, pp. 386-391

[30] Gu, CL, Wu, W, and Shao, KR: "Magnetic-field analysis and optimal-design of DC permanent- magnet coreless disc machine", IEEE TRANSACTIONS ON MAGNETICS, Vol. 30, No. 5, 1994, pp. 3668-3671

[31] Schmidt, K and Patterson, DJ: "Performance results for a high efficiency tropical ceiling fan and comparisons with conventional fans - Demand side management via small appliance efficiency", RENEWABLE ENERGY, Vol. 22, No. 1-3, 2001, pp. 169-176

[32] Eastham, JF, Profumo, F, Tenconi, A, Hill-Cottingham, R, Coles, P, and Gianolio, G: "Novel axial flux machine for aircraft drive: Design and modelling", IEEE TRANSACTIONS ON MAGNETICS, Vol. 38, No. 5, 2002, pp. 3003-3005

[33] Huang, S, Aydin, M, and Lipo, TA: "Comparison of (non-slotted and slotted) surface mounted pm motors and axial flux motors for submarine ship drives", 3RD NAVAL SYMPOSIUM ON ELECTRICAL MACHINES, PHILADELPHIA, 2000

[34] Pullen, KR, Mansir, H, Fenocchi, A: "High power density air cooled motor generators for automotive applications", IEE POWER DIVISION COLLOQUIUM ON ELECTRICAL MACHINE DESIGN FOR ALL-ELECTRIC AND HYBRID-ELECTRIC VEHICLES, LONDON, 1999, pp. 7/1-7/5

[35] Etemad, S: "High speed permanent magnet axial flux generator", IEE POWER DIVISION SEMINAR ON PERMANENT MAGNET MATERIALS – FUNDAMENTALS, DESIGN AND APPLICATION, LONDON, 2000, pp. 7/1-7/3

[36] Holmes, AS, Hong, G, Pullen, KR: "Axial flux permanent magnet machines for micropower generation", IEEE JOURNAL OF MICROELECTROMECHANICAL SYSTEMS, Vol. 14, No. 1, 2005, pp. 54-62

[37] Spooner, E and Williamson, AC: "Direct coupled, permanent magnet generators for wind turbine applications", IEE PROCEEDINGS-ELECTRIC POWER APPLICATIONS, Vol. 143, No. 1, 1996, pp. 1-8

[38] Spooner, E, Williamson, AC, and Catto, G: "Modular design of permanent magnet generators for wind turbines", IEE PROCEEDINGS-ELECTRIC POWER APPLICATIONS, Vol. 143, No. 5, 1996, pp. 388-395

[39] Muljadi, E, Butterfield, CP, and Wan, YH: "Axial flux modular permanent magnet generator with a toroidal winding for wind turbine applications", IEEE TRANSACTIONS ON INDUSTRY APPLICATIONS, Vol. 35, No. 4, 1999, pp. 831-836

[40] Lombard, NF and Kamper, MJ: "Analysis and performance of an ironless stator axial flux PM machine", IEEE TRANSACTIONS ON ENERGY CONVERSION, Vol. 14, No. 4, 1999, pp. 1051-1056

[41] Zhang, Z, Profumo, F, and Tenconi, A: "Axial flux wheel machines for electric vehicles", ELECTRIC MACHINES AND POWER SYSTEMS, Vol. 24, No. 8, 1996, pp. 883-896

[42] Profumo, F, Zhang, Z, and Tenconi, A: "Axial flux machines drives: A new viable solution for electric cars", IEEE TRANSACTIONS ON INDUSTRIAL ELECTRONICS, Vol. 44, No. 1, 1997, pp. 39-45

[43] Zhang, Z, Profumo, F, Tenconi, A, and Santamaria, M: "Analysis and experimental validation of performance for an axial flux permanent magnet brushless DC motor with powder iron metallurgy cores", IEEE TRANSACTIONS ON MAGNETICS, Vol. 33, No. 5, 1997, pp. 4194-4196

[44] Profumo, F, Tenconi, A, Zhang, Z, and Cavagnino, A: "Design and realization of a novel axial flux interior PM synchronous motor for wheel-motors applications", ELECTRIC MACHINES AND POWER SYSTEMS, Vol. 28, No. 7, 2000, pp. 637-649

[45] Cavagnino, A, Lazzari, M, Profumo, F, and Tenconi, A: "Axial flux interior magnet PM synchronous motor: parameters identification and steady-state performance measurement", IEEE TRANSACTIONS ON INDUSTRY APPLICATIONS, Vol. 36, No. 6, 2000, pp. 1581-1588

[46] Cavagnino, A, Lazzari, M, Profumo, F, and Tenconi, A: "A comparison between the axial flux and the radial flux structures for PM synchronous motors", IEEE TRANSACTIONS ON INDUSTRY APPLICATIONS, Vol. 38, No. 6, 2002, pp. 1517-1524

[47] Hredzak, B, Gair, S, and Eastham, JF: "Elimination of torque pulsations in a direct-drive EV wheel motor", IEEE TRANSACTIONS ON MAGNETICS, Vol. 32, No. 5, 1996, pp. 5010-5012

[48] Gair, S, Eastham, JF, and Canova, A: "Effects of slot closure by soft magnetic powder wedge material in axial-field permanent magnet brushless machines", JOURNAL OF APPLIED PHYSICS, Vol. 79, No. 8, 1996, pp. 5554-5556

[49] Johansen, PR, Patterson, D, O'Keefe, C, and Swenson, J: "The use of an axial flux permanent magnet in-wheel direct-drive in an electric bicycle", RENEWABLE ENERGY, Vol. 22, No. 1-3, 2001, pp. 151-157

[50] Mendrela, EA, Beniak, R, and Wrobel, R: "Influence of stator structure on electromechanical parameters of Torus-type brushless DC motor", IEEE TRANSACTIONS ON ENERGY CONVERSION, Vol. 18, No. 2, 2003, pp. 231-237

[51] Marignetti, F and Scarano, M: "An axial flux PM motor wheel", 3RD INTERNATIONAL SYMPOSIUM ON ADVANCED ELECTROMECHANICAL MOTION SYSTEMS, Patras, Greece, 1999

[52] Marignetti, F and Scarano, M: "Mathematical modelling of an axial flux PM motor wheel", PROC. INTERNATIONAL CONFERENCE ON ELECTRICAL MACHINES, HELSINKI, FINLAND, 2000, pp. 1275-1279

[53] Bianchi, N, Bolognani, S, and Zigliotto, M: "High-performance PM synchronous motor drive for an electrical scooter", IEEE TRANSACTIONS ON INDUSTRY APPLICATIONS, Vol. 37, No. 5, 2001, pp. 1348-1355

[54] Terashima, M, Ashikaga, T, Mizuno, T, Natori, K, Fujiwara, N, and Yada, M: "Novel motors and controllers for high-performance electric vehicle with four in-wheel motors", IEEE TRANSACTIONS ON INDUSTRIAL ELECTRONICS, Vol. 44, No. 1, 1997, pp. 28-38

[55] Tseng, KJ and Chen, GH: "Computer-aided design and analysis of direct-driven wheel motor drive", IEEE TRANSACTIONS ON POWER ELECTRONICS, Vol. 12, No. 3, 1997, pp. 517-527

[56] Caricchi, F, Crescimbini, F, Mezzetti, F, and Santini, E: "Multistage axial flux PM machine for wheel direct-drive", IEEE TRANSACTIONS ON INDUSTRY APPLICATIONS, Vol. 32, No. 4, 1996, pp. 882-888

[57] Solero, L, Honorati, O, Caricchi, F, and Crescimbini, F: "Nonconventional three-wheel electric vehicle for urban mobility", IEEE TRANSACTIONS ON VEHICULAR TECHNOLOGY, Vol. 50, No. 4, 2001, pp. 1085-1091

[58] Caricchi, F, Crescimbini, F, Dinapoli, A, Honorati, O, and Santini, E: "An innovative electric scooter", AEI AUTOMAZIONE ENERGIA INFORMAZIONE, Vol. 82, No. 3, 1995, pp. 52-57

[59] Caricchi, F, Crescimbini, F, and Honorati, O: "Low cost compact permanent magnet machine for adjustable-speed pump application", IEEE TRANSACTIONS ON INDUSTRY APPLICATIONS, Vol. 34, No. 1, 1998, pp. 109-116

[60] Caricchi, F, Crescimbini, F, Honorati, O, Lo Bianco, G, and Santini, E: "Performance of coreless-winding axial flux permanent magnet generator with power output at 400 Hz, 3000 r/min", IEEE TRANSACTIONS ON INDUSTRY APPLICATIONS, Vol. 34, No. 6, 1998, pp. 1263-1269

[61] Caricchi, F, Crescimbini, F, and Honorati, O: "Modular axial flux permanent magnet motor for ship propulsion drives", IEEE TRANSACTIONS ON ENERGY CONVERSION, Vol. 14, No. 3, 1999, pp. 673-679

[62] Ficheux, RL, Caricchi, F, Crescimbini, F, and Honorati, O: "Axial flux permanent magnet motor for direct-drive elevator systems without machine room", IEEE TRANSACTIONS ON INDUSTRY APPLICATIONS, Vol. 37, No. 6, 2001, pp. 1693-1701

[63] Crescimbini F, Di Napoli A, Solero, L and Caricchi F: "Compact permanent magnet generator for hybrid vehicle applications", IEEE TRANSACTIONS ON INDUSTRY APPLICATIONS, Vol. 41, No. 5, 2005, pp. 1168-1177

[64] Patterson, D and Spee, R: "The design and development of an axial flux permanent magnet brushless DC motor for wheel drive in a solar-powered vehicle", IEEE TRANSACTIONS ON INDUSTRY APPLICATIONS, Vol. 31, No. 5, 1995, pp. 1054-1061

[65] Lovatt, HC, Ramsden, VS, and Mecrow, BC: "Design of an in-wheel motor for a solar-powered electric vehicle", IEE PROCEEDINGS-ELECTRIC POWER APPLICATIONS, Vol. 145, No. 5, 1998, pp. 402-408

[66] Leung, WS and Chan, JCC: "A new design approach for axial-field electrical machines", IEEE TRANSACTIONS ON POWER APPARATUS AND SYSTEMS, Vol. PAS-99, No. 4, 1980, pp. 1679-1685

[67] Laithwaite, ER, "The goodness of a machine", PROC. IEE, Vol. 112, No. 3, 1965, pp. 538-541

[68] Brice CW and Patterson DJ: "Electric machine goodness: classic results revisited in light of contemporary machine design", PROC. INTERNATIONAL CONFERENCE ON ELECTRICAL MACHINES, BRUGGE, BELGIUM, 2002

[69] Huang, S, Aydin, M, and Lipo, TA: "A direct approach to electrical machine performance evaluation: torque density assessment and sizing optimization", PROC. INTERNATIONAL CONFERENCE ON ELECTRICAL MACHINES, BRUGGE, BELGIUM, 2002

[70] Campbell, P: "The magnetic circuit of an axial field DC electrical machine", IEEE TRANSACTIONS ON MAGNETICS, Vol. MAG-11, No. 5, 1975, pp. 1541-1543

[71] Nafisi, A and Campbell, P: "Composite iron powder materials for the armature of axial-field permanent magnet machines", IEEE TRANSACTIONS ON MAGNETICS, Vol. MAG-21, No. 5, 1985, pp.1753-1755

[72] Jensen, CC, Profumo, F, and Lipo, TA: "A low-loss permanent magnet brushless DC motor utilizing tape wound amorphous iron", IEEE TRANSACTIONS ON INDUSTRY APPLICATIONS, Vol. 28, No. 3, 1992, pp. 646-651

[73] Cvetkovski, G, Petkovska, L, Cundev, M, and Gair, S: "Improved design of a novel PM disk motor by using soft magnetic composite material", IEEE TRANSACTIONS ON MAGNETICS, Vol. 38, No. 5, 2002, pp. 3165-3167

[74] Lukaniszyn, M, Jagiela, M, and Wrobel, R: "Influence of magnetic circuit modifications on the torque of a disc motor with coaxial flux in the stator", PROC. INTERNATIONAL CONFERENCE ON ELECTRICAL MACHINES, BRUGGE, BELGIUM, 2002

[75] Evans, PD and Eastham, JF: "Slotless-disc alternator with AC-side excitation", IEE PROCEEDINGS-B ELECTRIC POWER APPLICATIONS, Vol. 130, No. 6, 1983, pp. 399-406

[76] Evans, PD and Eastham, JF: "Disk geometry single-phase alternator with slotless stator and AC-side excitation", IEE PROCEEDINGS-B ELECTRIC POWER APPLICATIONS, Vol. 133, No. 4, 1986, pp. 270-278

[77] Brown, NL, Haydock, L, Spooner, E, Mebarki, A, and Novinschi, A : "Introduction to a novel axial flux PM synchronous machine with excitation control", 2ND IEE PEMD CONFERENCE, 2004, pp. 868-872

[78] Mebarki, A, Spooner, E, Brown, NL, Novinschi, A, and Haydock, L: "A non-linear model of a novel axial flux permanent magnet machine with excitation control", 2ND IEE PEMD CONFERENCE, 2004, pp. 793-798

[79] Novinschi, A, Brown, NL, Spooner, E, Mebarki, A, and Haydock, L: "Finite element analysis of a novel axial flux PM synchronous machine with excitation control", 2ND IEE PEMD CONFERENCE, 2004, pp. 420-425

[80] Wu, W, Spooner, E, and Chalmers, BJ: "Design of slotless torus generators with reduced voltage regulation", IEE PROCEEDINGS-ELECTRIC POWER APPLICATIONS, Vol. 142, No. 5, 1995, pp. 337-343

[81] D'Angelo, J, Chari, MVK, and Campbell, P: "Three-dimensional finite element solution for a permanent magnet axial-field machine", IEEE TRANSACTIONS ON POWER APPARATUS AND SYSTEMS, Vol. PAS-102, No. 1, 1983, pp. 83-90

[82] Takano, H, Takashi, I, Mori, K, Sakuta, A, and Hirasa, T: "Optimum values for magnet and armature winding thickness for axial-field permanent magnet brushless DC motors", IEEE TRANSACTIONS ON INDUSTRY APPLICATIONS, Vol. 28, No. 2, 1992, pp. 350-357

[83] Furlani, EP: "Computing the field in permanent magnet axial-field motors", IEEE TRANSACTIONS ON MAGNETICS, Vol. MAG-30, No. 5, 1994, pp. 3360-3663

[84] Chalmers, BJ, Green, AM, Reece, ABJ, and Al-Badi, AH: "Modelling and simulation of the Torus generator", IEE PROCEEDINGS-ELECTRIC POWER APPLICATIONS, Vol. 144, No. 6, 1997, pp. 446-452

[85] Lukaniszyn, M and Wrobel, R: "A study on the influence of permanent magnet dimensions and stator core structures on the torque of the disc-type brushless DC motor", ELECTRICAL ENGINEERING, Vol. 82, No. 3-4, 2000, pp. 163-171

[86] Lukaniszyn, M, Wrobel, R, and Jagiela, A: "Reduction of the torque ripple in a brushless DC Torus motor", PROC. INTERNATIONAL CONFERENCE ON ELECTRICAL MACHINES, BRUGGE, BELGIUM, 2002

[87] Lukaniszyn, M, Jagiela, M, and Wrobel, R: "A disc-type motor with co-axial flux in the stator; - influence of magnetic circuit parameters on the torque", ELECTRICAL ENGINEERING, Vol. 84, No. 2, 2002, pp. 91-100

[88] Parvianien, A, Niemelä, M, and Pyrhönen, J: "Modelling of axial flux permanent magnet machines", IEEE TRANSACTIONS ON INDUSTRY APPLICATIONS, Vol. 40, No. 5, 2004, pp. 1333-1340

[89] Huang, SR, Luo, J, Leonardi, F, and Lipo, TA: "A comparison of power density for axial flux machines based on general purpose sizing equations", IEEE TRANSACTIONS ON ENERGY CONVERSION, Vol. 14, No. 2, 1999, pp. 185-191

[90] Aydin, M, Huang, S, and Lipo, TA: "Design and 3D electromagnetic field analysis of non-slotted and slotted torus type axial flux surface mounted permanent magnet disc machines", IEEE INTERNATIONAL CONFERENCE ON ELECTRICAL MACHINES AND DRIVES, BOSTON, 2001, pp. 645-651

[91] Aydin, M, Huang, S, and Lipo, TA: "Optimum design and 3D finite element analysis of non-slotted and slotted internal rotor type axial flux PM disc machines", IEEE POWER ENGINEERING SCOCIETY SUMMER MEETING, VANCOUVER, CA, 2001

[92] Martin, R, Bumby, JR, and Mueller, MA: "Finite element analysis and experimental test of an axial flux toroidal generator", 2ND IEE PEMD CONFERENCE, 2004, pp. 402-407

[93] Carter, GW: "The electromagnetic field in its engineering aspects (2nd edition)", LONGMANS, GREEN AND CO. LTD., 1967

[94] Strand7™ FEA system, release 2.2.5, ©2003 G + D Computing

[95] Spooner, E: "DC traction motor with slotless armature", IEE PROCEEDINGS-B ELECTRIC POWER APPLICATIONS, Vol. 132, No. 2, 1985, pp. 61-71

[96] Say, MG: "Alternating current machines (5th edition)", PITMAN PUBLISHING LTD., 1983

[97] Binns, KJ, Lawrenson, PJ, and Trowbridge, CW: "The analytic and numerical solution of electric and magnetic fields", JOHN WILEY AND SONS LTD, 1995, pp. 149-187

[98] Bumby, JR and Martin, R: "An axial flux air-cored generator: the Savonius generator", UNIVERSITY OF DURHAM, SCHOOL OF ENGINEERING, INTERNAL REPORT, 2005

[99] Wong, A: "Development of a small scale direct drive wind energy convertor", MENG FINAL YEAR PROJECT, UNIVERSITY OF DURHAM, 2005

[100] Bumby, JR, Stannard, N, Martin, R: "A permanent magnet generator for small scale wind turbines", PROC. INTERNATIONAL CONFERENCE ON ELECTRICAL MACHINES, CHANIA, CRETE, 2006, PAPER NO. 141

[101] Mitcham, AJ, Antonopoulos, G, and Cullen, JJA: "Favourable slot and pole number combinations for fault-tolerant PM machines", IEE PROC.-ELECTR. POWER APPL., Vol. 151, No.5, 2004, pp. 520-525

[102] Spooner, E, Gordon, P, Bumby, JR and French, CD: "Lightweight ironless-stator PM generators for direct-drive wind turbines", 2ND IEE PEMD CONFERENCE, 2004, pp. 29-33

[103] Spooner, E, Gordon, P, Bumby, JR and French, CD: "Lightweight ironless-stator PM generators for direct-drive wind turbines", IEE PROC.-ELECTR. POWER APPL., Vol. 152, No.1, 2005, pp. 17-26